QUANTIFYING BOUNDARY INTERACTION OF NEGATIVELY BUOYANT JETS

By Aditya Ramakanth

A thesis submitted in partial fulfilment of the requirements for the degree of Doctor of Philosophy in Civil Engineering

20th March 2016

Supervisors: Dr. Mark J. Davidson and Dr. Roger I. Nokes

University of Canterbury

Department of Civil and Natural Resources Engineering

Christchurch, New Zealand

Abstract

The use of desalination around the world has increased substantially over the past several decades to provide a sustainable source of water. Desalination plants employ turbulent negatively buoyant jets to dispose brine effluent that is produced from the desalination process. The effluent is characterised by elevated density and contaminant levels and potentially poses a direct threat to the marine environment if the discharge does not dilute to acceptable concentrations. This aspect has led to an important area of research where numerous studies have been conducted to investigate the mixing characteristics of these dense discharges. These studies have quantified the flow behaviour using dilution and geometry measurements. Despite this focused effort, significant variations exist between different studies particularly with regards to the flow dilutions. These differences have recently been attributed to the inconsistent placement of a horizontal lower boundary near the vicinity of the discharge location. The influence of the lower boundary is still unclear and the present study addresses this issue through a comprehensive experimental program. Boundary effects are analysed by comparing the flow behaviour with and without imposed boundary influences in a stationary and uniform ambient. Experiments have been conducted using the Laser Induced Fluorescence (LIF) technique which produces two-dimensional concentration fields.

Boundary influence is initially investigated using simple vertical flows discharged onto a raised horizontal circular platform with varying amounts of buoyancy. The flow impinges the lower boundary and spreads radially along the boundary. The behaviour of the flow field is characterised using dilution and velocity results, where velocity information was obtained from a previous researcher. The discharge height above the platform is varied and results are presented for a wide range of initial condition. Numerous flow parameters illustrate the

influence of the boundary and are used to define the extent of the impingement/impact region. An integral model is developed specifically for non-buoyant jet flows and predictions are reasonably consistent with experimental results.

This analysis is extended to inclined negatively buoyant jets where experiments have been conducted for three discharge angles of 30^o, 45^o and 60^o above the horizontal. This flow configuration is more representative of discharges from desalination plants. Experiments conducted without boundary influences have a minimum clearance of 720 mm between the source and the bottom tank wall. Geometric and dilution results from these experiments are consistent across all parameters tested. Boundary influences are imposed on the measured flow region using the raised platform which is placed at various heights below the discharge source. Empirical dilution and geometric coefficients are compared to experiments without the raised platform and reveal important distinctions in behaviour between the two series of experiments. At the maximum height, differences between each data set are minimal. Near the return point and the platform location, the influence of the boundary is more apparent as measurements are shown to increase linearly with the source height parameter. This parameter is also used to investigate inconsistencies between results reported in the literature. Results from previous studies show an intuitive variation with the source height, suggesting that these discrepancies are in part associated with this boundary condition.

Acknowledgements

It is with great pleasure that I acknowledge the assistance of my supervisors, colleagues, friends and family, without whom the completion of this PhD would not have been possible. Thanks must first go to my supervisor, Dr. Mark Davidson, who first introduced me to the topic of desalination in the final year of my undergraduate degree and gave me the confidence to pursue a PhD. You have guided me through each step of this process and your mentorship and support encouraged me to constantly push the boundaries of what I was prepared to do. To Dr. Roger Nokes, thank you for providing a valuable second opinion on many aspects of my research. Your vast technical knowledge was extremely helpful in making sense of a number issues that I encountered. Thank you to my friends and colleagues; Dr. Ayaka Kashima, Dr. Colin Whittaker, Jeff Tuck, Varun Joshi and Sam McHattie for the conversations we had. Special thanks must also go to Dr. Cameron Oliver and Dr. Adam Crowe for helping me during the initial stages of my research and showing me how to operate the experimental system. To Ian Sheppard and Kevin Wines, thank you for greatly assisting me with my experimental work. Ian, you were always there to organise anything that I needed and also suggest ways of solving various problems that I encountered. To Kevin, thank you for putting up with my incompetence and teaching me how to use basic workshop tools. In particular, thank you for spray painting the Perspex platform on multiple occasions. I know how much of a hassle it was and I appreciate you for doing that. Finally I would like to thank my parents, Asha and Ram for their support, both emotionally and financially. Your unwavering belief in my ability helped me through the tough times and eventually dragged me over the finishing line. Thank you for all the opportunities you have provided me over the past 26 years and for this reason I would like to dedicate this thesis to you both.

Table of Contents

Chapter 1 Introduction

1.1 Water Shortages and Desalination

With an ever growing population, the strain on natural resources such as fresh water is becoming increasingly evident. Clean potable water is progressively becoming a scarce commodity with many non-renewable sources of fresh water being depleted. It has been estimated that almost 20% of the world's population is facing a lack of access to safe drinking water (Danoun, 2007). Moreover, the United Nation's "World Water Development Report" suggests that more than 50% of countries will face water shortage issues by 2025 (United Nations, 2003). The urgent need to improve safe access to water has been highlighted on numerous occasions and most noticeably, was included in the Millennium Development Goals (MDG) at the United Nations Millennium Summit in September, 2000. Predictions suggest that water withdrawals will increase by 50% in developing countries and 18% in developed countries by 2025 leaving an unsustainable demand for fresh water (United Nations Environment Programme, 2007).

The challenge that has been presented is to find new, creative and lasting methods to address this problem. The development of desalination as a means of providing fresh water has become increasingly viable because of process improvements and associated cost reductions. Desalination is the process in which fresh water is extracted from salt water (typically seawater) for human consumption or irrigation purposes. Seawater represents approximately 97.5% of the world's total water supply, while fresh water comprises only 0.5%. Desalination can therefore provide a more sustainable solution for water distribution and ease the pressure on traditional sources such as surface water and ground water. This method has typically proved popular in semi-arid areas such as the Middle-east where desalination technologies have historically been at the fore-front. With the development of more energy and cost

efficient technologies, desalination plants have been utilised in areas such as Australia, Europe and North America. More than 17000 desalination plants currently exist with the capacity to produce in excess 80 million m^3 per day (International Desalination Association, 2014). Two methods have traditionally been utilised in large scale desalination plants; Multi-Stage Flash (MSF) and Seawater Reverse Osmosis (SWRO). MSF is a distillation process where seawater undergoes various stages of flash evaporation by reducing the pressure. The flashed water vapour is subsequently condensed to produce distillate. MSF was the original desalination method of choice and was first implemented in Saudi Arabia in 1928 (Al-Mutaz, 1996). The majority of large scale desalination plants still utilise distillation methods and in 1999 approximately 78% of the world's desalination capacity was made up of MSF plants while SWRO represented only 10%. Recently, there has been a trend towards SWRO desalination and its usage around the world is gradually increasing (Khawaji et al., 2008). For instance, desalination plants proposed in over 13 locations in Australia and 21 locations in the US state of California, all utilise reverse osmosis technology (Cooley et al., 2013; El Saliby et al., 2009). In SWRO plants, seawater is passed through a series of semi-permeable membranes which separates two solutions of differing salt concentration. An external pressure gradient is imposed across the membrane that exceeds the osmotic pressure of seawater. Seawater is made to flow in the opposite direction across the membrane leaving behind the dissolved salt. Compared to Multi-Stage Flash, SWRO desalination presents a number of economic and operational advantages. Reverse osmosis plants have proven to be more efficient in recovering freshwater and are more reliable in satisfying desired safe drinking water levels (Voutchkov, 2011). Moreover SWRO plants consume less energy per cubic meter of water produced than MSF plants, using only 4 – 7 kW H compared with 15.5 kW H (Wangnick, 2004). Differences in performance between MSF and SWRO plants are discussed in detail in Al-Mutaz (1996).

1.2 Environmental Impacts and Brine disposal

While the benefits of ocean water desalination to society are potentially significant, there are environmental drawbacks that must be considered. Construction and long-term operation can have adverse environmental impacts. Seawater is typically supplied to the plant through vertical bore holes constructed on a nearby beach or through pipelines connected to a water

intake (Bleninger and Jirka, 2010). The consequences of this process to the local marine environment have been well documented (Cooley et al., 2013; Lattemann and Höpner, 2008; Nellen, 2011). At the seawater intake marine organisms such as fish, invertebrates and even mammals can die upon collision with the intake screens (called impingement); while organisms small enough to bypass intake screens are entrained into the desalination facility and killed as saltwater is treated (Cooley, 2010). Various measures are taken to mitigate the impingement of aquatic life through physical barriers and behavioural deterrents which prevent fish from entering the intake area.

The most pressing environmental concern associated with desalination, is the management of the effluent that results from the desalting process. Lattemann and Höpner (2008) describes the nature of the effluent from the primary desalination methods. Effluent from Reverse Osmosis (RO) plants are typically high concentration brine discharges. The elevated salt concentrations results in negative buoyancy with an approximate 3% density difference in comparison with its surrounding ambient (~1050 kg/m^3 - 1065 kg/m^3 compared to typical seawater density levels of 1025 kg/m^3). Similarly, MSF desalination produce discharges with increased salinity (~1035 kg/m^3), but also significantly elevated temperatures in comparison with the ambient (approximately 5 to 15 ^0C above the ambient seawater level). In addition to increased salt concentrations and temperature levels, several types of chemicals used in the pre and post treatment operations are also present in the waste effluent. Chemicals such as Sodium hypochlorite (NaOCl), Ferric chloride ($FeCl_3$) and Sodium hexametaphosphate ($NaPO_3$)6 are introduced to remove suspended matter from the water and to minimise deterioration of the desalination facility (Ahmad and Baddour, 2014). The most common disposal method, carried out by over 90% of large scale plants, involves discharging this effluent back to the sea through an offshore outfall, thereby directly affecting the local marine environment. Many organisms can adapt to minor changes in their environment and may temporarily tolerate extreme situations. However a continuous exposure to unfavourable conditions can be fatal. Organisms can be attracted or repelled by the new environmental conditions causing a lasting change in species composition at the discharge site (Lattemann and Höpner, 2008). For these reasons, regulatory standards are set in relation to the minimum effluent dilution that must be achieved. The intensity of the imposed restrictions vary between regions due to differing marine environments and possibly due to discrepancies in

general awareness of the environmental implications of brine discharges (Einav et al., 2003). For example, the European Union water policy directives provide no clear regulations or limits with regards to the disposal of waste effluent from desalination plants in Mediterranean countries. Increased salinity levels are not considered to significantly affect marine life (Gibbons et al., 2008). In contrast, the Australian Environmental Protection Agency (EPA) requires an Environmental Impact Assessment to be submitted prior to construction showing no significant impacts to the surrounding ambient. For the Perth SWRO desalination plant the Australian EPA required that salinity levels remain within 1.2 ppt (parts per trillion) and 0.8 ppt of the original ambient levels within a mixing region of 50 m and 1000 m from the initial discharge point respectively (Welker Environmental Consultancy et al., 2002). The concept of a mixing region or zone is common for most regulatory frameworks where the concentration of the discharge must decay below a certain level within this area. Mixing of the brine with the ambient environment is promoted by discharging the effluent at high velocities through a series of subsurface discharge ports. The effluent is released as a turbulent flow which enables dilution to occur in an efficient manner. The increased salinity (and density) of the effluent relative to the receiving environment suggests that the resulting flow can be modelled as an inclined negatively buoyant jet (INBJ). Figure 1.1 depicts the ejection of reject brine from the outfall system. As shown, brine is transported along a pipeline before being discharged into the receiving ambient. Fluid is released at an upward inclined angle (typically 60^{o}), but it eventually descends towards the sea floor due to its elevated density and spreads laterally in all directions.

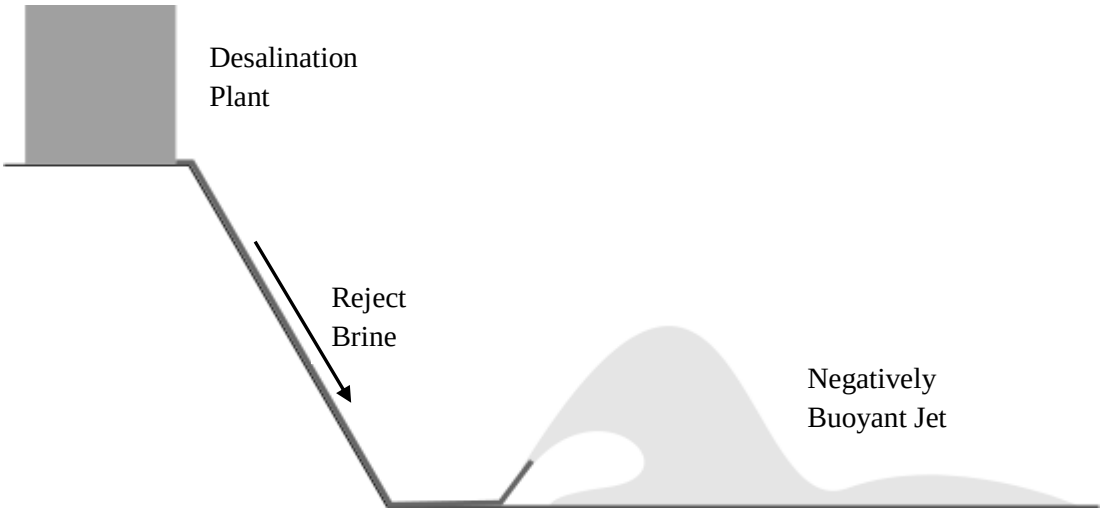

Figure 1.1: Transport of discharge of reject brine from a desalination plant outfall.

In practise, offshore outfalls utilise multiple ports at the end of the discharge pipe in order to manage the large volumes of brine created from the desalination process. Design parameters that must be considered include the length and diameter of the pipeline, the orientation and elevation of the ports above the seabed and the layout of the diffuser. Figure 1.2 has been taken from Ahmad and Baddour (2014) and illustrates different layouts of marine outfalls used in desalination plants around the world. The mixing zone corresponding to each outfall has also been outlined.

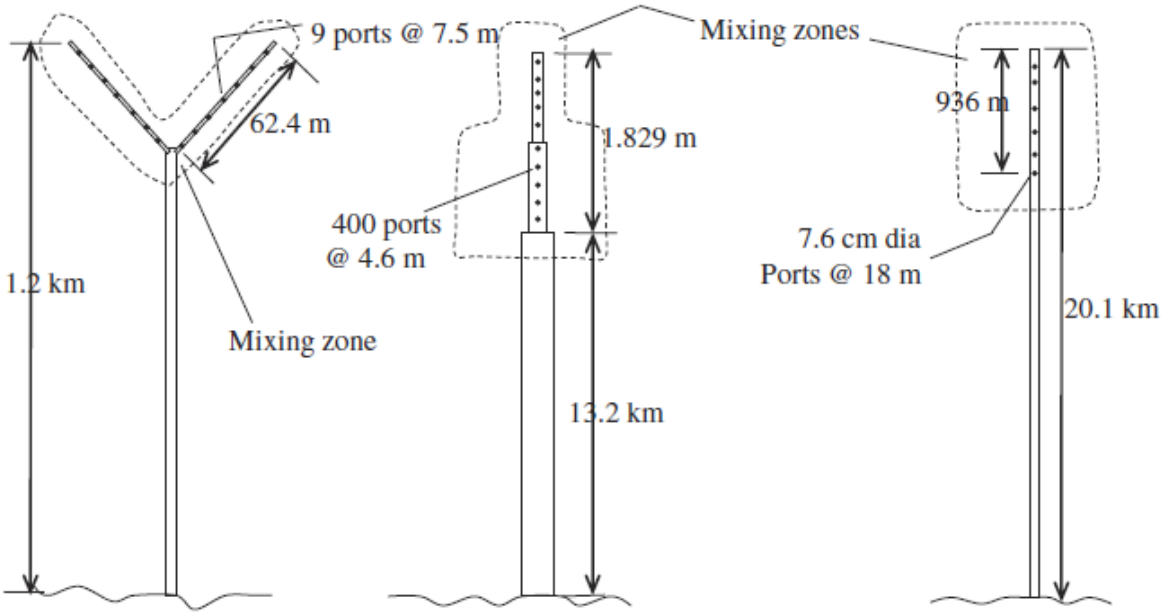

Figure 1.2: Various marine outfall layout systems with multiport diffusers. Figure taken from Ahmad and Baddour (2014).

The behaviour of the ensuing flow is dependent on the initial conditions selected for the diffuser system as well as the characteristics of the receiving environment. Initial conditions include the momentum flux imparted to the discharge, buoyancy flux (relative density of the brine and ambient fluid) and the angle of release. Different ambient conditions can also affect the flow trajectory and level of mixing that takes place. Ambient or ocean currents generally have a positive effect on dilution and their effects are not normally critical for design purposes (Jirka, 2004). However, confinement of the flow due to the proximity of the seabed

and variations in the density profile of the ambient (density stratified environments) can have adverse implications on the mixing potential of the flow. Interaction with the seabed poses a more likely threat to the mixing ability of such flows. Due to design constraints, discharge ports may be located near the seabed resulting in early impingement of the flow. As the effluent impacts the lower boundary the dilution potential is appreciably diminished as the volume of ambient (clean) fluid available to be entrained is reduced. As such, quantifying the extent to which seabed impingement affects the discharge is an important topic of study.

1.3 Scope of Investigation

Dense discharges from sub-marine outfalls and their interaction with solid surfaces such as the seabed is not yet fully understood in the literature. To address this issue, a comprehensive study has been carried out to investigate turbulent flows impacting a horizontal boundary. In recent years, the increased use of desalination around the world has coincided with a number investigations on the mixing properties of INBJ's. Previous studies include Kikkert et al. (2007), Lai and Lee (2012), Oliver et al. (2013), Papakonstantis et al. (2011b), Roberts et al. (1997), Roberts and Toms (1987). In each case, trajectory and dilution (concentration) information were obtained and comparisons between studies showed concerning inconsistencies. Oliver et al. (2013) suggested that differences in the location of a boundary below the discharge point might be partly responsible for variations in dilution measurements between studies. Very few studies have explicitly assessed lower boundary effects on INBJ's (Crowe, 2013; Shao and Law, 2010). Experimental results from these studies present some insight into the issue and provide direction for further investigating the implications of a lower boundary. The following research is a continuation of this process. Here, the issue of the lower boundary is qualitatively and quantitatively analysed through a series of experiments designed to assess this aspect of the flow behaviour. A summary of each chapter is given below.

Chapter 2: The fundamental concepts associated with inclined negatively buoyant jets are introduced as well as an extensive discussion on the relevant literature pertaining to the flow configurations investigated in the present study.

Chapter 3: A 2-D Laser Induced Fluorescence (LIF) system was employed to conduct experiments discussed in this thesis and is described in this chapter. LIF is a non-intrusive optical technique that measures concentration flow fields. In addition, a description of the experimental apparatus and the associated verification and post processing systems are provided.

Chapter 4: Results relating to vertically discharged buoyant jets impacting a horizontal lower boundary are presented in this chapter. Although the primary focus of this study is inclined negatively buoyant jets due to their direct application to desalination outfalls, boundary interaction could be explored in more detail using this flow configuration due to its relative simplicity. Concentration and velocity results obtained experimentally and analytically (integral model), have been used to investigate this flow type. These results provide guidance for investigating flow impingement of inclined negatively buoyant jets which are comparatively more complex.

Chapter 5: Experimental results on INBJs discharged into unbounded environments are analysed in this chapter. This data set verifies results from Oliver et al. (2013) who provide the only other data set not affected by lower boundary confinement. Concentration and geometric results are used to characterise this flow type and provide the basis for comparison for experiments discussed in the subsequent chapter.

Chapter 6: Boundary interaction of INBJs are analysed in this chapter. In order to appropriately ascertain the boundary's influence on the flow, the discharge height above the boundary (source height) was varied. The flow behaviour has been assessed using concentration and geometric data and investigated in the context of the source height above the boundary. Results are compared to experiments discussed in Chapter 5 and relevant studies in the literature.

Chapter 7: Finally, conclusions from this study are summarised, with areas for future work suggested.

Chapter 2 Background and Literature Review

2.1 Equations of Motion

A negatively buoyant jet, or more generally, a buoyant jet, exhibits properties associated with two asymptotic flow types; jets and plumes. By definition, a pure jet refers to a flow dominated by the momentum flux (per unit density) initially imparted to it (M_o) while a pure plume is buoyancy driven or a buoyancy dominated flow. The source of buoyancy may arise from density differences between the discharged and the ambient fluids whose magnitude is given by the buoyancy flux term (B_o). These quantities are defined below

$$M_o = u_0 Q_0 \qquad 2.1$$

$$B_o = g'_0 Q_0 \qquad 2.2$$

Note that $Q_0 (= \frac{\pi}{4} u_0 d^2)$ is the initial volume flux for a circular discharge source, d is the source diameter, u_0 is the initial velocity and $g'_0 (= g(\rho_0 - \rho_a)/\rho_a)$ is the modified gravity term with g representing the gravity term (9.81 ms^{-2}) and ρ_0 and ρ_a giving the initial flow density and ambient density respectively.

Mass, buoyancy and momentum flux equations are fundamental in understanding the behaviour of such flows. Consider a flow released into a uniform and still ambient. The discharge spreads radially as large scale rotational motions, known as eddies are generated from the resulting shear layer and entrain ambient fluid into the primary flow. The mass flux at a particular cross-section of area, A, is given in Equation 2.3.

$$\rho Q = \int_A \rho \, u \, dA \qquad 2.3$$

If we consider the mass flux that is entrained between the source and an arbitrary point along the flow, denoted 'n', the mass flux can be directly calculated as shown in Equation 2.4.

$$\rho_n Q_n = \rho_0 Q_0 + \rho_a Q_{entrained} \qquad 2.4$$

This relationship can be extended to show that the buoyancy flux is conserved along the flow path ($B_0 = g'_0 Q_0 = g'_T Q$). Variables with the subscript 'T' represent local average or 'top-hat' values. In general the buoyancy flux is expressed as:

$$B = \int_A u\, g'\, dA \qquad 2.5$$

The momentum fluxes in the flow are defined by Equation 2.6. The change in momentum flux in a particular direction between two points along the flow is equal to the net force acting on the flow in the same direction. In this instance, 'x' refers to the horizontal direction and 'z' refers to the vertical direction.

$$M_x = \int_A u\, u_x\, dA = \sum F_x \qquad a)$$

$$M_Z = \int_A u\, u_z\, dA = \sum F_z \qquad b) \qquad 2.6$$

For the jet case, external forces do not act on the flow ($\sum F_x = \sum F_z = 0$), hence the momentum flux at each location along the flow is equal to the initial momentum flux ($M_o = u_0 Q_0 = u_T Q$). In contrast the momentum flux of a plume changes in the vertical direction because of the buoyancy forces that arise from the density differences between the flowing and the ambient fluid. The momentum flux in the horizontal direction remains the same, however in the vertical direction, the momentum flux will be non-zero and the RHS of Equation 2.6b can be equated to the buoyancy generated momentum flux (M_B).

2.2 Dimensional Framework

The general framework used to analyse turbulent flows discharged into a still ambient is presented. Oliver (2012) describes a buoyant jet as an initially momentum flux (M_0) dominated flow with a non-zero initial buoyancy flux (B_0). Upon discharge, the flow acts as a jet, where its behaviour is governed by the initial momentum flux. As buoyancy generated momentum, M_B, increases relative to M_o, the flow undergoes a transition to the plume regime. The relative extent of the jet and plume regimes is dependent on the imposed initial conditions. Using scale analysis, two important length scales can be used to characterise flow transitions; the discharge length scale (l_{jQ}) and the jet to plume length scale (l_{jp}) (Fischer et al., 1979).

$$l_{jQ} \sim \frac{Q_0}{M_0^{\frac{1}{2}}} \qquad 2.7$$

$$l_{jp} \sim \frac{M_0^{\frac{3}{4}}}{B_0^{\frac{1}{2}}} \qquad 2.8$$

The discharge length scale (l_{jQ}) represents the relative importance of the initial volume flux to momentum flux and defines the region where the discharge geometry influences the flow properties. Any analysis of the flow beyond this point can neglect the volume flux at the source. Roberts et al. (2001) approximate this distance as $7l_{jQ}$ from the source. This region is referred to as the zone of flow establishment or the 'potential core' of the flow. In most turbulent flows, the relative size of this region is small and is therefore neglected when considering the overall flow behaviour. Further along the flow path, the contribution of buoyancy generated momentum flux will surpass the initial momentum flux, characterising the flow transition from a jet to a plume regime. The distance at which this regime change occurs is given by the jet to plume length scale (l_{jp}). The jet to plume transition is not instantaneous but occurs over a transition distance along the path length. Papanicolaou and List (1988) determined flow classifications based on l_{jp}, as shown in Equation 2.9, using experiments on round vertical buoyant jets discharged into unbounded ambient environments. Note that z is the vertical distance travelled by the flow.

Jet	$z/l_{jp} \leq 1.0$	a)	
Transitional Buoyant Jet	$1.0 < z/l_{jp} \leq 5.0$	b)	2.9
Plume	$5.0 < z/l_{jp}$	c)	

The first delineation (Equation 2.9a) was determined from the total momentum flux along the flow path. Beyond z/l_{jp} = 1.0 this quantity was observed to increase due to buoyancy generated momentum, thereby transitioning the flow to a buoyant jet state. The transition to plume flow is characterised by a rapid increase in the rate of volume flux entrainment. Hence this criteria was used to determine the inequality in Equation 2.9b and c. These classifications are generally consistent with other studies although minor variations do exist. For example Wang and Law (2002) marks the transition from jet to buoyant jet at z/l_{jp} = 0.6 while also stating that the plume transition occurs at a distance of z/l_{jp} = 6.0 from the source. The jet to plume length scale can also be represented as the densimetric Froude number ($F_0 = u_0/\sqrt{g_0'.d}$), which defines the ratio of inertial to buoyant forces initially acting on the discharge. The relationship between these two quantities is; $l_{jp} = (\pi/4)^{1/4}F_0 d$. The flows considered in the present study are turbulent upon discharge.

The Reynolds number ($Re_0 = u_0 d/\nu$), is a dimensionless quantity representing the ratio of inertial forces to viscous forces (represented by the viscosity, ν). For turbulent flows it is widely established that local mean parameters are independent of the Reynolds number. It is important that this condition is satisfied as the mixing potential of laminar flows (when Re_0 < 2000, Fischer et al., 1979) are significantly lower.

The source height above the boundary (H) is an important initial condition to the present study. The dimensionless form of the source height is dependent on the properties of the discharge above the boundary. For jet type discharges where the flow is momentum dominated, the source height is presented as H/d (Beltaos and Rajaratnam, 1974). When buoyancy is relevant to the discharge behaviour (plumes, buoyant jets), $H/F_0 d$ is a more appropriate form of the dimensionless source height (Shao and Law, 2010; Ulasir, 2001).

2.3 Flow properties

The general behaviour of turbulent flows can be described using velocity, concentration and flow geometry. Beyond the zone of flow establishment, the time-averaged concentration (or density) and velocity distribution along a cross-section perpendicular to the flow direction closely follows the Gaussian shape. Studies have indicated that these profiles have differing widths, the extent of which is denoted by the concentration to velocity spread (width) ratio (λ). Wang and Law (2002) reports values for this ratio of 1.23 for jets and 1.06 for plumes. Velocity and Concentration distributions can be represented using the following expressions:

$$\frac{U}{U_m} = e^{-r^2/b^2}, \quad \frac{C}{C_m} = e^{-r^2/(\lambda b)^2} \qquad 2.10$$

where b represents the characteristic radius of the velocity profile or spread; r is the radial distance from the flow centreline; U is the time-averaged velocity, C is the time-averaged concentration. The remainder of the thesis refers to the concentration spread as $b_c(=\lambda b)$. Each profile has been normalised by the corresponding maximum value in the perpendicular flow cross-section (denoted by the subscript m).

At this stage it is worth discussing the relationship between dilution and concentration. The dilution at any point along the flow trajectory is the initial concentration of the source fluid normalised by the local maximum concentration (C_0/C_m). This definition of dilution corresponds to the minimum dilution along the flow trajectory. The average or 'top-hat' dilution along a particular flow cross-section is given by C_0/C_T. Concentration is also representative of the flow density, hence g'_0/g'_m or g'_0/g'_T is an alternative determination of dilution. Note, the relative volume flux can also be used to define the dilution because the buoyancy flux is conserved along the flow path ($B_0 = g'_0 Q_0 = g'_T Q$).

$$\frac{Q}{Q_o} = \frac{g'_0}{g'_T} = \frac{C_0}{C_T} \qquad 2.11$$

2.4 Experimental Methods

Researchers have traditionally obtained flow information through the use of point measurements and images (continuous and still). Point measurements can provide accurate dilution information, however they require the insertion of probes into the region(s) of interest (thereby affecting the flow). Conductivity probes have been most widely used allowing salinity levels (and therefore concentrations) to be calculated through the changes in electrical conductance. Optical techniques involve the use of images and can obtain flow information in a non-intrusive manner. Methods such as Light Attenuation (LA), Laser Induced Fluorescence (LIF), Particle Tracking Velocimetry (PTV), Particle Imaging Velocimetry (PIV) and Shadowgraph have proved popular. These are described below:

Light Attenuation: When light of a given wavelength passes through a dye, it is absorbed or attenuated to some extent depending on the dye's sensitivity to that wavelength. The reduction in light intensity can be correlated to an 'integrated concentration' of the dye (and by extension the flow). The integrated concentration at a particular location represents the cumulative effect of all dye molecules along the path that extends from the light source to the camera. As such it is distinct from point measurements. The theory behind LA is based on the Beer Lambert law which is defined in Equation 2.12. This equation determines the proportion of the incident radiation that is absorbed by a chemical solution or coloured dye (LHS of the equation) based on the properties of the solution (RHS of equation).

$$\ln\left(\frac{I}{I_0}\right) = -\varepsilon r C \qquad 2.12$$

where I_0 is the intensity of an uninterrupted light source reaching the camera, I is the intensity of the light recorded by the camera, r (m) is the distance travelled through the solution (path length), C (mg/l) is the concentration of the solution and ε (mg /l m) is the coefficient of molar absorption which is specific to a particular wavelength of light. The log-linear relationship between the intensity and the concentration is only valid up to a critical tracer concentration. As the concentration increases, interactions between adjacent molecules make this relationship invalid (Kikkert, 2006).

Laser Induced Flourescence: LIF is the technique used in the present study to measure tracer concentrations. The discharged fluid is seeded with fluorescent dye which is illuminated by a thin light sheet. The excited dye molecules in turn emit light of a different wavelength to that of the original light sheet. A digital video camera with an attached filter records the flow, obtaining intensity measurements of light emitted from only the fluoresced dye. The emission intensity can be related to the tracer concentrations through a previously developed calibration process. Concentration data obtained using this method are also integrated concentrations, however as only a thin section of the flow has been illuminated (using the light sheet) this information can be interpreted as point measurements.

Particle Tracking Velocimetry and Particle Imaging Velocimetry: These techniques obtain velocity field information and involve seeding the discharged fluid with neutrally buoyant particles. Particles are illuminated by a thin light sheet and their motion is recorded in a continuous manner to provide a two dimensional view of the flow. To determine velocity patterns, algorithms are used to identify particles from frame to frame. PIV takes small windows of the intensity field in a video frame and correlates them with similar sized windows in the next frame. The location of the window with the maximum correlation determines the new position of the particles. Because the time step between frames is known, an estimate of the particle velocity can be calculated. PTV employs a more sophisticated approach as velocity fields are constructed by tracking individual particles from frame to frame.

Shadowgraph: This flow visualisation technique exploits the refractive index differences that exist between the discharged and ambient fluids to obtain flow information. A disturbance caused by the introduction of fluid of differing density to the receiving water is difficult to observe with the naked eye. However these disturbances refract light rays (due to differences in density and thus refractive index) and can be exposed by casting a shadow onto a nearby surface. Relative tracer concentrations can be qualitatively inferred by identifying areas where high density gradients exist. In comparison to the optical techniques described above, Shadowgraph is a relatively crude method of obtaining flow information.

2.5 Computational Modelling

Modelling is not a primary focus of the present study, however modelling results are used for design and research purposes. Empirical relationships from experimental data are also important from this perspective, but they do not provide insight into the physics of the mixing processes. In research and design, two techniques are primarily used: CFD (computational fluid dynamics) modelling and integral modelling.

Integral Models: Integral models are utilised more than CFD modelling in design due to their relative simplicity and shorter simulation run times. As a result, flow information is able to be obtained over a more practical time frame at a reduced cost. The pioneering works by noted researchers Morton, Taylor and Turner (Morton et al, 1956) form the basis of integral models. They presented a simple integral model that tracked a vertically discharged flow in homogenous and density stratified environment. This model uses concepts of momentum, buoyancy and mass flux conservation to define flow properties. The main assumptions behind this model are as follows:

- "That the rate of entrainment at the edge of the plume or cloud is proportional to some characteristic velocity at that height." This proportionality constant is known as the entrainment coefficient.
- "That the largest local variations of density in the field of motion are small in comparison with some chosen reference of density, this reference being taken as the density of the ambient fluid at the level of the source" This is also known as the Boussinesq assumption.
- "That the profiles of mean vertical velocity and mean buoyancy force in horizontal sections are of similar form at all heights" These profiles generally have a Gaussian form.

Entrainment coefficients have largely been established in the literature and are based on a characteristic velocity known as the entrainment velocity. Fischer et al. (1979) and List (1982) reported values of 0.0535 for a jet and 0.0833 for a plume. In a buoyant jet, the entrainment coefficient follows some relationship between these two limiting values. An alternate method to the entrainment assumption is to use a spreading rate. This relationship

directly describes how the radius of the flow (b) varies along its path (s). The width or spread measurement is taken as the perpendicular distance from the centreline to the point corresponding to $e^{-1}U_m$ or $e^{-1}C_m$ where U_m and C_m are the centreline velocity and concentration value. Experimental velocity measurements from Wang and Law (2002) suggest a spreading rate of 0.105 for jets and plumes. Concentration measurements from this study showed slightly higher spreading rates of 0.129 and 0.109 for jets and plumes respectively.

CFD Modelling: A more elemental approach to predicting the flow behaviour is through CFD modelling where a version of the Navier-Stokes equations are numerically solved. An important feature of CFD modelling is their ability to represent turbulence using turbulence models. The most accurate method is Direct Numerical Simulation (DNS) which resolves all spatial scales of turbulence on a computational mesh. This method is the most reliable and comprehensive, however large processing times are required making it impractical to model fully turbulent flows considered in this field of research. To simplify the problem at hand, a time-averaged form of the Navier-Stokes equations (termed Reynolds Averaged Navier-Stokes or RANS equations) can be used. After averaging, a non-linear term arises called the Reynolds stress which is estimated using relatively simple turbulence models such as k-ε turbulence models. A combination of the aforementioned methods is Large Eddy Simulation (LES) which models large scale turbulence using DNS and small scale turbulence using a simple eddy-viscosity model. Relatively accurate results are able to be obtained over a more practical time frame.

2.6 Literature Review

Previous studies have utilised experimental programs and modelling procedures to interpret flow behaviour. The following section reviews the literature relevant to the flow configurations analysed in this study. Due to the scope of the thesis, experimental studies are reviewed in greater detail. However many of these studies have included a modelling component to complement experimental data and to highlight issues surrounding the interpretation of important flow features.

2.6.1 Vertical Discharges and Boundary Impingement

Vertical discharges impinging a horizontal boundary have been investigated in the literature using the framework outlined in Figure 2.1. The discharge is released at a height (H) above the boundary with an initial momentum flux (M_0) and buoyancy flux (B_0) if relevant. The resulting flow field is split into three separate regimes; free flow region, impact/impact region and boundary flow region (Beltaos and Rajaratnam, 1974). Each region is clearly delineated in Figure 2.1. Within the free flow region the flow behaves in the same way as a discharge released into an unconfined environment (where no boundary is present). The end of this region and the start of the impact region is characterised by a reduction in the flow's mixing potential as a result of the boundary's growing influence. Within the impact region the flow is re-directed and a horizontal flow forms. At the location where this flow is established the boundary flow region begins.

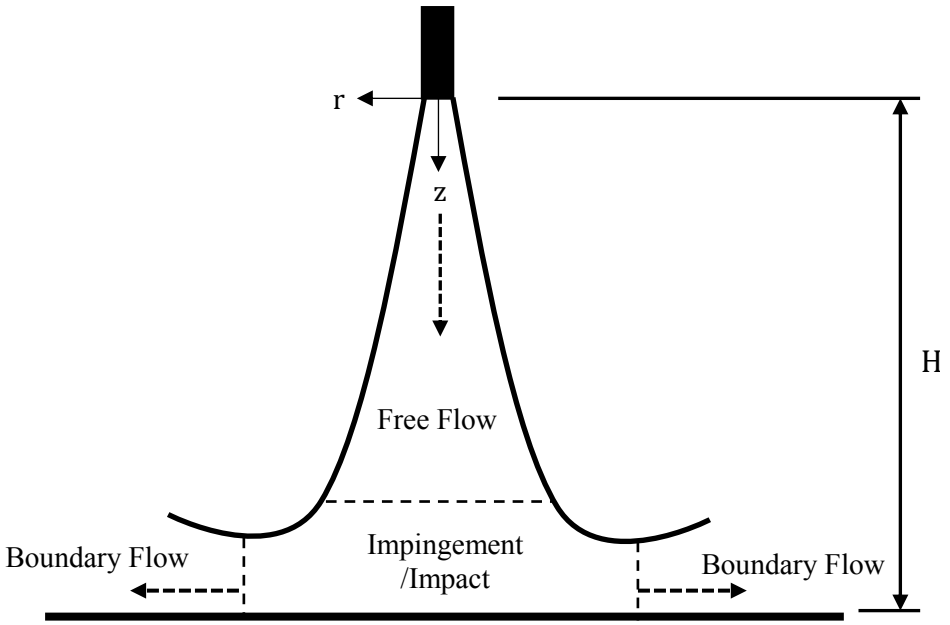

Figure 2.1: Flow configuration of a vertical discharge impinging a horizontal boundary.

2.6.1.1 Vertical Jets

Boundary interaction has predominantly been investigated using vertical jets. This discharge configuration presents a simple case with which to examine boundary impact as well as the ensuing boundary flow. Many of the basic integral formulations describing the behaviour of the free flow and boundary region have been included in Rajaratnam (1976). One of the first experimental studies on vertical jets was conducted by Beltaos and Rajaratnam (1974). Pressure and velocity measurements were obtained using a Pitot tube. The extent of each flow region was determined by setting pre-defined criteria and examining variations in flow measurements. For example, the end of the free flow region was marked by an abrupt decay in centreline velocity while the exit from the impact zone was defined when the excess pressure of the jet was zero and when the wall shear stress was at a maximum. Within the impact region, semi-empirical and analytical equations were developed to predict the variation of axial velocity and wall shear stresses. The flow along the boundary was termed the 'wall jet region' in this study and was shown to spread in a linear manner. Velocity profiles along the boundary illustrated the significant changes to the flow structure in comparison to the discharge above the boundary where simple Gaussian functions are used to model perpendicular flow profiles.

Other studies on vertical jets have focused their efforts on specific sections of the flow. Guillard et al. (1998) obtained concentration data of a pure jet impacting a horizontal boundary using Lase Induced Fluorescence. The flow region above the boundary was examined and the location of the incipient boundary influence was determined by observing variations in the spreading rate as well as concentration fluctuation statistics. The spreading behaviour was compared with LES (large eddy simulation) predictions and showed a noticeable increase in the spreading rate near the boundary. This region was termed the deflection zone. Although LIF was used, mean concentrations were not used to investigate boundary influence. Furthermore the flow behaviour near the boundary was not able to be captured and this was possibly due to calibration issues associated with incorporating a boundary in the experimental setup.

Maurel and Solliec (2001), examined the impact region of vertical jets using velocity data obtained from particle image velocimetry (PIV) and laser Doppler velocimetry experiments.

The extent of the impact region was assessed by analysing turbulent statistics such as Reynolds stresses. The variation of this parameter with the path distance was analysed and showed a consistent reduction near the boundary for different experiments. This approach was also employed by Koched et al. (2011) and they obtained results that are consistent with Maurel and Solliec (2001). Other researchers that have looked at similar turbulent parameters near the boundary include Rajaratnam et al. (2010) and Cooper et al. (1993), both of whom obtained velocities from probe measurements. Mean results were also presented by these studies, which include centreline velocities and the form of velocity profiles near the boundary. Near the boundary, centreline velocities were observed to drop while velocity profiles deviated from the Gaussian form.

Time-averaged and temporal statistics have also been obtained for the flow along the boundary. Knowles and Myszko (1998) described the turbulent and spreading behaviour of wall jets using velocities obtained from probe measurements. Turbulence measurements showed the fluctuating component normal to the boundary to be approximately 60% of the component parallel to the boundary. Turbulent velocity and mean velocity profiles achieved self-similarity at 4.5 and 2.5 diameters away from the impact point respectively. The spreading rate of the flow along the boundary began to grow linearly following a distance three diameters from the impact point. Poreh et al. (1967) conducted a study with a similar scope and the form of the mean velocity profile along the boundary was examined in great detail. Differences between the Gaussian form of these profiles in the free flow region and those of the wall jet were clearly evident in the measured data.

More detailed time-averaged information was provided in Fairweather and Hargrave (2002a, 2002b) where velocity and concentration measurements along the boundary were obtained using PIV and laser Raman spectroscopy methods respectively. Experiments were conducted with relatively low discharge heights, so that the flow in the free flow region was not fully established before reaching the impact region and hence the relevance of these results to situations where fully established jets impact a boundary is less clear. Birch et al. (2005) conducted a similar study where mean velocity and concentration parameters along the boundary were presented. Velocity and concentration profiles and boundary spread measurements from this study compared reasonably well with Fairweather and Hargrave (2002a, 2002b). Birch et al. (2005) also presented centreline concentrations within the free

flow region, however measurements near the boundary were not included to the extent that boundary influences were not evident.

The influence of relatively small source heights on flow behaviour was investigated by Beltaos and Rajaratnam (1977). They considered a range of non-dimensional source heights (H/d) and the behaviour within the impact region was found to be independent of H/d when flows were released less than 5.5 nozzle diameters from the boundary and were termed 'small'. The expected dependence on source height was evident when $H/d > 8.3$. Discharge heights between these limits were termed 'transitional'. These conclusions were obtained by observing axial velocity measurements and increases in pressure measurements as the flow approached the boundary. Based on this criteria experiments conducted by Guillard et al. (1998), Fairweather and Hargrave (2002a, 2002b), Cooper et al. (1993) would fall into the 'small' or 'transitional' category.

Rajaratnam and Mazurek (2005) investigated the influence of boundary roughness on the flow behaviour in the impact and wall jet regions. Boundary roughness was introduced by adding spherical protrusions to the boundary where the depth of these protrusions varied between 1.73 mm to 15.18 mm. Stagnation pressures were measured and it was found that this parameter displayed some dependence on the boundary roughness. Within the wall jet region however, spread and velocity measurements were compared to the smooth case and results remained unchanged for all cases tested.

A comprehensive investigation on vertical jet impingement was recently conducted by Ghaneeizad et al. (2015) using modern experimental methods. Experiments were conducted to replicate conditions in a jet-erosion test (JET) designed to assess sediment erosion parameters in the field. Particle Image Velocimetry (PIV) was employed to acquire flow velocities in the entire flow field. Volume flux, momentum flux and turbulent statistics such as Reynolds, normal and shear stresses were measured as the flow transitioned through the impact region. The dimensions of the experimental tank intentionally confined the flow to a relatively small ambient environment. Limited fluid was available for entrainment and re-circulation of the ambient was reported to have contributed to the observed flow behaviour.

2.6.1.2 Vertical Buoyant Jets

Buoyant vertical flows have not received the same amount of attention as the non-buoyant case however the body of work on this flow type is still significant. Cavalletti and Davies (2003) examined the boundary influence on flow characteristics prior to impingement. Experiments were conducted for vertical buoyant jets discharged from a rectangular slot where the source height parameter (H/l_{jp}) was varied between 1.6 and 7.0. Velocity and concentration field measurements were obtained using 2-D imaging techniques. The purpose of this investigation was to verify the flow's dependence on the densimetric Froude number ($F_0{}^{4/3}$), which was subsequently exhibited by multiple parameters. Velocity data was primarily used to demonstrate this where axial velocities and distortions to the velocity profile were measured along the flow path. Concentration fields highlighted the presence of side vortices near the impact region. The height of these vortices above the boundary was used as an indicator of the bottom boundary influence. These measurements also displayed dependence on the densimetric Froude number noted above.

Christodoulou et al. (2015) is one of the few studies where concentration measurements within the impact region were obtained. Experiments were conducted for round vertical dense jets discharged onto a lower boundary. Concentrations were measured at pre-defined locations using a microscale conductivity and temperature instrument. Centreline results showed that the flow continues to dilute up to a certain distance before stabilising prior to impacting the boundary. This measurement correlated well with the corresponding source height. The dilution at various locations within the impact region were recorded and plotted against the source height. Linear empirical relationships were developed, however significant scatter was evident in these figures. This scatter was highlighted by the associated goodness of fit coefficients (R^2) which were between 0.42 and 0.88 for each empirical equation. The results from this investigation provide the most direct comparison to experimental results presented in Section 4.3 of this thesis.

The literature relating to this flow type contains a plethora of studies where the mixing characteristics of the boundary region have been the main focus (Chen, 1980; Koop and Browand, 1979; Lawrence and Maclatchy, 2001; Ulasir, 2001; Ulasir and Wright, 2003; Wright et al., 1991). Unlike the wall jet where only source induced mixing drives the flow,

the contribution from buoyancy is shown to impact the flow behaviour. The presence of buoyancy within the boundary region is a stabilising influence and it suppresses shear induced turbulent mixing arising from the momentum flux imparted to the flow at the source. Entrainment of ambient fluid into the main flow is discontinued following the collapse of these mixing processes. This marks the transition from the near field region of the boundary flow, where source induced mixing continues to dilute the flow, to the far field region, where the flow has stabilised and its eventual fate is governed by ambient conditions.

Mixing within the near field region of the boundary flow was investigated by Wright et al. (1991). Prior to the flow stabilising (i.e. end of near field mixing), the dilution of the discharge was found to significantly increase within the near field region between three to five times. A model was developed to predict mixing in this region using a density jump approach. This method was first proposed by Wilkinson and Wood (1971) and employs concepts used to calculate a hydraulic jump in open channel flow. The end of this mixing zone was characterised by when local Froude Number (F_L) reduced to a value of one. This indicates the beginning of the far field region where buoyancy forces are significant enough to stabilise mixing processes and confine the flow to the boundary surface. Dilution predictions from the model were plotted against the corresponding source height (H/l_{jp}) and compared to experimental results. The model performed reasonably well however discrepancies were apparent for larger values of H/l_{jp}. The framework outlined in Wright et al. (1991) was expanded in Ulasir (2001) and Ulasir and Wright (2003). Negatively buoyant fluid was discharged onto an elevated circular boundary and concentration and velocity measurements were taken with a conductivity probe and a MicroADV. A similar model to Wright et al. (1991) was presented that predicted the dilution at the end of the near field mixing zone. Assumptions pertaining to the impact region are of particular interest. This region was not explicitly modelled however it was assumed that significant entrainment of ambient fluid did not occur, so the mass flux of the flow remained unchanged. Reasonable consistency was found between experimental results and model predictions, but discrepancies were still evident for larger source heights (H/l_{jp}). The influence of downstream topographical controls on the boundary flow was also investigated. A weir was placed at the outer rim of the boundary surface which restricted the distance over which entrainment could occur. As a result, the dilution at the end of the near field mixing zone was found to be lower

compared to the case where fluid was allowed fall over the edge of the boundary. The flow behaviour was also compared using two circular boundaries of differing diameter, 150 cm and 300 cm. No dependence on the diameter of the lower boundary was exhibited by the average flow properties.

2.6.2 Inclined Negatively Buoyant Jets

The flow configuration of an inclined negatively buoyant jet discharged above a boundary is depicted in Figure 2.2. The dense fluid is released at an angle (θ_0) above the horizontal and it immediately experiences a negative buoyancy force due to the density difference between the discharge and the lighter receiving water. The negative buoyancy, or buoyancy generated momentum flux (M_B), acts to reduce the vertical component of the initial momentum flux and eventually causes a flow reversal, driving the effluent towards the floor of the receiving body (sea bed). Kikkert et al. (2007) defines a negatively buoyant jet based on the initial vertical momentum flux being in the opposite direction of the buoyancy generated momentum flux. For a positively buoyant jet, these two momentum flux contributions act in the same direction.

Figure 2.2 highlights two regions of interest; the maximum height where the flow reaches its highest vertical trajectory and the return point, where the flow returns to its original source height. These points are important from a practical perspective and serve as reference locations when comparing flow properties between studies. The maximum height is the closest point of the flow to the free surface. It is desirable that no interaction with the free surface occurs as the discharge behaviour may be adversely influenced by surface effects (not included in the present study). Here, the distance to the centreline location (x_m, z_m) and vertical distance to the flow edge (z_{me}) is measured. The return point is a convenient reference location for comparative purposes and in practise, is in close proximity to the seabed. Important measurements include the horizontal distance to the centreline ($x_r, 0$) and the horizontal distance to the flow edge ($x_{re}, 0$) (Davidson and Oliver, 2012).

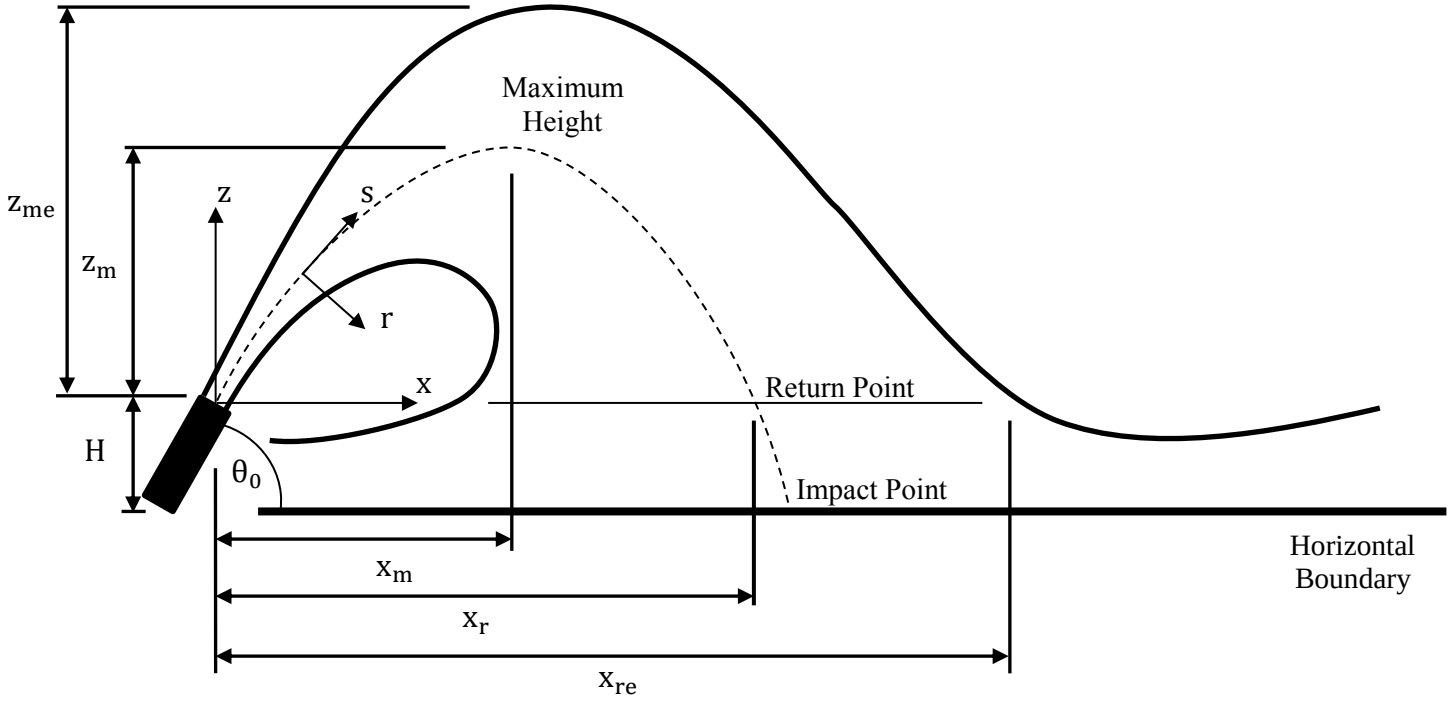

Figure 2.2: Flow configuration of an INBJ released onto a horizontal boundary located within the vicinity of the discharge location.

2.6.2.1 Geometric Data

Early studies on inclined negatively buoyant jets were constrained by the limited capabilities of the experimental systems. As such, these studies were confined to defining the geometric properties of the flow. Some recent studies have also focused on geometric parameters, however they have used relatively sophisticated optical techniques such as LIF to obtain more detailed information. Geometric coefficients from each study have been included in Table 5.1.

One of the first dedicated studies on dense jets was conducted by Bosanquet et al. (1961). Discharges were visualised using a magnetite slurry source fluid which provided colour and increased the flow density relative to the receiving ambient. Results for horizontal and 45^o inclinations were presented. Variations in the concentration along the flow path were not discernible due to the high concentration of the source fluid. Only the edges could be observed and provided the basis for delineating the trajectory of the flow. The flow centreline was determined by calculating the mean position of the upper and lower edges of the flow

field. The fluid at the source was also heated and vertical distributions of the temperature were measured using a fine-wire thermocouple. The temperature profile indicated that the maximum concentration axis was near to the axis of symmetry. The centreline trajectory was subsequently compared to an integral model where predictions matched experimental results for the horizontal case, but performed poorly for the 45^o inclination.

Zeitoun et al. (1970) conducted experiments within the context of desalination plant outfall design. Three discharge angles (30^o, 45^o and 60^o) were tested and the flow was visualised by adding Rhodamine B to the source fluid. Flow edge measurements at the maximum height were found to vary with the nozzle angle while recordings at the return point were the same for each inclination. The product of these measurements was calculated and the maximum value corresponded to a release angle of 60°. Under the same ambient conditions they reasoned that this release angle would produce the maximum dilution due to the available mixing length. Concentration (dilution) measurements were also taken by extracting samples from the flow and measuring their density. There were difficulties in determining the flow trajectory hence exact measurements at the centreline could not be taken.

Shadowgraph experiments were conducted by Lindberg (1994) for discharge angles of 30^o, 45^o, 60^o and 90^o. Photographic records of the flow structure were used to measure the dimensions of discharge. The geometry of the flow was described using edge measurements at the maximum height.

Bloomfield and Kerr (2002) analysed the maximum rise height that could be achieved by an INBJ, considering discharge angles ranging from 30^o to 90^o (fountain flows) above the horizontal. Experiments were visualised using the shadowgraph method and it was determined that a discharge inclination of 80^o produced the greatest maximum rise height. 90^o discharges were initially found to produce the greatest rise height, however continuous interaction between the ascending and descending flow reduced the final steady state height achieved by the flow.

Cipollina et al. (2005) also conducted experiments using a coloured dye to visualise dense flows. Images were recorded over 40 – 50 seconds and digital image processing on MATLAB allowed the centreline trajectory to be discerned. Distances to the centreline

maximum height and return point were accordingly taken. Each geometric parameter was found to correlate well with the corresponding Froude number.

Detailed information regarding the flow trajectory was obtained by Ferrari and Querzoli (2010). Experiments were conducted using the Laser Induced Fluorescence method and concentration fields were generated. Steep angle discharges were tested and the effect of re-entrainment was investigated. Similar to Bloomfield and Kerr (2002), this study found that discharge angles above 80^o resulted in re-entrainment of the descending flow into the ascending flow. The maximum rise height achieved by the flow was found to reduce as a result of this interaction. Moreover, re-entrainment caused the flow trajectory to bend inwards towards source. Concentration profiles along different cross-sections of the flow were presented and illustrated the lack of separation between the rising and falling arms of the flow. This study also examined the onset of Kelvin-Helmoholtz instabilities in relation to the discharge Froude number and the discharge angle. This phenomena was investigated using concentration variance data as the onset of this instability coincides with large concentration fluctuations. The distance from the source to where billows are initially formed was subsequently measured based on this criteria. A linear variance with the Froude number was evident and this observation was independent of the discharge angle.

Similar experimental studies were conducted by Papakonstantis et al. (2011a) and Bashitialshaaer et al. (2012). Both obtained an extensive set of geometric measurements for a wide range of discharge angles using flow visualisation techniques. Distances to the maximum height and return point were measured and scaling relationships with the Froude number and source diameter were confirmed. The relationship between these various geometric parameters and the discharge angle also aligned with observations made in previous studies.

2.6.2.2 Concentration and Dilution Data

Experimental dilution results reported in the literature display a concerning lack of consistency, especially with regards to measurements at the return point. This observation was noted in Oliver et al. (2013) who conducted an extensive experimental investigation on INBJ's, testing multiple discharge angles using LIF. Figure 2.3 summarises the various

studies that have reported return point dilution measurements for different discharge angles. Oliver et al. (2013) comments regarding the discrepancies in return point dilution data "This reflects the difficulty of measuring accurate dilution rates in a region where eddy timescales are considerable". There are a number of factors that may have contributed to these discrepancies, however the most likely is the use of different experimental setups. In particular many of these studies have included a lower boundary within the vicinity of the discharge location. Moreover the non-dimensional source height (H/F_0d) is not consistent between studies. Some studies in Figure 2.3 were specifically conducted to examine boundary effects (Roberts et al., 1997; Shao and Law, 2010) hence discrepancies are expected for these results. Oliver et al. (2013) is the only study to have removed boundary influences from the recording region where the smallest boundary condition tested was H/F_0d = 2.7. Dilution and geometric results from this study were consistent for all parameters tested (when scaled appropriately) and thus were independent of the boundary condition.

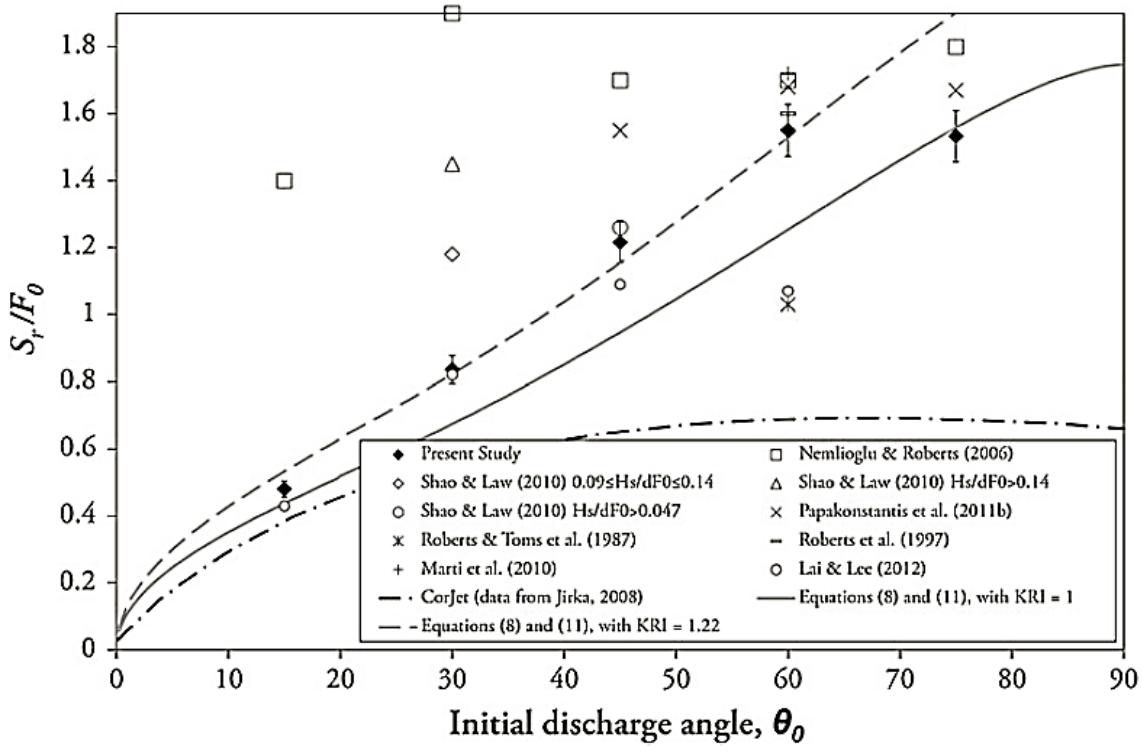

Figure 2.3: Dilutions taken at the return point for various discharge angles. Figure taken from Oliver et al. (2013).

Lai and Lee (2012), Papakonstantis et al. (2011b) and Roberts and Toms (1987) each conducted experiments where non-dimensional source heights were below 1.39, 0.92 and 0.08 respectively. Lai and Lee (2012) utilised imaging techniques (LIF) to obtain concentration data while Papakonstantis et al. (2011b) and Roberts and Toms (1987) measured flow densities using probe instruments. Roberts and Toms (1987) added Rhodamine B dye to the source fluid and concentrations of vacuum extracted samples were determined by fluorometer measurements. A vertically arranged rack of sampling tubes were positioned at perceived locations of the maximum height and impact point. In addition to the lower boundary, the intrusive nature of this measuring system may have affected the quality of the data. In Papakonstantis et al. (2011b), the density was measured by taking salinity and temperature recordings using a portable instrument. The probe was re-positioned within the flow field using a 3D traversing system and probe movement was slow to avoid disturbances.

Results from Marti et al. (2011) are from a field study of the Perth Seawater Desalination Plant. Dilution recordings were made using conductivity-temperature-depth profiling and were taken 50-150 m from the diffuser site. The diffuser height was 1 m from the seabed and recordings were taken for H/F_0d values between 0.32 and 0.90. Dilutions were taken at an estimated location of the impingement point. Given the scale of the flow, accurately identifying the impingement point proved difficult so empirical relationships from Roberts et al. (1997) were used to determine this location.

It is unclear whether lower boundary effects were a feature of Nemlioglu and Roberts (2006), where concentrations were measured using 3-D LIF. Return point dilutions are considerably greater than other studies and their values are almost the same for each angle tested. These results contradict the trend suggested by the remaining data sets in Figure 2.3, hence factors other than the boundary may have contributed to the observed discrepancies.

2.6.2.3 Boundary Interaction

The influence of the boundary on inclined dense discharge configurations has been investigated by a limited number of studies. Roberts et al. (1997) investigated the flow along the boundary and quantified the extent of the mixing region (near field) post impingement. Experiments were conducted for 60° inclinations for source heights (H/F_0d) between 0.30

and 0.47. The flow was visualised using LIF, however concentration measurements were acquired using a microconductivity probe. The end of the near field mixing zone (transition to the far field) was defined as the location where effluent concentration fluctuations collapse to 5% of the mean effluent concentration. After impingement, it was estimated that dilution increased by 63% before the flow transitioned to the far field. This is considerably lower than Wright et al. (1991) who reported a three to five fold increase in the flow dilution. Doneker and Jirka (1999) identified a potential issue with how experiments were conducted in this study. The narrow flume that was used may have resulted in lateral boundary interaction and would have affected results obtained beyond the impingement point. Abessi and Roberts (2015) extended this study to include a wider range of discharge angles between 15º and 85º. Concentration fields were acquired using the LIF technique and geometric and dilution results were presented at the maximum rise height and impact point. Each flow parameter demonstrated some dependence on the discharge angle, although the impact dilution was relatively insensitive over the range 45º – 65º. 60° discharges demonstrated the highest level of dilution at the impact point and also resulted in the highest additional dilution achieved along the boundary. The behaviour of the flow within the impact region was of particular interest, where it was observed that centreline time-averaged dilutions decreased along the flow trajectory as it approached the boundary. A thin layer of highly concentrated fluid was evidently present along the boundary for each experiment. This was attributed to a decrease in flow intermittency and hence an increase in the accumulation of higher concentrated fluid within the region.

Shao and Law (2010) carried out experiments on negatively buoyant jets released at 30° and 45°. A combined PIV and LIF experimental system enabled velocity and concentration data to be simultaneously obtained. Boundary influence was determined by varying the source height ($H/F_0 d$) between 0.05 and 0.47. Mean concentration and velocity profiles were analysed prior to and following boundary interaction. Along the boundary, dilution was observed to increase with distance, consistent with the findings from Roberts et al. (1997). The potential of Coanda attachment effects arising from the placement of the lower boundary was also discussed in this study. Coanda effects can occur if the discharge nozzle is placed close to the lower boundary. This configuration reduces the amount of ambient fluid able to be entrained on one side of the flow. Consequently a pressure differential arises between the

outer and inner edge of the flow that may cause the jet to be drawn towards the lower boundary. This was noticeable for 30^o discharges where the trajectory of the ascending flow was inhibited. In contrast, 45^o discharges exhibited no variance in behaviour for all source heights tested. A relatively narrow range of sources heights was investigated and comparisons were not made with data where the lower boundary has no influence and hence it was difficult to quantify boundary influences in this study.

A more comprehensive study on boundary influence for INBJs was conducted by Crowe (2013). In this study experiments were conducted for source heights ranging between H/F_0d = 0.3 and 0.9, and were compared to experiments where the lower boundary was not present. PTV was employed and the flow behaviour was characterised using velocity and geometric measurements. At the maximum height of the flow trajectory, geometric and velocity coefficients were consistent with boundary free experiments for all discharge angles tested. Boundary effects were predominantly experienced near the return point when the flow is close to a solid boundary. In comparison with boundary free experiments return point distances from the source were greater and return point velocities were lower. The shape of the flow centreline was altered as the trajectory was observed to change direction near the boundary. The vertical location of this feature above the boundary correlated well with the source height. Boundary influence was formally characterised by identifying the location above the boundary where velocities reached a minimum value. These measurements also displayed good correlation when plotted against the source height. Numerous other flow parameters were presented in this study including the inner and outer side flow spread, velocity profiles and turbulent statistics such as TKE (turbulent kinetic energy) and shear stress intensity. In each case, distinct changes in behaviour were observed as the flow entered the impact region and evolved into a boundary flow.

2.6.2.4 Modelling

Inclined negatively buoyant jets have mostly been modelled without considering lower boundary influences. In comparison to experimental data many of the proposed models in the literature under-predict the centreline dilution response. This is counter intuitive to expectation given that the lower boundary, which has been included in most experimental studies, is likely to inhibit mixing and hence dilution. For instance commercial integral

models such as CorJet (Jirka, 2004) and JetLag (Cheung and Lee, 1990), have been shown to under-estimate average experimental dilutions by 50% - 65% (Palomar et al., 2012). One reason for these discrepancies between model predictions and experimental outputs is the detrainment process, where fluid falls from the inner side of the flow because of unstable density gradients. This flow feature has previously been referred to as 'buoyancy induced instabilities' and it creates additional mixing that is rarely accounted for in the modelling process (Kikkert et al., 2007; Lane-Serff et al., 1993). Lane-Serff et al. (1993) made the following observations regarding the flow behaviour; "Close to the source the plume is symmetrical but a pronounced asymmetry develops downstream. This asymmetry results from the opposite effects of the buoyancy force on the two sides of the plume. On the upper side, buoyancy forces create a stabilising stratification which tends to inhibit entrainment of the environmental fluid. On the lower side, the buoyancy forces produce a convectively unstable configuration and there is enhanced mixing between the plume and the environment." Buoyant instabilities are illustrated in Figure 2.4 which shows a time-averaged concentration field of the discharge. Falling fluid mass is evident by the extension of the concentration contours along the inner side of the flow. Recent integral models have attempted to simulate the effects of buoyant instabilities by relaxing certain conservation laws. Yannopoulos and Bloutsos (2012) proposed one such model where fluxes are lost from the control volume depending on the local flow conditions. The model utilises numerous constants which are optimised to minimise differences between model predictions and experimental data. Despite this, model outputs were shown to over-estimate the dilution. Oliver (2012) and Crowe et al. (2016) proposed models that specifically reduce buoyancy flux from the main flow. Oliver (2012) originally used this concept where the loss of buoyancy flux was limited to the ascending arm of the flow. Overall, this adjustment was shown to significantly improve dilution predictions. The model in Crowe et al. (2016) is an improvement to Oliver (2012) as losses in buoyancy flux are not confined to a specific section of the flow but are instead dependent on local flow parameters.

CFD models have also been developed to represent INBJ behaviour. Oliver et al. (2008) used a k-ε turbulence model and results indicated that buoyancy induced instabilities were being replicated on the inner side of the discharge. However the model overestimated the influence of stabilising density gradients on the outer side which resulted in the dilution being once

again under-predicted. Recent publications have trialled LES models to predict flow behaviour. Gildeh et al. (2015) assessed the performance of five RANS turbulence models and compared outputs from 30^o and 45^o discharge angles to experimental results. Dilutions from 45^o inclinations compared reasonably well with experiments however results from 30^o discharges exhibited unintuitive behaviour. Simulations pertaining to this angle indicated that the dilution at the maximum height and return point was greater than flows discharged at 45^o contradicting the general trend in the literature. Zhang et al. (2015) simulated 45^o discharge angles using Smargorinsky and Dynamic Smargorinsky sub-grid scales to model small scale turbulence. Both approaches produced similar outputs and it was reported that dilutions at face value were still being under-predicted.

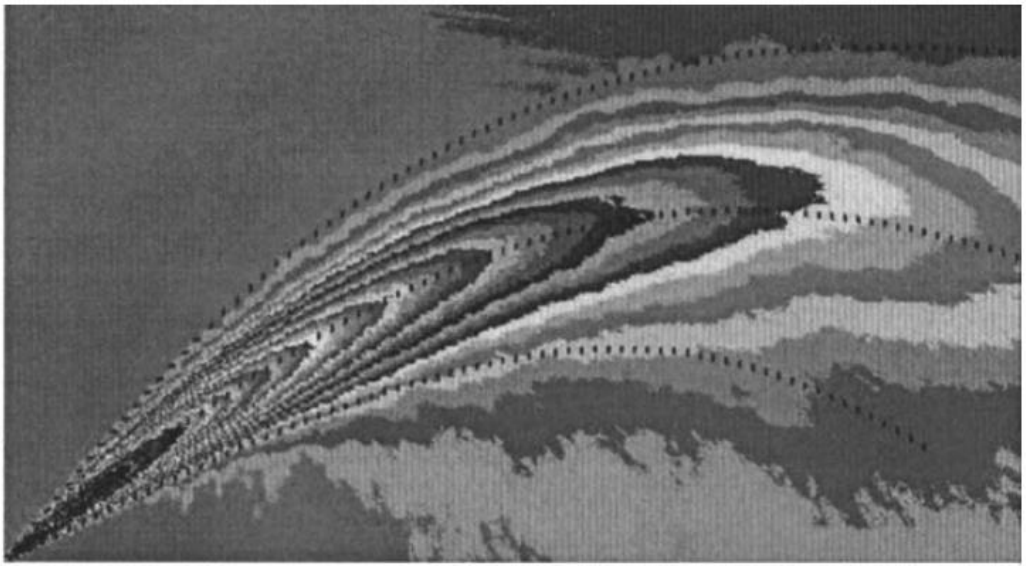

Figure 2.4: Averaged LIF image showing the path and additional mixing with a NBJ. Figure adapted from Kikkert et al. (2007).

2.7 Summary

The relevant studies on boundary impingement of vertical and inclined negatively buoyant flows have been reviewed in this chapter. The existing literature provides important insight into the behaviour of these flow types, however there are clearly a number of opportunities to

address various issues that have not received sufficient attention. The literature is already extensive in its coverage of vertical discharges impinging a boundary. However most studies have predominantly described the flow behaviour using velocity measurements, while concentrations and hence dilution have rarely been reported. Many of these studies have suggested a reduction in mixing near the boundary, however the extent to which the flow dilution is affected is still unclear. The literature on inclined negatively buoyant jets has developed more recently. This flow configuration is relatively more complex and consensus has not been reached regarding the flow behaviour. Discrepancies between previous studies have been partially attributed to the presence of a lower boundary and results in Oliver et al. (2013) highlight the need to conduct experiments where the lower boundary is investigated using a structured framework.

The present study aims to address gaps in the literature by conducting a comprehensive experimental programme to collect reliable concentration data on vertical and inclined flows impinging a boundary. The LIF method is employed to obtain 2-D concentration fields along the centre plane of the discharge in a non-intrusive manner. Experimental results are obtained for a wide range of initial conditions and new information on flow impingement is presented that enables boundary effects to be more systematically quantified.

Chapter 3 Experimental Methodology

The primary feature of the experimental program is the 2-D Laser Induced Fluorescence system (LIF). This imaging technique enables concentrations or temperature fields of liquid flows to be tracked using a fluorescent tracer. One of the first studies to investigate the use of LIF to obtain flow information was Ferrier et al. (1993). Quantitative statistics for flows in a stratified ambient were acquired. Unfortunately due to the limitations imposed by their equipment only a few statistical quantities could be obtained which did not include flow concentration fields. Prior to this, fluorescence based experiments were used primarily for flow visualisation due to the clear images that could be resolved. Since then numerous studies have managed to quantify concentration measurements in aqueous flows (Crimaldi, 2008; Karasso and Mungal, 1997; Webster et al., 2003). In the context of negatively buoyant flows, LIF has routinely been used to investigate the mixing behaviour where studies such as Lai and Lee (2012), Shao and Law (2010) and Oliver et al. (2013) have utilised this tool. Outside of fluid mechanics, the application of LIF can be found in biochemistry (determination of biological compounds from metabolic processes such as protein and enzymes), industrial chemistry (analysis of dyes and pigments, crude oil differentiation) and forensic analysis.

Much of the work conducted in Oliver (2012) has been used to develop the 2-D LIF system in the present study. The experimental system is reviewed and the processes employed to obtain reliable flow information are discussed including a detailed description of experimentation, calibration and results extraction methods. A horizontal platform was added to the existing apparatus which introduced new challenges to maintaining high quality outputs from the system. This aspect is highlighted in the text as well as the associated verification procedures conducted to ensure that potential issues are mitigated.

3.1 Equipment

Figure 3.1 shows a plan view of the major components involved with the experimental process. These include; the tank where source fluid was stored and discharged, the laser head unit and parabolic mirror used to create the light sheet and the CCD camera which captured images of each experiment at a specified frequency. A detailed description of each component is provided in the following sections.

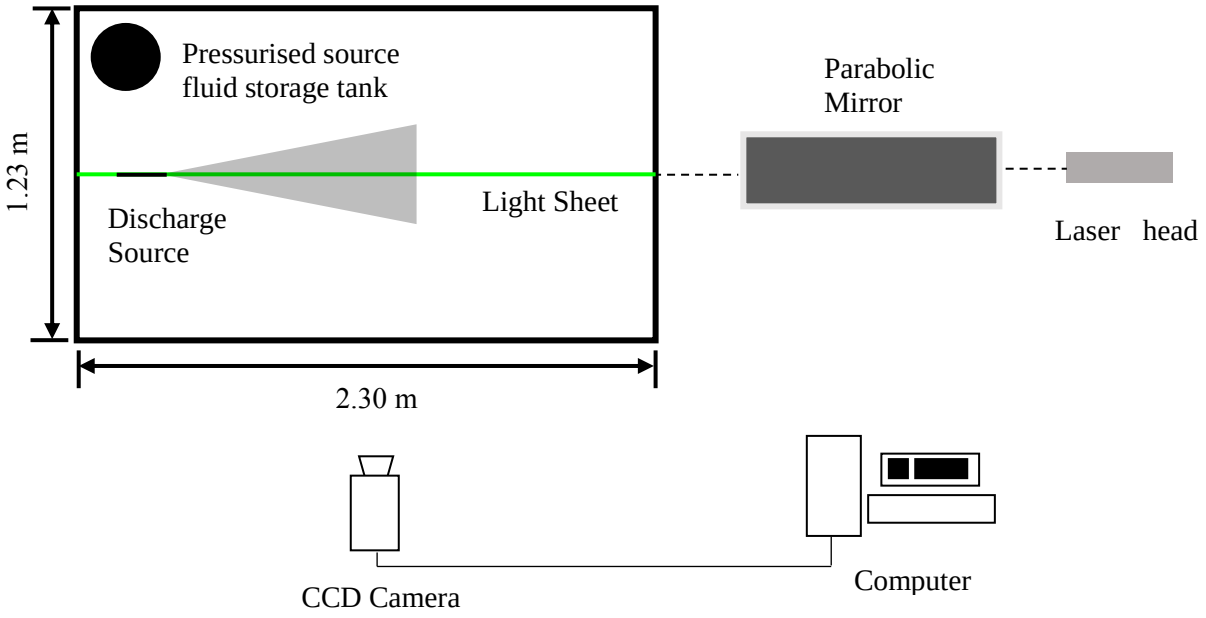

Figure 3.1: Plan view of each component of the experimental system.

3.1.1 Tank Facility and Discharge System

Experiments were conducted in a 5000 L tank measuring 1.78 m high by 2.30 m long by 1.23 m wide (Figure 3.2). The tank was filled with filtered tap water (using a 5 μm filter) and took approximately 40 minutes to fill and empty. Source fluid was also comprised of tap water and was mixed with salt and a small amount of fluorescent dye. A 50 L pressurised cylinder was used to store source fluid and was located within the tank to minimise temperature differences between the source fluid and the ambient environment. The cylinder was positioned in the corner of the tank so that it would not physically interfere with the discharged fluid and painted black to avoid any unwanted reflections. Source fluid was

initially transported from the pressurised cylinder to a constant head container located approximately 2 m above the main tank and was subsequently fed back down to the discharge nozzle. This arrangement allowed source fluid to be discharged with constant head thereby maintaining a uniform flow rate for the duration of the experiment. Figure 3.3 illustrates how source fluid was stored and dispensed with consistent head.

Figure 3.2: Tank facility used to conduct experiments. Tank was filled with water, simulating the environment into which outfall discharges are released.

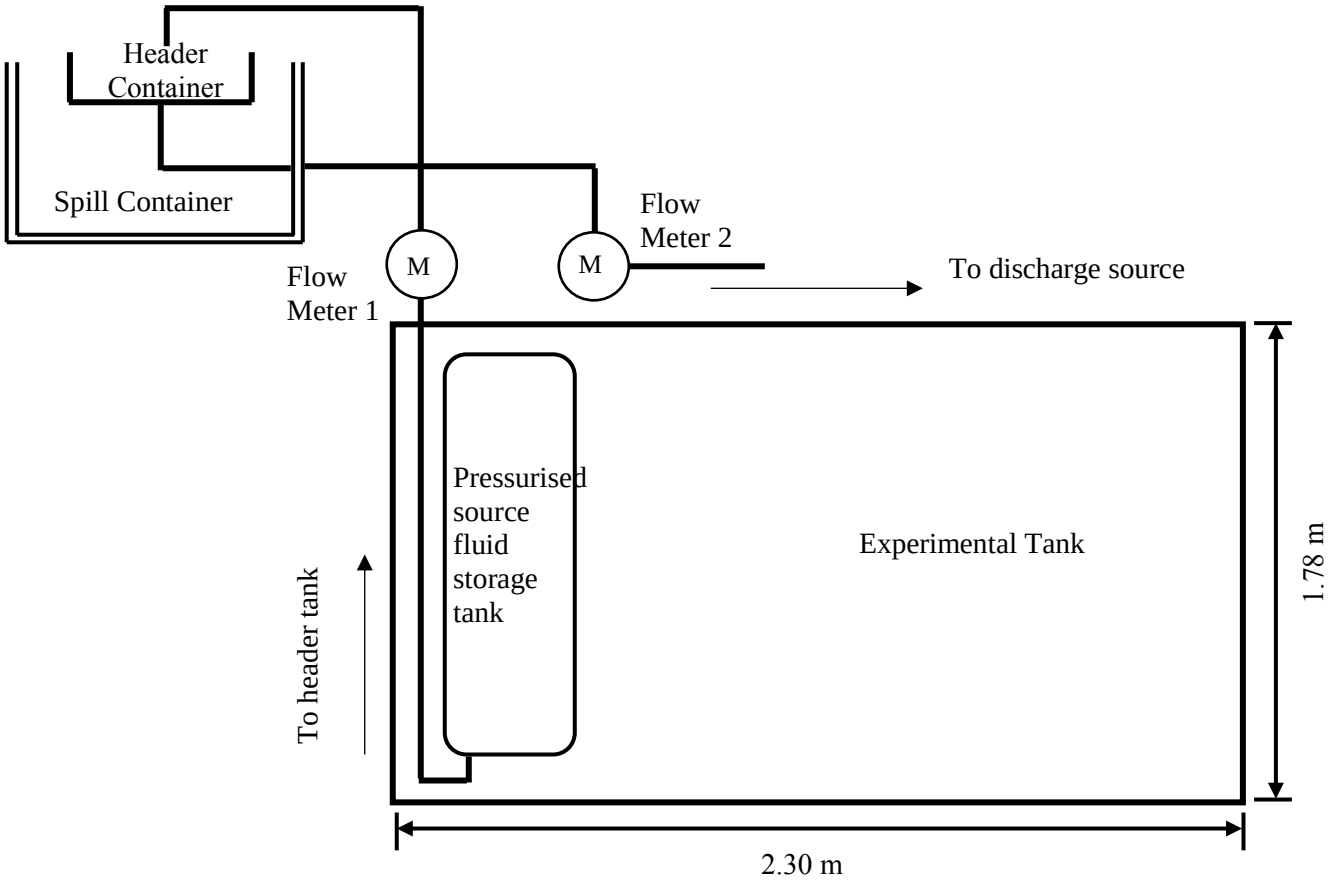

Figure 3.3: Storage and discharge of source fluid with constant head.

Fluid was initially pumped from the storage cylinder up to the header tank, after which it was fed down through a connecting pipe and into the main tank via the discharge source. Two flow meters (Krohne IFC 010D) were connected to the system allowing the flow to be regulated. The inlet flow rate to the constant head reservoir (measured using flow meter 1) was set approximately 1.5 times greater than the flow rate exiting the discharge source (measured using flow meter 2). This ensured that fluid was always present within the header container and this reservoir was consistently spilling fluid during the course of the experiment. Consequently, changes to the flow rate of the discharged fluid as a result of decreasing head were prevented. The constant head reservoir was positioned directly above a larger vessel (spill tank) which stored spilt fluid. For each experiment, instantaneous values of the flow rate were recorded at 0.3 second intervals from flow meter 2 and transferred onto an excel spreadsheet. A representative sample of flow meter readings over the course of an

experiment is given in Figure 3.4. Measurements are given as a percentage difference from the mean flow rate.

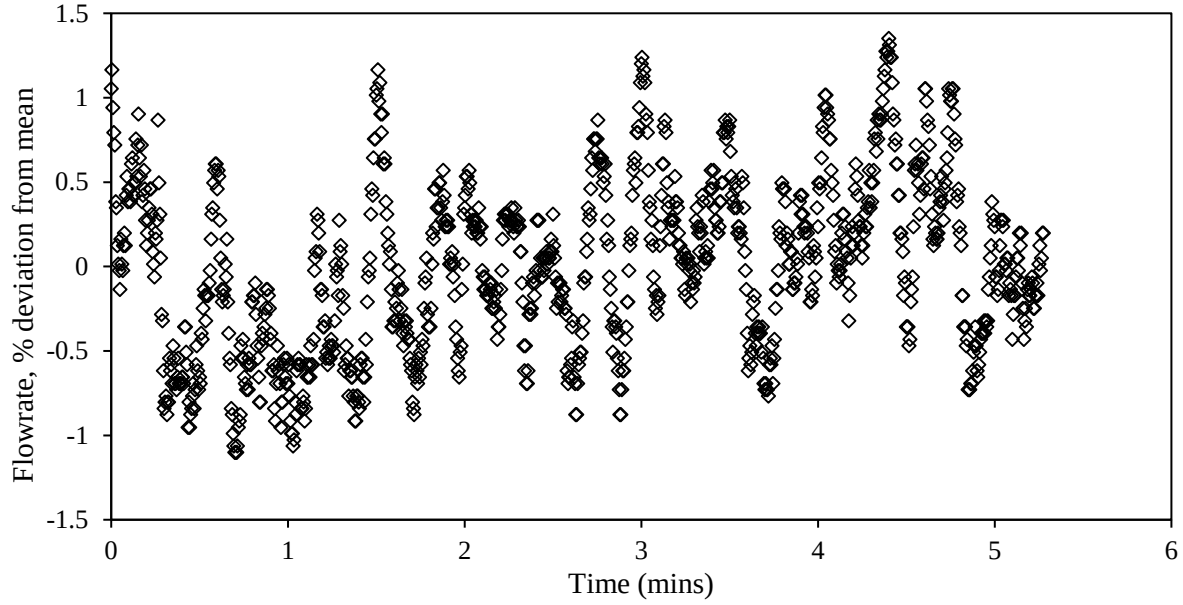

Figure 3.4: Flow rate measurements recorded every 0.3 seconds. Values are given as a percentage difference from the mean.

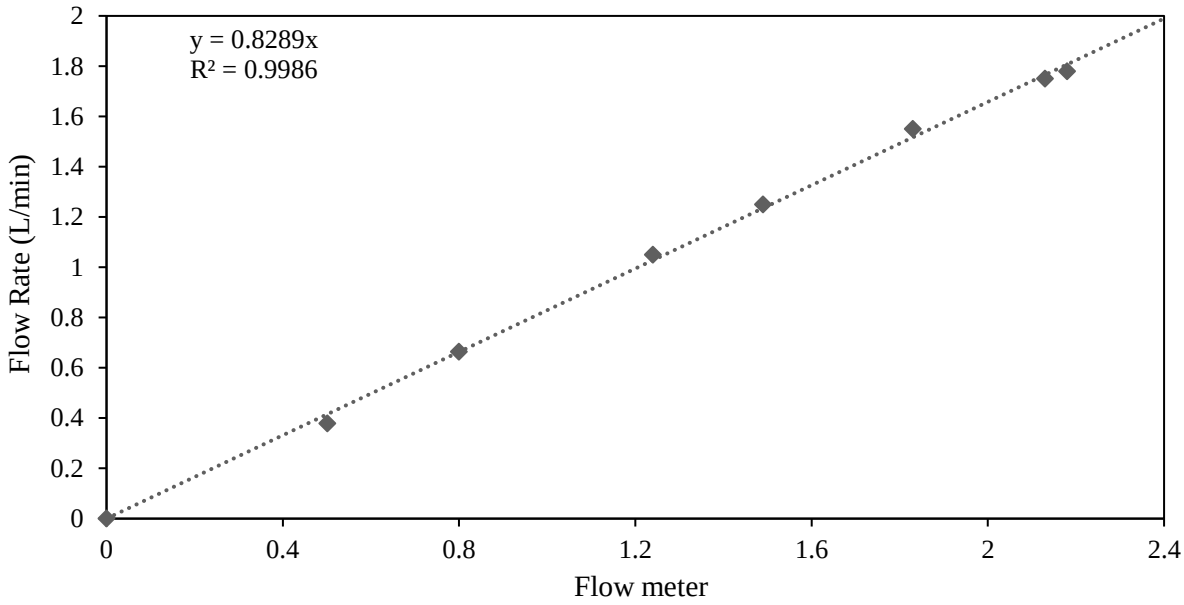

Figure 3.5: Flow rate – Flow meter calibration relationship.

The readings obtained directly from the flow meter did not correspond to the actual discharge conditions at the source. A separate calibration process was required to determine the relationship between the values recorded by the flow meter and the flow rate. This was carried out by setting the meter to a specific reading and measuring the average time taken to fill a 2000 ml measuring cylinder. A number of readings were taken and the resultant flow rate was plotted against the flow meter readings (Figure 3.5).

The discharge nozzle was held in place by a frame which could be adjusted vertically in 40 mm increments (Figure 3.6) and boundary influence was investigated by placing a circular platform (Figure 3.7) at a height of 715 mm above the tank floor. There was a minimum distance of 100 mm between the platform edge and the tank walls, which allowed the negatively buoyant fluid to fall off the edge of the platform rather than building up and interfering with the incoming flow. Thus the flow along the platform was steady for an extended period and relatively long experimental durations were permitted with this setup. When boundary influence was not being investigated, the platform was removed and a minimum clearance of 720 mm between the discharge nozzle and the bottom of the tank was ensured.

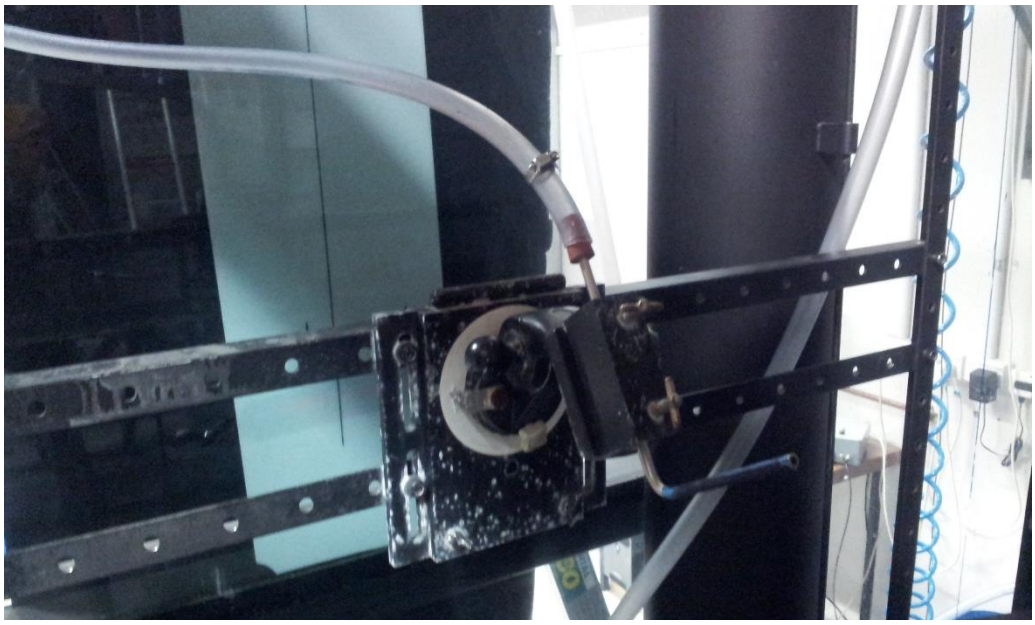

Figure 3.6: Discharge nozzle. Source fluid is released into the tank through this circular pipe.

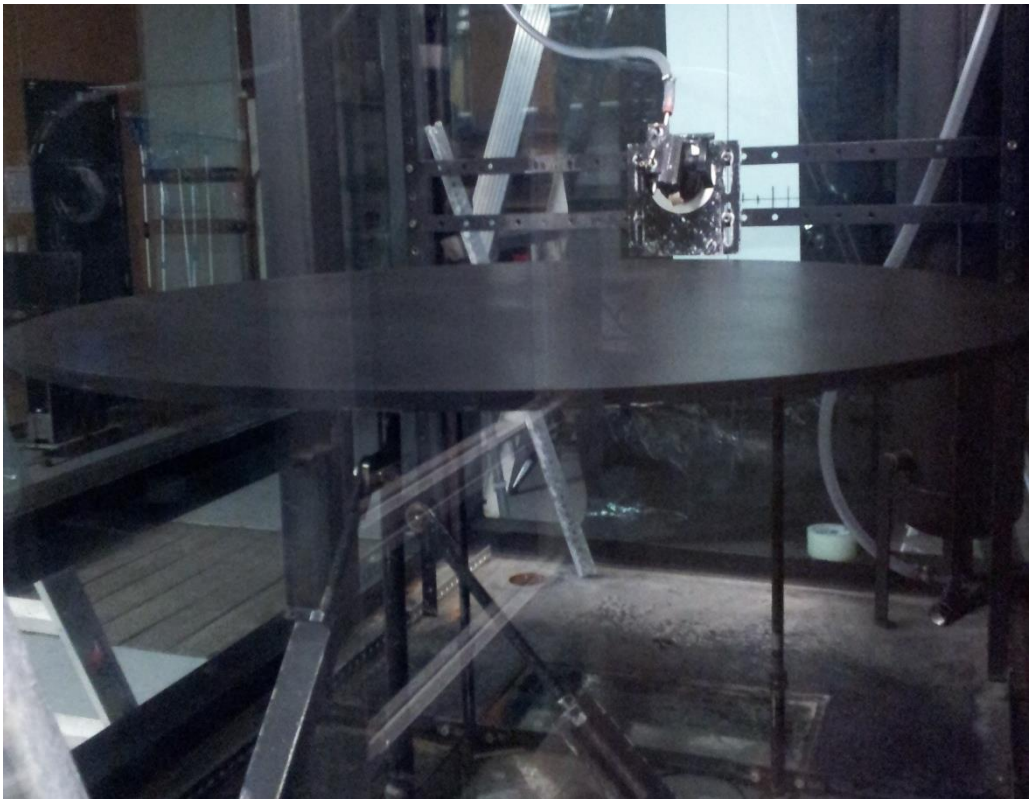

Figure 3.7: Circular platform placed below the discharge nozzle for boundary experiments.

3.1.2 Camera

A Jai Pulnix TM-2030 CL camera was positioned perpendicular to the flow at distance of 6 m away from the centre plane of the discharge. A GoYo 1” 50 mm f/0.95 fixed focal length lens was used and provided a centreline viewing area of approximately 640 mm high by 1135 mm wide. Greyscale images were obtained and written to a high speed hard drive through a Correco imaging card. The TM-2030 CL is a charge coupled device (CCD) camera in which a sensor is employed to convert light intensity into an electrical charge. Once the light intensity has been converted, the accumulated charge is determined and digitised to produce an intensity value that is assigned to an appropriately located pixel. Various camera settings can manipulate the relative pixel intensity value as well as change the overall image quality. These are described below.

3.1.2.1 Image Quality

The image depth indicates the number of discrete levels that can be used to represent the intensity at a pixel. For example, an image depth of 8 bits is able to characterise the intensity at a pixel over 256 levels ($2^8 = 256$) while an image depth of 10 bits is able to represent the intensity of the same pixel over 1024 levels ($2^{10} = 1024$). Therefore the greater the image depth the higher the quality of image that is able to be produced. The camera in question was able to resolve images using 8, 10 and 12 bit depth with a frame capture rate of 16 Hz or 32 Hz. If the latter frame rate was employed, the image depth was limited to only 8 bits. As time-averaged results are of primary interest in this study, using a higher frame rate is not necessarily advantageous. However, maximising the image quality can improve the quality of LIF results, therefore 12 bit images were selected and captured at a rate of 16 Hz. While this allowed pixels to be resolved up to 4096 levels ($2^{12} = 4096$), the full range of discrete levels was not normally utilised for a particular image. The dynamic range between the strongest and weakest pixel intensities could be increased by adjusting the gain setting on the camera. It is beneficial to increase the gain as it decreases the concentration of fluorescent dye required in the source fluid. Lower dye concentrations are desirable because of potential attenuation issues (discussed in Section 3.2.2.1). A disadvantage of increasing the gain is the resultant effect on the background noise which also tends to increase. Signals from all electronic devices are susceptible to random fluctuations from a variety of sources. Thermal noise, which arises through the agitation of electrons within the sensor, is a significant contributor. Fluctuations generated internally are also observed in the raw light intensity signal of a particular image pixel. An example of this is provided in Figure 3.8 where the background intensity signal (no light) has been plotted against time for a gain setting of 50%. If these fluctuations are large (in a relative sense) they may hinder the quality of results. The relationship between noise and different gain settings was investigated in Oliver (2012) where the fluctuation percentage was plotted against the corresponding intensity for five different gain levels. For the experiments conducted in the present study it was determined that a 100% gain level was suitable. The potential of background noise influencing the quality of results is discussed in Section 3.6.2.

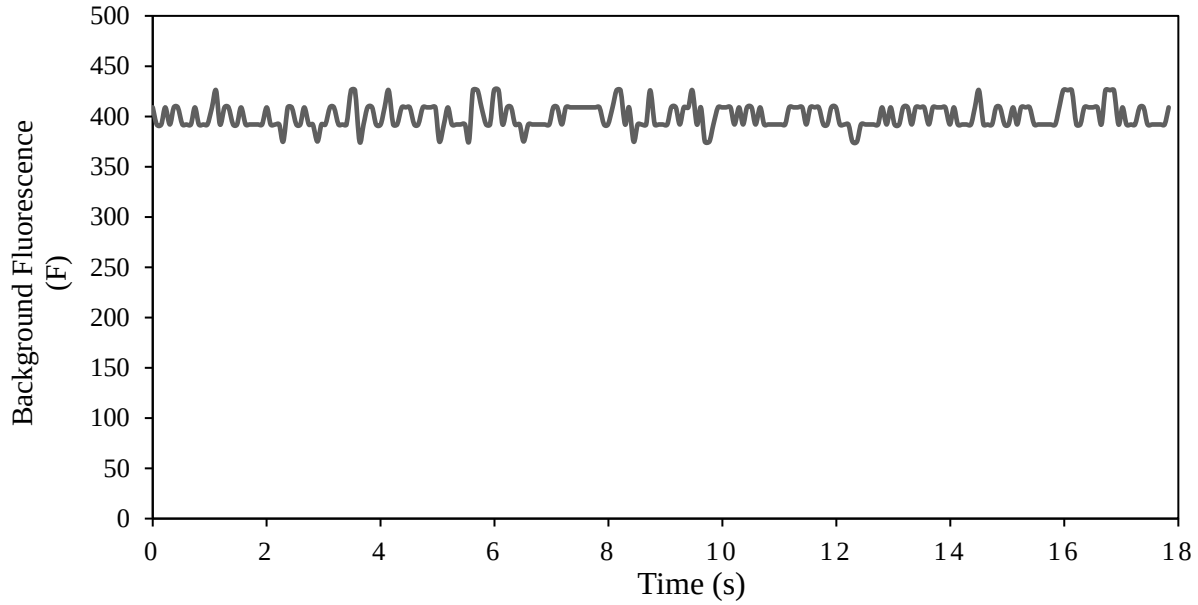

Figure 3.8: Fluorescence time-series from background image (no light). Gain setting of 50%.

3.1.2.2 Optical effects

Before each experiment, the camera was focused by placing an object within the recording area in line with the light sheet. Achieving precise focus was not possible for every area of the image as it was found that focusing the centre of the image caused the outer parts of the image to be slightly out of focus (and vice versa). Crowe (2013) observed the same effect and attributed it to Petzval curvature, which occurs due to the difference in shape of the lens image (curved) and the CCD (flat surface). The camera was focused based on the centre of the viewing field, thereby causing the outer edges of the image to remain slightly out of focus. The intensity of light in these out of focused areas of the image is not altered but instead spread over a number of pixels. PTV and PIV experiments are typically more susceptible to error from out of focus images as particles need to be well defined in order for particle tracking algorithms to define velocity fields. In comparison, time-averaged concentration measurements are relatively unaffected if the image is slightly out of focus and camera settings are kept consistent between testing and calibration processes. Areas near the source where high concentration gradients exist will be affected to some extent by spatial smoothing of the concentration field. Fortunately this region of the flow was typically

neglected due to light saturation. The intensity of light recorded was too high to be assigned a representative intensity value by the camera. It is reasonable to assume that the error associated with the remaining flow field is negligible. Petzval curvature effects could be minimised by reducing the aperture setting on the camera lens (increasing the f-number). Larger apertures result in a relatively shallow depth of focus so that the images captured are more susceptible to focus issues. Decreasing the aperture reduces the amount of light able to be detected by the internal sensor thereby lowering the fluorescent intensity. In most 2-D planar LIF applications it is desirable to maximise intensity readings using a low f-number. Given that out of focus regions can be localised to the outer regions of the image, eliminating these effects proved to be inconsequential to the overall quality of results.

Optical aberrations from barrel and pincushion effects can potentially distort images that are being recorded by the camera. These distortions originate from an optical axis and cause the image to magnify in a symmetrical manner about this point. Figure 3.9 illustrates how these effects can alter the image. In barrel distortion, images are magnified less and less with distance from the optical axis. Images captured using wide angle lenses are more likely to suffer from this type of distortion. Pincushion distortion results in the opposite effect where image magnification increases with distance from the optical axis. The third type of distortion is called moustache distortion and is a combination of both the aforementioned aberrations. A number of methods are available to remedy these distortions, however both Oliver (2012) and Crowe (2013) concluded that these effects are insignificant for the experimental setup in this study.

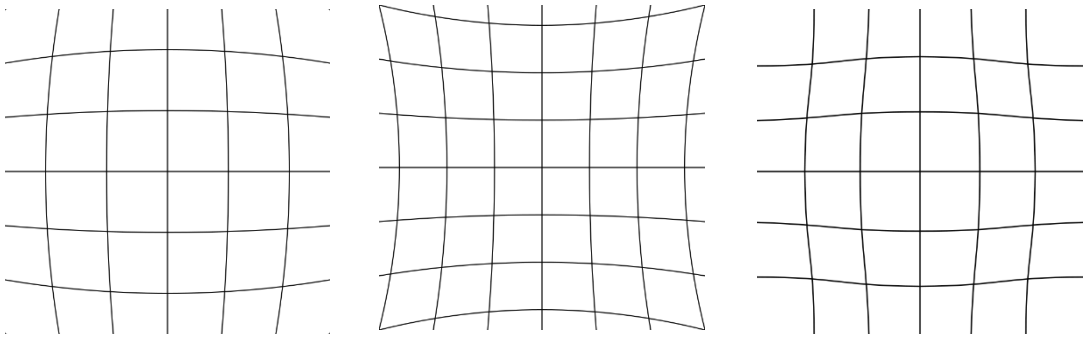

Figure 3.9: Potential optical distortions, a) Barrel distortion, b) Pincushion distortion, c) Moustache distortion.

3.1.3 Light Sheet

Figure 3.10 depicts a schematic diagram of the light sheet used to illuminate the flow. The laser head unit emitted a continuous beam of light which was converted into a thin sheet of light using a series of mirrors. The light sheet (~ 3 mm sheet width, approximated as 2-D) was positioned in line with the discharge nozzle and illuminated the centre plane of the discharge. The quality of the output was affected by the stability of the mirrors; particularly the spinning and parabolic mirrors, and the monochromatic laser output. These components are discussed in the following sections.

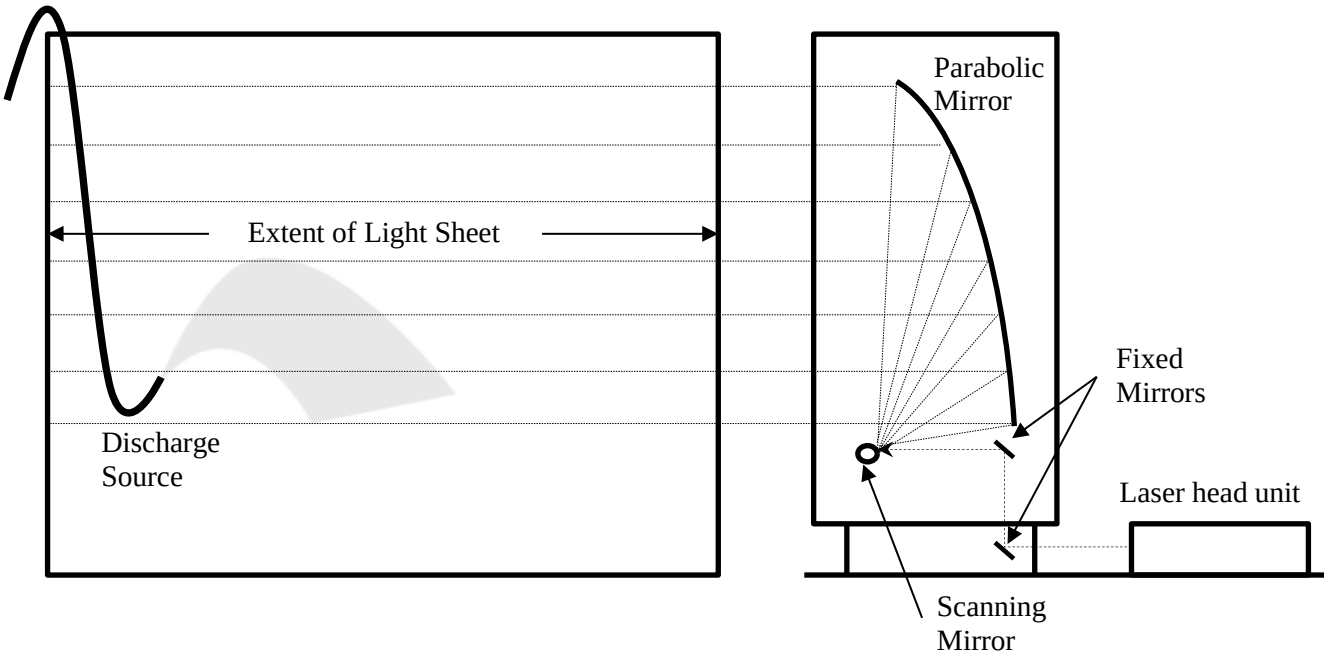

Figure 3.10: Generation and projection of the light sheet through the tank.

3.1.3.1 Laser Head Unit

A Verdi G-series optically pumped semiconductor laser (OPSL) delivered a monochromatic beam at a wavelength of 532 nm. The laser head unit could be operated at a maximum of 5 Watts and provided a very consistent output with a noise RMS percentage of below 0.2% (Coherent Inc, 2016). An independent investigation was conducted on the performance of the laser output using a Newport optical light meter. The power setting as per the head unit was

compared to the output measured by the light meter and the results are presented in Figure 3.11. Recordings were obtained by the light meter for 10 minutes and averaged. As shown, the setting on the head unit is almost the same as the output measurement from the light meter. The average standard deviation across all recordings was calculated to be 0.48 %.

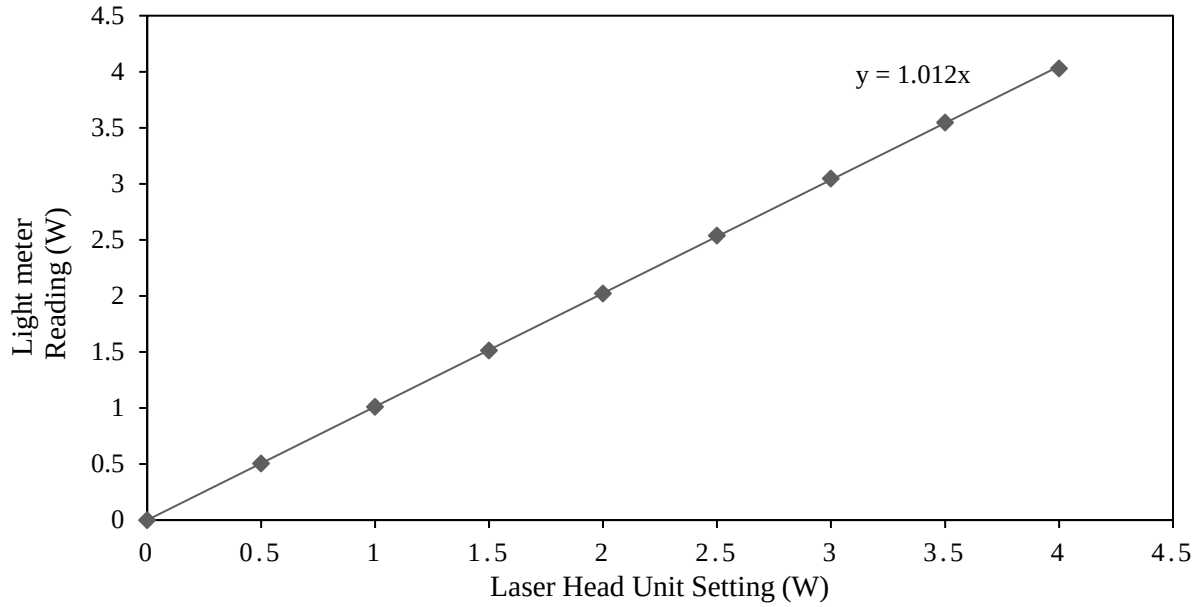

Figure 3.11: Laser Power as measured by the head unit and the Newport optical light meter.

3.1.3.2 Mirrors

Fixed mirrors were used to direct the beam onto the spinning mirror and then onto the parabolic mirror creating a thin light sheet. These mirrors could be adjusted to shift the light sheet horizontally as well as changing the vertical extent of the sheet. The spatial variability of the light sheet was extremely sensitive to any changes made to the mirrors, therefore it was important that conditions remained the same between experiment and calibration. Fortunately these mirrors proved to be stable and remained fixed in place during testing. The spinning mirror could potentially be a source of error if the rotational speed was not fast enough or significant fluctuations in rotational speed were observed to occur. In such cases, the stability of the intensity recordings would be compromised. There were numerous instances where it was observed that this source of error could be neglected. Most notably, Figure 3.16

(included in Section 3.2.2.2) plots the fluorescent intensity signal of a Rhodamine 6G solution irradiated by the light sheet and recorded by the camera over 40 minutes. Intensity readings were stable over the duration of the test. As the spinning mirror was used to produce the light sheet, it is possible to infer that its performance did not hinder the quality of the intensity signal. The positioning of the parabolic mirror was integral in achieving accurate centreline measurements. This mirror was held in place by a tensioned tape against two flat metal sheets that created a parabolic shape. Unlike the fixed mirrors, the position of the parabolic mirror was not as stable. Subtle twisting and side to side movement could shift the light sheet off the centre plane of the discharge. Simple methods were employed to straighten the light sheet that involved placing small shims between the mirror and the supporting pieces. This method did not guarantee that the light sheet would remain permanently in place and subtle tuning of the mirror was required at regular intervals. The position of the light sheet in relation to the centre plane of the discharge was checked regularly throughout the experimental process and during calibration.

3.2 Fluorescence and Fluorescent Dyes

Certain substances have the ability to fluoresce upon being subjected to electromagnetic radiation (or light) within a specific band of wavelengths. Molecules that exhibit this property are referred to as fluorophores. When an external light source provides a continuous supply of photons they are absorbed by the fluorophores. The energy (joules) of each photon depends only on their wavelength, λ (or frequency, f).

$$E = hf = hc/\lambda \qquad 3.1$$

where h is Planck's constant and c is the speed of light measured in a vacuum (also a constant). The magnitude or power (P) of the irradiating light source is measured in joules/second or Watts. The number of photons that are being released per second by a light source can be calculated using Equation 3.2.

$$\frac{\text{Photons}}{\text{second}} = \frac{P}{hf} = \frac{P}{E} \qquad 3.2$$

After absorbing these photons, fluorophores are raised from their ground state to an excited state. They are unable to stay in this excited state and are brought back down to their original level within an extremely short space of time (1 – 10 ns duration). This fall in energy state is usually accompanied by an emission of photons (light) thereby allowing the substance to be visualised. The intensity of re-emitted light is proportional to the concentration of the fluorophore and also the intensity of the incoming light. While in this excited state, some of the absorbed energy is partially dissipated, therefore the wavelength of the re-emitted light increases. The ratio of photons emitted to photons absorbed is referred to as the quantum yield of fluorescence (Equation 3.3):

$$Q = \frac{\text{Photons}_{\text{emitted}}}{\text{Photons}_{\text{absorbed}}} \qquad 3.3$$

There are mechanisms other than fluorescence emission that can return excited molecules back to their ground state. The implications of this are important to the accuracy of LIF and these are elaborated in Section 3.2.2. The quantum yield can also represent the relative extent to which these other processes (which hinder fluorescence emission) occur.

A number of dyes can be used for fluorescence based experiments. For aqueous based testing Rhodamine B (RB) and Rhodamine 6G (R6G) are typically used due to their solubility in water. The suitability of a particular dye is dependent on a number of factors. The fluorescence sensitivity of each dye to factors such as temperature and pH must be considered in relation to the specific parameter that is being measured. The fluorescence of a Rhodamine B solution varies significantly with temperature, therefore this dye is particularly suitable to track temperature changes in flows. For experiments where changes in concentration are the sole parameter of concern, Rhodamine 6G would be the dye of choice due to its insensitivity to variations in temperature. Furthermore, consideration must be given to whether the absorption spectrum of the dye is compatible with the available excitation wavelength (i.e. wavelength of laser light) and whether there is sufficient separation between the absorption and emission wavelength. The full absorption (excitation) and emission spectra for Rhodamine 6G in ethanol is depicted in Figure 3.12. Whilst the spectrum for aqueous R6G is more relevant, the peak absorption (λ_{abs}) and emission (λ_{em}) wavelengths are very close to the corresponding aqueous values. Table 3.1 provides these values for R6G and RB as well as

other key properties relating to these dyes. Values for each parameter have primarily been obtained from Crimaldi (2008) unless otherwise stated.

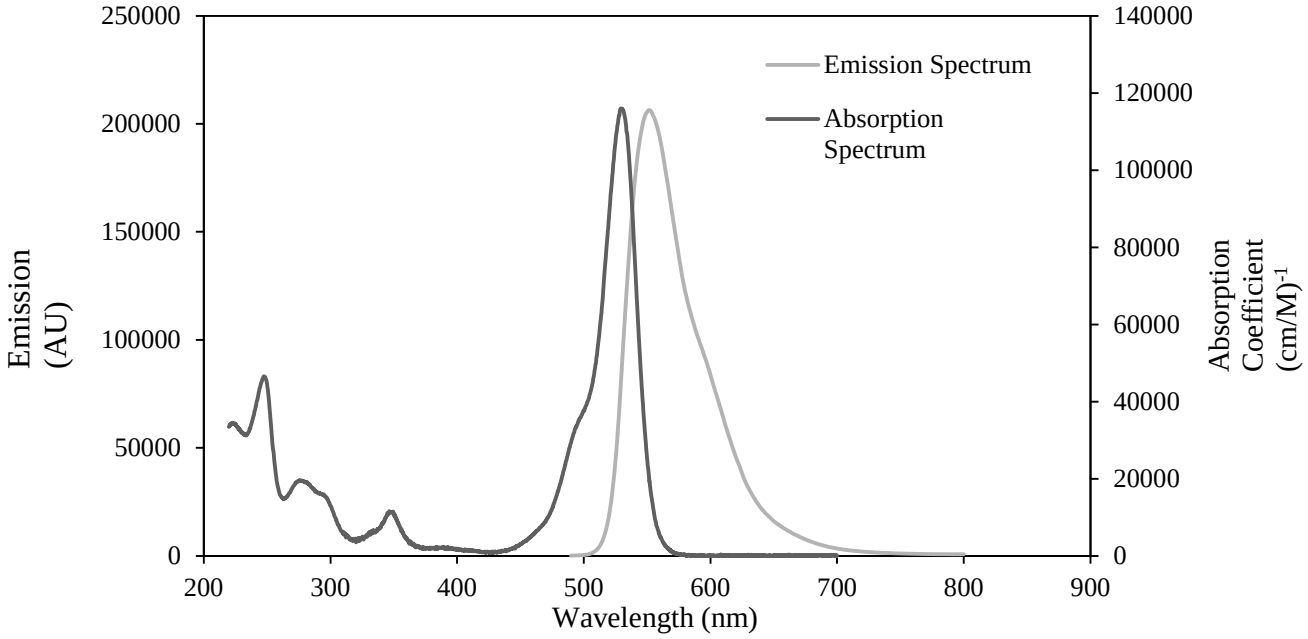

Figure 3.12: Absorption and emission spectrum for Rhodamine 6G in ethanol.

Table 3.1: Fluorescent properties of Rhodamine 6G and Rhodamine B.

Dye	λ_{abs} (nm)	λ_{em} (nm)	ε (cm M)$^{-1}$	Fluorescence % change per ℃	Quantum Yield (Q), at 25℃ [1]
Rhodamine 6G	*525*	*555*	*110000*	-	*0.95*
Rhodamine B	*555*	*580*	*86000*	*-1.8*	*0.65*

The absorption coefficient for each dye, ε, describes the extent to which the intensity of the incoming radiation is reduced as a result of passing through fluorophores. The significance of this parameter is related to the attenuation of laser light caused by the fluorescent dye (discussed in Section 3.2.2.1). Based on the characteristics of the two fluorescent dye choices, Rhodamine 6G was selected as the preferred fluorescent dye over Rhodamine B due to its

[1] Kubin and Fletcher (1982)

insensitivity to temperature changes. Physical mixing (concentration) is the primary flow characteristic of concern for the present study therefore it would be undesirable for measurements to be affected by other processes. While measures were taken to homogenise the temperature of the source and the surrounding ambient fluid, the potential effect of even small temperature changes on the fluorescence level was enough to adversely affect the accuracy of concentration measurements. The quantum yield of R6G is also much higher than RB, meaning that lower dye concentrations could be used to produce the same intensity of fluoresced light.

3.2.1 Fluorescence – Concentration Relationship

The relationship between the incoming excitation intensity (or laser power, I), the dye solution concentration (C) and raw fluorescence value recorded by the camera (F) is shown in Equation 3.4 (Crimaldi, 2008):

$$F \propto \frac{I}{1 + I/I_{sat}} C \qquad 3.4$$

where I_{sat} represents the saturation intensity of the dye. This is different to the saturation referred to in section 3.1.2.2 where the light detected by the camera is too high to assign an appropriate representative value. Fluorescent dye saturation occurs when the excitation rate of the dye solution exceeds the de-activation rate. The irradiating light is intense enough that each fluorophore is constantly being hit (and subsequently excited) by photons before they have the opportunity to return to their ground state and fluoresce. As a result increasing the power of the light source no longer increases the intensity of the resulting fluoresced light. A non-linear relationship is then observed between F and I. However if $I \ll I_{sat}$, Equation 3.4 can be linearised to the following form.

$$F \propto IC \qquad 3.5$$

As stated, the fluorescence signal can be amplified by either increasing the dye concentration (C) or by increasing the intensity of the irradiating light (I). This relationship forms the foundation of the laser induced fluorescence method which allows dye concentrations to be quantified. If the excitation intensity (I) is kept constant (i.e. constant laser power) only m

and b (as per Equation 3.6) need to be calculated to determine the relationship between the dye concentration (C) and the intensity of the fluorescence (F) emitted from the dye

$$F = mC + b \qquad 3.6$$

The constant b represents the fluorescence level when no dye is present. Usually referred to as the black level, it is subtracted from each fluorescent image prior to determining the constant m. The linearity associated with this equation is only valid for low concentrations of the fluorescent dye. A non-linear relationship is observed when large dye concentrations are used, due to variations in radiation absorbance by the dye molecules. Ferrier et al. (1993) investigated this aspect by recording the fluorescence level of increasing R6G solutions, while keeping the laser power constant. Their results are shown in Figure 3.13. Non-linearities in the fluorescence – concentration relationship are clearly observed beyond a concentration of 50 μg/L. An alternative to varying the concentration (C) to calibrate experiments, is changing the excitation intensity (or laser power) for a fixed R6G concentration. In this case a relationship would be obtained that relates the recorded fluorescence (F) to the excitation intensity (I) (Equation 3.7).

$$F - b = mI \qquad 3.7$$

The excitation intensity (I) is varied based on the power output of the laser (measured in watts). In many ways this technique is more advantageous than varying the concentration during calibration. Changing the concentration requires the arduous task of filling and emptying the calibration cell (and main tank) every time a new R6G solution is to be tested. By comparison the laser power is a much easier variable to manipulate, allowing a large number of intensity values (I) to be tested within a relatively short timeframe. For this reason it is more desirable to carry out the calibration procedure with a fixed R6G concentration while testing different laser power outputs. To verify the legitimacy of using the laser power output, a 4 L Perspex box was filled with various concentrations of R6G (from 0.0016 - 0.0122 mg/l) and irradiated with different laser intensities. Approximately 200 images were recorded for each concentration/laser power combination and the fluorescence was averaged over the entire area of the box. Figure 3.14 illustrates how the laser power and R6G concentration are equivalent to each other. Two data sets are plotted in Figure 3.14; the first

represents the fluorescence level of different R6G concentrations while maintaining a laser power of 4W, while the second shows the fluorescence level of the 0.0122 mg/l solution at various laser powers ranging from 0W to 4W.

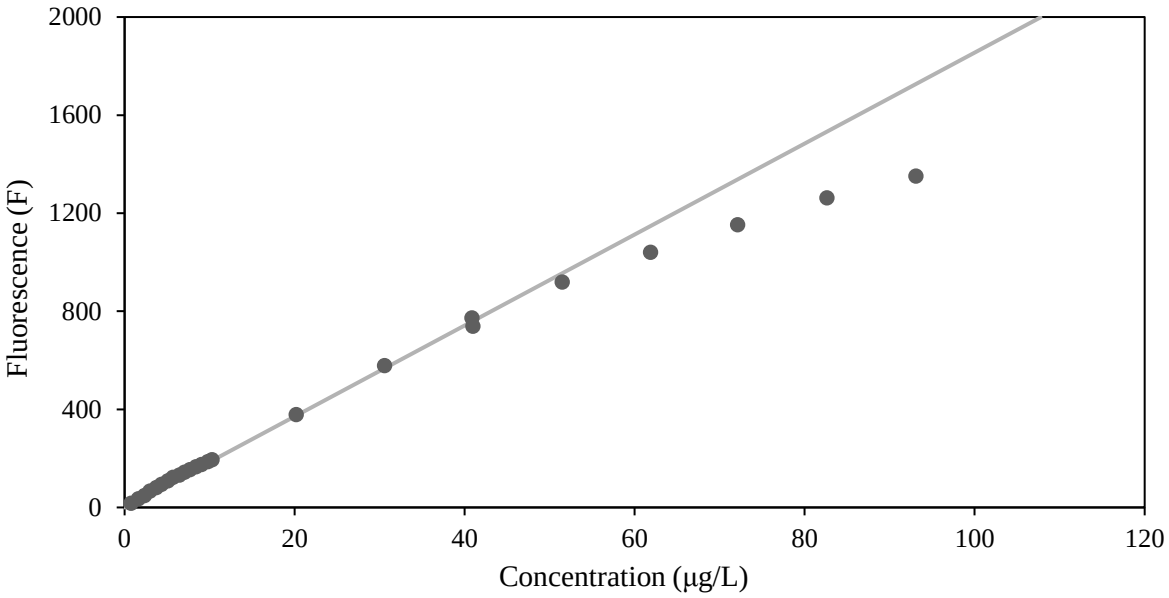

Figure 3.13: Fluorescence recorded for various concentrations of R6G dye by Ferrier et al. (1993).

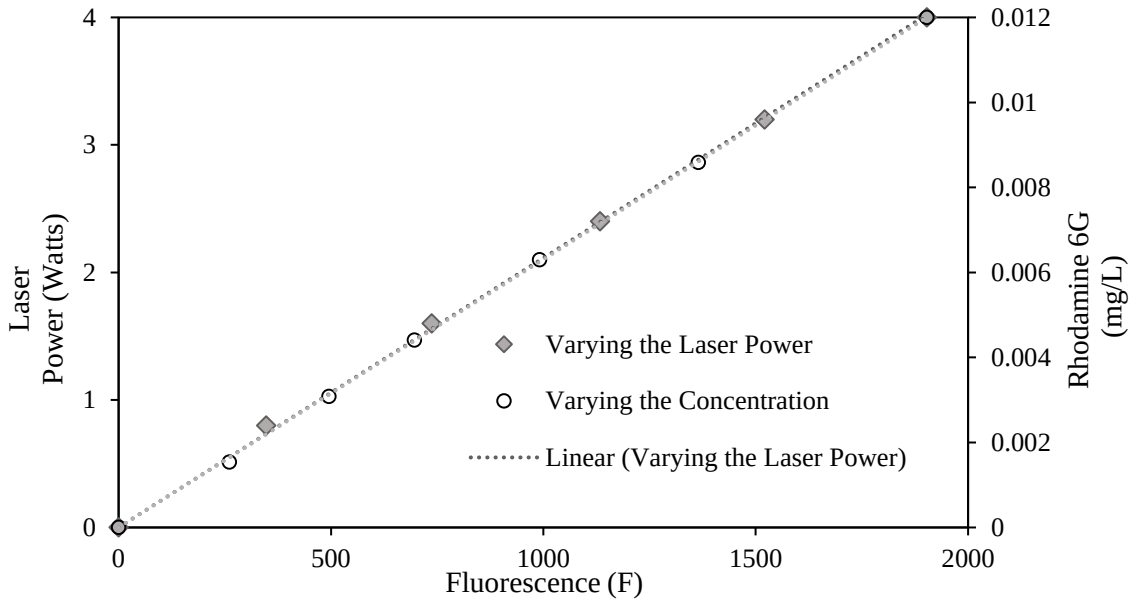

Figure 3.14: Relationship between Laser Power, R6G concentration and Fluorescence. Laser power fixed at 4 W while different concentrations were tested and R6G concentration fixed at 0.0122 mg/L while different laser powers were tested.

3.2.2 Fluorescence Alteration

LIF is a sensitive optical method where fluorescence measurements can be adversely affected by a number of factors. These can artificially alter the level of fluorescence that is recorded thus affecting the quality of results. Therefore it is important to mitigate the occurrence of these processes. These can include light attenuation, photobleaching and quenching. Many of the verification procedures required to assess how influential these processes are on LIF measurements have already been carried out and detailed in Oliver (2012). A summary is presented here.

3.2.2.1 Laser Light Attenuation

When fluorophores are subjected to laser light (or another radiation source) they absorb the incoming photons. Consider a cell of a certain width filled with fluorescent dye of a given concentration that is exposed to a light source. The fluorophores closest to the source are the first to absorb photons and subsequently fluoresce without any hindrance. However these initial dye molecules obstruct or 'attenuate' photons from reaching fluorophores that lie behind them. Subsequently the likelihood of photons reaching the far side of the cell is reduced, thereby decreasing the amount of fluoresced light that is observed within that region. The longer the light source must travel through the cell, the more appreciable the effect of attenuation has on the dye fluorescence. In addition to the distance travelled by the laser light through the fluorescent dye, attenuation can be intensified if the dye concentration or salt content is increased. In this scenario there are more molecules (including both fluorophores and salt molecules) per unit area to absorb photons before they are able to reach the far side of the cell. Attenuation is not an issue if the effect is constant between experimental runs for the entire flow field. In this case the resulting effect could be accounted for during calibration. Unfortunately attenuation at a particular pixel changes between each physical experiment and the corresponding calibration recording. The percentage of irradiating light that is attenuated (Att) over a certain distance (x, measured in cm) of fluorescent dye can be calculated using Equation 3.8 (Tian and Roberts, 2003).

$$\mathrm{Att} = \mathrm{e}^{-\mathrm{ax}} \qquad 3.8$$

where a is the attenuation coefficient given in Equation 3.9

$$a = a_w + 0.000124C_{salt} + 0.00023C_{R6G} \quad 3.9$$

where C_{salt} and C_{R6G} represent the concentrations of salt (g/l) and Rhodamine 6G (µg/l) respectively. Equation 3.9 also includes an extra term describing the attenuation caused by water (a_w) which is generally not considered during calibration. Given that the camera setup does not change between each experiment (and calibration recording) the laser light travels through a constant amount of water to reach a particular location, therefore any attenuation that results is fixed for the entire flow field.

To appropriately deal with attenuation Equation 3.9 must be applied to each pixel within the image or the setup must be arranged so that attenuation is negligible. Past studies have used Equation 3.9 for calibration images and neglected any attenuation that occurs during the physical flow experiments. This assumption is largely valid given the physical scale of the flow and the relatively low concentrations that are present throughout most of the flow field (due to rapid turbulent mixing). Furthermore, accurately quantifying the attenuation for each image captured during an experiment is too difficult due to the turbulent nature of the flow. Attenuation can be quantified by considering the concentration of Rhodamine 6G and the physical distance that the irradiating light must travel through (i.e. calibration cell width). Figure 3.15 plots the percentage of laser light that has been attenuated along the cell width for various R6G concentrations as per Equation 3.9. A threshold attenuation level of 2% was deemed to be acceptable. A line has been included to highlight the dye concentrations and cell widths that meet this criteria. Oliver (2012) initially investigated the viability of using a 1 m wide calibration cell. The fluorescence signal along the width of the cell was mapped for various R6G concentrations. Attenuation was observed for most concentrations tested due to the wide cell width, so smaller options were investigated. It was found that using a cell width below 160 mm and R6G concentrations of under 0.003 mg/l resulted in negligible attenuation. This concentration is well within the limits required for a linear response (defined in Figure 3.13) and below the 2% threshold shown in Figure 3.15. The calibration method was ultimately designed around these parameters where a calibration cell measuring 160 mm was used.

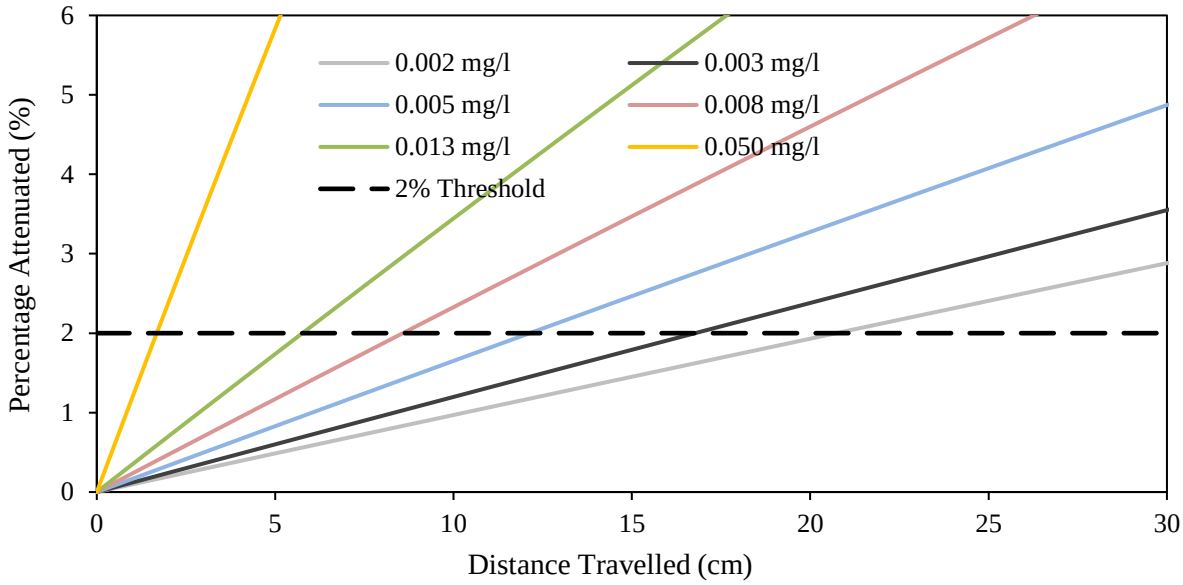

Figure 3.15: Light attenuation based on the distance travelled by light and different R6G concentrations.

3.2.2.2 Photobleaching and Quenching

The fluorescence properties of Rhodamine 6G can be affected if subjected to intense illumination for long periods of time. This phenomenon is known as photobleaching which is defined as the photochemical destruction of a dye molecule. Fluorophores can permanently lose their ability to fluoresce due to chemical reactions with other molecules present within the environment (e.g. oxygen). Instead of solely transitioning to an excited singlet state, the molecules may reach an excited triplet state which is relatively long lived in comparison. Molecules now have a longer timeframe to exist in an excited state before grounded and releasing energy in the form of fluorescence. The number of excitation and emission cycles that fluorophores must undergo in order to experience photobleaching is dependent on the nature of their environment. In some cases photobleaching may be observed after a very short period of time while in other cases it may take up to a million cycles before a noticeable decrease in fluorescence occurs.

Quenching has a similar effect to photobleaching as the fluorescence level of the dye solution is also observed to reduce. There are two primary types of quenching; collisional and static. Collisional quenching occurs when fluorophores in an excited state collide with other molecules in the solution resulting in deactivation of the fluorophore and a return to its

ground state. Collisions may occur with ions, oxygen or other fluorophores (referred to as self-quenching.). Static quenching refers to the case where fluorophores undergo reactions with other molecules in their ground state. In both cases the fluorescence of the solution is reduced as the quenching process has reduced the number of fluorophores that can absorb and emit laser light. Clearly these effects are undesirable if they occur during the course of an experiment or between experiments. While it is difficult to determine conclusively whether quenching affected experiments (as this can occur while fluorophores are in their ground state), photobleaching was investigated by irradiating a sample of R6G dye for a period of time. This was carried out using A 4 L Perspex box filled with R6G dye and exposed to the laser light sheet (set at 4W) for 40 minutes. This time scale was deemed acceptable as it reflects the maximum duration that the dye would be irradiated during an experiment or calibration. Recordings were taken approximately 10 minutes after the light sheet was turned on. The fluorescence recorded over time is plotted in Figure 3.16. As shown, no discernible decrease in fluorescence is observed over the testing period. The largest discrepancy between measurements was 1.4%.

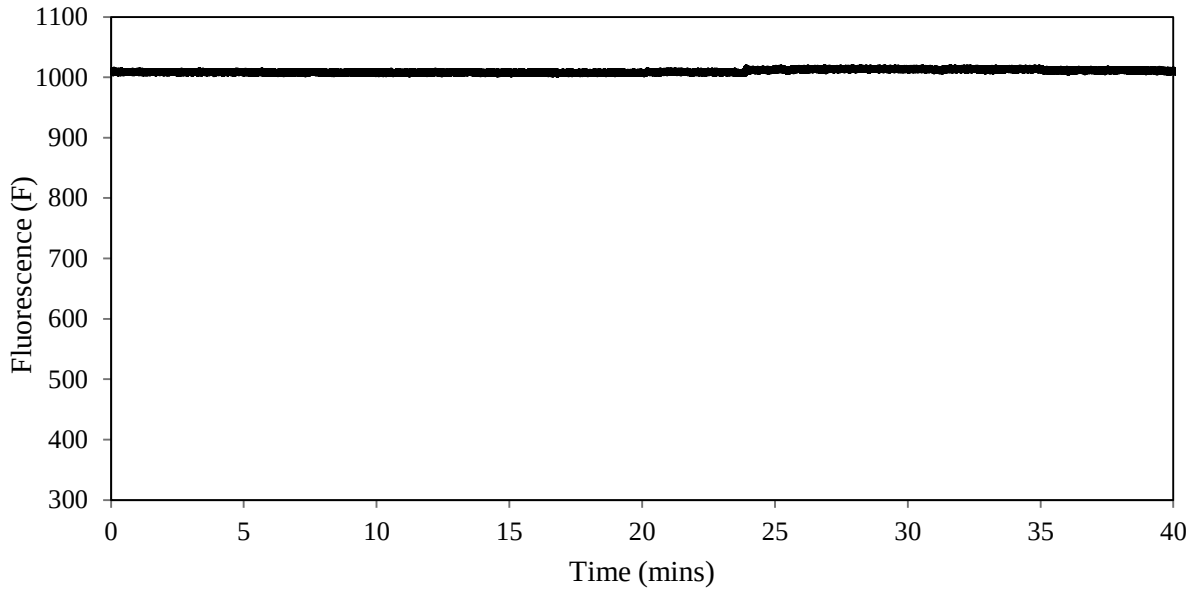

Figure 3.16: Fluorescence of R6G solution irradiated over 40 minutes, 0.003 mg/l, 50% Gain.

3.3 Extraneous Sources of Light and Reflections

Whenever the camera recorded light from sources other than the fluorescent dye, the accuracy of the experimental system was compromised. Flow concentrations were based solely on the intensity of light recorded by the camera, therefore it was critical that any additional light entering the flow region (including reflections) was eliminated, or remained constant between experiment and calibration. The latter approach was more difficult to implement so experiments were conducted under blackout conditions. This required turning off all lights and ensuring that the laser light could not be reflected off any surfaces. Apparatus placed within the tank (rear glass panel, storage cylinder metallic discharge nozzle) were painted matte black to mitigate these effects. The laser light itself was also eliminated from the camera image using a Schott OG 550 optical filter placed in front of the camera lens. The importance of the absorption and emission wavelength difference is highlighted here as fluorescent light emitted by the flow can be distinguished from the background light intensity. This filter only permitted light of wavelength 550 nm and over to be identified by the camera, therefore background laser light (532 nm) was blocked while fluorescent light from the dye (555 nm) could still be measured. These efforts to mitigate any potential influence from unwanted light sources were successful for flow cases where the lower horizontal platform was not present. When the platform was added to the setup an additional layer of complexity was introduced to the system. The platform was made of clear Perspex and positioned within the vicinity of the discharge location. The light sheet interacted with the solid surface, resulting in undesirable reflections. Furthermore, the platform could not remain in place during calibration so these effects were not accounted for in the calibration process. Consequently the fluorescence (and concentration) of the flow near the boundary could be artificially increased. To alleviate these reflections, the platform was painted matte black and the bottom of the light sheet was blocked so that it would not interact directly with the boundary. Centreline dilution results from simple vertical jets impinging a boundary suggest that these modifications to the setup were successful. The centreline dilution response is plotted against the path length from three experiments of differing discharge heights from the boundary (H/d) in Figure 3.17. The path length (z) is represented as the distance in mm from the solid platform. For clarity purposes, the entire path length has not been included. The centreline dilution is presented in its non-dimensional form ($C_0 d/$

$C_m H$) hence measurements at the boundary collapse for each test. If the path length was non-dimensionalised as well, each plot would collapse onto each other. Figure 3.17 shows the dilution levels off as the flow approaches boundary and it is clear that this point varies with the boundary height condition (H/d). Based on this result it is appropriate to assume that this response is a function of the flow behaviour as opposed to the experimental system. In the latter case it is expected that this location would be the same regardless of the boundary height. Additionally the concentration may increase if reflections from the boundary are significant.

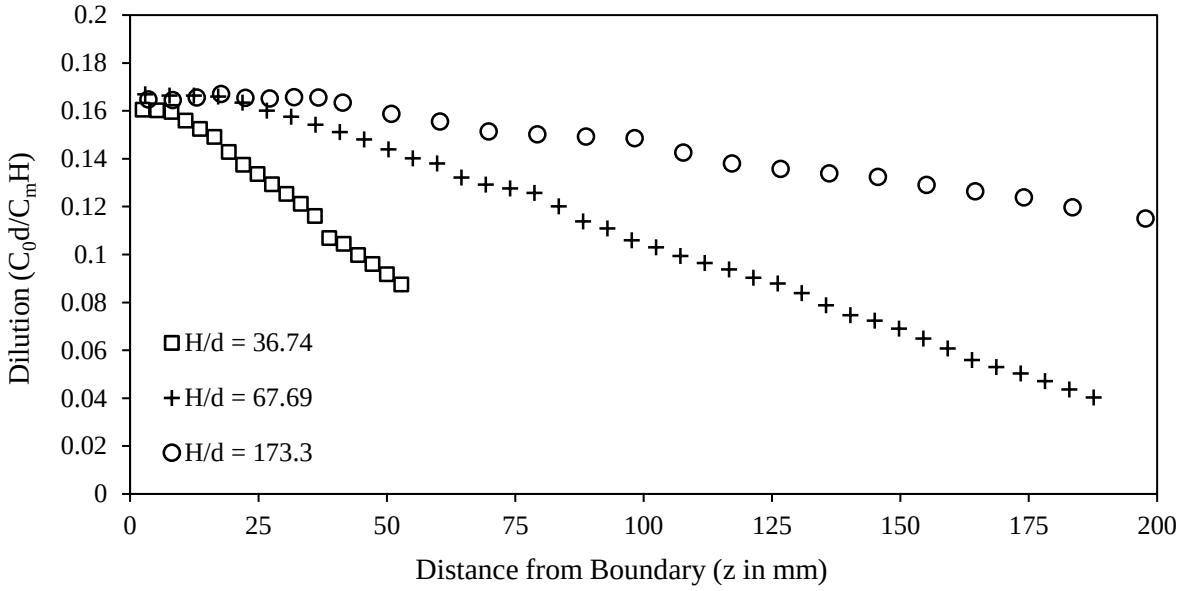

Figure 3.17: Centreline dilution response of vertical jets near a horizontal boundary.

3.4 Experimental Processes

3.4.1 Testing

The steps taken to conduct each test are described as follows.

1) Preliminary setup of the testing facility involved
   - Cleaning the tank walls

- If boundary influence was being investigated, the circular platform and discharge nozzle were set up in accordance with the chosen source height above the boundary.
- Setting the desired discharge angle or re-positioning the source (if vertical flows were being investigated).
- Positioning the light sheet in line with the source.
- Preparing the source fluid. Approximately 78 litres of source fluid was prepared for each testing session which allowed 3 – 4 experiments to be completed.

2) While the tank was filling up with water, the source fluid density was measured and recorded using an Anton Parr density meter and then transferred to the pressurised cylinder located within the tank walls. The tank filling process took approximately 40 minutes.

3) For each test, initial conditions were pre-determined and recorded. These included; source pipe diameter (d), angle of discharge (θ), Froude Number (F_0), source height above boundary (H) and source fluid density (ρ). The selected Froude number, source fluid density and pipe diameter determined the required discharge flow rate.

4) The head unit and spinning mirror were turned on and left for around 10 - 15 minutes before use.

5) While the tank was filling, air bubbles would often stick to the tank walls and to the boundary platform (if being used). Before experiments were conducted, bubbles were swept away from areas of the tank that were within the viewing field of the camera.

6) Prior to the commencement of each experiment, a blank intensity image was taken.

7) Source fluid in the storage cylinder was pressurised to 20 psi and pumped up to the header tank. Fluid was allowed to flow down to the valve placed just before the discharge source.

8) Once the header tank was filled, the valve preceding the discharge source was set in accordance with the desired flow rate and fluid was discharged through the source pipe and into the tank. When the flow rate was observed to stabilise, flow rate recordings were logged and the camera began capturing images.

9) The duration of each experiment was around 7 - 12 minutes, depending on the physical scale of the flow. When the initial conditions selected resulted in a larger flow scales, the tank would fill up with source fluid relatively quickly and this limited the time that reliable data could be obtained. After each test was completed, the camera, laser and flowmeter logger were stopped. The images were transferred to an external hard drive ready for further analysis.

3.4.2 Calibration

LIF is a sensitive method where results can be affected by small changes in the experimental equipment. While the camera settings and source concentration remained constant for all experiments the positioning of the light sheet proved problematic at times. If left for extended periods of time (over the course of days) the sheet would sometimes move slightly away from the centreline. On each occasion this occurred, the calibration process would be carried out. Calibrations were performed by filling a Perspex cell with a known concentration of R6G solution. The cell was placed along rails attached to the top of the tank and positioned in line with the laser light sheet. Since the calibration cell was only 160 mm wide (for attenuation levels to be acceptable), it did not cover the full extent of the camera image. In order to achieve this coverage, eight positions were marked out along the railing and images were taken of the cell at each position. This arrangement is illustrated in Figure 3.18. Figure 3.14 showed that a single concentration of 0.0122 mg/l could be used to obtain a linear fluorescence response by varying the laser wattage. Here concentrations were substituted with laser light intensity values so that fluorescence (F) – intensity (I) relationships were obtained instead. Results related to concentration measurements are presented in the form of a dilution. Therefore as long as the initial discharge concentration is converted to a corresponding laser wattage, the dilution results are consistent. Images were captured at each position and averaged (over 10 seconds, 16 hz frame rate) using laser powers of 4, 3, 2 and 1

watts. An additional background image of the tank was taken without the calibration cell. In total 33 images were obtained for each calibration.

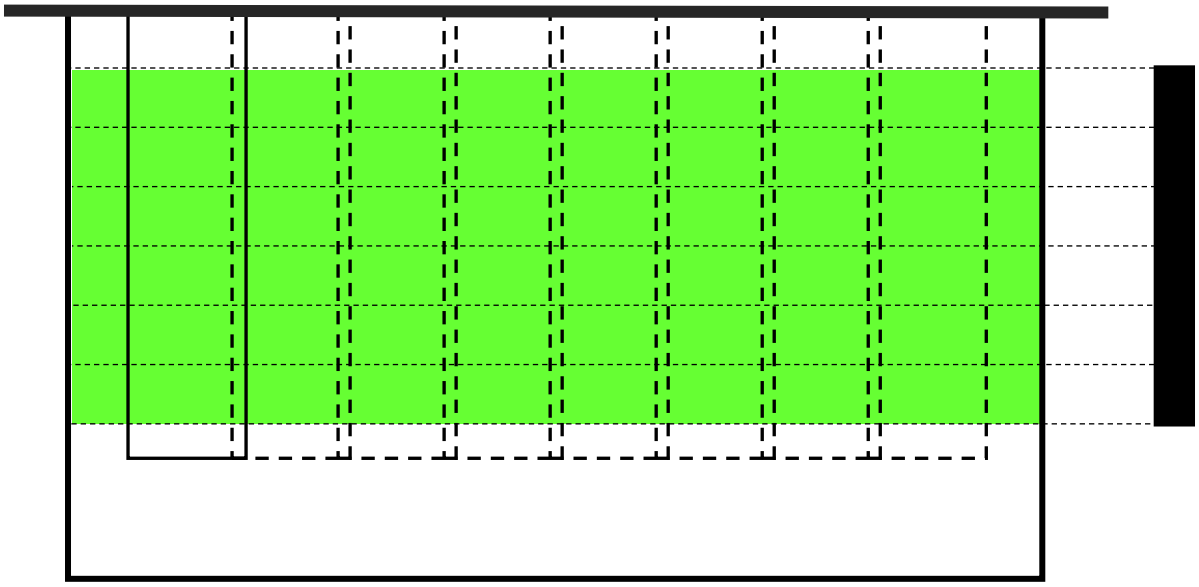

Figure 3.18: Configuration of calibration cell within tank. Images of the cell are taken at eight different positions and stitched together.

After the necessary calibration images were collected, they were uploaded to a MATLAB program and further processed. Calibration was performed on a pixel by pixel basis so a fluorescence – intensity relationship could be obtained for each pixel within the field of view. The following steps were taken to achieve this.

1) For each laser power setting 8 images were stitched together. Prior to this, it was necessary to identify pixels affected by dust and other solid particles. Artificially high intensities were observed wherever the light sheet interacted with these unwanted particles. Each image was subjected to a filtration algorithm which identified and replaced these pixels based on the average fluorescence of pixels surrounding them.

2) Once each image had been filtered for spurious intensities they were stitched together. An overlapping region existed between adjacent images and fluorescence values were simply averaged. Figure 3.19 shows an example of a stitched calibration image. Attenuation

effects were accentuated when more salt was added to the source and sometimes increased beyond the threshold value of 2%. When this occurred, pixel intensities were adjusted using Equations 3.8 and 3.9. Figure 3.20 illustrates the use of these equations. Fluorescence values along each column were averaged and plotted against the horizontal distance across the image, prior to and after using Equations 3.8 and 3.9. Note that the light sheet was entering the tank from the right hand side of the image. The spatial variability shown in Figure 3.19 and Figure 3.20 did not pose any issues as it was accounted for during calibration.

3) Each pixel in the flow field has five fluorescence (F) values (including the black level image which is taken away from the remaining images) with which to obtain a fluorescence (F) – intensity (I) relationship. A linear best fit line was applied (while fixing the y-intercept at 0) and the term m was determined for each pixel (refer to Equation 3.7) and stored. Intensity values for each pixel could be 'looked up' and applied to raw images. As stated, processed images were perceived as equivalent laser intensities (measured in watts) as opposed to concentrations. Results related to concentration measurements have been presented in the form of a dilution. Therefore as long as the initial discharge concentration is converted to a corresponding laser wattage, dilution results are consistent. The MATLAB code used to convert raw intensity images to calibrated concentration fields is included in Appendix A.

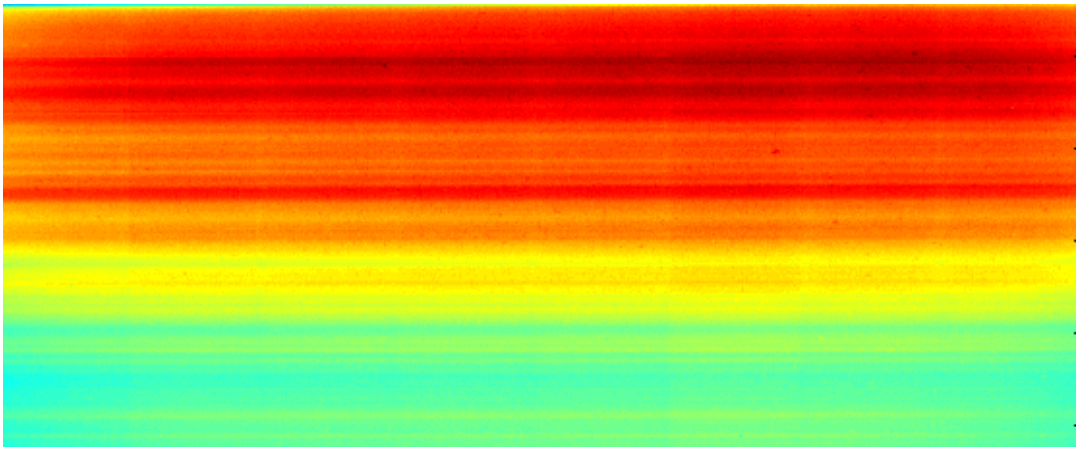

Figure 3.19: Calibration Image after stitching, C_c = 0.0035 mg/l, Density difference w.r.t ambient = 0.35%, Laser Power = 4 W.

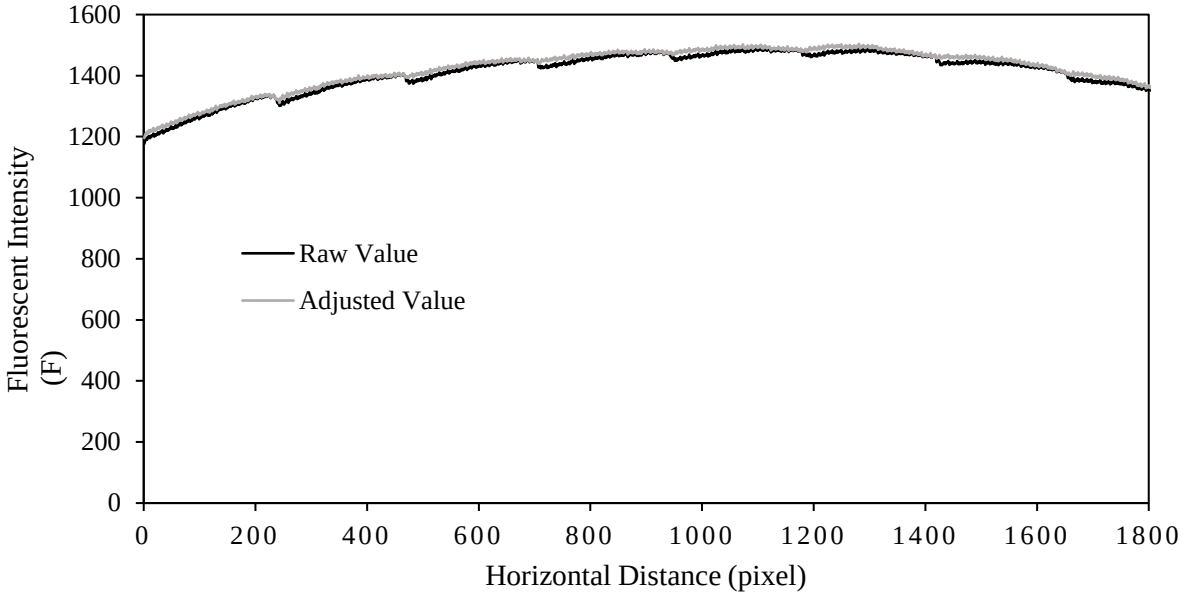

Figure 3.20: Fluorescence values averaged over each column and plotted against horizontal pixel distance. Both the original and attenuation adjusted values have been plotted C_c = 0.0035 mg/l, Density difference w.r.t ambient = 0.35%, Laser Power = 4 W.

3.5 Post Processing Systems

3.5.1 Image Selection

Most of the results presented in this study have been derived from time-averaged data, where the images acquired from each test have been averaged. However not all images obtained were suitable for inclusion in the averaging process. Experimental results were initially analysed to determine when steady state conditions had been achieved and to determine when boundaries other than the lower platform were influencing flow behaviour. The flow near the return point was more susceptible to these boundary influences so conditions at this location were primarily used to determine the period where the flow behaviour was essentially steady. Experiments without the platform were typically not affected by issues associated with these boundaries such as fluid re-entrainment. Because the discharge nozzle was placed near the centre of the tank (~ 720 mm of clearance to the bottom of the tank, 600 mm either side of the nozzle) confinement of the tank walls was not an issue over the image capturing period.

Introducing the platform to the experimental setup added complexity to this situation. Although there was space between the tank walls and the platform (which allowed the boundary flow along the boundary to fall into the region below the platform), fluid was still observed to eventually reach the tank walls and re-entrain into the primary flow. Figure 3.21 shows fluorescence signal from a point along the platform, near the flow edge plotted as percentage difference from the mean value. Measurements are also reported as two minute moving averages. After 10 minutes it is clear that the recorded value gradually increases, indicating a loss of steady state conditions.

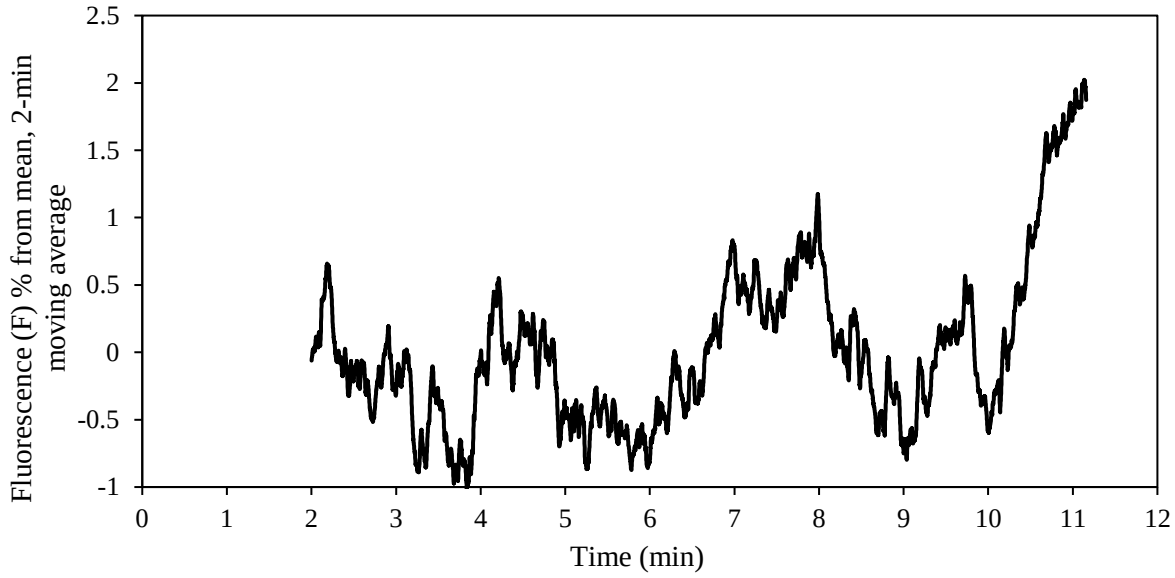

Figure 3.21: 2-minute moving average of the fluorescence signal taken at the flow edge, near the platform. Values are taken as percentages from the mean value of the signal over the entire recording period.

3.5.2 Initial Concentration

Dilution measurements were obtained by scaling the centreline concentration with the initial concentration of the discharged fluid. However, in some cases accurately estimating this value proved challenging. Calibration provided an initial estimate of the source concentration, and the accuracy of this estimate was then assessed based on the behaviour of the flow within the jet region. It has been well established that dilution growth within the initial region of the flow path follows that of a pure jet. Oliver (2012) also employed this method to quality assure dilution results. The dilution of a jet is described in Equation 3.10.

$$\frac{C_0}{C_m F_0} = \frac{s}{F_0 d} \times \frac{1}{5.608} \qquad 3.10$$

Where C_0 the initial concentration is, C_m is the centreline concentration and $s/F_0 d$ is the path length. From the literature (Oliver, 2012) and the experimental data presented in Chapter 5 and 6, the jet solution is valid for a negatively buoyant jet up to a path length of approximately $s/(F_0 d) = 2.0$. Beyond this location the flow is observed to transition to plume which resulted in an increased dilution rate. For each experiment, the centreline dilution (using the calibration estimate of the initial concentration) was plotted against the flow path alongside the jet solution from Equation 3.10. When necessary, dilution measurements were adjusted by a single coefficient until they matched the jet solution. The initial discharge concentration was subsequently adjusted based on this coefficient. Figure 3.22 and Figure 3.23 illustrate how dilutions were adjusted based on the jet solution. In Figure 3.22, F_0 = 48.15 is clearly an outlier data set and is adjusted to match the theoretical jet solution in Figure 3.23. Since every centreline dilution measurement pertaining to a single experiment was adjusted by the same factor, the relative level of mixing between different locations along the flow path remained the same. Oliver (2012) reasoned that this method ensured that dilution results between experiments are presented in the most reliable manner as accumulated error would be avoided. It should also be noted that results relating to the flow geometry were unaffected by changes to the initial concentration.

Near the source, extrapolation of the calibration curve was required where raw intensity readings were higher than the calibration images. For most INBJ tests concentration statistics have been presented from $s/F_0 d = 0.50$ onwards. As shown in Equation 3.11 the extent of this extrapolation increased with decreasing Froude number

$$\text{Extrapolation } \% = \left(\frac{C_0}{F_0}\frac{s}{F_0 d}\frac{C_m}{5.608}\right) \times 100 \qquad 3.11$$

The general consistency between experimental results of differing Froude numbers suggests that this extrapolation did not have a significant impact of the data quality near the source. This is consistent with concentrations being at a level where a linear response is maintained.

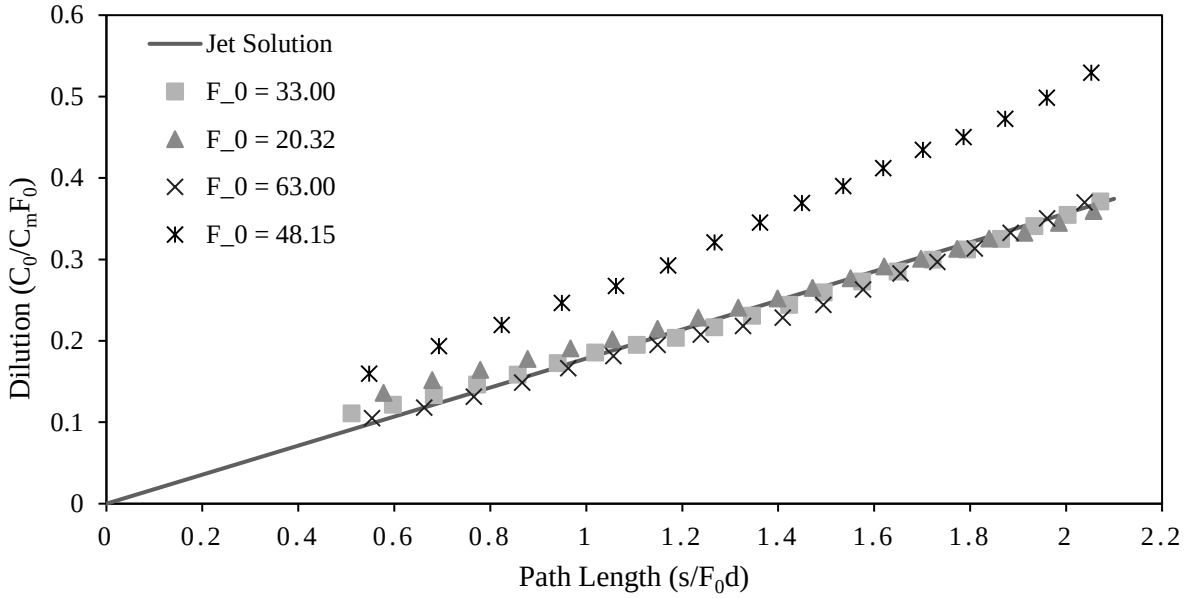

Figure 3.22: Centreline dilution within jet region for various INBJ experiments, with C_0 taken as initial estimate.

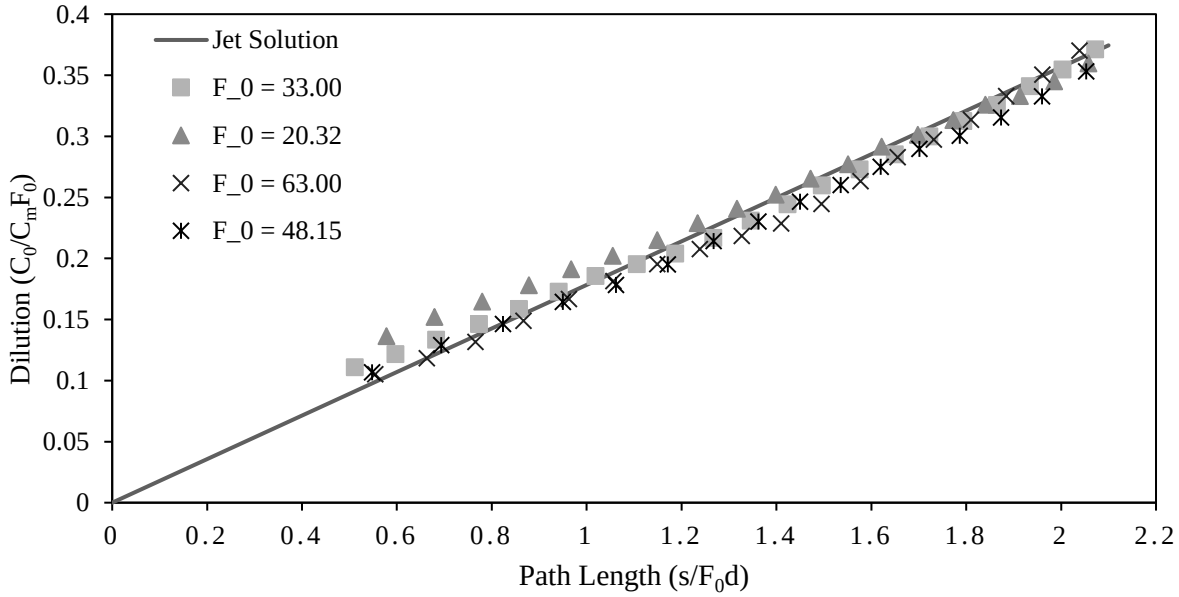

Figure 3.23: Centreline dilution within jet region for various INBJ experiments, with C_0 adjusted using jet solution.

3.5.3 Time-Averaged Results

After each test was time-averaged and calibrated, an algorithm developed in MATLAB was utilised to extract relevant flow statistics relating to flow geometry and centreline dilutions. As flow configurations ranged from inclined discharges to vertical jets, different processing codes were used. For each flow configuration a source file was created detailing the initial conditions tested (Pipe Diameter (d), Froude Number (F_0), Source Fluid Concentration (C_0), Source Coordinates) and the extent of the flow region to be analysed. Most results are presented in the context of the behaviour of the flow centreline as this point corresponds to the maximum concentration (or minimum dilution). Therefore determining the position of the flow centreline formed the basis of our analysis. In order to perceive the flow centreline, cross-sections perpendicular to the centreline flow path were examined. The following sections describe how results were obtained for each flow configuration.

3.5.3.1 Vertical Discharges

Vertical discharges were relatively simple to analyse as the horizontal location of the flow centreline did not deviate following discharge. Horizontal slices were taken through the flow field and the maximum concentration (C_m) and Gaussian spread (b_c) was initially estimated by locating values along the slice that met the required criteria. These initial estimates were refined by fitting Gaussian profiles through the concentration data between the limits $-1.00 \leq r/b_c \leq 1.00$, where $r/b_c = 0$ represents the flow centreline. This was carried out using the curve fitting tool in MATLAB which subsequently determined a more representative value for C_m and b_c. Along the platform, a similar approach was taken when extracting results. Vertical slices were taken (as opposed to horizontal slices) through the flow between the limits $0 \leq z/b_c \leq 1.00$, where $z/b_c = 0$ represents the flow at the boundary height.

3.5.3.2 Inclined Discharges

By comparison, examining inclined discharges posed more challenges. Due to the curved trajectory of the flow path, the centreline was determined using the iterative process described below. The MATLAB algorithm used to process inclined flows is included in Appendix A.

1) An initial estimate of the centreline was determined by taking slices (approximately perpendicular) through the flow at various locations. The origin of each slice was located on the underside of the flow, below the return point and in between the ascending and descending arms of the discharge. Flow concentrations were recorded along each slice and the point corresponding to the maximum concentration value defined the centreline. While these slices were not exactly perpendicular to the flow they provided an adequate first estimate of the flow centreline.

2) A 4th order polynomial was applied to the initial centreline estimate as these curves provided the most representative centreline fit. More accurate perpendicular cross-sections could be taken to define the flow centreline more precisely. Crude estimates for C_m and b_c were obtained along each cross-section by determining values that met the required criteria.

3) The centreline position was further refined by applying a Gaussian function to each cross-section. Profiles were fitted between $-0.25 \leq r/b_c \leq 1.00$ using the curve fitting tool in MATLAB. The bounds for the fitting process were selected due to the observed asymmetry of inclined negatively buoyant flows and is consistent with Crowe et al. (2015), Kikkert et al. (2007) and Oliver et al. (2013). Values for C_m and b_c were also obtained from this process. 4th order polynomials were again fitted to the centreline flow path and this process was repeated until the 'goodness of fit' or R^2 value associated with the fitted curve was adequate. A threshold level for R^2 was set at 0.96 however most curves exceeded this value (closer to $R^2 = 0.99$).

4) Once values for the centreline location, C_m and b_c had been established, they were scaled with the appropriate initial conditions. For each test, a table of results was produced with the following headings: Horizontal co-ordinate (x/F_0d), Vertical co-ordinate (y/F_0d), Path length (s/F_0d), Dilution (C_0/C_mF_0), Spread (b_c/F_0d).

   Note: the path length, s/F_0d between two points along the centreline was calculated using the following formula:

$$s/F_0d = \int_a^b \sqrt{1 + (f'(x/F_0d))^2}\ d(x/F_0d) \qquad 3.12$$

where the function $f(x/F_0d)$ is the 4th order polynomial fit obtained from step 2).

Extracting results near the lower boundary from inclined negatively buoyant jet experiments proved problematic at times. As described in Section 3.5.3.2, centreline statistics were extracted by applying Gaussian fits to concentration profiles perpendicular to the centreline trajectory. The platform would often interrupt this process when the flow close to the boundary was considered. As a result, some information within this region could not be obtained. However, prior to impacting the boundary, the dilution is shown to level off at a particular value. The dilution at the impact point could therefore be inferred from this behaviour as the concentration is not expected to vary between this point and the impact location of the flow centreline. Dilutions recorded for vertical discharges also exhibited the same behaviour and validate this assumption (see Figure 3.17). For these tests, results pertaining to at least 98% of the total flow path were extracted. It should be noted that the shortcomings of the post processing algorithm for INBJ experiments never extended to the return point. In each test, the results obtained included conditions at the return point as well as data points where the centreline dilution stabilised. Therefore geometric and dilution coefficients determined within this region are reliable. Abessi and Roberts (2015) provided arguments against using the 'levelling off' value as the dilution at the impact point. In their experiments the centreline dilution was also observed to stabilise, however directly at the boundary, the flow field included a thin layer of high concentration fluid (i.e. the dilution decreased). The impact dilution was subsequently reported based on this result. Precautions were taken in this study to avoid reflections from the boundary and verification tests were carried out to confirm that the system would not interfere with fluorescent recordings. It is still inconceivable that the dilution can decrease along the flow path because this would imply that the flow is mixing with higher concentration fluid, which (it is assumed) does not exist within the system. However, this perceived layer of high concentration fluid (3 – 5 mm) was also observed at times in the present study. This behaviour was not consistent between experiments. Therefore, this small region of the flow field was deemed unreliable, which

potentially reflect an unresolved issue with the experimental system as opposed to counterintuitive flow behaviour.

3.5.4 Temporal Statistics

Temporal statistics are useful metrics that can effectively describe the behaviour of turbulent flows in a qualitative manner. This study presents root mean squared (RMS) and intermittency values. RMS describes the relative magnitude of fluctuations for a varying quantity. For the present study, this calculation can be applied to a series of instantaneous concentration measurements using the following equation.

$$\mathrm{RMS}(C') = \sqrt{\overline{C'^2}} = \sqrt{\frac{\sum_{i=1}^{n}(C_i - \bar{C})^2}{n}} \qquad 3.13$$

where C_i is the instantaneous concentration measurement, C' is the fluctuating component of C_i and $\bar{C}$ is the mean component of C_i. The RMS value associated with the concentration signal is a combination of the real turbulent fluctuations (C_t') as well as noise from the measuring system (C_n'). The background component (i.e. noise) can be filtered out using Equation 3.14 leaving only the contribution from turbulent fluctuations (Oliver, 2012). This required RMS values of the background noise to be independently calculated for each pixel.

$$\mathrm{RMS}(C_t') = \sqrt{(\mathrm{RMS}(C'))^2 - (\mathrm{RMS}(C_n'))^2} \qquad 3.14$$

Intermittency (γ) can be defined in a number of ways. In a general sense this quantity refers to the probability distribution of a pre-defined event. In the present study intermittency at a particular location within the flow field is defined as the proportion of the concentration signal that does not exceed a specified threshold value over the duration of an experiment. Equation 3.15 describes the intermittency calculation where C_i refers to an instantaneous concentration and C_{th} is the threshold concentration. Thus an intermittency of 0 indicates that the signal did not fall below the threshold value and an intermittency of 1 indicates the signal did not exceed the threshold value. Wherever intermittency is discussed in the text, the

corresponding concentration threshold used to generate the intermittency field has been specified.

$$\text{Intermittency } (\gamma) = P(C_i < C_{th}) \quad 3.15$$

3.6 Error and Variability of Results

3.6.1 Time-averaged Statistics

In order to determine the reliability of time-averaged results, it is necessary to evaluate the error in the measuring system as well as the variability in results associated with the sampling of turbulent flows. Calibration is a significant component of the measuring system and its ability to reliably convert raw fluorescence values into equivalent concentrations is integral to the overall accuracy of time-averaged data. The accuracy of this process can be affected in a number of ways and the various checks to determine the significance of these issues have been discussed throughout the chapter (Sections 3.2.2 and 3.3). The calibration relationships are assumed to be linear and the appropriateness of this assumption can be measured in terms of the goodness of fit or R^2 value of the fluorescence - intensity relationship for each pixel. A frequency plot of R^2 values is given in Figure 3.24. Over 98% of pixels have R^2 values above 0.995, suggesting that the overall contributions of these individual calibration recordings to the error of the experimental system is negligible. More significant errors are likely to come from potential attenuation effects, which were capped at 2% and the stability of the fluorescent intensity signal which was found to vary by 1.4% over 40 minutes.

Due to fluctuations in the recorded signal, time-averaged turbulent flows always have some degree of inherent variability and the degree of this variability is dependent on the number of images recorded and the recording time period. Longer time scale fluctuations are attributed to the existence of large scale eddies which entrain ambient fluid into the primary flow. The time scale of these fluctuations is related to the eddy rotational time or 'turnover time'. If each experimental record incorporates enough 'eddy turnovers', then fluctuations can be averaged out in a consistent manner. Larger scale flows (i.e. large $F_0 d$) involve larger eddies, hence demand longer averaging periods and are susceptible to greater variability.

Consequently, inconsistencies in time-averaged results differed based on the flow configuration tested. For example centreline concentrations recorded for vertically discharged experiments within the free flow region displayed good consistency. However the flow recorded along the boundary contained larger scale eddies and therefore results were more variable. Concentration recordings from INBJ experiments were relatively consistent up to the maximum height (within the jet region), however near the return point, the scale of the flow was larger and the variation in the results reflected this observation. The recording period was constrained by the confinement of the tank walls and the maximum running duration allowed was between 7 - 12 minutes (~ 6000 to 11000 images) depending on the flow type and initial discharge conditions.

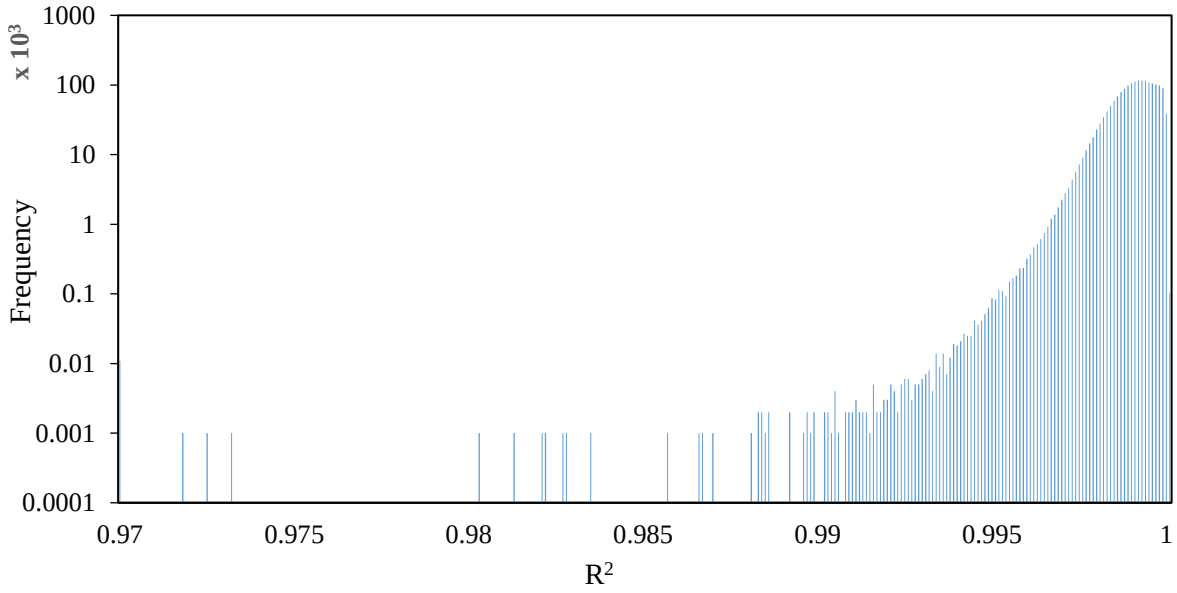

Figure 3.24: Frequency plot of R^2 values determined for each pixel during a single calibration test.

Confidence in the experimental system should solely be based on the ability to deliver the correct equivalent concentration (or intensity, I) at a particular pixel. The primary sources of error are represented by potential attenuation effects and signal quality, hence the total error has been estimated between ± 3% to 4%. Oliver (2012), whose experimental system was similar to the present study, estimated the error of time-averaged dilutions at ± 5% based on the quality of the recorded intensity signal.

3.6.2 Temporal Statistics

Temporal statistics were predominantly affected by the noise generated from the experimental apparatus (i.e. background noise). Ideally, fluctuations in the intensity signal should be dominated by turbulence as opposed to background noise. As discussed in Section 3.1.2.1, background noise can be increased or lowered based on the gain setting on the camera. The worst case scenario was when the camera gain was set at 100%, which was necessary for some experiments. The background noise could however be removed from the concentration RMS flow field using Equation 3.14. In theory, the RMS statistic should be zero within areas where the flow was not present, however residual fluctuations still remained. These residual fluctuations represent the error associated with these measurements. To quantify the average error, an empty area (fluid free region) of the RMS flow field was considered from an INBJ test. The RMS values in this region (after background noise was removed) were subsequently averaged and returned a mean value of 0.02. Therefore the error for RMS measurements is estimated at ± 0.02. Approximately 8.3 x 10^6 pixels or 25% of the viewing field was included as this represented a sufficient sample size over which to determine the error. This value is an absolute error as it is expected that background noise is purely a function of the experimental apparatus as opposed to the flow behaviour. The significance of this error is therefore dependent on the relative amount of turbulence within the flow region considered. For example, the maximum RMS value along the cross-section of a simple jet flow is approximately 0.20, hence the error associated with this measurement would be ± 10 %.

The variability of temporal data is a function of the sampling frequency (fixed at 16 hz) and duration and these were constrained by the experimental apparatus used. ‘Minimum’ sampling frequencies and durations were therefore not considered and temporal results were produced using the maximum amount of raw data able to be acquired. For example vertical jet experiments produced more variable results than buoyant experiments as sampling durations were more limited by the tank boundaries. Based on the images and results obtained, it was apparent that in general, temporal data required longer sampling durations than time-averaged data to achieve high quality results.

3.7 Summary

The objective of this chapter was to illustrate that reliable and repeatable experimental data for the relevant flow configurations could be obtained. Sections 3.1 and 3.2 included a description of the experimental apparatus and the theory behind the laser induced fluorescence (LIF) method. The potential issues surrounding the various components of the system and their ability to influence accuracy of time-averaged and temporal statistics have also been discussed. These issues centred on the importance of maintaining conditions between calibration and experiment and ensuring the quality of the recorded fluorescence signal. In particular, adapting the existing LIF system to flow configurations where a lower boundary was present provided additional challenges because the boundary could not be included during calibration (Section 3.3). Various checks were performed to assess the significance of these issues and finally determine whether they could be neglected, mitigated or whether they needed to be accepted as a limitation of the process. Ultimately the success or failure of the system is determined by the consistency of the spatial and concentration results extracted from each experiment.

Chapter 4 Boundary Interaction of Vertical Buoyant Jets

Lower boundary effects are investigated using simple vertical discharges impinging a raised horizontal boundary. The experiments discussed in this chapter are termed 'buoyant jets' as they include a certain amount of negative buoyancy at the source. The extent of this buoyancy serves as the criteria for flow categorisation where each discharge is classified as a jet, transitional buoyant jet or plume type flow. Results from jet type flows are discussed in Section 4.2. Table B.1 of Appendix B details the initial conditions used in each experiment. These flows have been released at non-dimensional heights from the platform (H/d) ranging between 36.30 and 173.3. Concentration measurements, obtained from LIF experiments have been used to describe the flow behaviour as well as velocity field data, from a previous researcher (Crowe) who conducted PTV experiments on a similar discharge configuration. These results have previously not been reported however the methodology used to conduct these experiments is available in Crowe (2013). An integral model has been developed to provide a relatively simplistic framework for quantifying and interpreting the flow behaviour. The data sets enable the scale of the impact region to be defined based on the ability of integral techniques to model the flow entering and leaving this region. These data sets also offer insights into the flow behaviour in the impact region and they provide the basis for determining the influence of the impact region on the flow behaviour. Section 4.3 focuses on discharges with a more significant buoyancy component (transitional buoyant jets and plumes) impinging a boundary. Concentration measurements were obtained from experiments where the non-dimensional source height ($H/F_0 d$) was varied between 3.25 and 6.16. The behaviour of the overall flow is not dealt with in the same depth as the jet case however the experimental results provide insight into the influence of the boundary on buoyant flows and enable sound comparisons to be made. While an integral model is not

presented, the extent of the impact region is defined and flow statistics at the entrance and exit from this region are provided to form the framework for the development of future models. Finally a qualitative examination of the boundary flow for buoyant discharges is given describing the transition from the near field mixing region to the far field region where mixing becomes negligible.

4.1 Flow Classification

Recalling Section 2.2, buoyant jets can be categorised based on the distance travelled (z) relative to the jet to plume transition length (l_{jp}). These inequalities are re-stated in Equation 4.1 where z/l_{jp} is expressed as $H/F_0 d$ in order to classify flow conditions at the boundary.

Jet	$H/F_0 d \leq 0.94$	a)	
Transitional Buoyant Jet	$0.94 < H/F_0 d \leq 4.71$	b)	4.1
Plume	$4.71 < H/F_0 d$	c)	

As stated in Section 2.2, the governing non-dimensional source height can be expressed as either H/d for jet flows, or $H/F_0 d$ if the flow is a transitional buoyant jet or plume like. The delineations outlined in Equation 4.1 do not take into account where boundary influences begin to take effect above the solid platform. Consequently it is likely that the flow behaviour at the boundary does not exactly conform to the constraints stipulated above.

4.2 Vertical Jets

4.2.1 Analysis and Model Framework

The generic discharge configuration of a jet discharge impinging a horizontal platform is shown Figure 4.1, where a vertical discharge of non-buoyant fluid impinges a horizontal platform. Following Beltaos and Rajaratnam (1974) three distinct regions define this flow configuration (Free flow, Impact/Impingement and Boundary/Wall jet regions). To assist in

the interpretation of the experimental results for vertical jets, a relatively simplistic modelling framework is developed for non-buoyant discharges based on integral models with "top-hat" or average velocity and concentration profiles. The discharge is released a height H above the boundary where it has a diameter d and initial velocity U_0. Recalling that the initial volume flux (Q_0) is given by $U_0 \frac{\pi}{4} d^2$ and the initial momentum flux (M_0) is defined by $U_0 Q_0$. The non–dimensional source height (H/d) links the flow to the solid boundary and is thus an important scaling parameter. Near the source the flow behaviour is not influenced by the boundary and its behaviour can be modelled as a jet in an unbounded environment. However as the flow approaches the boundary it reaches a distance ($k_{H1}H$) where the model is no longer valid and at this point the flow enters the impact region. Note k_{H1} is a coefficient that defines the location of the entry to the impact region. Within the impact region the flow is re-directed and it leaves this region as a horizontal wall jet at a radius R ($= k_{H2}$ H), where k_{H2} defines the location of the exit from the impact region. Within the boundary region the flow has a self-similar form and its behaviour can again be modelled using integral modelling techniques. It is not possible to extend the integral modelling framework into the impact region because of the loss of self-similarity. However, establishing the conditions at the entrance to and exit from the impact region provides the basis for quantifying the transformation that occurs as the flow passes through the impact region. In Figure 4.1 the entrance spread, velocity, volume and momentum fluxes are defined by b_{TH}, U_{TH}, Q_H and M_H respectively. The corresponding conditions at the exit from the impact region are denoted as b_{TR}, U_{TR}, Q_R and M_R. Below we outline the integral models in the free flow and boundary regions that provide the basis for relating the conditions at the entrance of the impact region ($k_{H1}H$) to the exit conditions ($R = k_{H2}H$). By establishing these relationships it is possible to define the behaviour in the wall jet region in the context of the initial discharge conditions.

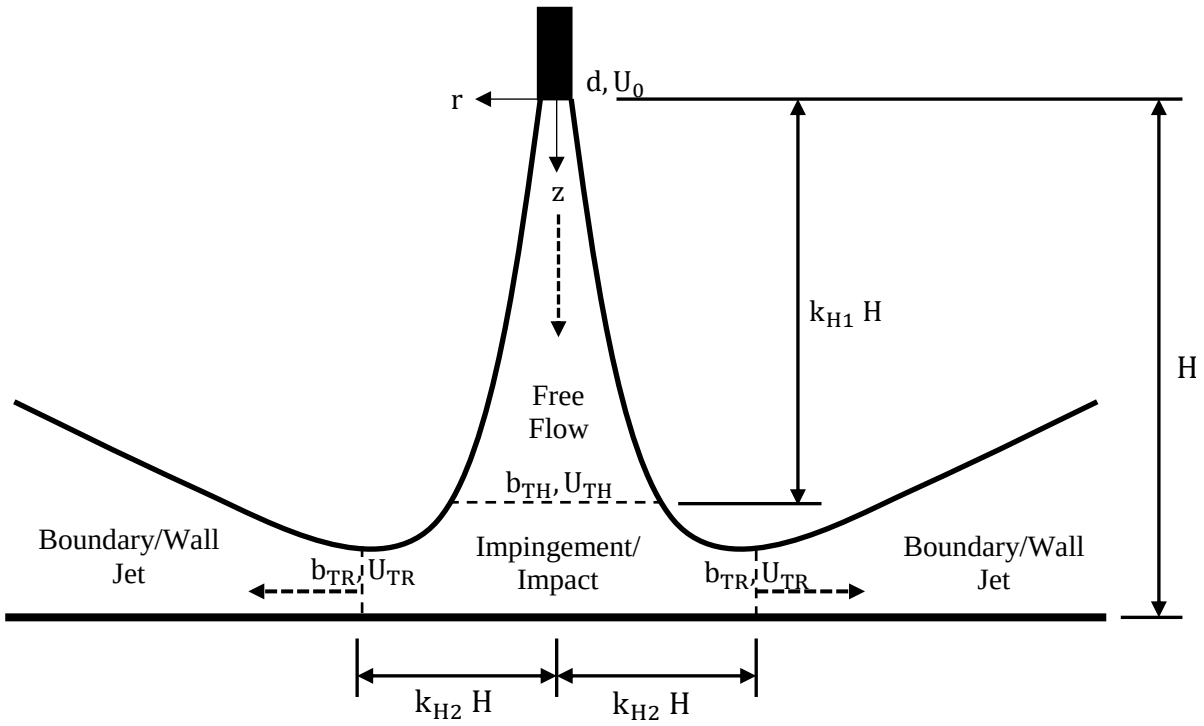

Figure 4.1: Flow configuration of a vertical jet impinging a boundary.

4.2.1.1 Free Flow Region

Integral formulations for jets are very well established (Fischer et al., 1979; Rajaratnam, 1976) and in the present context we make use of the linear spread assumption. Thus the flow radius (b_T) at z is defined by (k_T = 0.147, from Kikkert, 2006):

$$b_T = k_T z \qquad 4.2$$

There is no change in momentum flux within this region because there is no net force acting on the flow, hence the flow momentum flux (M) at z can be written as:

$$\frac{M}{M_0} = 1 \qquad 4.3$$

Thus the velocity (U_T) of the flow at z can be written in the form:

$$\frac{U_T}{U_0} = \frac{d}{2\,k_T\,z} \qquad 4.4$$

Similarly the volume flux (Q) at z can be written as:

$$\frac{Q}{Q_0} = \frac{2\,k_T\,z}{d} \qquad 4.5$$

Incorporating the source height parameter (H/d) into Equation 4.5 gives the following expression.

$$\frac{Qd}{Q_0 H} = \frac{2\,k_T\,z}{H} \qquad 4.6$$

4.2.1.2 Boundary/Wall Jet Region

Experimental data to date indicates that the spread of the radial flow perpendicular to the boundary is linear (Birch et al., 2005; Fairweather and Hargrave, 2002a, 2002b; Poreh et al., 1967) and hence we can express the flow spread b_T along the boundary as:

$$b_T = b_{TR} + k_{TB}(r - R) \qquad 4.7$$

where k_{TB} is the spreading rate of the wall jet and recalling that R is the radial distance from the impact point denoting the start of the boundary region and b_{TR} is the spread at the start of the boundary region. The non-dimensional from of the above equation is:

$$\frac{b_T}{b_{TR}} = 1 + \frac{k_{TB}}{k_{TR}}\left(\frac{r}{R} - 1\right) \qquad 4.8$$

where k_{TR} represents the 'virtual' linear spread rate in the impact region. The momentum flux of the radial boundary flow ($M = U_T{}^2 b_T r$) can be written in non-dimensional form as:

$$\frac{M}{M_R} = \frac{r}{R}\ \frac{b_T}{b_{TR}}\ \left(\frac{U_T}{U_{TR}}\right)^2 \qquad 4.9$$

Thus the velocity of this flow can be written in the form:

$$\frac{U_T}{U_{TR}} = \sqrt{\frac{\frac{M}{M_R}}{\frac{r}{R}\left[1 + \frac{k_{TB}}{k_{TR}}\left(\frac{r}{R} - 1\right)\right]}} \qquad 4.10$$

Similarly the volume flux of the radial flow ($Q = U_T b_T r$) can be written in non-dimensional form as:

$$\frac{Q}{Q_R} = \frac{r}{R}\ \frac{b_T}{b_{TR}}\ \frac{U_T}{U_{TR}} \qquad 4.11$$

Hence it is given by:

$$\frac{Q}{Q_R} = \sqrt{\frac{M}{M_R}\ \frac{r}{R}\left[1 + \frac{k_{TB}}{k_{TR}}\left(\frac{r}{R} - 1\right)\right]} \qquad 4.12$$

To make use of the above relationships it is necessary to define the variation of the momentum flux with radial distance. This requires that the potential impact of boundary shear stresses on the flow behaviour be incorporated into the model. Assuming the boundary stress (τ_B) can be written as,

$$\tau_B = k_f\, \rho U_T^2 \qquad 4.13$$

where k_f is a friction coefficient, the variation of momentum flux with radial distance can be derived as follows:

$$F_{\tau B} = k_f\, \rho U_T^2\, 2\pi r\, dr \qquad 4.14$$

where $F_{\tau B}$ is the friction force along the boundary. Therefore the change in radial momentum flux is given by:

$$\frac{d(\rho M)}{d(r)} = k_f \rho U_T^2 2\pi r \qquad 4.15$$

$$\frac{d\left(\frac{M}{M_R}\right)}{d\left(\frac{r}{R}\right)} = -k_f \frac{r}{b_{TR}} \left(\frac{U_T}{U_{TR}}\right)^2 = -\frac{k_f}{k_{TB}} \frac{M}{M_R} \frac{R}{r} \qquad 4.16$$

And integration of this equations gives:

$$\frac{M}{M_R} = \left(\frac{r}{R}\right)^{-\frac{k_f}{k_{TB}}} \qquad 4.17$$

It is generally useful to define the above parameters in the context of the original discharge. Given the vertical distance from the source to the entrance to the impact region is $k_{H1}H$, then the free flow region relationships define the spread (b_{TH}), velocity (U_{TH}) and volume flux (Q_H) conditions at the entrance to the impact region as:

$$\frac{b_{TH}}{d} = k_T k_{H1} \frac{H}{d} \qquad 4.18$$

Thus the velocity of the flow can be written in the form:

$$\frac{U_{TH1}}{U_0} = \frac{d}{2\, k_T\, k_{H1}\, H} \qquad 4.19$$

Similarly the volume flux of the radial flow can be written as:

$$\frac{Q_H}{Q_0} = \frac{2\, k_T\, k_{H1}\, H}{d} \qquad 4.20$$

It is then necessary to relate the impact region entrance conditions to those at the exit from the region. To do this it is assumed that this exit is located at a radial distance $R = k_{H2}H$

from the centre of the impact region. The conditions at the exit from the impact region (b_{TR}, Q_R, M_R) are then related to those at the entrance to the impact region (Q_H, M_H ($= M_0$) and H) through the following relationships:

$$b_{TR} = k_{TR}R = k_{TR}k_{H2}H \quad 4.21$$

$$Q_R = k_Q Q_H \quad 4.22$$

$$M_R = k_M M_H = k_M M_0 \quad 4.23$$

Combining equations 4.21, 4.22 and 4.23 then gives:

$$\frac{U_{TR}}{U_0} = \frac{k_{H2}\, k_Q\, k_T}{4\, k_{H2}} \frac{d}{b_{TR}} = \frac{k_{H1}\, k_Q\, k_T}{4\, k_{TR} k_{H2}^2} \frac{d}{H} \quad 4.24$$

It is also worth noting that the combination of equations 4.21, 4.23 and 4.24, yields the following relationship for the momentum flux coefficient (k_M):

$$k_M = \frac{M_R}{M_0} = \frac{k_Q^2 k_T^2 k_{H1}^2}{2\, k_{TR} k_{H2}^2} \quad 4.25$$

The spread, velocity and volume flux relationships for the established radial flow can then be written with reference to the discharge initial conditions as follows:

$$\frac{b_T}{H} = k_{TR}k_{H2}\left[1 + \frac{k_{TB}}{k_{TR}k_{H2}}\left(\frac{r}{H} - k_{H2}\right)\right] \quad 4.26$$

$$\frac{U_0 d}{U_T H} = 4\frac{k_{H2}^{3/2} k_{TR}\sqrt{k_M}}{k_Q k_T k_{H1}} \sqrt{\frac{M_0}{M}\frac{r}{H}\left[1 + \frac{k_{TB}}{k_{TR}k_{H2}}\left(\frac{r}{H} - k_{H2}\right)\right]} \quad 4.27$$

$$\frac{Qd}{Q_0 H} = 2\frac{k_Q k_T k_{H1}}{\sqrt{k_{H2}k_M}} \sqrt{\frac{M}{M_0}\frac{r}{H}\left[1 + \frac{k_{TB}}{k_{TR}k_{H2}}\left(\frac{r}{H} - k_{H2}\right)\right]} \quad 4.28$$

Experimental results provide guidance in quantifying the coefficients in the above equations. These coefficients define the scale of the impact region (k_{H1}, k_T, k_{H2} and k_{TR}) and changes in the volume and momentum fluxes of the flow as it passes through the impact region (k_Q and k_M). The boundaries of this region are determined from the applicability of the integral models for the jet and radial flow regions. For the wall jet equations, the spreading rate (k_{TB}) and boundary friction coefficient (k_f) are also needed to predict the flow behaviour.

4.2.1.3 Top-hat conversion factors

The velocity and concentration profiles of these flows do not have a top hat form and it is therefore necessary to develop relationships to move between the characteristic parameters of the measured profiles (b, U_m and C_m) and those of the top hat profiles (b_T, U_T, C_T). This process is well established in the free flow region where standard Gaussian functions are used to represent cross-section profiles. Typical mapping coefficients (from Kikkert, 2006; Oliver, 2012), are as follows:

$$b = 0.757b_T, \qquad U_m = 1.818U_T, \qquad C_m = 1.558C_T, \qquad 4.29$$

In the boundary region, Figure 4.2 depicts the relevant concentration (density) and velocity profiles and the corresponding top-hat equivalent profiles. In this region, the maximum velocity and concentration values occurs near or along the boundary.

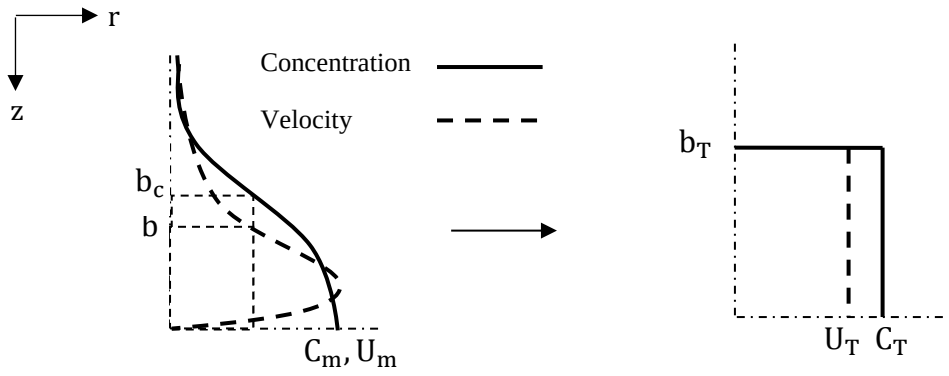

Figure 4.2: Concentration and velocity profiles in the boundary flow region converted into top-hat equivalent forms.

Mean concentration distributions can be represented by a half Gaussian function given in Equation 4.30. Note: λ_B is the concentration to velocity spread ratio taken as 1.20 from the present study (refer to Figure 4.11).

$0 \leq r/b < \infty$

$$\frac{C}{C_m} = e^{-z^2/(\lambda_B b)^2} \qquad 4.30$$

Mean velocity distributions along the boundary are slightly more complex. Ulasir (2001) proposed the following relationship to define the velocity profile:

$0.189 \leq z/b < 1.690$:

$$\frac{U}{U_m} = \left[1 - \left(0.5797\left(1.141\frac{z}{b}\right)\text{-}0.1244\right)^{1.5}\right]^2 \qquad 4.31$$

Equation 4.31 is representative of the data between the limits prescribed above. An additional function is needed to define the form of the velocity profile from r/b = 0.189 to the boundary. Equation 4.32 represents the form of the velocity profile in this region and was obtained by fitting a power function through cross-section velocity data from Poreh et al. (1967).

$$\frac{U}{U_m} = 1.083 - \frac{0.03085}{\left(1.141\frac{z}{b}\right)^{0.651}} \qquad 4.32$$

where U is the local velocity. Note the factor of 1.141 has been introduced to provide consistency between the spread definitions for the theoretical and measured profiles. Figure 4.3 compares Equations 4.31 and 4.32 with measured radial velocity data obtained from PTV experiments (Crowe) and Poreh et al. (1967). These equations provide a reasonable representation of the data and given their self-similarity form, they have been employed to determine the mapping coefficients for the boundary jet region. Law and Herlina (2002) proposed an alternative form of Equation 4.31 to represent the velocity profile within the boundary region which incorporated a log function. This form was investigated and found to be incompatible with Crowe's PTV data.

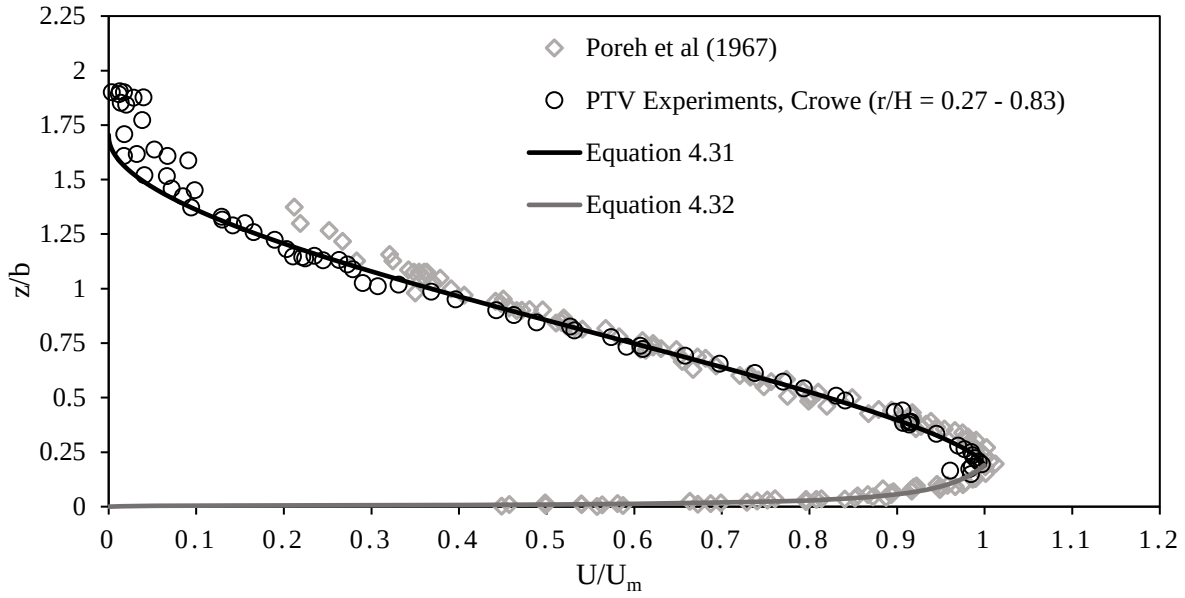

Figure 4.3: Collapsed velocity profiles from PTV experiments (Crowe), $H/d = 90.91$, $Re_0 = 3205$ and Poreh et al. (1967). Equations 4.31 and 4.32 are plotted alongside.

Determination of top-hat conversion factors requires equating mass, momentum and tracer (buoyancy) fluxes (per unit density) to the corresponding top-hat form (Oliver, 2012). For each equation, the flux at an arbitrary radial distance (R_A) from the impact point is given below.

$$\text{Volume Flux} = 2\pi R_A U_T b_T = 2\pi R_A \int_0^\infty U\, dz = I_{WQ} 2\pi R_A U_m b \qquad 4.33$$

$$\text{Momentum Flux} = 2\pi R_A {U_T}^2 b_T = 2\pi R_A \int_0^\infty U^2\, dz = I_{WM} 2\pi R_A {U_m}^2 b \qquad 4.34$$

$$\text{Tracer Flux} = 2\pi R_A C_T U_T b_T = 2\pi R_A \int_0^\infty U\, C\, dz = I_{WQC} 2\pi R_A U_m C_m b \qquad 4.35$$

Reynolds decomposition allows the velocity and concentration to be separated into their mean and fluctuating components: $U = \overline{U} + U'$ and $C = \overline{C} + C'$. The average of individual fluctuating components is zero, however averaging the product of two fluctuating components is not zero and represents the turbulent contribution of momentum or tracer flux.

Consequently we can write:

$$I_{WQ} = \int_0^{\infty} \frac{U}{U_m} \frac{dz}{b} \quad 4.36$$

$$I_{WM} = \int_0^{\infty} \left[\left(\frac{U}{U_m} \right)^2 + \overline{\left(\frac{U'}{U_m} \right)^2} \right] \frac{dz}{b} \quad 4.37$$

$$I_{WQC} = \int_0^{\infty} \left[\left(\frac{U\,C}{U_m C_m} \right)^2 + \overline{\left(\frac{U'C'}{U_m C_m} \right)^2} \right] \frac{dz}{b} \quad 4.38$$

The turbulent contributions to the momentum and tracer flux were taken as 14% (Knowles and Myszko, 1998) and 11% (Law and Herlina, 2002) of the corresponding mean flux. Law and Herlina (2002) studied 3-D wall jets (as opposed to radial wall jets) and hence the extent to which these results are applicable to the current discharge configuration is not clear. However it is the most relevant data available to quantify this value. By substituting the relevant velocity and concentration distributions, the following coefficients can be derived.

$$I_{WQ} = 0.845 \quad 4.39$$

$$I_{WM} = 0.629 \quad 4.40$$

$$I_{WQC} = 0.673 \quad 4.41$$

Rearranging Equations 4.33 - 4.35 and incorporating the results from Equations 4.39 - 4.41, the following conversion relationships are obtained.

$$b = 1.004 b_T, \qquad U_m = 1.178 U_T, \qquad C_m = 1.132 C_T, \quad 4.42$$

4.2.2 Experimental Observations and Results

4.2.2.1 Flow Observations

As noted above, the impact region represents a complex portion of the flow field where the flow transitions from the vertical free flow region to the horizontal wall jet region. A primary feature of the impact region is an elevated pressure field that includes a stagnation region

near the boundary, where fluid remains for extended periods as part of the re-direction process. Images of the impact region are shown in Figure 4.4, where instantaneous raw intensity, time-averaged concentration, root-mean squared (RMS) and intermittency images of the impact region are presented. The intermittency data presented here is based on a threshold concentration value of 2.4% of the initial concentration (C_0). Selecting different threshold values has a quantitative influence on the images and profiles presented, but the information presented remains qualitatively the same. The RMS intensity field reveals some asymmetry on either side of the radial boundary flow. This was attributed to minor inaccuracies in the experimental setup as well as shorter recording durations for vertical jet experiments due to tank confinement.

Large-scale eddies within the vicinity of the exit from the impact region are evident in Figure 4.4a, where an instantaneous image of the flow is presented. These vortices are a similar vertical scale to the radial boundary flow and were observed to have moved through the impact region, hence their origin could be traced back to the vertical free flow region (Didden and Ho, 1985; MacLatchy, 1993). As the distance from the impact region increases these structures have a tendency to merge and become less distinct as mixing takes place. The ability of uncontaminated ambient water to reach the boundary reduces as the flow develops along the boundary. Ulasir (2001) observed similar changes to the flow structure when discussing impact and radial flow regions for negatively buoyant discharges. In Ulasir's experiments these larger scale structures persisted up to radial distances between H – 3H. However, the turbulent structures within these flows were influenced by stable density gradients and hence comparisons with the present study are problematic. For a given level of boundary friction, it is conceivable that this distance would increase for non-buoyant boundary flows. The collapse of these turbulent structures was not observed in the present study as physical limitations of the current experimental setup limited flow observations to radial distances of up to H.

There is an expectation of reduced mixing in the impact region because this mixing occurs across a pressure gradient that is induced by the presence of the boundary. There is some evidence of this in Figure 4.4c and d. where there is clearly a reduction in the intensity of the turbulent fluctuations and intermittency in the region of higher flow curvature. It is also evident that the concentration fluctuations intensify as the boundary induced pressure

gradient reduces and the flow leaves the impact region. Mixing is clearly evident within the impact region and although it is inhibited by the presence of the boundary, it is important to determine the extent of the mixing that takes place during the re-direction process.

Time-averaged concentration profiles from the impact region are shown in Figure 4.5a. These profiles were extracted along lines radiating from a reference point that was representative of the centre of curvature for the flow in this region (depicted in Figure 4.6). For each test, this point was located at a horizontal and vertical distance of 0.30H and 0.86H respectively from the impact point. These coordinates represent the horizontal and vertical extent of the impact region determined in Sections 4.2.2.2 and 4.2.2.3 . Each profile has been labelled according to where it intersects the centreline (z/H) or boundary (r/H). The profiles have been scaled based on the maximum concentration (C_m) and the flow spread (b_c, the radius at $e^{-1}C_m$) and they are compared with a standard Gaussian function. Mean concentration profiles extracted in this way clearly have a self-similar Gaussian form hence C_m and b_c can be adequately characterised. However, it is important to note that because of the complexities of the velocity and pressure fields in this region the application of integral modelling techniques is problematic. Some reduction in the variation of the concentration beyond that expected of a Gaussian profile is evident near the peak of these profiles as they cut through the stagnation region. For example, the profile corresponding to $z/H = 0.98$ essentially remains constant through to a distance of $0.13b_c$ from the flow centreline.

Profiles of concentration fluctuation intensity (RMS) and intermittency have also been extracted from the impact region at the same locations as the mean concentration profiles and these are shown in Figure 4.5b and c. The intermittency and RMS profiles do not maintain a self-similar structure and their form clearly evolves as the flow passes through the impact region. The influence of the stagnation zone within the impact region is evident in these profiles, where the strength of the fluctuations and the intermittency of the flow close to the centreline are significantly reduced. Relatively high fluctuation intensities and intermittencies are observed towards the outer edge of the flow. As the profiles approach the exit from the impact region the strength of the concentration fluctuations and the associated intermittency increases and the higher fluctuation strength zone migrates towards the flow boundary. The additional complexity of the flow behaviour within the impact region is evident in the images and profiles presented here. However, it is important to quantify the global influence of the

impact region on key parameters such as volume flux, so the relatively simple flow that exits in this region can be modelled effectively. Before the influence of this region can be quantified, it is necessary to define its scale through systematic definitions of the location of the entrance to and exit from the impact region.

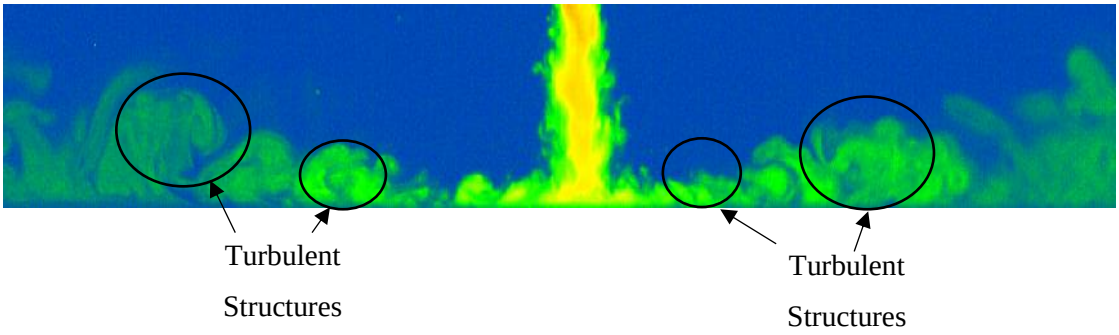

a) Instantaneous raw intensity field.

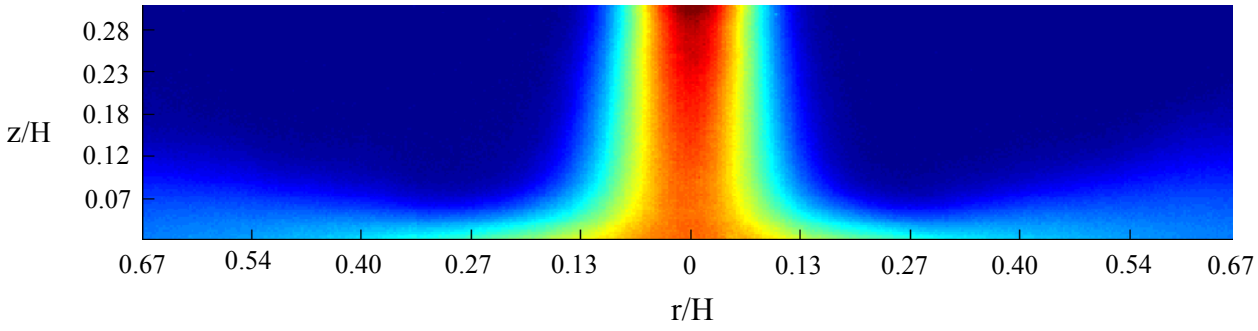

b) Time-averaged concentration field.

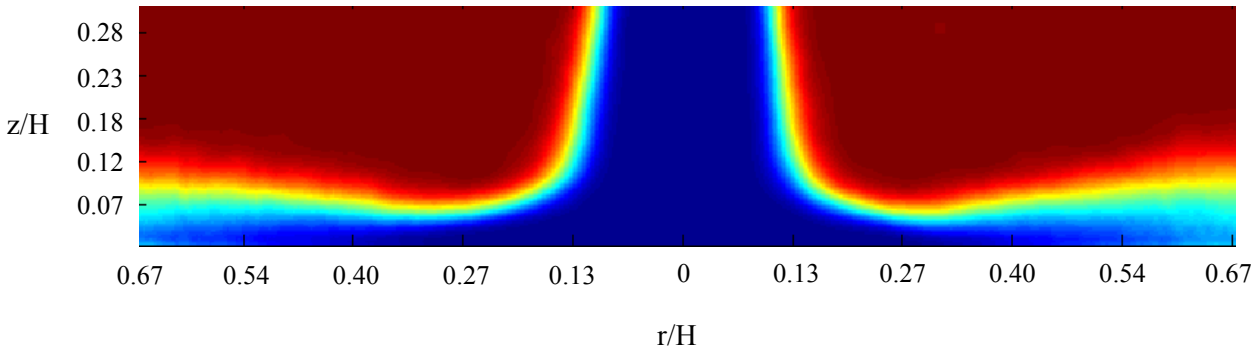

c) Intermittency field. Intermittency is defined such that a value of 0 (blue) indicates that the tracer concentration was consistently above the specified threshold value and a value of 1 (red) indicates that the threshold was never exceeded.

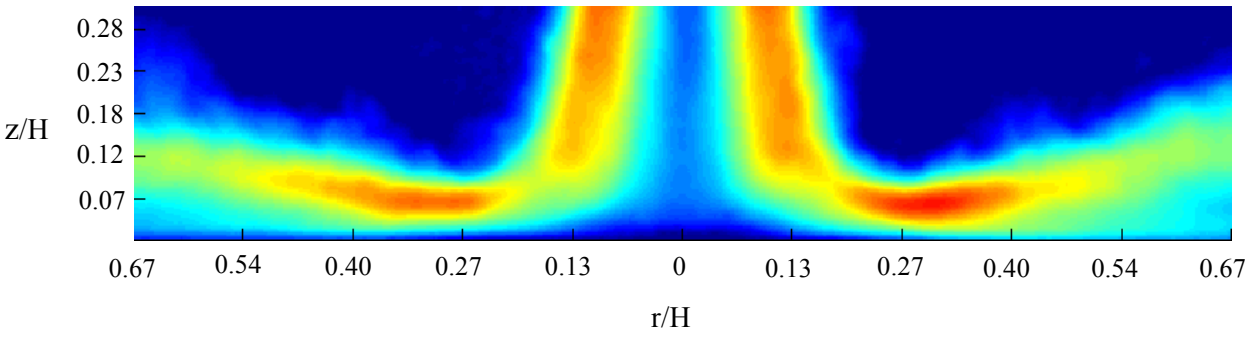

d) Concentration RMS field.

Figure 4.4: Flow field images within impact region, H/d = 67.69, Re_0 = 6008.

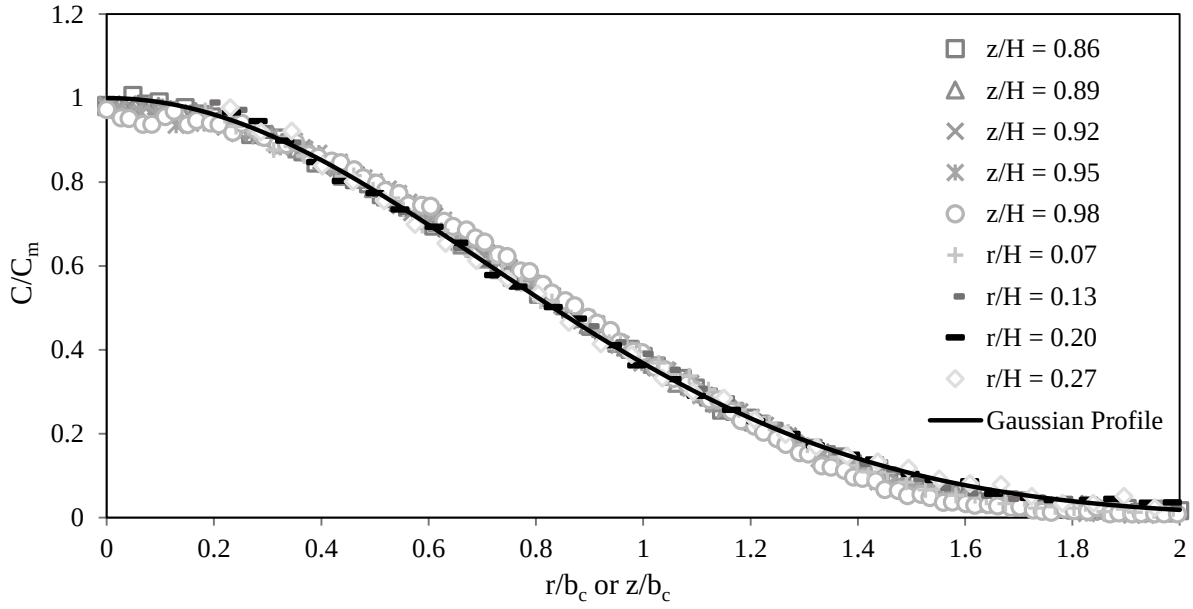

a) Time-averaged concentration profiles.

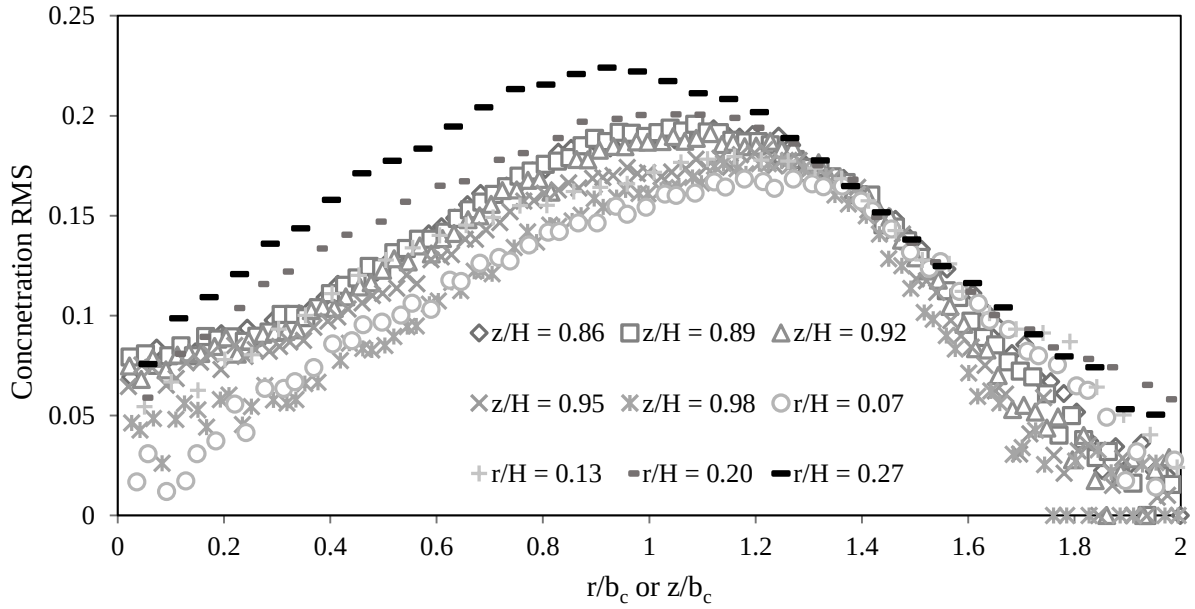

b) Concentration RMS profiles.

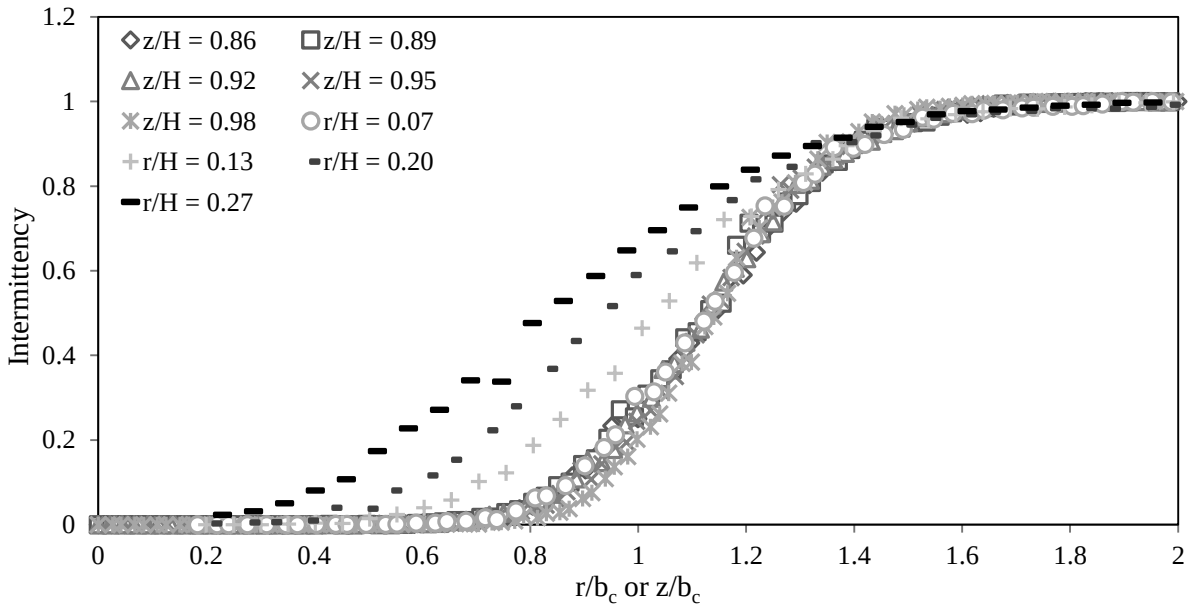

c) Intermittency profiles.

Figure 4.5: Cross-section profiles within impact region, $H/d = 67.69$, $Re_0 = 6008$.

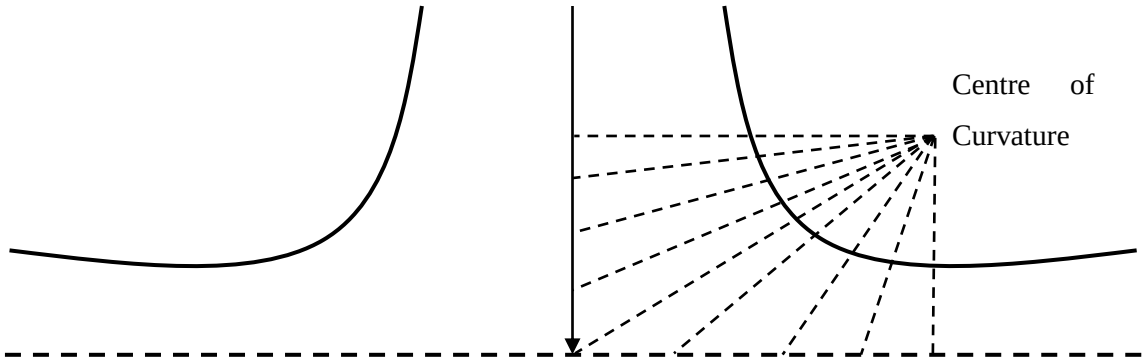

Figure 4.6: Cross-sections taken within the impact region taken from a selected 'centre of curvature'.

4.2.2.2 The Free Flow Region and Entrance to the Impact Region

There are clearly multiple ways to define the location of the entrance to the impact region and following on from that, the values of key parameters at this entrance. Here the location of the entrance is defined based on the failure of the integral model in the free flow region. Comparisons of integral model predictions with concentration field data provide the criteria for identification of the failure location.

Centreline dilution data from LIF experiments are presented in Figure 4.7. It is evident that the rate of centreline dilution declines as the flow approaches the boundary because the mixing processes are inhibited in the impact region (as previously discussed). Model predictions (Equation 4.5) are included in Figure 4.7 and diverge from the experimental data at $z/H = 0.94$. In this instance, Equation 4.5 is presented in terms of centreline dilution using the top-hat concentration conversion factor in Equation 4.29. The scaling laws stipulated in Equation 4.5 appear to be valid as results from each source height collapse onto a single curve, thereby indicating flow dependence on this parameter. It is not possible to directly compare this observation with past studies because centreline dilutions near the boundary have not been previously reported for jet type flows. Birch et al. (2005) presented centreline concentration values leading up to the boundary, however the extent of their data did not

encompass the region where the dilution rate reduces because their data was limited to distances of $z/H = 0.89$ from the source. They estimated that the centreline dilution reduces somewhere between $z/H = 0.86$ - 0.92, although it is clear from their data that the dilution continues to increase at $z/H = 0.89$. Alternatively centreline velocities have been employed to determine the location where boundary influences affect the flow behaviour. On this basis Cooper et al. (1993) and Beltaos and Rajaratnam (1974) report locations of $z/H = 0.88$ and 0.8 respectively.

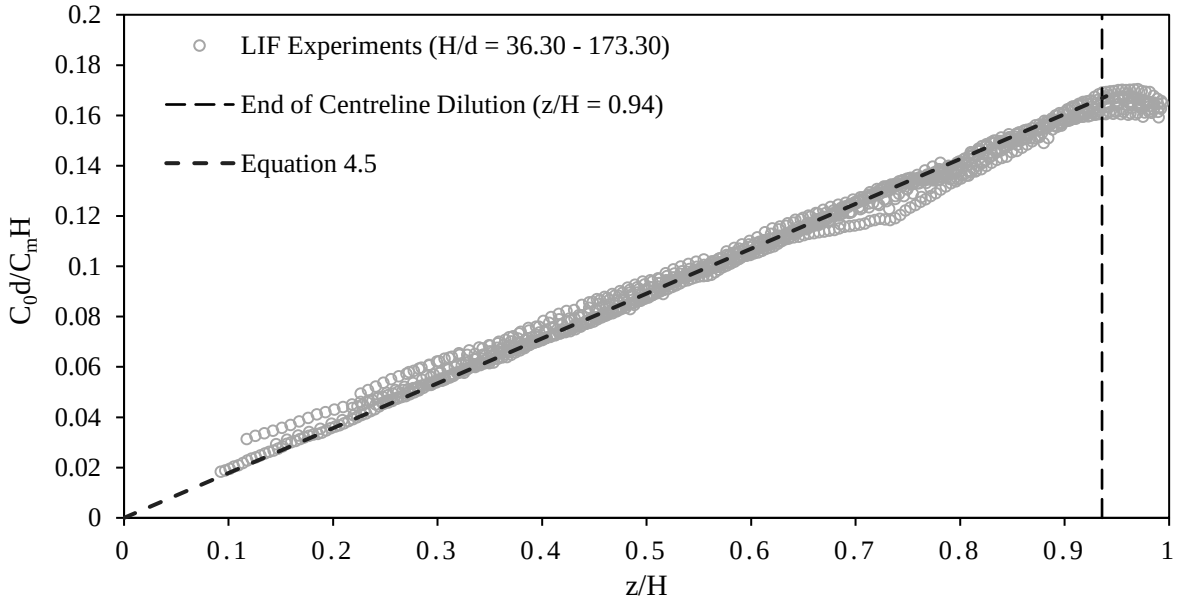

Figure 4.7: Centreline dilutions along the flow path within the free flow region and entry to the impact region, Multiple tests $H/d = 36.30 – 173.30$. Predictions from Equation 4.5 are included as well.

In the context of flow spread, departure of the measured data from the integral model predictions occurs further from the boundary at $z/H = 0.86$ where comparisons have been made to the 37% contour in Figure 4.8 (i.e. b_c). This plot includes results based on different definitions of spread. For example the 10% spread contour relates to the distance from the centreline corresponding to $0.1C_m$ along a perpendicular cross-section. Figure 4.8 also demonstrates that the influence of the boundary progresses from the extremities of the flow cross-section towards the centreline as the flow approaches the boundary. Spread data based on a 10% contour deviates from a linear path at $z/H = 0.81$, whereas the deviation from the linear spread of the 80% contour occurs at $z/H = 0.90$. The progression of the boundary

influence towards the flow centreline explains the difference between the locations of integral model failure based on spread (b_c) and centreline dilution or velocity data. A flow spread criteria was also employed by Guillard et al. (1998) to establish where boundary influences are first evident. A 10% flow spread contour was used and deviation from a linear growth rate was observed slightly before the present study at approximately $z/H = 0.77$. This difference is within 5% of the present study.

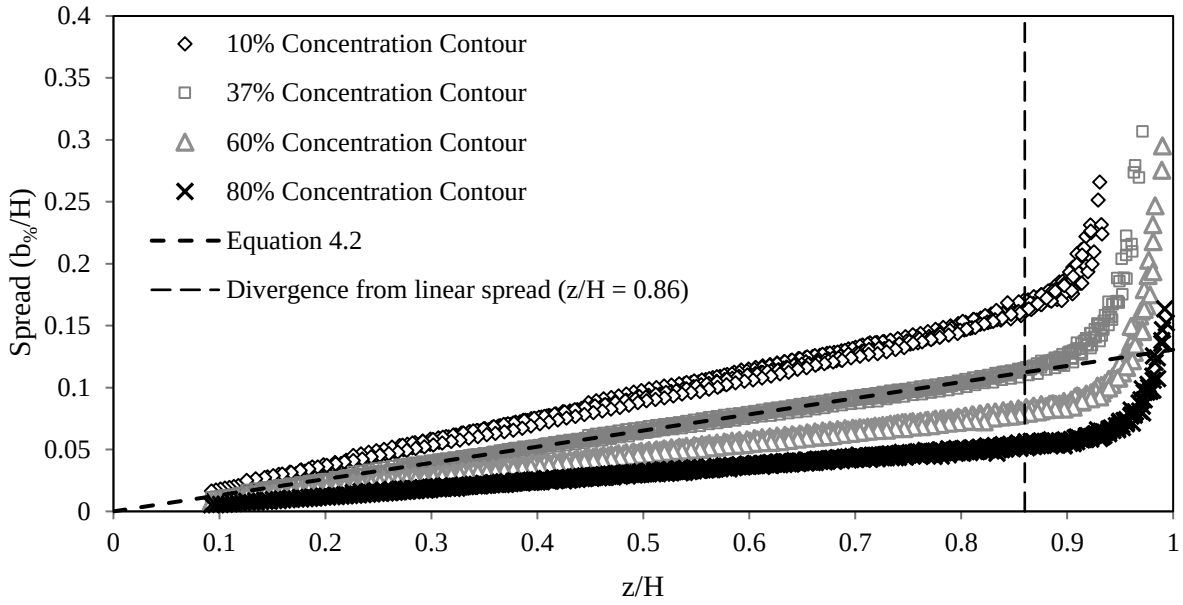

Figure 4.8: Flow spread along the flow path from LIF experiments within the free flow region and entry to the impact region based on different spread definitions. Multiple tests $H/d = 36.30 – 173.30$. Predictions from Equation 4.2 are included as well.

Additional insight into this progressive change of behaviour is evident in Figure 4.9, where a series of concentration profiles are presented in the vicinity of the entrance to the impact region. Each axis is scaled using the centreline concentration (C_m) and the spread value (b_c). This data highlights a loss of self-similarity as the flow approaches the boundary for profiles taken perpendicular to the centreline. These profiles indicate that the deviations in the spread near the outer edges of the flow do not become obvious until after $z/H = 0.91$ and hence self-similarity is maintained for the bulk of the profiles through to this distance. The changing form of the profiles and non-linear spreading rates are expected as the flow decelerates towards the stagnation region and the process of diverting mass radially begins. The loss of velocity profile self-similarity near the boundary has been investigated by Rajaratnam et al.

(2010) and Beltaos and Rajaratnam (1974). They found that self-similarity of these profiles was lost at approximately z/H = 0.93 and z/H = 0.95 respectively. Discrepancies in the determination of the location of the loss of self-similarity could in part be due to differences in the spread parameter selected to scale the radial distance as well as lower spatial resolution with which to determine this location.

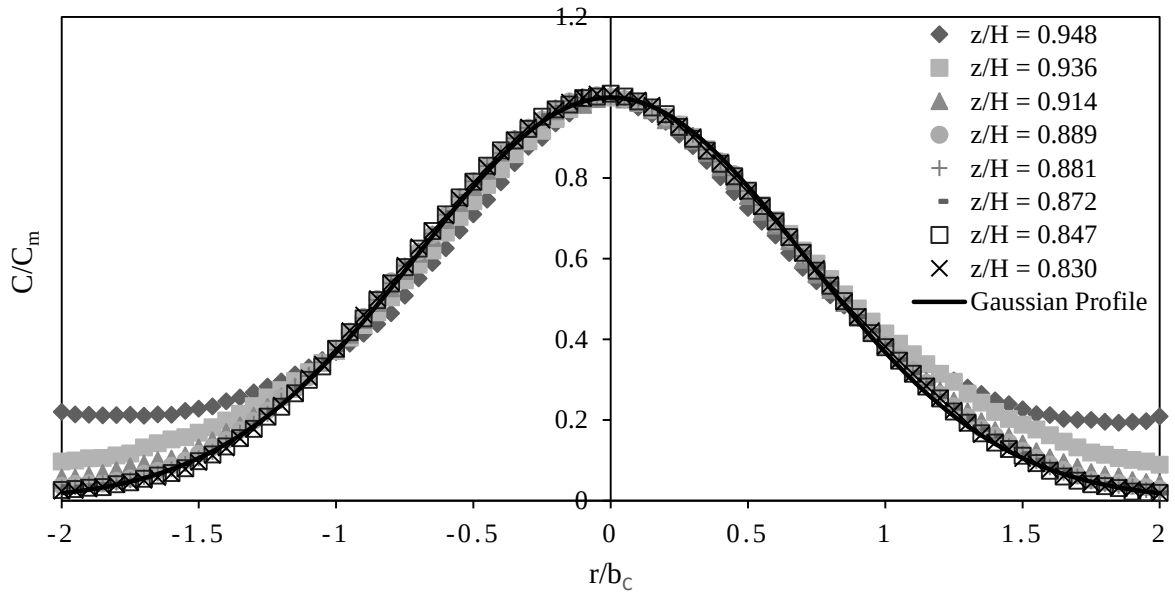

Figure 4.9: Collapsed concentration profiles near the boundary from LIF experiments, H/d = 87.03, Re_0 = 5579.

It is also expected that the strength of turbulent fluctuations (RMS measurements) will decline as the flow enters the impact region as noted with reference to Figure 4.5b. Figure 4.10 shows the normalised strength of the turbulent fluctuations along the jet centreline. For each experiment, RMS values have been scaled by the corresponding maximum RMS value recorded along the centreline. The reduction in the strength of these fluctuations as the flow enters the impact region is clearly evident and is consistent for the range of initial conditions considered in this study. The location when the reduction begins is essentially the same as that for the centreline dilution (z/H = 0.94), which again indicates that this is where the progressive changes in the flow structure associated with the presence of the boundary reach the centreline of the flow. Cooper et al. (1993) plotted velocity fluctuations along the centreline and RMS values were observed to reduce at a similar location to the present study (z/H = 0.95). Rajaratnam et al. (2010) conducted a similar analysis and observed a reduction

in the measured RMS values at approximately $z/H = 0.90$. Reynolds stress measurements have also been used to characterise the location where boundary influences are detected. Maurel and Solliec (2001) defined the location of incipient boundary influence based on the measured Reynolds shear stresses reducing to zero and this occurred when $z/H = 0.87$. The same definition was also employed by Koched et al. (2011) and they reported a range of values ($z/H = 0.87$ - 0.90). Their data suggested the location moved further upstream for higher discharge Reynolds numbers, but it was difficult to assess the extent of this dependence based on four experiments.

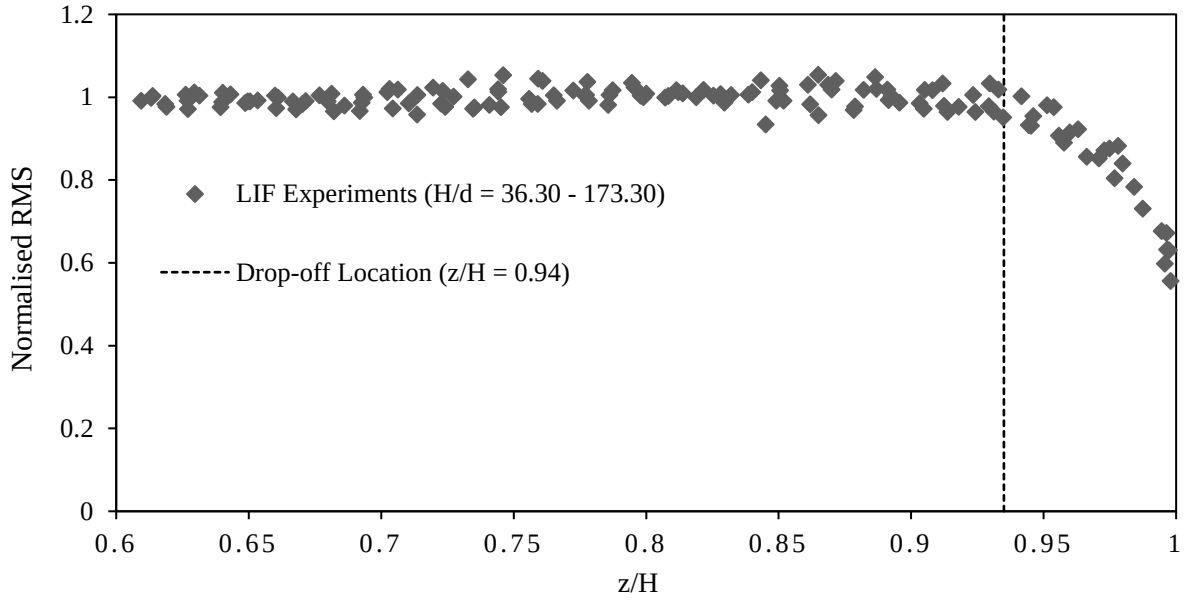

Figure 4.10: Normalised concentration centreline RMS values from LIF experiments, Multiple tests H/d = 36.30 – 173.30.

Data from the present study suggests that it is possible to define the location of the entrance to the impact region from $z/H = 0.81$ - 0.94 and these values are generally consistent with previous observations. However, if the location of the entrance is specifically defined based on the failure of the free flow integral model, then the data indicates that the entrance to the impact region is located at $z/H = 0.86$ and hence $k_{H1} = 0.86$. This is the location where the linear spread (based on the 37% concentration contour) is no longer valid. Making use of this definition enables the conditions at entrance to the impact region (Q_H, U_{TH} and b_{TH}) to be defined based on the free flow integral model solution.

4.2.2.3 Exit from the Impact region and Radial Boundary Flow

As with the entrance to impact region, it is possible to define the exit from this region in multiple ways, but here again we will focus on the failure of the relevant integral model, that is, the radial wall jet model outlined in Section 4.2.1.2. This model relies on a linear spread assumption and departure from this assumption provides an obvious initial estimate of the location of the exit from the impact region. Top-hat spread along the boundary (and impact region) is presented in Figure 4.11 where the relevant conversion factors have been applied to concentration and velocity spread values. Although the conversion factors do not apply to the impact region these data points have been included in order to determine where the flow begins to spread linearly along the boundary. From Figure 4.11 it is evident that the linear spread assumption does not become valid until $r/H = 0.30$. This is similar to the value of $r/H = 0.25$ suggested by Tani and Komatsu (1966) based on a relatively crude set of velocity measurements. Beyond this radial distance integral model predictions are consistent with the measured data. Note these predictions are based on a k_{TR} value of 0.135, which establishes a reasonable estimate of the spread at the exit from the impact region and a k_{TB} value of 0.158, which provides spread predictions that are consistent with the data. The corresponding concentration (k_{boc}) and velocity spreading rates (k_{bo}) of 0.190 and 0.158 respectively suggest a ratio of the concentration to the velocity spreading rates (λ_B) of approximately 1.20. This λ_B value is somewhat lower than suggested in previous studies (1.25 from Fairweather and Hargrave, 2002b and 1.36 from Birch et al., 2005), however, the value is consistent with the spreading rate ratio in the free flow region. It is also worth noting that fitting trend lines through the data sets suggests a value of 1.34 for λ_B, but this value reduces to 1.20 if data near the exit from the impact region is neglected $0.30 < r/H < 0.38$. This zone is associated with the smaller scale profiles that are more difficult to resolve, particularly with the relatively sparse velocity field measurements. Alternatively the variation in relative spreading rates suggests that some level of flow establishment continues within this zone, which will have some influence on the quality of the integral model predictions near the exit from the impact region. It is also worth noting that the velocity spreading rates measured in PTV experiments are larger than those measured for air jets impacting on a horizontal boundary. Birch et al. (2005), Fairweather and Hargrave (2002a) and Poreh et al. (1967) reported spreading rates of 0.11, 0.09 and 0.08 respectively. Model

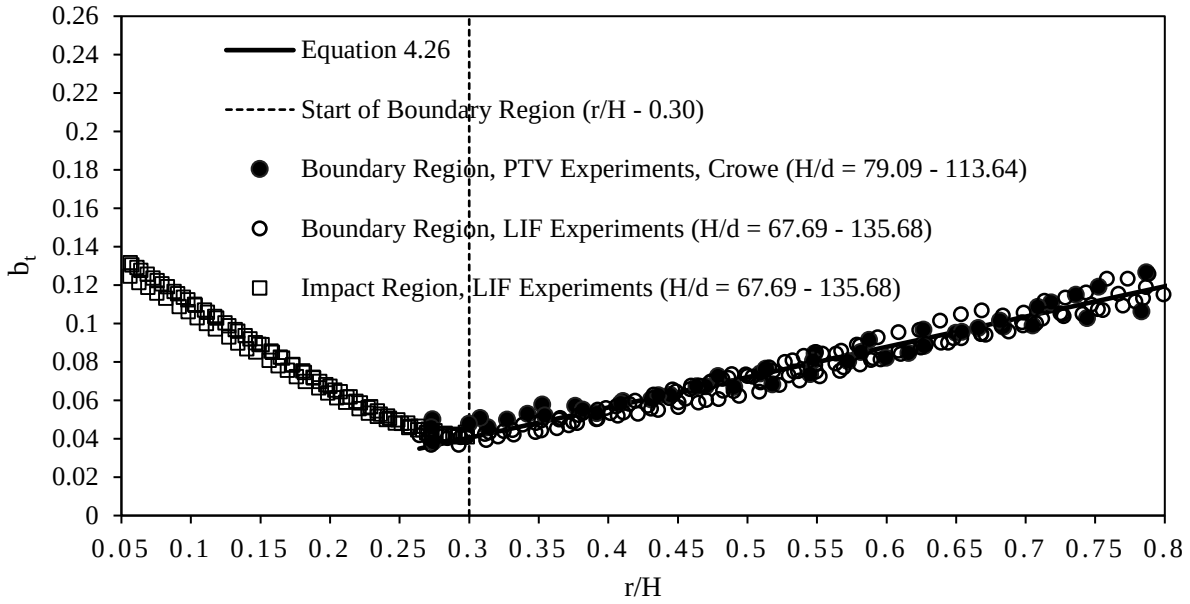

Figure 4.11: Top-hat spread measurements obtained from concentration (LIF experiments) and velocity data (PTV experiments, Crowe) within the boundary and impact region. Predictions from Equation 4.26 are included as well.

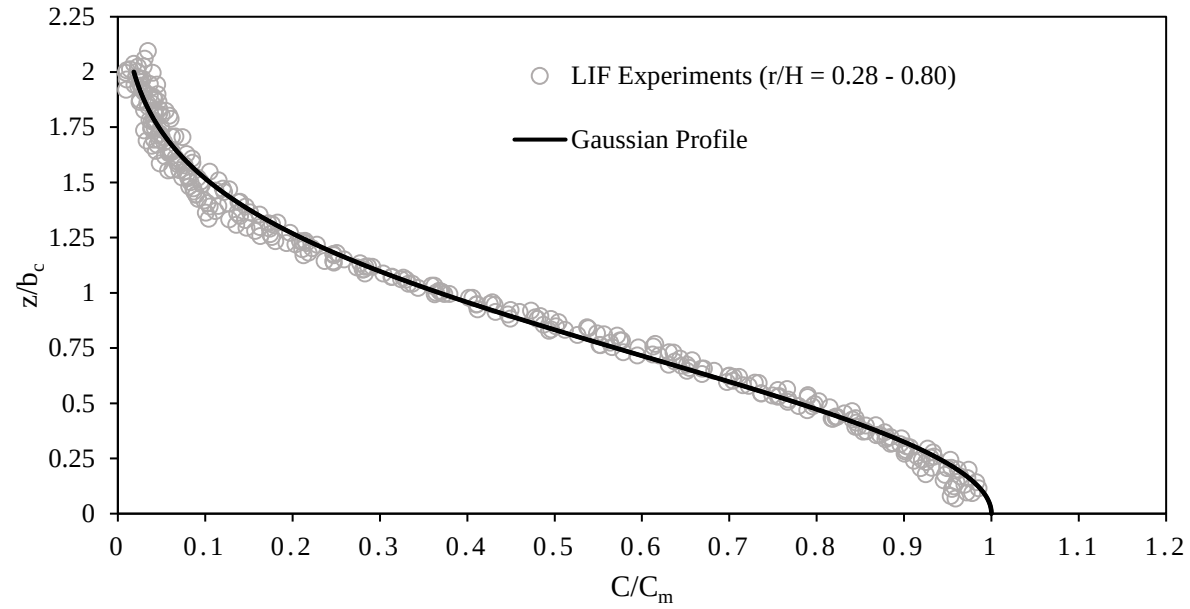

Figure 4.12: Collapsed concentration profiles (LIF experiments) within the boundary region, H/d = 67.69, Re_0 = 6008.

validity is also dependent on the self-similarity of concentration profiles within the radial boundary region and this is clearly the case in Figure 4.12. Velocity profiles taken within this region from PTV experiments were previously shown to exhibit a self-similar form in Figure 4.3.

Velocity profiles can be integrated to estimate the growth in volume flux (Q) of the boundary flows (given in Equation 4.43), where r represents the horizontal distance between the point along the boundary considered and the point of impact.

$$Q = 2\pi r \int^{\infty} u \, dz \qquad 4.43$$

Comparisons with the model (Equation 4.28) are also provided in Figure 4.13. Assuming boundary friction effects are negligible along the length of the recording area ($k_f = 0$), the volume flux data at this location suggests a k_Q value of 1.22. This value combined with the coefficients defined above provides a value of 0.97 for k_M (Equation 4.25). The k_Q value also defines the gradient for the growth of volume flux between the end of the free flow region and the start of the boundary region. The value determined for k_M implies that little momentum is lost as the flow moves through the impact region and transitions to a radial boundary flow. Assumptions pertaining to friction effects along the physical boundary appear to be valid as the model equation matches the data reasonably well. Equation 4.27 can also be compared to the boundary or minimum dilution using the concentration top-hat conversion factor (Equation 4.42). There is some doubt surrounding this conversion factor and hence the applicability of the model comparison. The primary concern surrounds the turbulent contribution to tracer flux which was determined from experiments on plane wall jets as opposed to radial wall jets. The minimum dilution along the boundary region is given in Figure 4.14 alongside Equation 4.28. Initial comparisons showed inconsistencies between the two data sets suggesting that the conversion factor may not be correct. In order to match the experimental data a friction coefficient of $k_f = 0.09$ was introduced to Equation 4.28, while the remaining coefficients were kept the same. It is possible that friction effects may have influenced concentration recordings due to the adjustments made to the solid platform for the LIF system, after PTV experiments were carried out. A black coating was applied to the boundary to reduce reflections from the light sheet which may have altered the boundary

friction to some extent. The minimum dilution within the impact region ($r/H < 0.30$) has also been included in Figure 4.14. A slightly lower dilution rate is observed within the impact zone in comparison with the boundary region. This is expected given the suppression of mixing processes that takes place as the flow is re-directed towards a horizontal configuration.

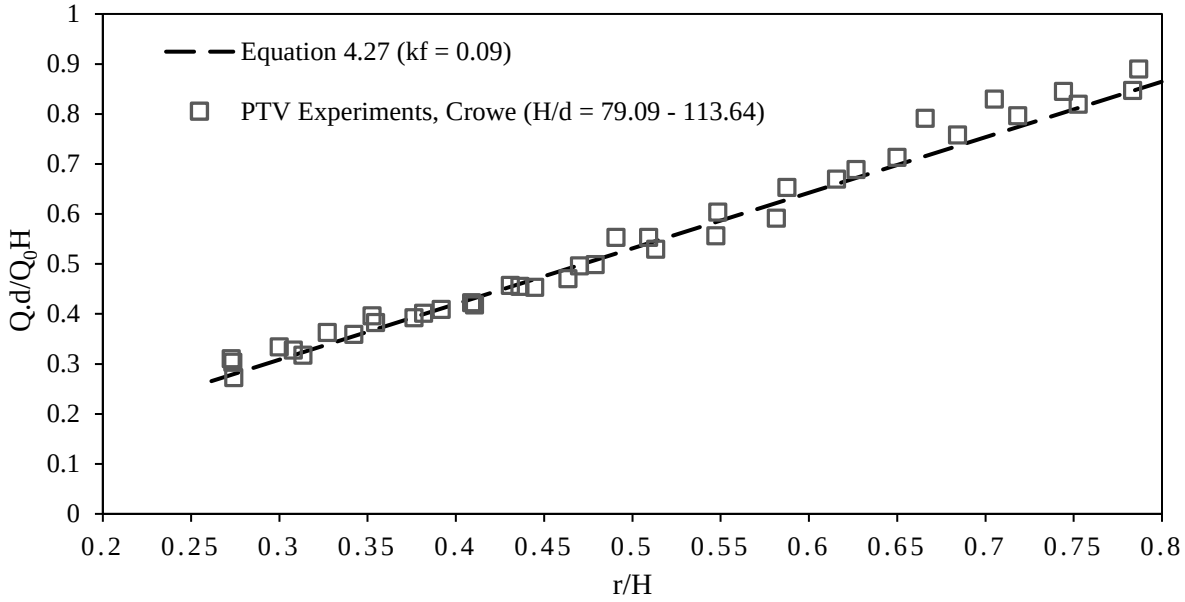

Figure 4.13: Volume flux measurements from PTV experiments (Crowe) and model predictions from Equation 4.27 within the boundary region.

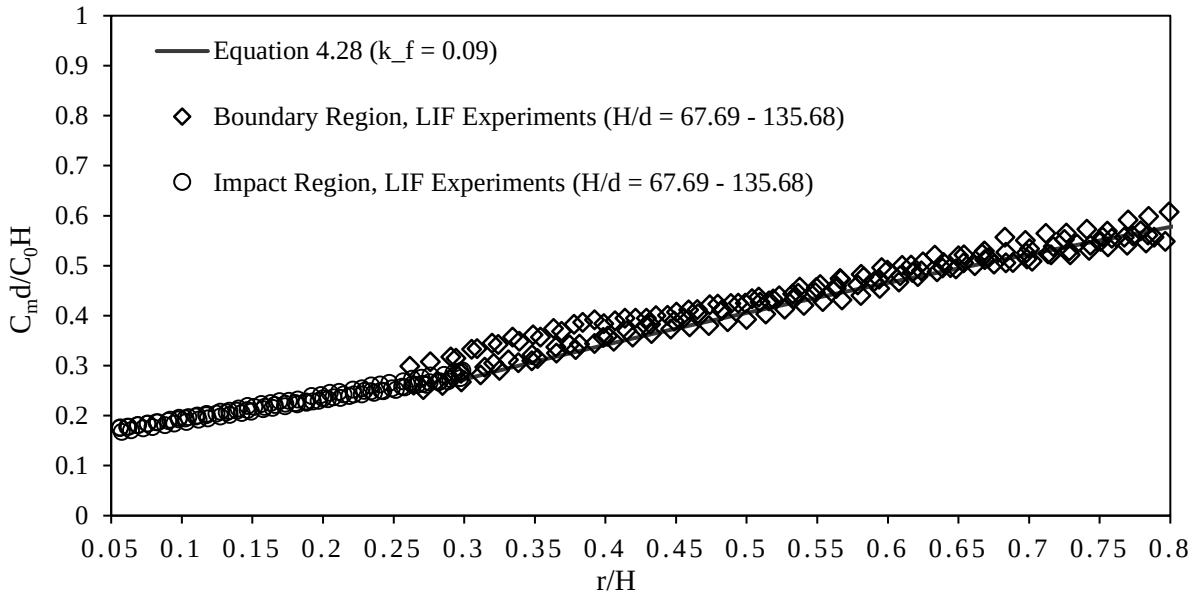

Figure 4.14: Minimum dilution measurements from LIF experiments within the impact and boundary regions. Predictions from Equation 4.28 are included with a friction coefficient of 0.09.

Comparisons with velocity measurements are also favourable as model predictions (Equation 4.27) are generally consistent with the experimental data. Maximum velocities were originally extracted along the boundary region and converted to average or top-hat values using the relevant conversion factor. Results from Ghaneeizad et al. (2015) have also been included in Figure 4.15 and a line of best fit has been used to represent their data. Their results lie slightly above the present study and the model prediction, however the growth rates between each data set are similar.

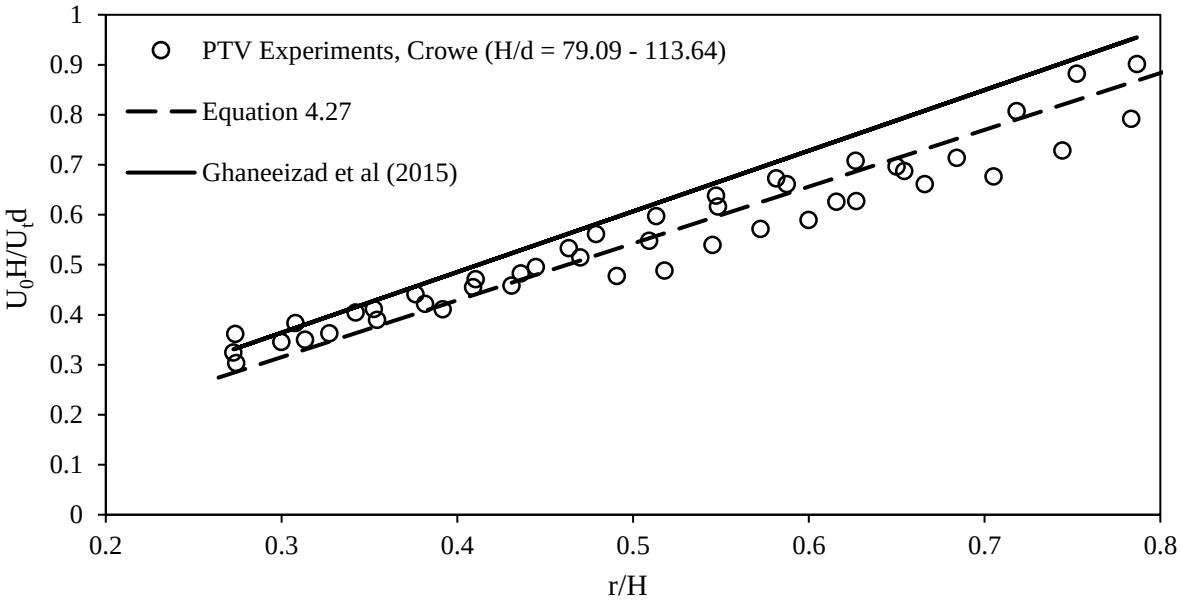

Figure 4.15: Top-hat velocity measurements from PTV experiments (Crowe) and model predictions from Equation 4.27 within the boundary region. Experimental results from Ghaneeizad et al. (2015) are also included.

In summary the scale and influence of the impact region is now defined by the values of the coefficients determined from concentration field data measured during this study along with previously measured velocity field data. In particular the volume flux increases by 22% ($k_Q = 1.22$) as the flow passes through this region, whereas the momentum flux remains essentially constant ($k_M = 0.97$). The entrance to the impact region is located at 14% of the source height (H) above the boundary ($k_{H1} = 0.86$), where the flow conditions are defined by a free flow integral solution. The radius at the exit from impact region is 30% of the source height ($k_{H2} = 0.30$) and the scale ('top-hat') of the flow at this location is 4% of the source height ($b_{TR}/H = 0.041$).

4.3 Vertical Buoyant Jets and Plumes

4.3.1 Analysis

The flows relevant to this section include both buoyant jets and plumes impacting the lower boundary. The scaling laws used to analyse the flow behaviour are applicable to plume flows, however using this framework, behavioural differences between the two flow types can be identified at the entrance and exit from the impact region. Within the free flow region, the centreline dilution rate for a pure plume is well established (Fischer et al., 1979; Wang and Law, 2002) and is given in Equation 4.44.

$$\frac{C_0}{C_m F_0} = k_P \left(\frac{z}{F_0 d}\right)^{5/3} \qquad 4.44$$

When a boundary is inserted, the non-dimensional source height ($H/F_0 d$) must be included in the analysis. The final centreline dilution recorded at the end of the free flow region (k_{PF}) can be expressed using Equation 4.45.

$$\frac{C_0}{C_m F_0} \left(\frac{F_0 d}{H}\right)^{5/3} = k_{PF} \qquad 4.45$$

This relationship can be extended to the minimum dilution at end of the impact region/start of the boundary region (k_{PI}), however the constant on the RHS of the equation will change.

$$\frac{C_0}{C_m F_0} \left(\frac{F_0 d}{H}\right)^{5/3} = k_{PI} \qquad 4.46$$

If k_{PF} and k_{PI} are converted into equivalent volume fluxes, the ratio of these terms is analogous to the k_Q coefficient determined for jet flows and describes the mixing that takes place within the impact region.

A key distinction between buoyant and non-buoyant flows is the behaviour within the boundary region. Unlike the wall jet, buoyant flows along the boundary temporarily entrain ambient fluid before visibly transitioning to the far field regime where mixing is negligible

due to the stabilising influence of buoyancy (Ulasir, 2001; Ulasir and Wright, 2003; Wright et al., 1991). As such, the boundary flow is considered as two separate segments; the near field region and the far field region (Figure 4.16). Flow statistics within the boundary region are not within the scope of this section however a qualitative description of the transition from the near field region to the far field is provided.

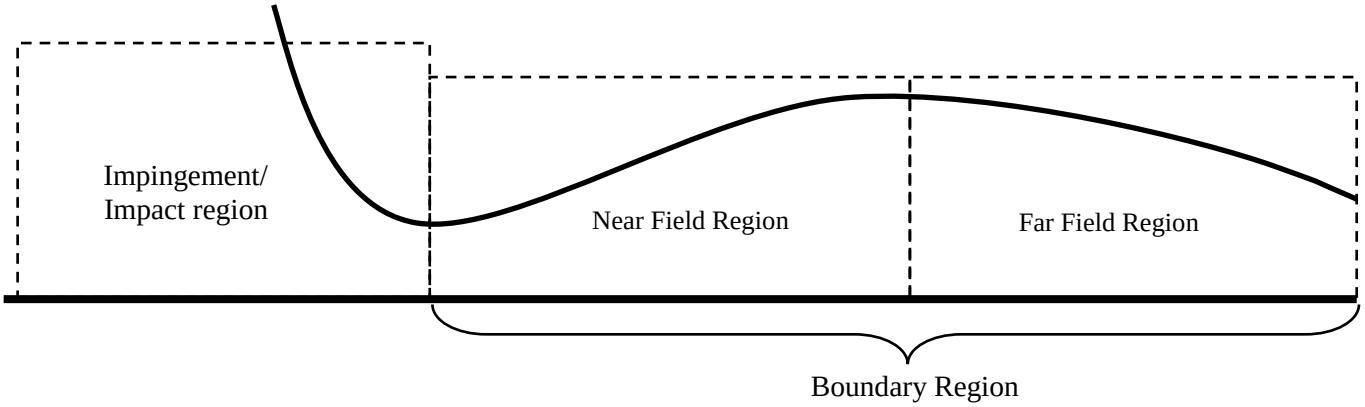

Figure 4.16: Configuration of the boundary region from a vertical plume impinging a horizontal boundary. The near field and far field regions of the flow are delineated.

4.3.2 Free Flow Region

Centreline dilutions within the free flow region are shown in Figure 4.17. Each variable has been scaled as per Equation 4.44 (unbounded solution) to illustrate the discontinuation of dilution along the centreline. Only four experiments have been included in Figure 4.17 for clarity purposes. The final centreline dilution from each experiment has been extracted and plotted against the non-dimensional boundary height in Figure 4.18 as per Equation 4.45. As shown, results from the two largest parameters tested are constant while the remaining tests exhibit a linear relationship with $H/F_0 d$. These results do not exactly concur with the flow regime definitions provided in Papanicolaou and List (1988). Discrepancies are expected given that only six experiments are included and that the influence of the boundary is likely to affect measurements prior to flow impingement. Average dilutions (top-hat) at the start and end of the near field region (along the boundary) were plotted against $H/F_0 d$ and were variable up till $H/F_0 d \sim 4.71$. More direct comparisons can be made with Christodoulou et al. (2015) who reported centreline dilutions within free flow and impact regions for a similar

flow configuration. Comparable flow behaviour was observed as the centreline dilution was shown to level off prior to impingement. The centreline dilution at 1 cm above the boundary was reported in this study and is included in Figure 4.18. Due to the proximity of this location to the boundary, it is assumed that this value is close to the final centreline dilution achieved by the flow (prior to impacting the boundary). The range of source heights tested is not large enough to provide more definitive conclusions with regards to the dilution behaviour in the free flow region. However, the dilutions reported in Christodoulou et al. (2015) are within the vicinity of the present study and appear to follow a similar trend.

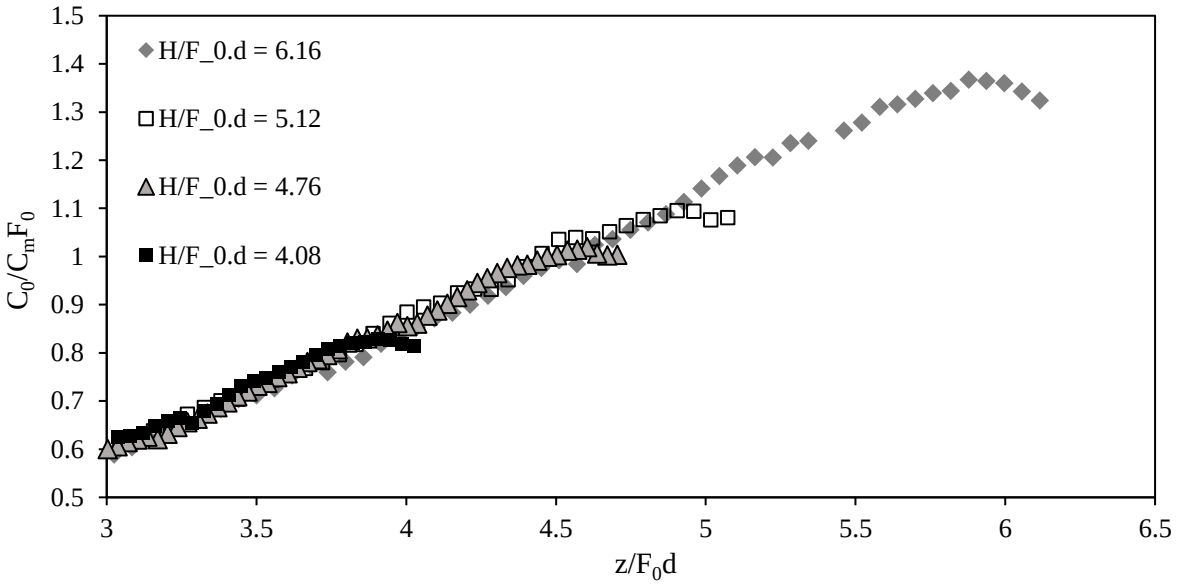

Figure 4.17: Centreline dilution along the flow path within the free flow region and entry to the impact region.

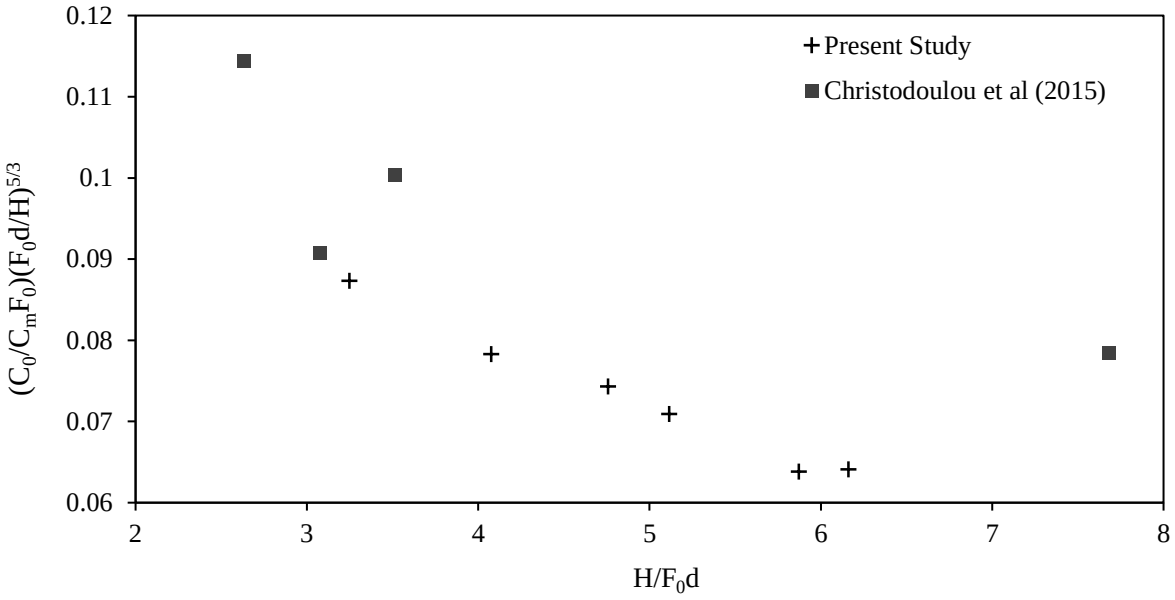

Figure 4.18: Centreline dilution at z/H = 0.93 plotted against source height.

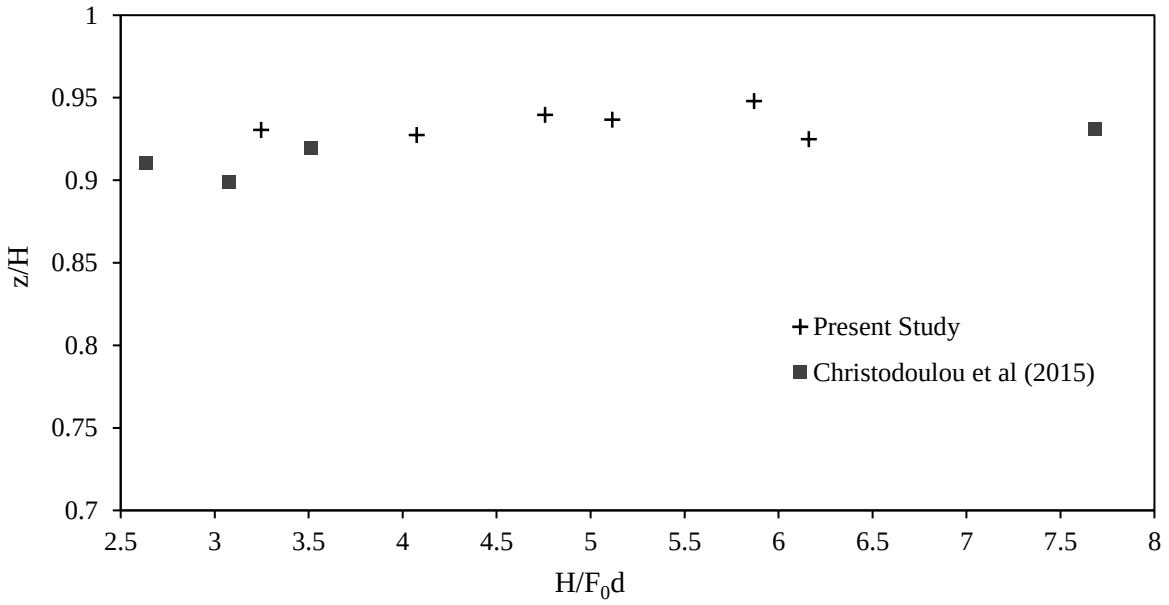

Figure 4.19: Location along the path length where dilution ceases within the free flow region.

The height above the boundary beyond which the centreline dilution ceases is plotted in Figure 4.19. Christodoulou et al. (2015) also recorded this height using the same definition and results from this study are also included. From Figure 4.19 the distance from the source where centreline dilution ceases appears to be consistent across all experiments, highlighting the boundary's role in governing the flow behaviour in this region. For the present study this location is at $z/H = 0.93$ while Christodoulou et al. (2015) suggests $z/H = 0.92$. These values are also similar to the corresponding jet case where the centreline dilution was observed to conclude at $z/H = 0.94$ for all source heights tested.

In accordance with the model framework for simple jet flows, the deviation of spread (b_c) from the linear function was the criteria used to determine the end of the free flow region. The flow spread measured for each buoyant jet and plume test is provided in Figure 4.20. Here, the traditional definition of spread is used (i.e. distance from centreline corresponding to $e^{-1}C_m$). Although the spreading rate for a plume is linear, plumes disperse at a slightly slower rate than jets ($b_{c,Jet}/b_{c,Plume} \sim 1.18$ from Wang and Law, 2002). As stated, most of the flows tested were buoyant jets and the relative extent of the jet region in comparison to the boundary height (H) was different for each test. Therefore discrepancies in spread measurements near the boundary are expected. However, the accelerated growth in spread as a result of the boundary appears to be consistent and is visually estimated to occur at $z/H = 0.88$, and is very similar to the jet case ($z/H = 0.86$). Within the context of a model framework, $z/H = 0.88$ would delineate the end of the free flow region based on the failure of simple integral models to predict the spread past this location (or $k_{H1} = 0.88$). Therefore the corresponding centreline dilutions at this location are of particular interest. These are provided in Figure 4.21 for each experiment. Given the consistency between each flow regime it is likely that boundary influence based on this criteria is independent of the source height conditions. This result also suggests that the flow classification criteria in Equation 4.1 should be adjusted to account for the change in flow region above the boundary (from free flow to impact region). Based on a transition distance of $z/H = 0.88$ and 0.86 (for buoyant flows and jets respectively) the inequality associated with transition regime should be changed to $1.09 < H/F_0d \leq 5.35$.

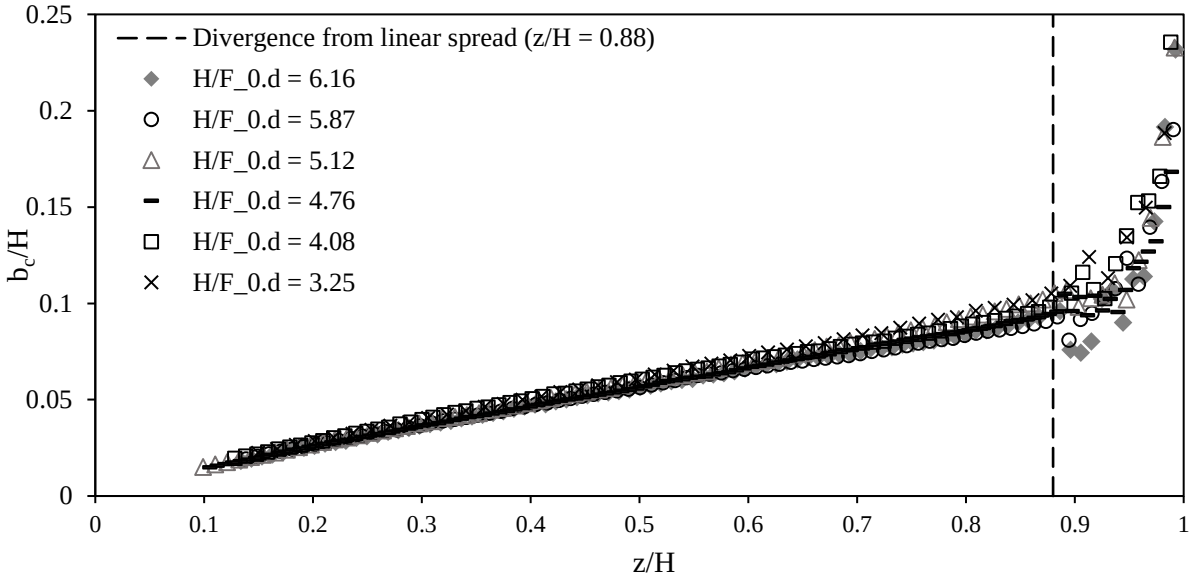

Figure 4.20: Concentration spread development along the flow path within the free flow region and entry to the impact region.

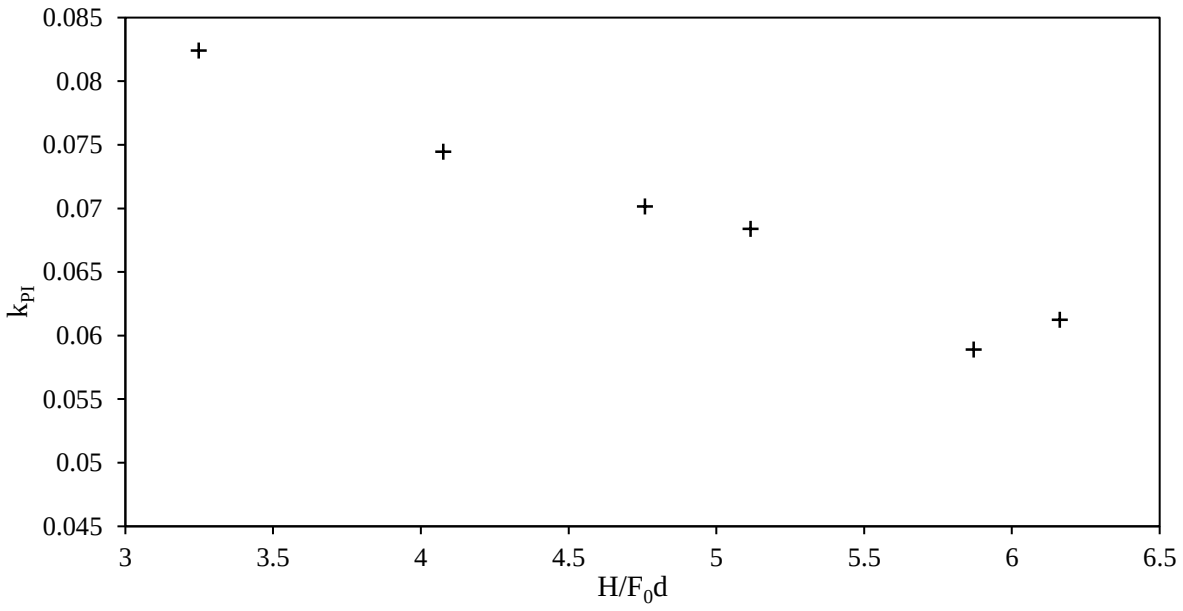

Figure 4.21: Centreline dilution at z/H = 0.88 (end of free flow region) plotted against source height.

4.3.3 Impingement/Impact Region

Spread and dilution results have been obtained from the impact region. Values were extracted by taking cross-sections of the flow originating from a reference point. The same approach was taken when analysing the impact region of the jet (refer to Figure 4.6). Concentration profiles within this region are given in Figure 4.22. Each axis has once again been scaled using C_m and b_c. Profiles intersecting the boundary have only been considered hence each plot is labelled in terms of r/H. Information near the boundary (5 ~ 3 mm) could not be used for this set of tests therefore a gap is present between $z/b_c = 0$ and the first data point in each profile. The spread development within this region has been considered in Figure 4.23 and results from each test are shown to collapse relatively consistently onto each other. In accordance with the framework established for radial jets, the end of the impact region/start of the boundary region is defined as the commencement of a linear spread rate along the boundary. The spread is plotted up to $r/H = 0.40$ using the conventional definition for spread. A linear growth rate becomes apparent at approximately $r/H = 0.28$, which is very close to the corresponding radial jet case ($r/H = 0.30$). Given that these locations are similar it is conceivable that the commencement of the boundary region (or k_{H2}) for all vertical flows is the same regardless of flow conditions at the source. The corresponding minimum dilution at this location is plotted for each experiment in Figure 4.24. As expected a decreasing trend is apparent as the boundary parameter increases. Unlike the free flow region, the dilution is not shown to explicitly level off however more tests are required to accurately gauge the behaviour of the flow at this location.

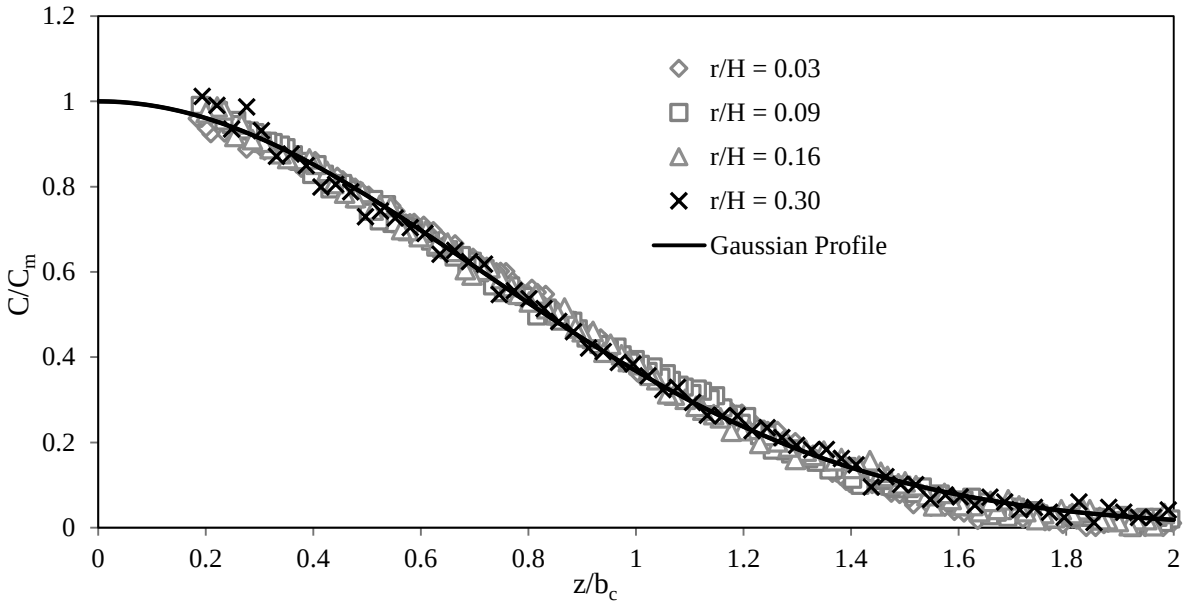

Figure 4.22: Concentration profiles within the impact region, $H/F_0d = 3.25$, $Re_0 = 3035$.

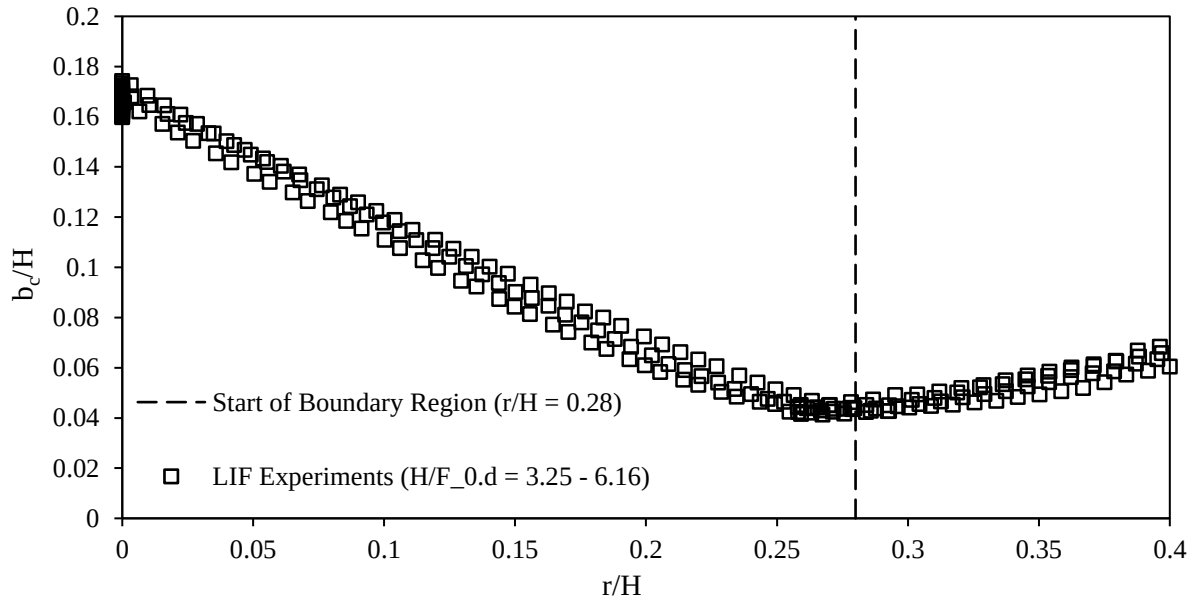

Figure 4.23: Spread development within the impact region and entrance to boundary region. Multiple tests, $H/F_0d = 3.25 – 6.16$.

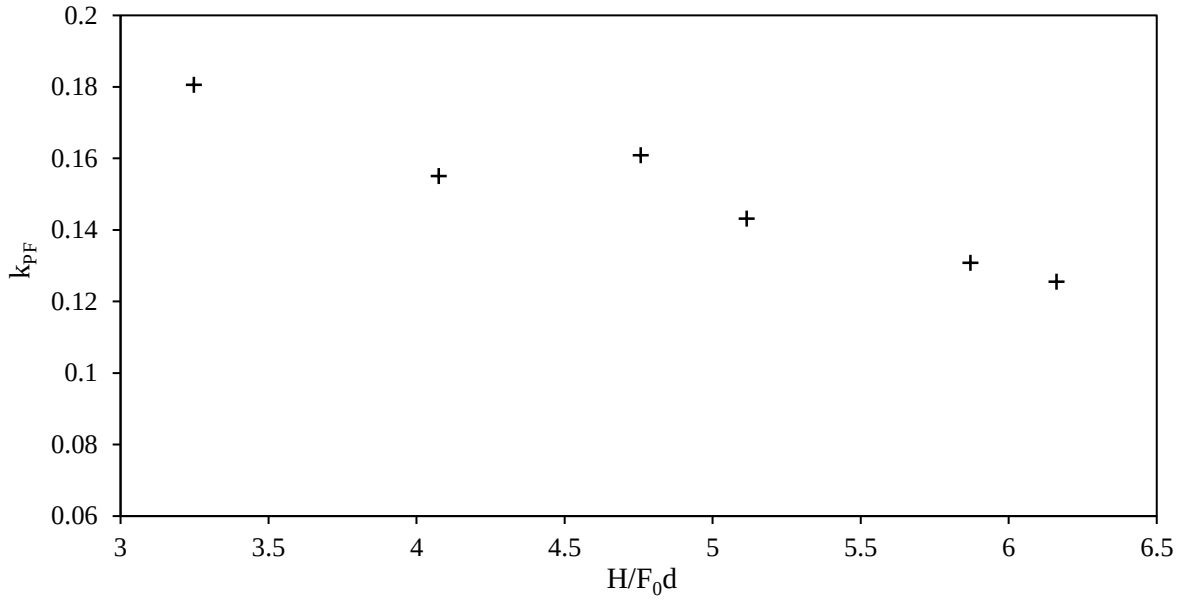

Figure 4.24: Minimum dilution recorded at r/H = 0.28 (end of impact region) plotted against source height.

Determining the coefficient k_Q was difficult for this flow configuration due to the lack of information regarding turbulent contributions to momentum and tracer flux along the boundary. Consequently, dilutions could not be converted into equivalent volume fluxes. However an indication of the level of mixing that takes place within the impact region could be ascertained by determining the ratio of the minimum dilution at r/H = 0.28 (exit from impact region) and at z/H = 0.88 (entrance to impact region). This ratio is referred to as k_D and is plotted for each experiment in Figure 4.25. As shown, this value exhibits no dependence with the non-dimensional source height and is approximately $k_D = 1.90$ based on the mean value over each experiment. This ratio was also calculated for jet experiments and yielded a similar value of $k_D = 1.83$. This is an important result as it indicates that the relative level of mixing that takes place within the impact region is the same irrespective of flow conditions at the source. In addition to Figure 4.19 and Figure 4.20 these results highlight the boundary's role in governing the flow behaviour within this region.

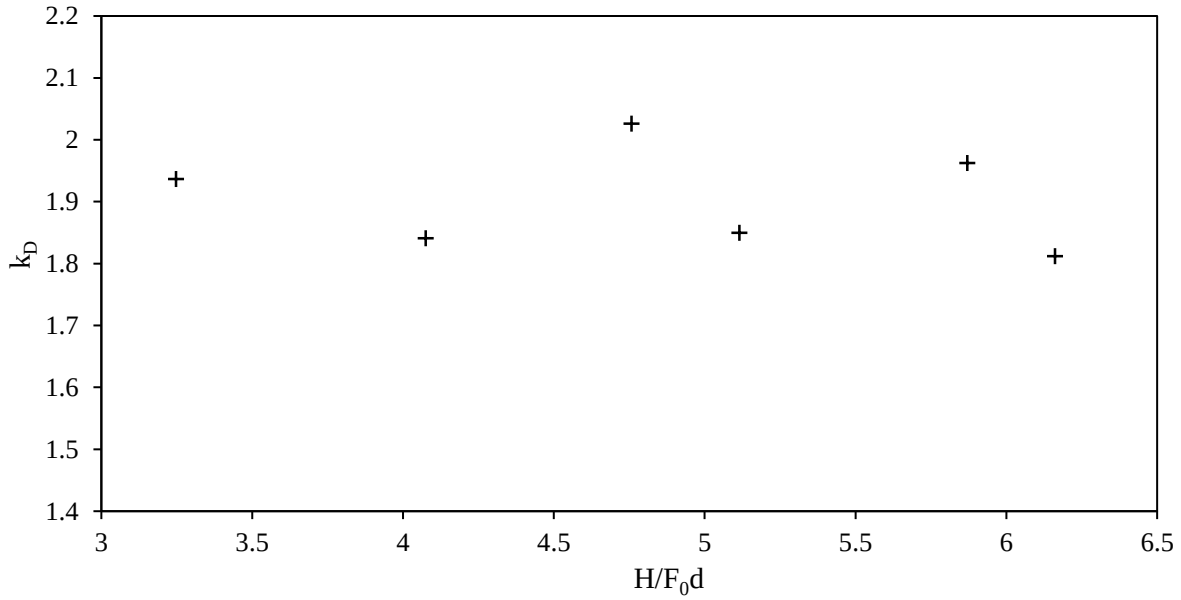

Figure 4.25: k_D coefficient calculated as the ratio of the minimum dilution at $r/H = 0.28$ and at $z/H = 0.88$, plotted against source height.

4.3.4 Boundary Flow

The flow behaviour along the boundary is discussed in a qualitative manner using concentration profiles. As previously stated the boundary flow is considered as two separate regimes; the near field and the far field. Each region is governed by a combination of horizontal inertial forces (from source conditions) which destabilises the flow and promotes mixing, and buoyancy forces, which act in the vertical direction and stabilises the flow. These forces act in a conflicting manner and the relative contribution of each component determines the behaviour of the flow. The near field mixing zone is predominantly a momentum driven flow where the radial layer entrains ambient fluid and grows in thickness. Beyond a certain point however, the two force contributions reach equilibrium marking the transition to the far field region. The interfacial shear between the flow and ambient layers is insufficient to generate further mixing and the flow is shown to collapse as evidenced by the discontinuation of vertical spreading. The relative contributions of the horizontal inertial force and buoyancy force are directly linked to the local Froude number. Given that the end of the near field region is associated with a balance of these terms, the local Froude number at this transition

is expected to be close to one (Chen, 1980; Lawrence and Maclatchy, 2001; Ulasir and Wright, 2003)

The fate of the far field region is dependent on the downstream conditions. The experimental setup utilised in the present study included a horizontal platform of finite length. As the flow reached the edge of the platform it is shown to drop off. The effect of this downstream control was reflected upstream, where it was evident from Figure 4.26 that once the far field region has been established, the flow thickness steadily reduced. Lean and Willock (1965) observed that the flow thickness of the far field is proportional to the Froude number at the start of the boundary region. Experimental results from Koop and Browand (1979) confirm this statement where radial flows with larger initial horizontal momentums were associated with larger spreading layer thicknesses following the transition to the far field.

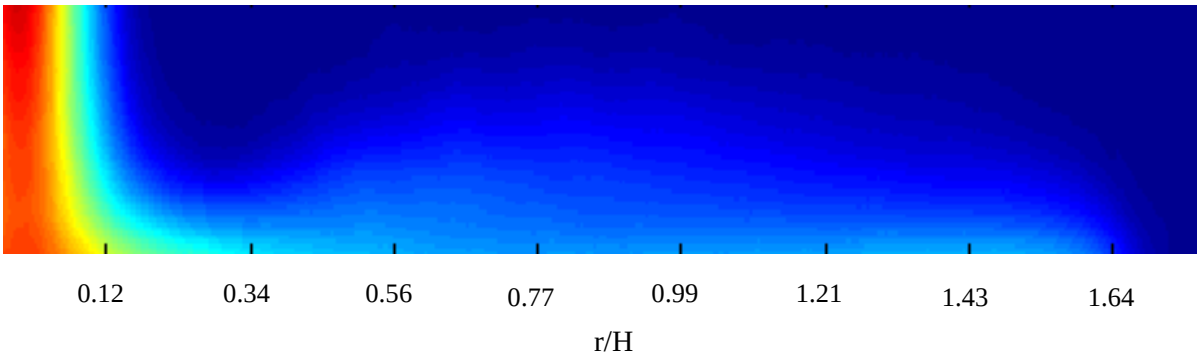

Figure 4.26: Calibrated concentration intensity field of the boundary region, $H/F_0d = 3.25$, $Re_0 = 3035$.

For wall jets, self-similarity of concentration profiles was heavily utilised for modelling purposes and to extract results along the boundary in a standardised and reliable manner. In contrast concentration profiles from buoyant flows are shown to change along the boundary and diverge away from the familiar Gaussian profile. The gradual change in behaviour of the boundary flow is reflected in the shape of the vertical concentration profiles which evolve with distance from the impact point. The model presented in Ulasir (2001) assumes a Gaussian form for concentration profiles within the near field of the boundary region however profiles in Figure 4.27 would suggest otherwise. Although the Gaussian profile is not applicable, these profiles have been scaled by the boundary concentration (C_m) and spread (b_c) using a Gaussian fit. Within the initial stages of the boundary flow (Figure 4.27a),

concentration profiles consistently assume the Gaussian form. This observation is expected as the flow composition is similar to a radial jet spreading along the boundary. The flow is still dominated by horizontal momentum and continues to entrain ambient fluid. As profiles are considered further away from the impact point, the form of the profile begins to gradually change. Divergence from the Gaussian function is particularly evident in Figure 4.27b, where the concentration gradients appear to increase near the boundary and tend towards a linear response. Similar density profiles were also reported in Wright and Ulasir (2000) where the shape of these profiles are between Gaussian and linear. In order to establish a modelling framework for the boundary flow region, this feature must be accounted for.

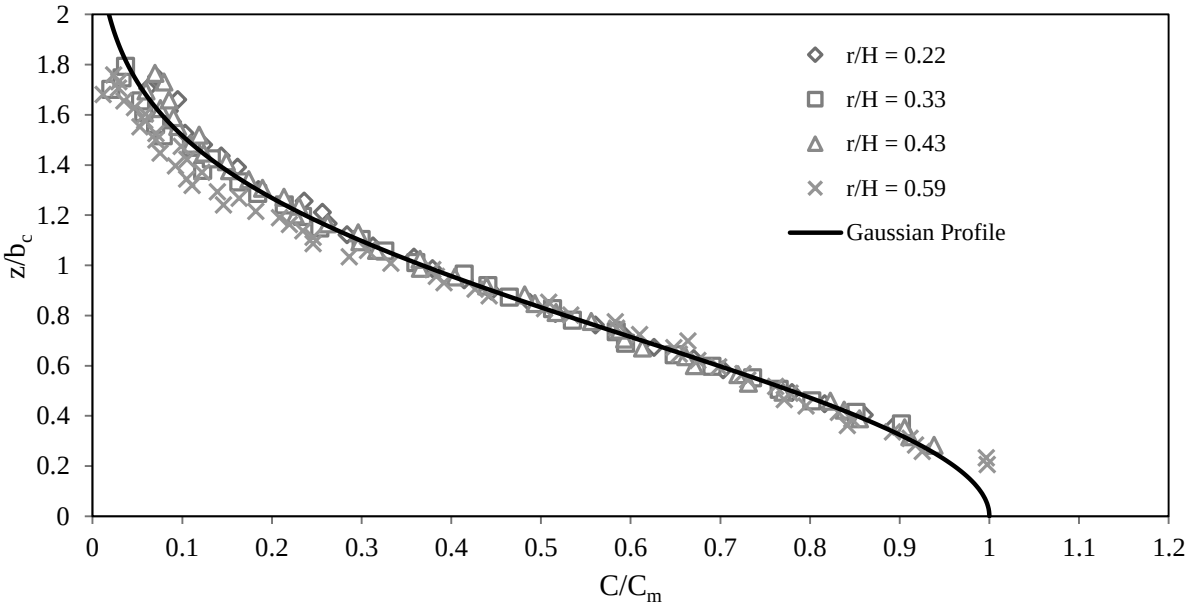

a)

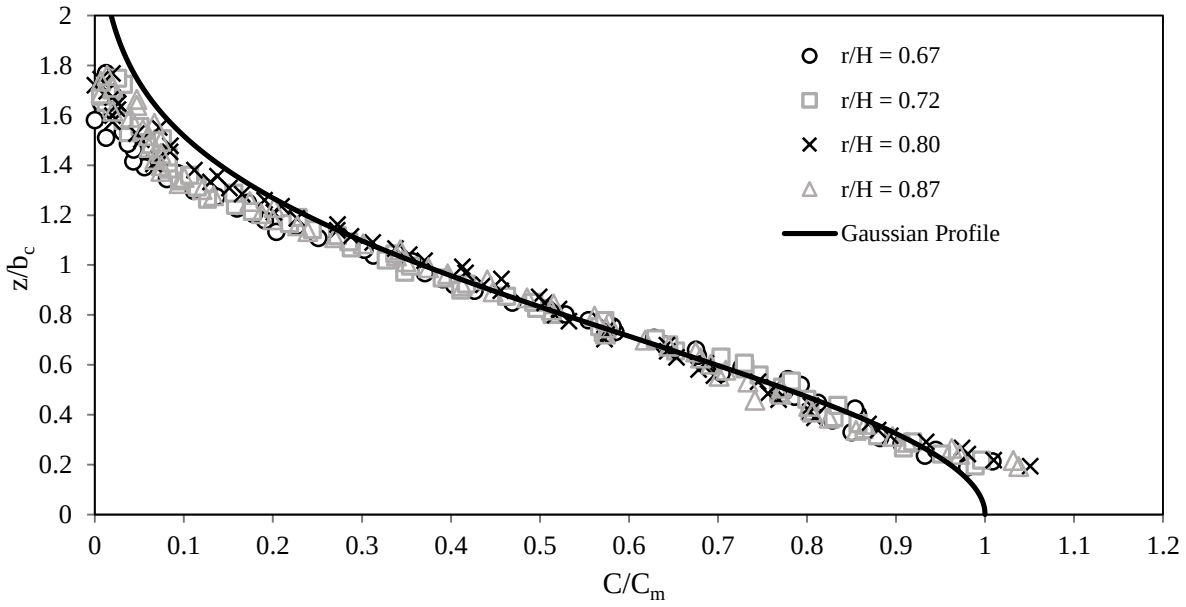

b)

Figure 4.27: Concentration profiles within the boundary region, $H/F_0d = 3.25$, $Re_0 = 3035$.

4.4 Summary

Experimental data investigating the behaviour of vertical flows impinging a solid horizontal boundary have been presented. The chapter is divided into two sections where jet flows (Section 4.2) and buoyant flows (transitional buoyant jets and plumes, Section 4.3) are assessed in some detail.

Jet impingement was examined using concentration and velocity measurements acquired from multiple experiments within the range $H/d = 36.30 – 173.30$. Three regions of the flow were analysed; the free flow, impact/impingement and boundary/wall jet regions. Integral model equations that predict the behaviour within the free flow and boundary regions were developed. In contrast to other flow regions, the impact region did not exhibit self-similarity and consequently was not included within the integral modelling framework. The complexities associated with this area are evident in the temporal statistics (Concentration RMS and Intermittency profiles). Within the free flow region, dilutions were observed to level off prior to the flow impinging the boundary, at approximately $z/H = 0.94$. This location also coincided with a significant drop off in RMS concentrations along the centreline. However, the start of the impact region was determined based on spread

measurements which were observed to diverge from the linear function at $z/H = 0.86$. This marked the extent to which integral model equations were applicable in the free flow region. The linearity of the spread function was also employed to define the location of the exit from the impact region, which was estimated to occur at $r/H = 0.30$. Within the impact region mixing produced an increase in volume flux of 22%, while the magnitude of the momentum flux remained essentially unchanged. Comparisons between integral model predictions and experimental data proved encouraging however discrepancies were apparent when concentration data within the boundary region was considered. Issues surrounding the validity of top-hat conversion factors and the possibility of boundary friction effects from changes in the experimental setup may have contributed to the observed inconsistencies.

Experiments on transitional buoyant jet and plumes were conducted for source heights ($H/F_0 d$) ranging from 3.24 to 6.16 and the flow was examined using concentration measurements. The behaviour in the free flow region was similar to the jet case where centreline dilutions were observed to level off at approximately $z/H = 0.93$. Spread measurements in the free flow and boundary regions were used to define the size of the impact zone and divergence from the linear function marked the vertical and horizontal limits. These were estimated to be $z/H = 0.88$ and $r/H = 0.28$ for all source heights tested. The size of the impact region was essentially the same for jet discharges as well. The corresponding dilution at the vertical ($z/H = 0.88$) and horizontal extent ($r/H = 0.28$) of the impact region was noted and the ratio of these values was found to be 1.90 for all source heights. This ratio was also calculated for jet experiments and yielded a similar value of $k_D = 1.83$. The combination of these results demonstrated that the flow behaviour in the impact region is independent of source conditions and predominantly governed by the boundary. The resulting flow along the boundary was analysed in a qualitative manner. Within this region, ambient entrainment was temporary and the flow was observed to stabilise as demonstrated by the visible discontinuation of vertical spreading. This observation was attributed to the influence of vertical buoyancy forces which inhibited the mixing processes. Here, the flow is said to have transitioned from the near field to the far field region where mixing is negligible. The transition to the far field region was reflected by the gradual distortion of concentration profiles away from the familiar Gaussian curve that is a feature of wall jets. With the exception of this region, the analysis on this configuration suggests that the modelling

framework required to represent flows with a significant buoyancy component is similar to the jet case. Adjustments would be required to account for changes to the flow profile and the transition to the far field mixing regime.

Chapter 5 Inclined Negatively Buoyant Jets

Inclined negatively buoyant jets discharged into an unbounded ambient are discussed in this chapter. This flow configuration has been the focus of a number of studies in the last decade or so due to its practical significance to desalination discharges. This practical focus requires the flow to interact with a boundary located in the proximity of the source (i.e. the seabed), but inconsistent methods of dealing with this boundary have resulted in data sets that are difficult to compare. The presence of this boundary further complicates comparisons with results from integral model formulations that typically do not incorporate the effects of the lower boundary on flow behaviour. At present only Oliver et al. (2013) (and Oliver, 2012) have reported dilution results from experiments where the influence of the boundary is removed from the measured flow domain. Crowe et al. (2015) also provides a data set using the same experimental conditions, however results are derived from velocity measurements. The purpose of this chapter is to provide an additional set of concentration field data under the same experimental conditions and confirm Oliver's findings. The initial conditions for each experiment are detailed in Table B.2 of Appendix B. In summary three discharge angles have been tested (30^o, 45^o and 60^o) and geometric and centreline (minimum) dilution parameters are reported at typical reference points (maximum height, return point). Results from other studies are also considered with a focus on identifying whether boundary influences can be discerned from these comparisons. A more detailed analysis of previously measured data, where the presence of a lower boundary influences the results, in the context of data where the boundary influence has been removed, provides some understanding into the nature and significance of those influences. New insight into buoyancy induced instabilities, which is a defining feature of this flow type, is also presented by examining the spread function along the inner side of the flow. The behaviour of this flow property is assessed in relation to the corresponding discharge angle and also the dilution recorded along the flow centreline.

5.1 Flow Configuration

The generic discharge configuration of the experiments discussed in this chapter is shown in Figure 5.1. The centreline is represented by a dashed line and the limits of the flow have been delineated by solid lines. These limits are termed the inner and outer edge of the flow. The location of key reference points are highlighted. They include the maximum height of the discharge and the return point where the flow reaches the initial discharge elevation. Results from three initial discharge angles are provided (θ_0 = 30°, 45° and 60°) with Froude numbers (F_0) varying between 21.0 and 69.1. To ensure boundary influence was not an issue, discharges were released at a distance of 720 mm above the tank bottom. This corresponded to a minimum non-dimensional source height ($H/F_0 d$) of 3.55.

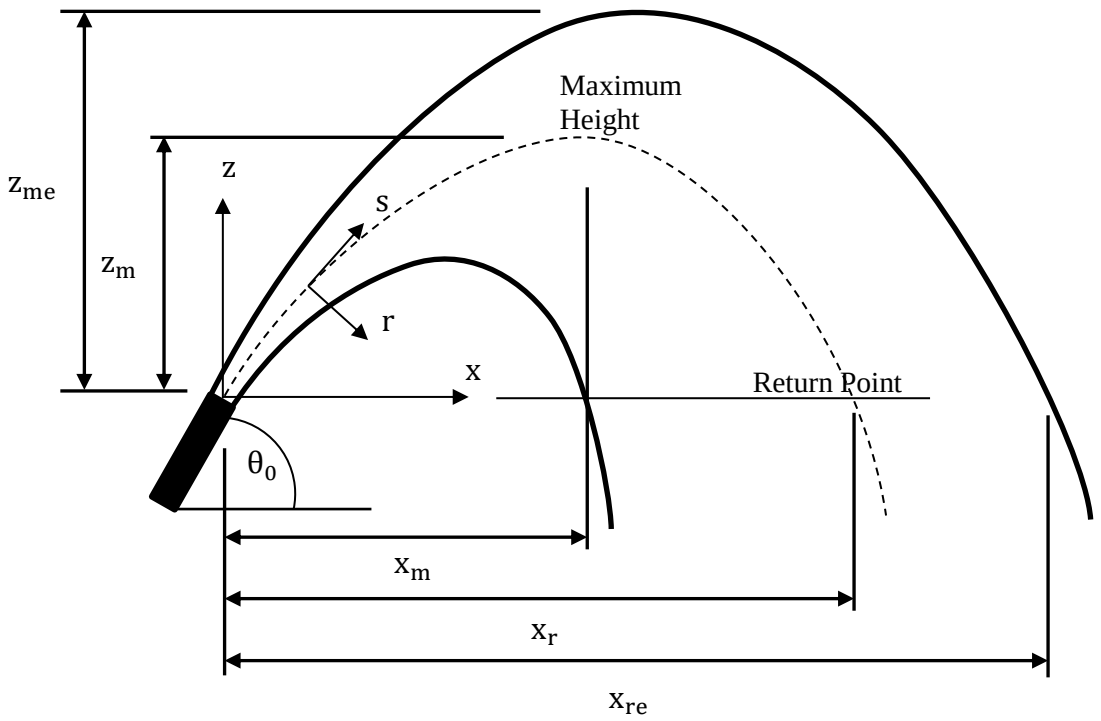

Figure 5.1: Flow configuration of an INBJ discharged into an unbounded environment. Key reference locations include the maximum rise height (x_m, z_m, z_{me}) and the return point (x_r, x_{re}).

5.2 Flow Observations

Figure 5.2a – c show instantaneous central plane images of inclined negatively buoyant jet experiments taken at various times within the recording period. Images are shown for three discharge configurations with source inclinations of 30^o, 45^o and 60^o and Froude numbers (F_0) of 59.76, 64.21 and 61.80 respectively, all at similar Re_0 (~ 4000). The physical mixing mechanisms contributing to the dilution of the flow are evident in these images. These mixing mechanisms have been discussed in some detail in the literature. The initial jet region of the flow, which is governed by the momentum imparted to it, continuously exhibits a well-defined structure. This is apparent prior to the reversal point, after which the influences of the fluid buoyancy become more evident. Near the reversal point, parcels of tracer fluid are able to break free from the primary flow motion in a fluctuating manner. This behaviour was also reported by Oliver (2012) where fluid with enough velocity would 'punch out' beyond the perceived flow boundaries despite the changing flow curvature associated with vertical reversal of the flow. Following this reversal in flow direction, the fluid motion is more chaotic, which reflects the progressive change to a buoyancy (negative) governed flow. As the fluid propagates downwards, the formation of large rotating groups of tracer (on the outer side of the flow), reflecting the dominance of large-scale eddy motions, become increasingly evident. These eddies facilitate the entrainment and transport of clean ambient fluid into the primary flow. A unique aspect of the flow is the occurrence of falling fluid mass or detrainment from the inner side originating near the flow reversal point. This flow feature is referred to as buoyancy induced instabilities. These occur because of the unstable density gradient that is present in this region where the mixed fluid overlies the less dense ambient. Fluid parcels near the edge of the inner side of the flow are unable to overcome the effects of negative buoyancy from the density difference between the fluid and the ambient. As a result the mixed fluid parcel is removed from the entrainment process and falls away from the primary flow. In contrast, stable density gradients occur along the outer edge and the distinct conical form is able to be maintained over longer distances along the flow path. In general, discharges from each angle demonstrate similar visual behaviour. However there are some differences with regards to the overall flow. Buoyant instabilities are clearly more significant for steeper discharge angles. Due to the limited contribution of horizontal momentum, the initial flow structure is lost relatively early as detrainment occurs along the inner side of the

flow. Steeper inclinations also result in more turbulent behaviour where obvious gaps in the flow field are present, most noticeably within the descending arm of the flow. This observation reflects the fact that the transition to a buoyancy dominated flow (plume) occurs closer towards the reversal zone for steeper discharges. For vertical discharges (90°) these two points are expected to coincide.

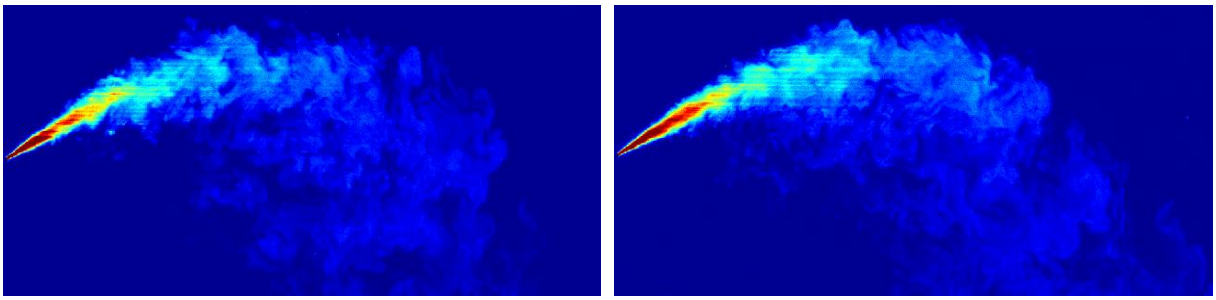

a) 30° discharge, F_0 = 60.1, Re = 3986.

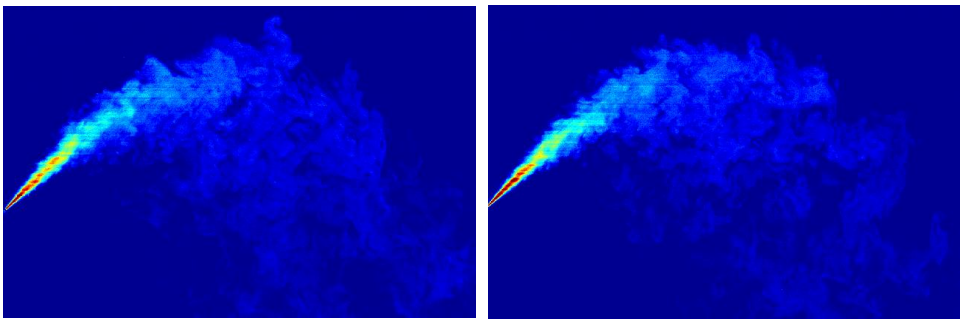

b) 45° discharge, F_0 = 64.6, Re = 4268.

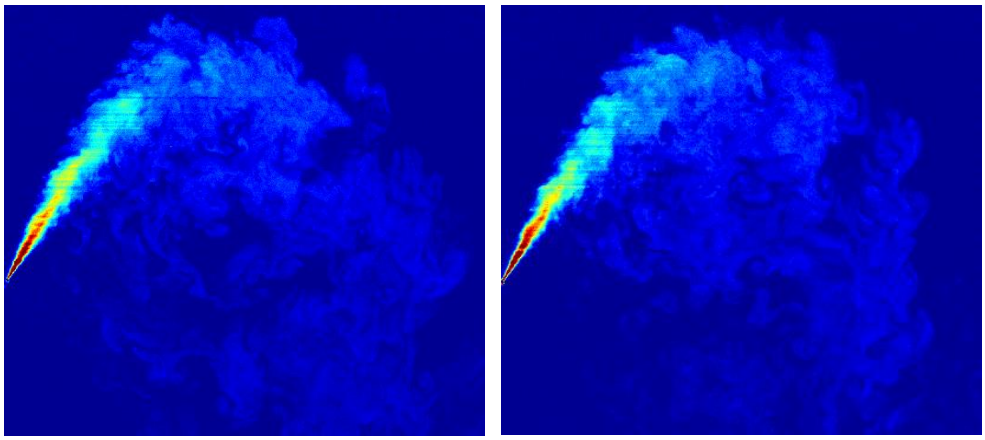

c) 60° discharge, F_0 = 62.2, Re = 4122.

Figure 5.2: Instantaneous concentration fields taken at two different time periods for each angle.

5.3 Flow Geometry

Geometric results obtained for 30º, 45º and 60º discharges are presented in this section. The flow trajectory measurements are considered along centreline and the outer flow edge. Reference locations have been identified along the flow path and measured (with respect to the discharge point) for comparative purposes. Typically these locations include the vertical and horizontal positions of the maximum centreline height (z_m, x_m), the horizontal position of the centreline return point (x_r, 0), and outer edge measurements of the maximum height (z_{me}) and return point (x_{re}). The centreline path length to the maximum height and the return point have also been included and discussed. Most studies normalise geometric parameters using the nozzle diameter (d) and the discharge Froude number (F_0) for comparative purposes. These values are expressed using k notation in the form shown in Equations 5.1 - 5.4 and are a function of the initial discharge angle (θ_0).

Vertical location of maximum centreline/maximum edge height:

$$\frac{z_m}{F_0 d}, \frac{z_{me}}{F_0 d} = k_{zm}(\theta_0), k_{zme}(\theta_0) \quad 5.1$$

Horizontal location of maximum centreline height:

$$\frac{x_m}{F_0 d} = k_{xm}(\theta_0) \quad 5.2$$

Horizontal location of centreline/edge return point:

$$\frac{x_r}{F_0 d}, \frac{x_{re}}{F_0 d} = k_{xr}(\theta_0), k_{xre}(\theta_0) \quad 5.3$$

Centreline path length to the maximum height/return point:

$$\frac{s_m}{F_0 d}, \frac{s_r}{F_0 d} = k_{sm}(\theta_0), k_{sr}(\theta_0) \quad 5.4$$

5.3.1 Centreline Trajectory

The centreline trajectory is presented in this section. Previous studies (Crowe et al., 2015; Kikkert et al., 2007; Lai and Lee, 2012; Oliver et al., 2013; Papakonstantis et al., 2011a) have shown that self-similarity can be achieved if the vertical and horizontal co-ordinates are normalised using the initial Froude number (F_0) and nozzle diameter (d). Therefore it is important to establish this feature in order to verify the credibility of each experiment conducted. Centreline trajectories are shown in Figure 5.3a – c for the three discharge angles tested. For each experiment, a similar trajectory is observed as centreline points successfully collapse onto one another. Ferrari and Querzoli (2010) noted that the descending arm of the flow began to move back towards the origin for $F_0 = 31$. This change in form is not evident here as the shape of each experiment does not differ depending on the Froude number. Although each data set is generally consistent, variability in the flow paths becomes relatively more apparent with increasing distance from the discharge point. It is generally expected that results are less consistent near the return point as indicated by a number of studies. Oliver et al. (2013) described the difficulties associated with obtaining consistent results near this region where the larger eddy sizes demand longer averaging times. Furthermore, any errors associated with the measurement of initial conditions are amplified further along the flow path. In the present study the consistency between data points is comparable and in many cases less variable than centreline measurements reported in previous studies. Oliver et al. (2013) noted that the shape of the trajectory from all angle inclinations is the same when the centreline co-ordinates are normalised using (z_m) and (x_r). This is illustrated in Figure 5.4 where the trajectory for every test conducted has been re-plotted using these scaling parameters. The consistency and overall quality of these experiments is further emphasised by this result. The location of the outer edge of the flow has also been included in Figure 5.3a – c. Each point was determined by adding twice the outer spread ($2b_c$) to the corresponding centreline coordinate in the direction normal to the centreline trajectory. The variability between data sets follows the same behaviour as the corresponding centreline trajectory. Self-similarity is clearly a feature of both the centreline and the outer edge trajectories thereby confirming its dependence on the initial Froude number (F_0) and nozzle diameter (d). This feature is utilised in the following sections when comparing reference location measurements with past studies.

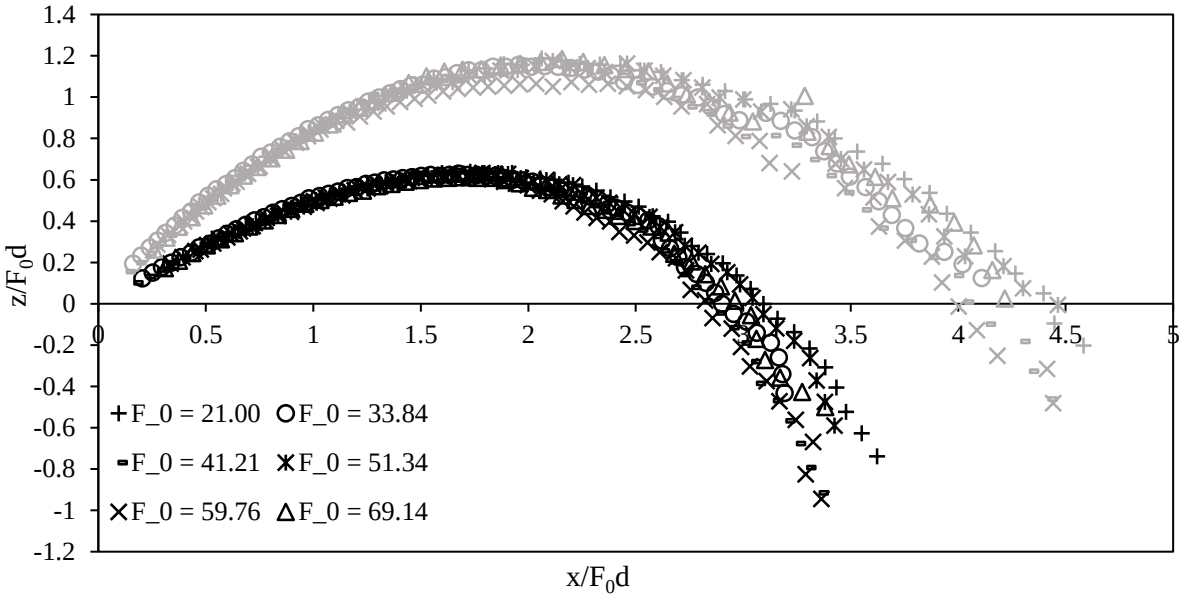

a) 30º discharges.

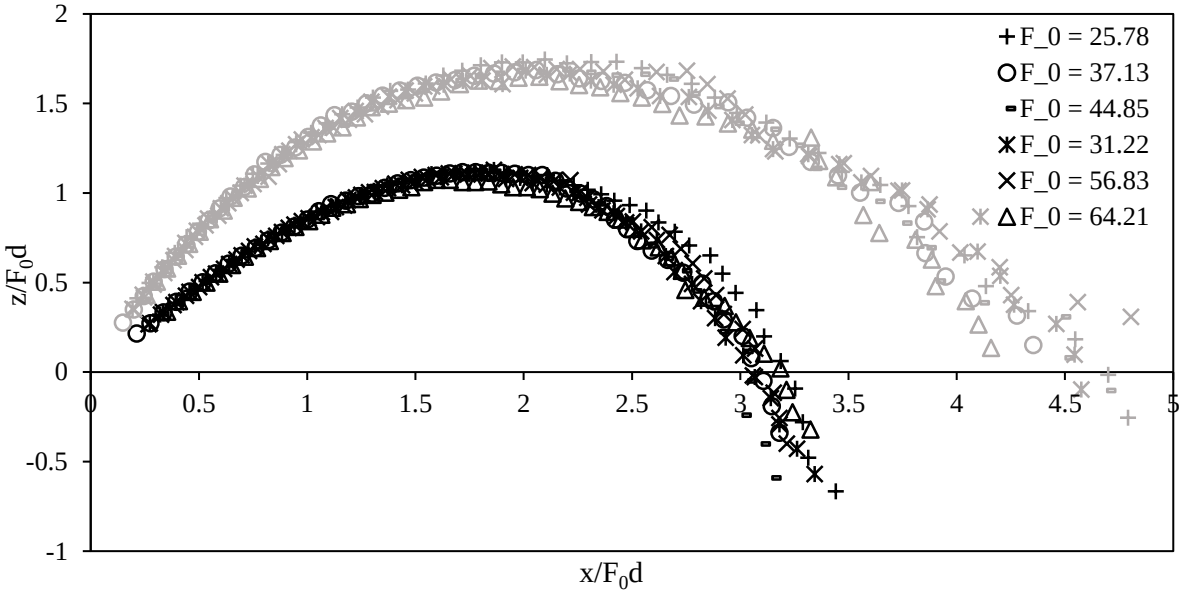

b) 45º discharges.

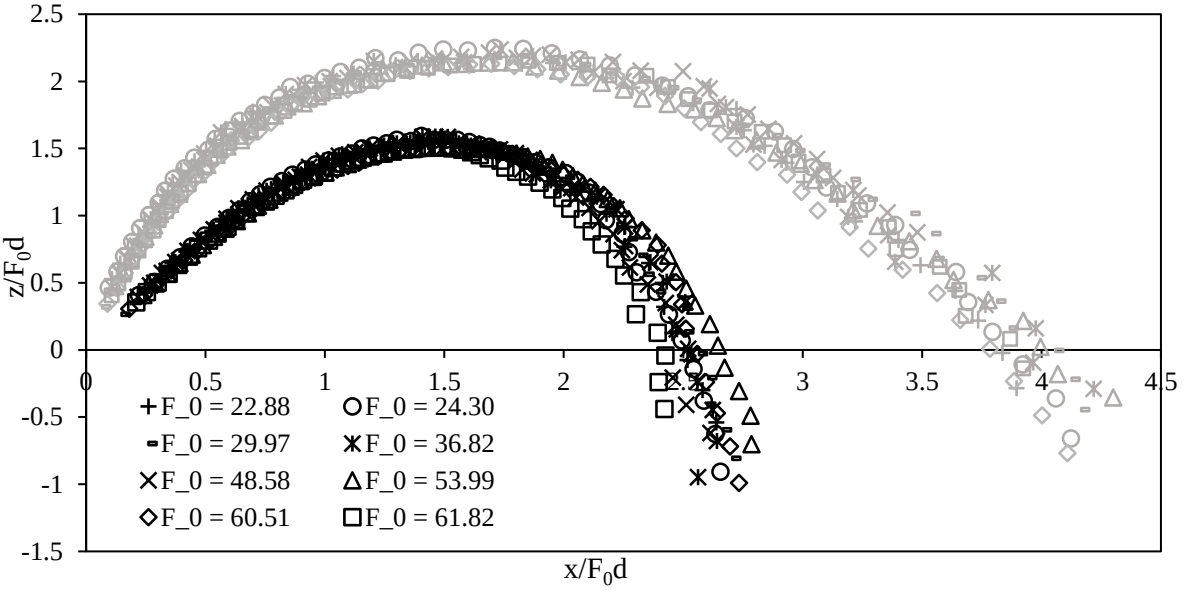

c) 60° discharges

Figure 5.3: Centreline and outer edge trajectory. Centreline co-ordinates represented by black symbols, outer edge co-ordinates represented by grey symbols.

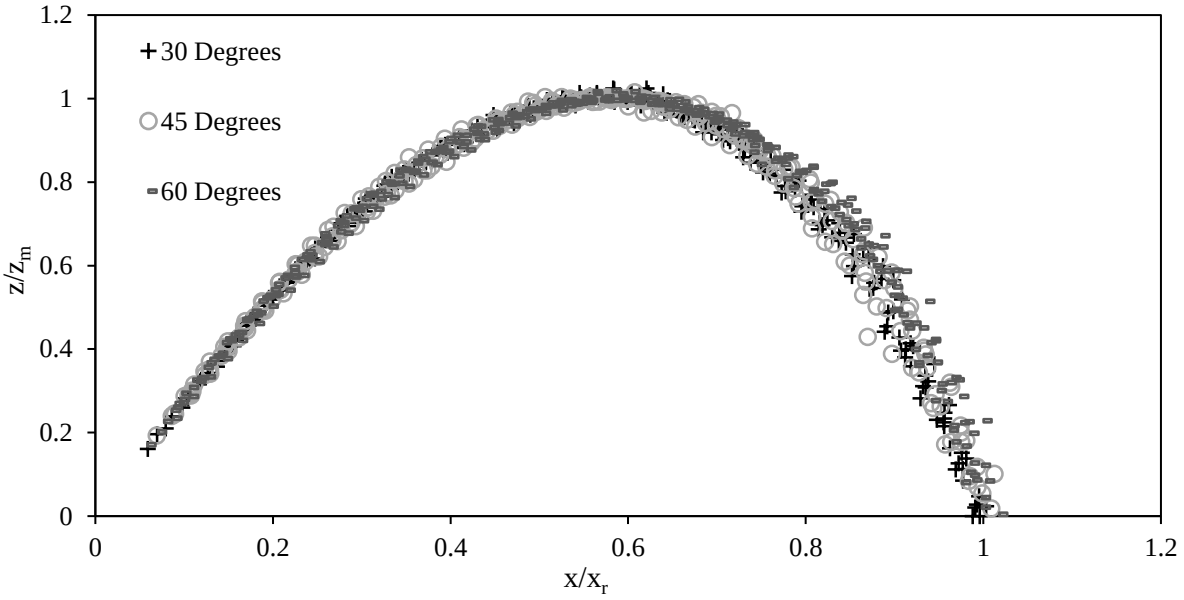

Figure 5.4: Centreline trajectory for each angle collapsed onto a single curve, with horizontal and vertical co-ordinates normalised using the horizontal distance to the return point and the vertical distance to the maximum centreline height respectively.

5.3.2 Geometric Parameters

From the flow trajectories, reference locations have been obtained. Many of these points were extracted by fitting 4th order polynomials to the trajectories and determining where along the curve the required criteria was met. For flow edge measurements at the return point (x_{re}) horizontal cross-sections through the return point were examined and the flow edge was taken as the point corresponding to $0.018C_m$. This distance approximately represents two Gaussian spread distances (b_c) from the centreline. Figure 5.5 - Figure 5.11 plot each reference location against the discharge Froude number (F_0) for all angles tested. Linear best fit lines have also been included (represented by a dashed line). Each data set exhibits a linear dependence with F_0. Measurements at the return point are comparatively less consistent than at the maximum height; in line with observations relating to the flow trajectory. Flow measurements at the return point (x_{re}) display the most variability and some measurements from different discharge angles are shown to overlap each other. Oliver (2012) noted that when scaled measurements (k-coefficients) are plotted against the Froude number, a slight negative trend is observed. When these coefficients were plotted against the Froude number in the present study, a discernible trend could not be perceived. Lai and Lee (2012) and Papakonstantis et al. (2011a) provided similar figures, where k_{zm} was plotted against F_0. Both studies showed no visible trend for tests conducted where $F_0 > 25$. In comparison to the rest of the literature, Oliver (2012) acquired the most comprehensive data set which provided a sounder basis to assess the variation of geometric parameters with F_0.

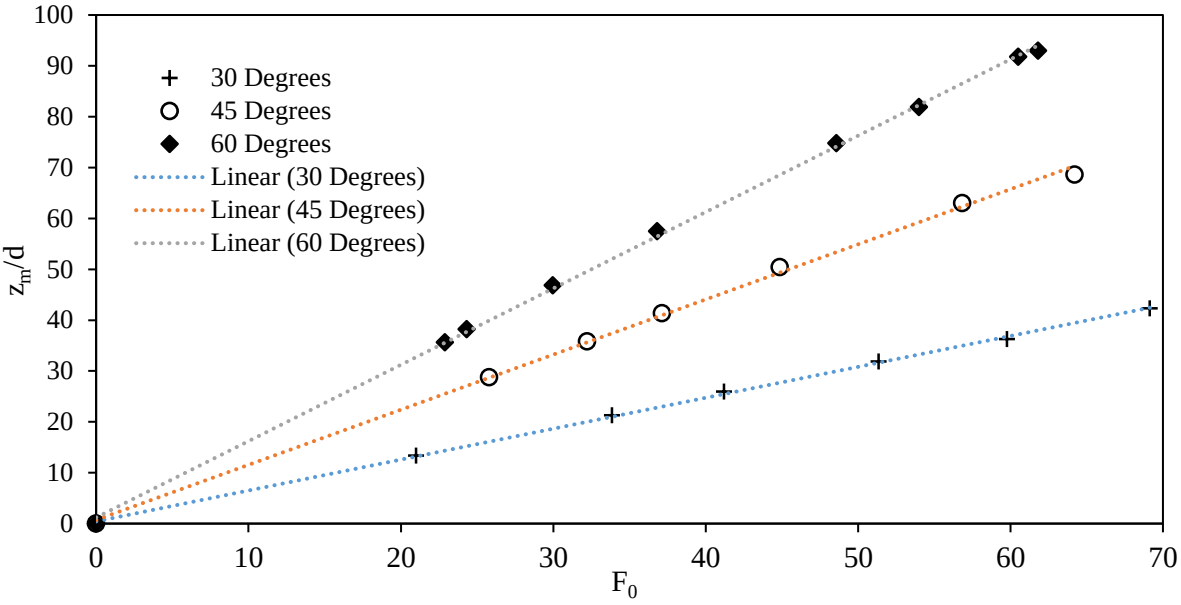

Figure 5.5: Vertical distance to centreline maximum height against Froude number.

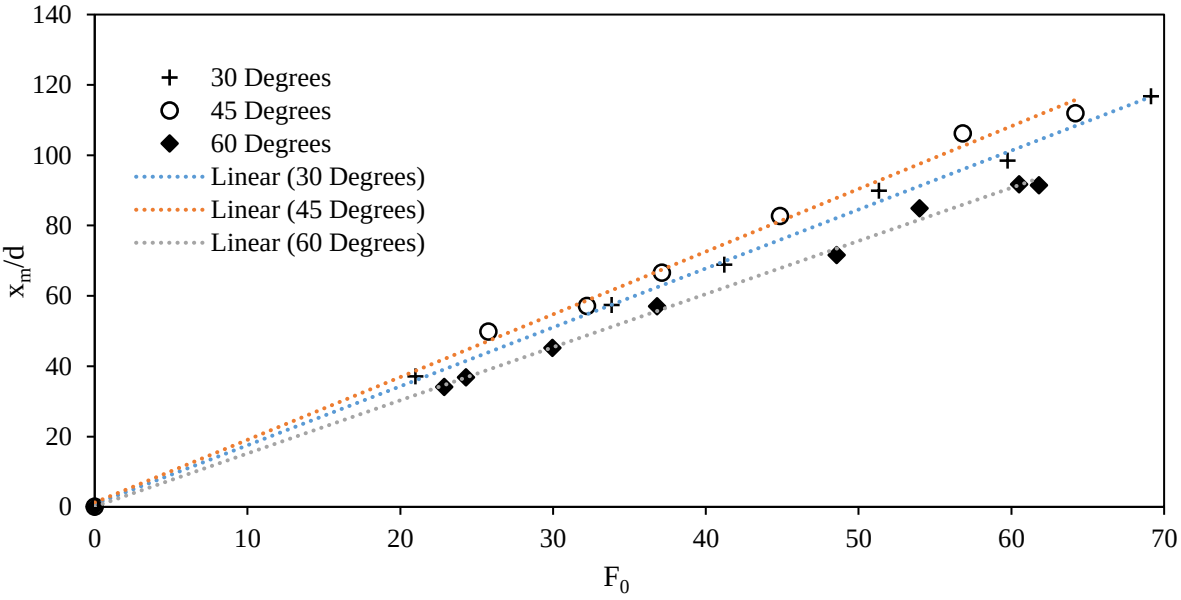

Figure 5.6: Horizontal distance to centreline maximum height against Froude number

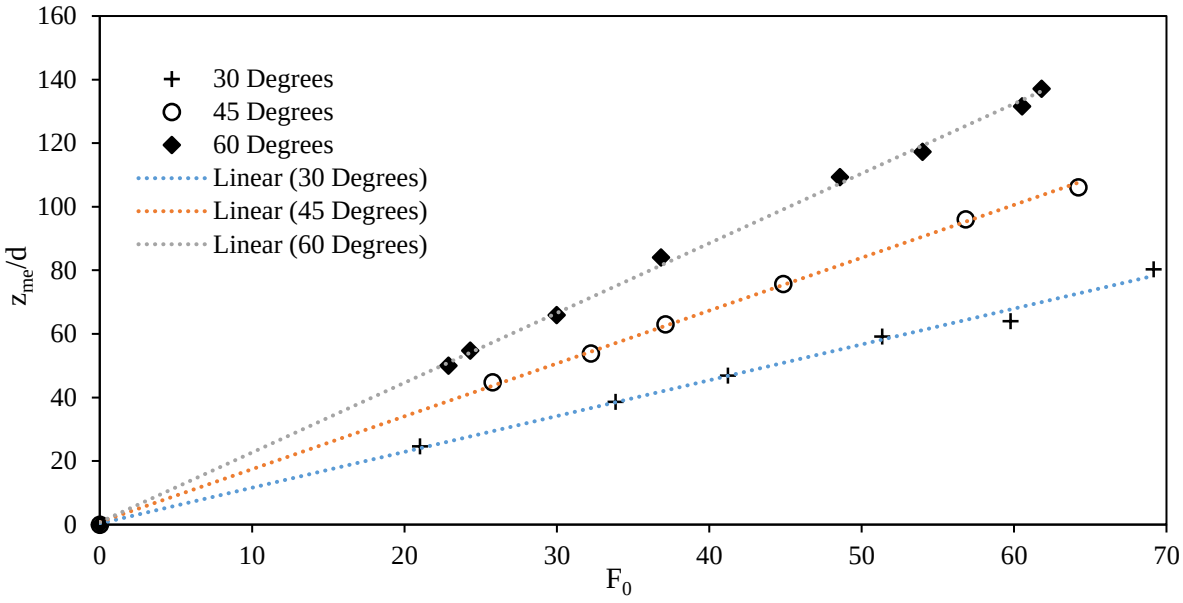

Figure 5.7: Vertical distance to maximum flow edge height against Froude number.

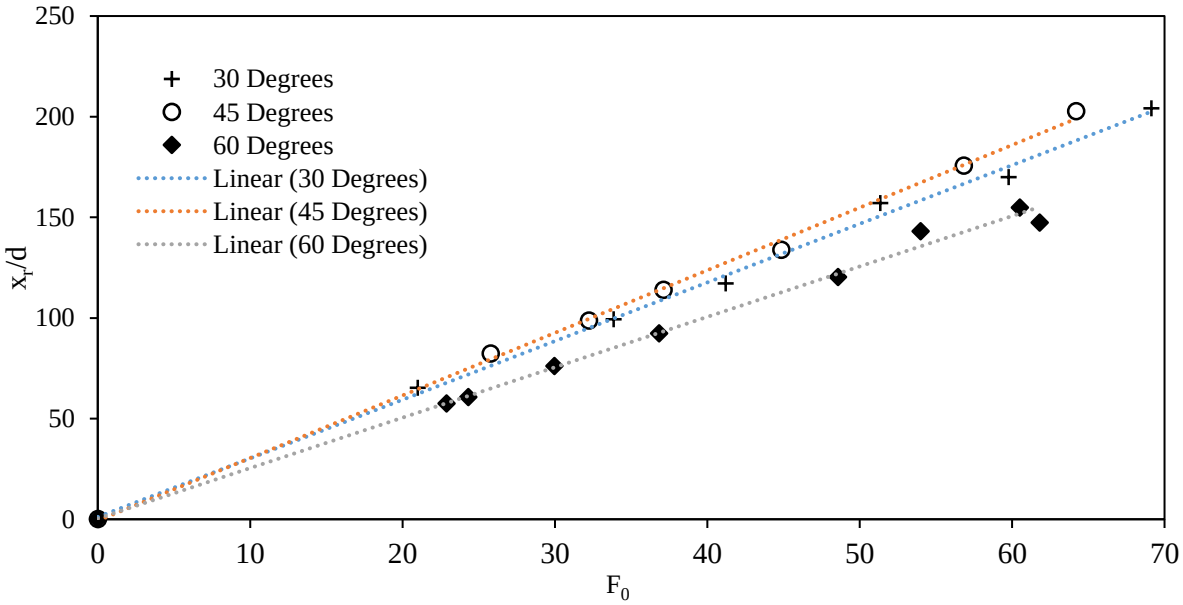

Figure 5.8: Horizontal distance to centreline return point against Froude number.

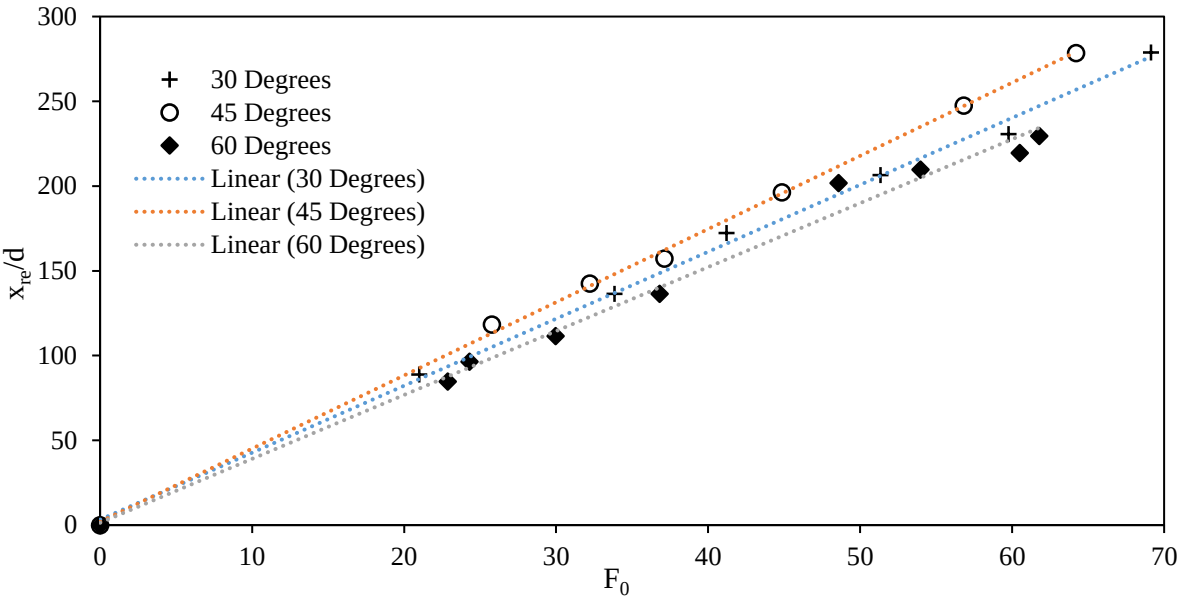

Figure 5.9: Horizontal distance to flow edge return against Froude number.

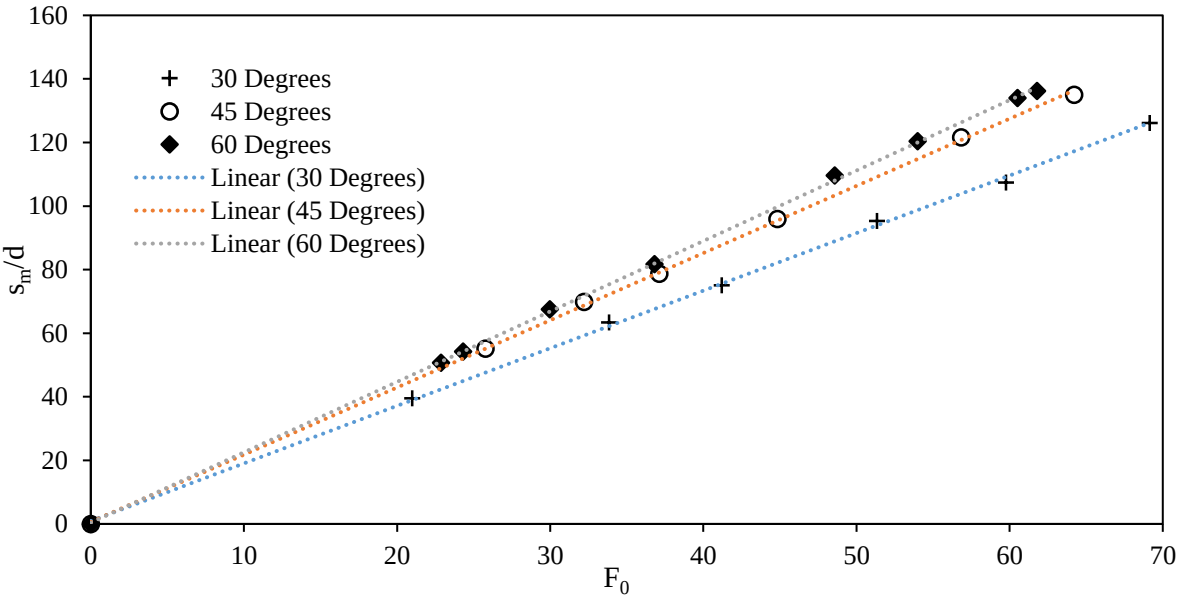

Figure 5.10: Path distance to centreline maximum height against Froude number.

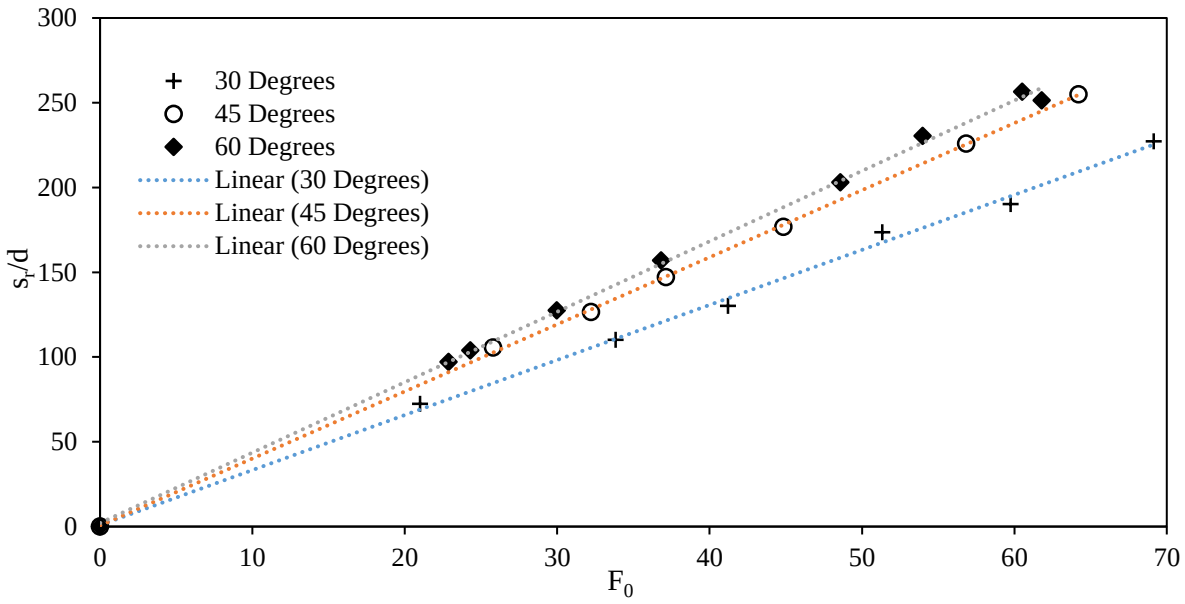

Figure 5.11: Path distance to centreline return point against Froude number.

A summary of previously reported geometric results is presented in Table 5.1 and Table 5.2. Average and standard deviations from literature results are included with obvious outliers being removed from mean calculations. Data were identified as being outliers if they were over 25% greater or lower than the mean value across all studies. Mean values were subsequently re-calculated after each outlier had been removed. Overall, standard deviations range between 5 to 13%, with results at the return point predictably displaying the most variation. Maximum edge height measurements (k_{zme}) also display significant variation where average deviations from the mean are over 10% for all three angles. The reasons for these differences have been discussed at length in the literature. Differing methods of trajectory identification are likely to introduce discrepancies between reported values. Older studies have generally based their measuring techniques on visual observations which involve a level of subjectivity. Studies that have employed more sophisticated optical techniques (LA, LIF) are able to produce more detailed flow field information. As a result more standardised techniques such as Gaussian curve fitting can been used to identify reference locations. In addition the quantity of information available for analysis contributes to the accuracy of the results and this is dictated by different limits on the duration and sampling frequency of experiments. The existence of a lower boundary also has implications for these

measurements, although the behaviour at the return point is more likely to be influenced than flow conditions at the maximum height. With the exception of Oliver et al. (2013)/Oliver (2012) and Crowe et al. (2015) most studies have incorporated a boundary in their respective experimental setups. For this reason particular attention is paid to these studies as they provide the most relevant comparison. Comparisons with model predictions have been limited to the Modified Reduced Buoyancy Flux (MRBF) model from Crowe et al. (2016). Traditional commercial models such as CorJet and VisJet are not included as the issues associated with these predictions have already been discussed extensively in the literature. Crowe et al. (2015), Oliver et al. (2013), Palomar et al. (2012), Lai and Lee (2012) and Kikkert et al. (2007) have all shown that these models under-predict the distance to the aforementioned reference locations. As steeper discharge angles are considered, the discrepancies between model predictions and the experimental data are amplified.

5.3.2.1 Maximum Height

Measurements at both the maximum centreline and edge height have been the most commonly reported reference locations in the literature due to their practical significance in relation to desalination discharges. From Table 5.1, it is apparent that the present study compares favourably with past studies, as most results are within one standard deviation of the literature mean. Centreline measurements for 60^o experiments (k_{xm}, k_{zm}) are towards the lower end of previously reported values, however are within 2% of Oliver et al. (2013). The same experimental facility was used by Crowe et al. (2015), however results from this study are generally greater than the present study and Oliver et al. (2013). An important distinction is the use of velocity information as opposed to concentration data. An additional parameter of note for 60^o discharges is k_{zm}/k_{xm} (plotted in Figure 5.12). Most results indicate that this ratio is close to unity however Cipollina et al. (2005) is the only study where k_{zm} is considerably greater than k_{xm}. This observation suggests that a discharge angle steeper than 60^o may have been used.

The outer edge measurement at the maximum rise height (k_{zme}) for all three angles also compares well with previous studies. In the present study k_{zme} was determined from the trajectory of the outer edge of the flow where a 4th order polynomial was fitted. While most studies visually measured this location, Crowe et al. (2015), Kikkert et al. (2007) and Oliver

et al. (2013), inferred k_{zme} by adding $2b_c$ to z_m (b_c corresponds to the outer spread at the centreline maximum height). This method was not employed in the present study as it is clear from trajectory plots that the horizontal distance to the maximum flow edge height does not exactly coincide with the centreline height. A comparison of these two methods was carried out and it was found that estimates were within 4% of each other.

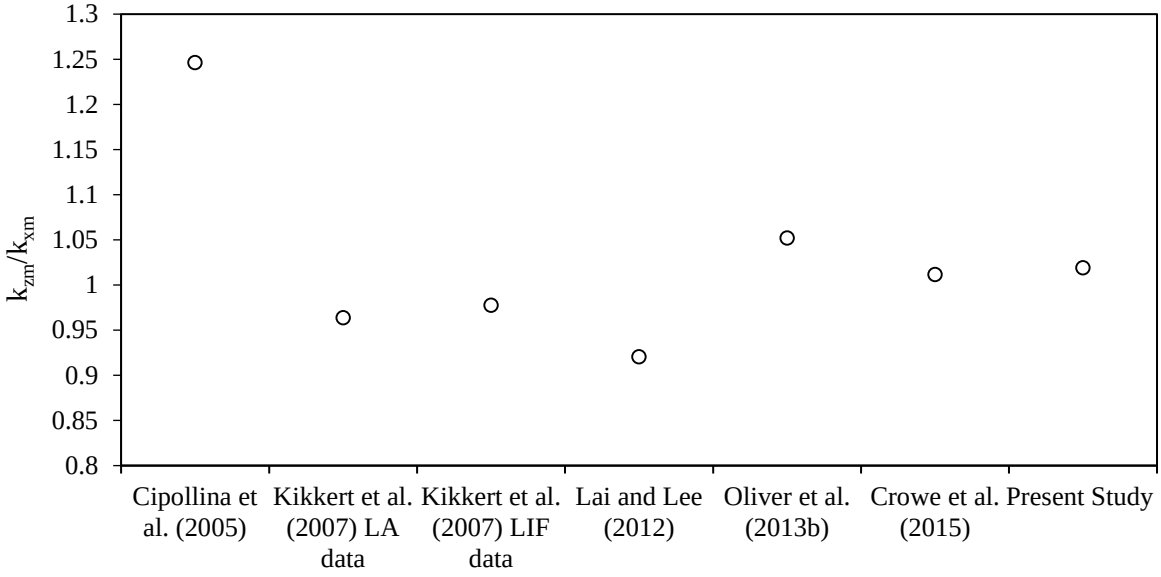

Figure 5.12: Ratio of vertical and horizontal distance to maximum centreline height (k_{zm}/k_{xm}) for 60° discharges.

As stated, some data points were excluded if they were deemed outliers. $k_{xm}(30^o)$ values from Lindberg (1994) were found to be 33% greater than the tabulated average in Table 5.1. While only this coefficient met the outlier criteria, the remaining data points for 45° and 60° discharges follow trends that are inconsistent with other studies. In a relative sense, their data is contradictory to the trend suggested in the literature which indicates that $k_{xm}(30^o)$ and $k_{xm}(45^o)$ should be similar and $k_{xm}(60^o)$ should be lower. Bosanquet et al. (1961) reports unusually high values for $k_{xm}(45^o)$ and $k_{zm}(45^o)$, which may stem from their primitive measurement techniques. Centreline data at the maximum rise height was determined by visually locating the centre of the outer and inner edge limits of the flow. Given that the cross-sectional profiles are asymmetrical due to buoyant instabilities, this definition of the flow centreline is inconsistent with those based on the peak concentration or velocity. Values

from Nemlioglu and Roberts (2006) are also relatively high in comparison to other studies. Only k_{zme} was reported at the maximum height and their values for 30° and 60° discharge angles were dismissed as outliers.

5.3.2.2 Return Point

With the exception of Zeitoun et al. (1970), centreline results at the return point have been reported from studies where sophisticated imaging techniques were used. Literature values for $k_{xr}(30^o)$ and $k_{xr}(45^o)$ are relatively consistent with the present study. Table 5.2 indicates that there is little variation between different studies. More variability is observed for $k_{xr}(60^o)$ where average deviations from the mean are relatively high. Nemlioglu and Roberts (2006) and Cipollina et al. (2005) report distances that are almost 20% either side of the tabulated mean value. Notably, results for $k_{xr}(60^o)$ from Nemlioglu and Roberts (2006) were higher than corresponding values at 45° and 30° inclinations. Similar to Lindberg (1994) with regards to k_{xm}, this behaviour conflicts with most studies, where 60° inclinations typically result in the lowest return point distance. The $k_{xr}(60^o)$ values from the present study are slightly lower than those from previous studies (9% lower than the mean) with only Roberts et al. (1997) and Cipollina et al. (2005) reporting lower distances. Despite this discrepancy, individual coefficients between tests exhibited very little variance. The relative standard deviation is similar to experiments from Crowe et al. (2015) and significantly lower than the overall variation of published results.

There is limited information available at the return point edge and in many cases, measurements have been visually derived (Bloomfield and Kerr, 2002; Zeitoun et al., 1970). Crowe et al. (2015) and Oliver et al. (2013) also provide details at the flow edge and were the only studies to provide both centreline and edge measurements. These studies used an alternate method to the present study when locating the edge of the return point. k_{xre} was inferred using the formula; $x_{re} = x_r + 2b_c/-\sin(\theta_r)$ where θ_r represents the gradient of the centreline trajectory at the return point and b_c is the outer spread value at the return point. Despite different methods of determination, results from Crowe et al. (2015) and Oliver et al. (2013) compare well to the present study across all three angles. MRBF model predictions are also reasonably consistent with the experimental coefficients. The consistency between these more recent studies is illustrated in Figure 5.13 where the percentage difference of the

k_{xre} coefficient from the mean is plotted for the three discharge angles. Note, in this case the mean value was calculated only using studies included in Figure 5.13. The maximum discrepancy from the mean across the three discharge angles is only 6%. In contrast to studies where visual detection methods were employed, these results at the flow edge are noticeably higher. It is also worth remembering that most results in the literature were obtained with a lower boundary in place (with the exception of the present study, Crowe et al., 2015 and Oliver et al., 2013). Therefore in the context of potential boundary influence, this comparison is counter-intuitive to expectation. In such cases where the boundary is in close proximity to the return point, it is expected that the boundary would extend the distance to the flow edge due to the accelerated lateral spread upon impact. Evidence of boundary influence could also not be clearly identified from centreline return point measurements (k_{xr}). Although more data is available, the variation amongst reported values provides no systematic indication of boundary influences.

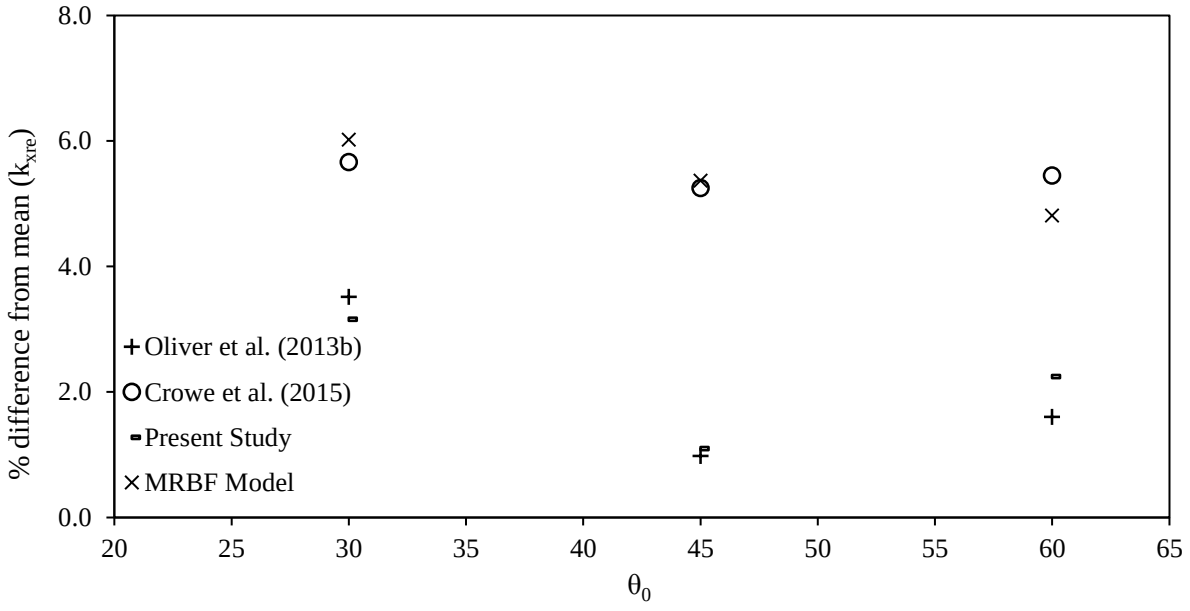

Figure 5.13: Distance to flow edge (k_{xre}) for 30°, 45° and 60° discharges. Data points are presented as a percentage difference from the mean value (determined from studies included in the above figure).

Table 5.1: Centreline and flow edge measurements at the maximum height from the present study and the literature. Average and standard deviations are calculated from past studies. Excluded values are marked with *.

	Horizontal Dist. Centreline Max. Height (k_{xm})			Vertical Dist. Centreline Max. Height (k_{zm})			Vertical Dist. Flow Edge Max. Height (k_{zme})		
	30°	45°	60°	30°	45°	60°	30°	45°	60°
Bosanquet et al. (1961)		*2.68**			*1.67**				
Roberts and Toms (1987)									*2.04*
Zeitoun et al. (1970)							*1.15*	*1.43*	*2.08*
Lane-Serff et al. (1993)							*1.10 ± 0.11*	*1.77 ± 0.20*	*2.33 ± 0.34*
Lindberg (1994)	*2.39 ± 0.32**	*1.68 ± 0.25*	*1.82 ± 0.24*				*1.27 ± 0.17*	*1.57 ± 0.21*	*2.16 ± 0.29*
Roberts et al. (1997)									*2.20*
Bloomfield and Kerr (2002)							*1.19*	*1.76*	*2.32*
Ferrari and Querzoli (2004)					*1.22*	*1.68*			
Cipollina et al. (2005)	*1.95*	*1.80*	*1.42*	*0.79*	*1.17*	*1.77*	*1.08*	*1.61*	*2.32*
Nemlioglu and Roberts (2006)							*1.40**	*2.00*	*2.85**
Kikkert et al. (2007) LA data	*1.79*	*1.86*	*1.66*	*0.60*	*1.09*	*1.60*	*1.06*	*1.71*	*2.28*
Kikkert et al. (2007) LIF data	*1.86*	*2.01*	*1.80*	*0.69*	*1.21*	*1.76*	*1.20*	*1.78*	*2.45*
Shao and Law (2010) $0.10 \leq H_0/l_m \leq 0.15$	*1.70*			*0.66*			*1.05*		
Shao and Law (2010) $H_0/l_m > 0.15$	*1.54*			*0.66*			*1.05*		
Shao and Law (2010) $H_0/l_m > 0.05$		*1.69*			*1.14*			*1.47*	
Papakonstantis et al. (2011a)		*2.03 ± 0.13*	*1.83*		*1.17*	*1.68*		*1.58 ± 0.03*	*2.14 ± 0.04*
Lai and Lee (2012)	*1.94*	*2.08*	*1.76*	*0.65*	*1.18*	*1.62*	*0.95*	*1.57*	*2.06*
Bashitialshaaer et al. (2012)				*0.69*	*1.00*	*1.40*	*0.92*	*1.30*	*1.70*
Oliver et al. (2013)	*1.75*	*1.75*	*1.53*	*0.66*	*1.09*	*1.61*	*1.15*	*1.65*	*2.21*
Crowe et al. (2015)	*1.87 ± 0.03*	*1.96 ± 0.07*	*1.69± 0.04*	*0.69 ± 0.01*	*1.22 ± 0.04*	*1.71± 0.02*	*1.09 ± 0.06*	*1.73 ± 0.05*	*2.23 ± 0.04*
Literature Average	*1.80 ± 0.14*	*1.87 ± 0.15*	*1.69 ± 0.15*	*0.68 ± 0.05*	*1.15 ± 0.07*	*1.65 ± 0.11*	*1.09 ± 0.10*	*1.62 ± 0.17*	*2.16 ± 0.24*
Present Study	***1.70 ± 0.05***	***1.83 ± 0.07***	***1.51 ± 0.03***	***0.62 ± 0.01***	***1.11 ± 0.02***	***1.54 ± 0.03***	***1.14 ± 0.04***	***1.69 ± 0.03***	***2.22 ± 0.04***
MRBF model, Crowe et al. (2016)	*1.68*	*1.74*	*1.48*	*0.63*	*1.11*	*1.57*	*1.04*	*1.58*	*2.08*

Table 5.2: Return point measurements at flow centreline and flow edge from the literature and the present study

	Horizontal Dist. Centreline Return Point (k_{xr})			Horizontal Dist. Edge Flow Return Point (k_{xre})		
	30°	45°	30°	45°	30°	45°
Zeitoun et al. (1970)				*3.48*	*3.33*	*3.28*
Roberts et al. (1997)			*2.40*			
Ferrari and Querzoli (2004)		*3.23*	*2.78*			
Cipollina et al. (2005)	*3.03*	*2.82*	*2.25*			
Nemlioglu and Roberts (2006)	*3.30*	*3.20*	*3.25*			
Kikkert et al. (2007)	*3.17*	*3.31*	*2.78*			
Shao and Law (2010) $0.10 \leq H_0/l_m \leq 0.15$	*2.88*					
Shao and Law (2010) $H_0/l_m > 0.15$	*3.00*					
Shao and Law (2010) $H_0/l_m > 0.05$		*2.83*				
Papakonstantis et al. (2011a)		*3.16*	*2.75*		*3.78 ± 0.16*	*3.57 ± 0.10*
Lai and Lee (2012)	*3.17*	*3.32*	*2.81*			
Bashitialshaaer et al. (2012)	*3.12*	*3.12*	*2.66*			
Oliver et al. (2013)	*3.08*	*3.13*	*2.76*	*4.34*	*4.29*	*3.96*
Crowe et al. (2015)	*3.56 ± 0.05*	*3.43 ± 0.09*	*2.93 ± 0.06*	*4.43 ± 0.10*	*4.56 ± 0.10*	*4.11 ± 0.09*
Literature Average	*3.15 ± 0.20*	*3.16 ± 0.20*	*2.74 ± 0.27*	*4.15 ± 0.45*	*3.94 ± 0.48*	*3.69 ± 0.34*
Present Study	***2.96 ± 0.11***	***3.09 ± 0.07***	***2.52 ± 0.07***	***4.06 ± 0.13***	***4.38 ± 0.12***	***3.81 ± 0.12***
MRBF model, Crowe et al. (2016)	*2.96*	*3.10*	*2.70*	*3.94*	*4.10*	*3.71*

5.3.2.3 Path distance to maximum height and return point

The path distance measured along the centreline trajectory has rarely been reported by previous studies. Figure 5.14 plots the path distance to the two reference points of concern from the present study and from Crowe (2013) and Oliver (2012). The measurements are fairly consistent with one another. In particular the present study compares well with Oliver (2012) where all values are within 6% of the each other. Crowe (2013) provides values that are relatively higher where differences of up to 13% exist. The path distance represents an important parameter as it can be used as an indicative measure of the level of mixing that has taken place. Zeitoun et al. (1970) used this reasoning to conclude that 60^o was the optimum source angle. The path length was not explicitly calculated, however it was inferred that 60^o discharges resulted in the longest path length by taking the product of z_{me} and x_{re} for each angle. Figure 5.14 confirms this assertion where 60^o results in the longest path length at the return point. At the maximum height, the path length for 60^o experiments are only slightly longer than 45^o across all studies included in Figure 5.14. The relationship between path length and dilution proposed in Zeitoun et al. (1970) is subsequently confirmed in Section 5.5 where 60^o discharges result in the highest dilution.

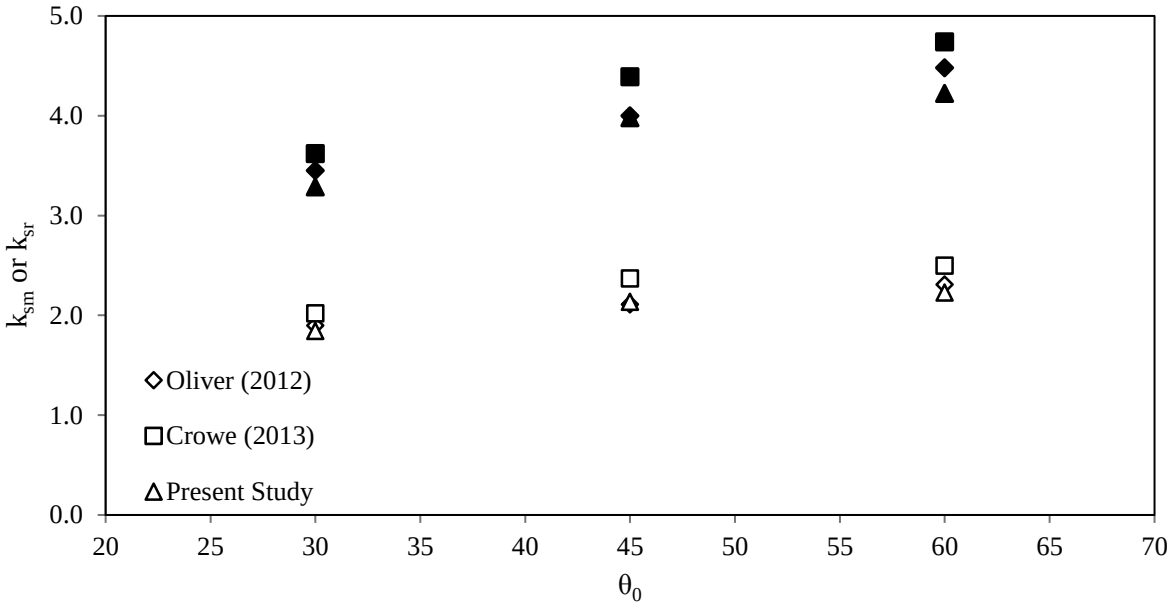

Figure 5.14: Path length to centreline maximum height (k_{sm}, empty symbols) and return point (k_{sr}, filled symbols) as a function of discharge angle (θ_0).

5.4 Concentration Profiles and Spread

5.4.1 Concentration Profiles

Figure 5.15a – c show concentration profiles obtained from three experiments, each at a different source angle. Profiles from three different positions along the flow path have been selected, that is; near the source discharge, near the maximum height and near the return point. The radial axis of the cross-section has been non-dimensionalised using the outer spread parameter (b_c), while concentration values are non-dimensionalised using the centre-line concentration (C_m) value. The outer spread parameter is defined as the distance from the centreline concentration to the point corresponding to $e^{-1}C_m$ above the centreline (or one standard deviation away from the maximum concentration) along a cross-section perpendicular to the flow direction. Due to the asymmetry of inclined negatively buoyant flows, the outer side of the flow is used exclusively to determine the flow spread. This definition of spread has been used by both Kikkert et al. (2007) and Oliver et al. (2013). Lai and Lee (2012) used an alternate method where the spread was defined as the point where $0.25C_m$ occurs. The behaviour exhibited in Figure 5.15 has frequently been reported in the literature. Near the source (within the jet region), each profile is predictably Gaussian as buoyant instabilities have little influence. Further along the flow path, profiles exhibit a distinct asymmetry where the inner edge of the flow deviates from the Gaussian profile, while the outer edge of the cross-section maintains its original form. Figure 5.15b and c appears to show a slight reduction in concentration near the outer edge of the recorded flow and an increase in concentration towards the centre line in comparison with the theoretical Gaussian profile. Kikkert et al. (2007) attributed this to the stable density gradient in the region of the flow, where mixed fluid lies beneath less dense ambient fluid. In addition, flow curvature within the reversal region may dampen turbulence and inhibit the entrainment process to some extent. In Figure 5.15b and c, at the maximum height and return point respectively, the extent of the asymmetry slightly varies with the discharge angle. In accordance with observations relating to instantaneous flow images in Figure 5.2, flows from shallower source angles appear to maintain their original structure over longer distances than steeper discharges.

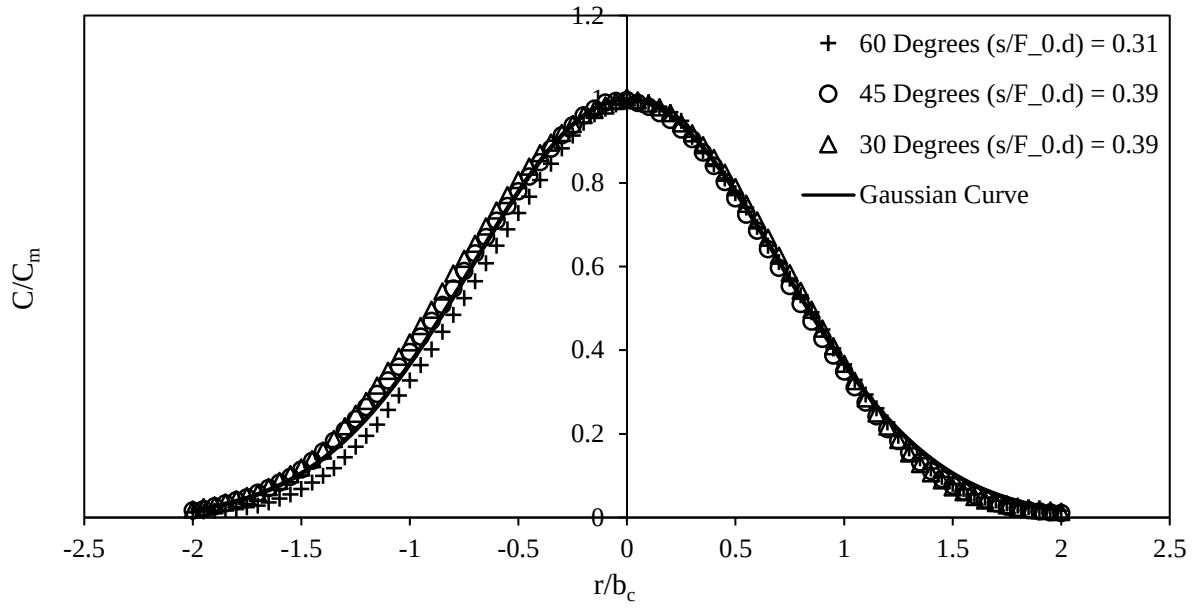

a) Near source.

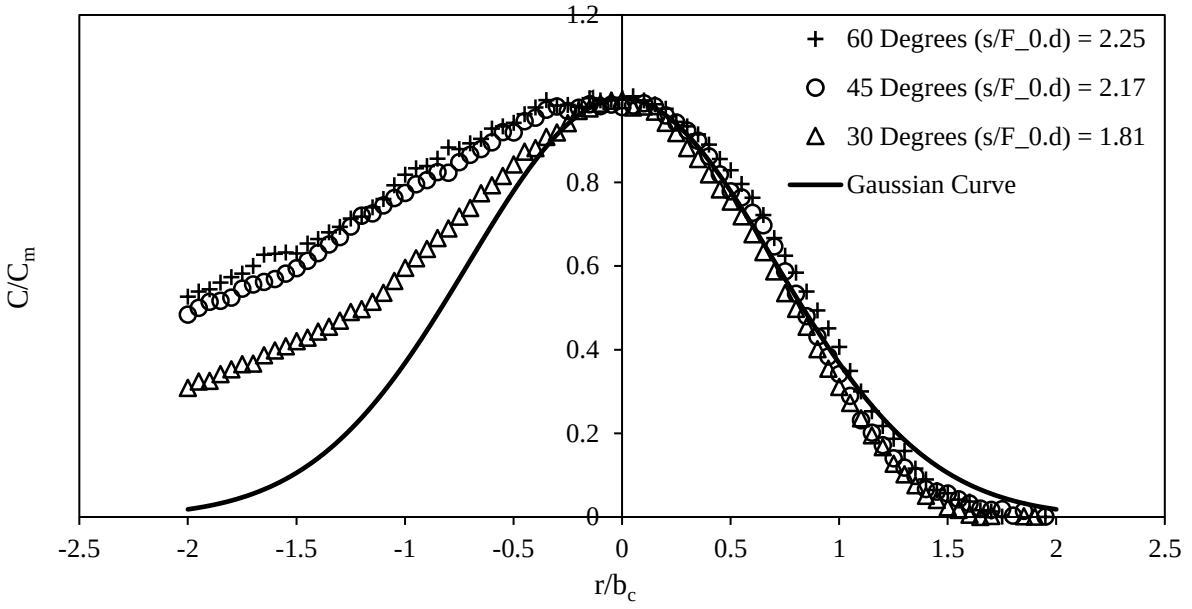

b) Near maximum height.

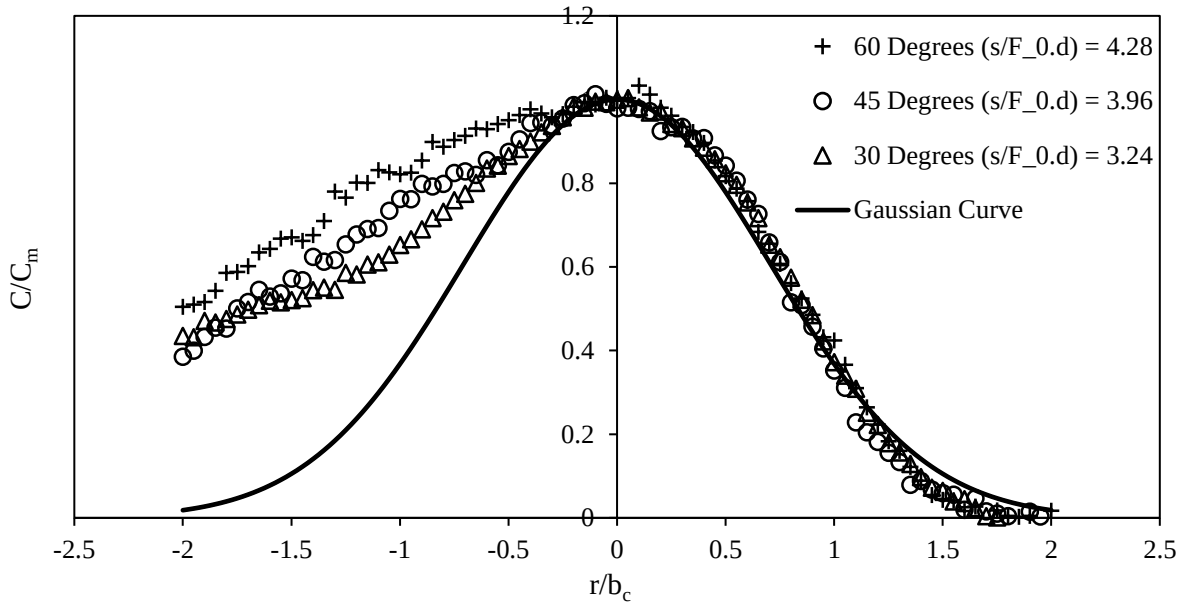

d) Near return point.

Figure 5.15: Concentration flow profiles.

5.4.2 Flow Spread

Figure 5.16a – c plots the outer (b_c) and inner (b_{ci}) spread against centreline path length. The linearity of the outer spread has been confirmed by a number of studies and clearly holds true in Figure 5.16. The spread coefficient (k_{bc}) is determined using a linear best fit line through the outer spread plot and is consistent for the three angles tested. Data points up to the maximum height ($s/F_0 d < 2.2$) have been used to determine the outer spread coefficient due to the scatter that is apparent within the plume region. However, predicted spread values fall within the scatter of the spread data within this region. The spread coefficient from the present study of 0.132 is within 5% of the corresponding value reported in Kikkert et al. (2007) of 0.127. A more significant discrepancy is evident when compared with Lai and Lee (2012) (k_{bc} = 0.123). This is lower than Kikkert et al. (2007) and the present study, however the expectation based on their criteria (b_c corresponding to $0.25C_m$) is that their spread coefficient should be higher. Oliver (2012) reported that the spreading rate subtly decreases upon approach to the maximum height, citing that the formation of eddies may be inhibited

due to the stable density gradient along the outer side of the flow. No such change is evident in the present study.

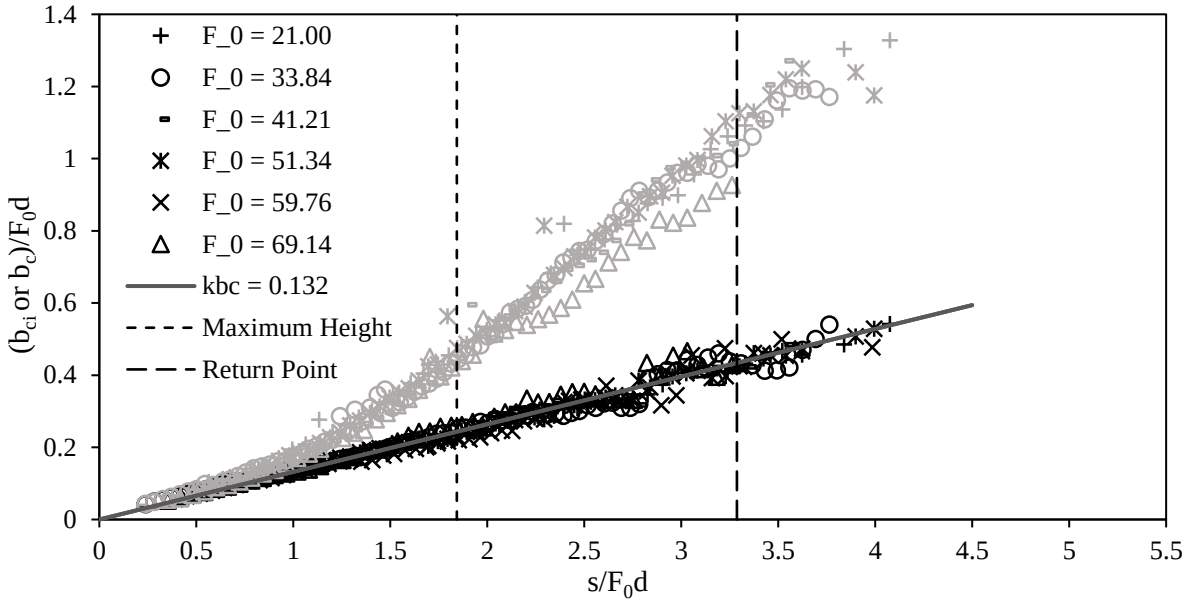

a) 30º discharges.

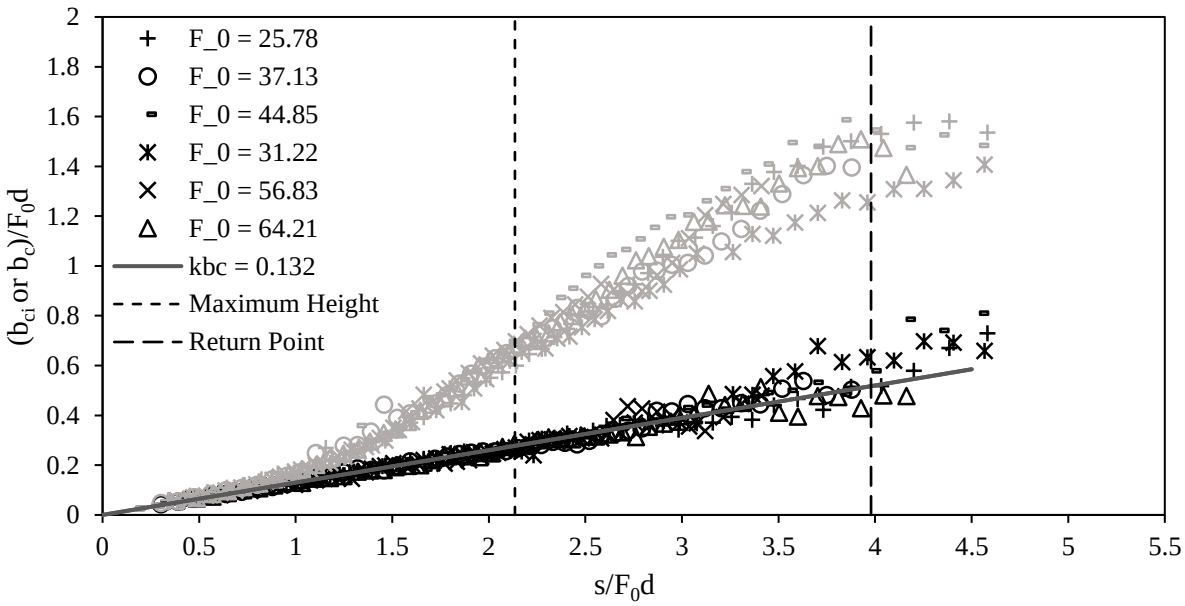

b) 45º discharges.

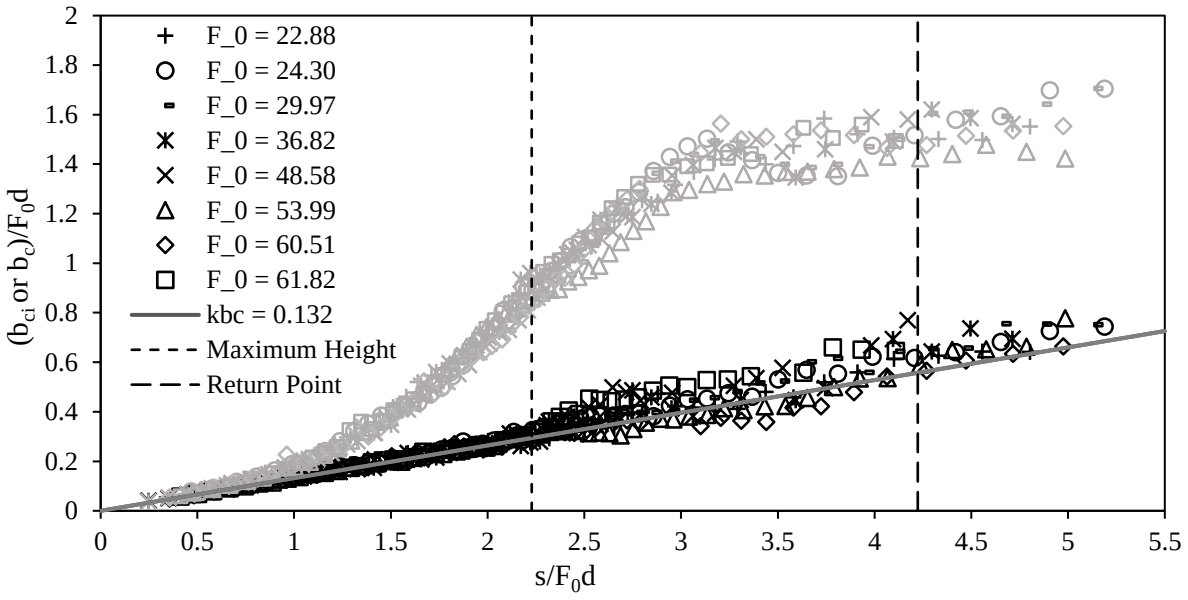

c) 60° discharges.

Figure 5.16: Spread development along the path length. Outer spread values (b_c) represented by black symbols and inner spread values (b_{ci}) are represented by grey symbols.

Due to the linearity exhibited on the outer side, it is more common to characterise the flow spread based on this region alone. The inner spread has also been included in Figure 5.16 to illustrate the non-linear development of the flow in this region. Very few studies have looked at the inner spread and only Crowe et al. (2015) provides data that is comparable to Figure 5.16. Near the point of discharge, the spread growth between the inner and outer sides of the flow is almost the same. At approximately $s/F_0d = 0.8$, the inner spread begins to diverge and its growth is accelerated due to the influence of buoyant instabilities from the unstable density gradient. Beyond a certain distance the spreading rate appears to decrease and stabilise towards a linear rate. The behaviour of the inner spread highlights two points of interest; the location where the data first diverges from the outer spread measurements and the point at which the inner spreading rate noticeably reduces. These two points are referred to as k_{s1} and k_{s2} respectively. Figure 5.16 shows that the initial point of divergence (k_{s1}) is the same for each angle ($s/F_0d = 0.8$). A similar observation was made in Crowe et al. (2015) however this point occurred further along the flow at approximately $s/F_0d = 1.0$. Between k_{s1} and k_{s2}, where the inner spread growth is accelerated, the corresponding

gradient exhibits dependence on the discharge angle. Buoyant instabilities are more prominent for steeper discharge angles thereby resulting in a faster spreading rate along the inner side of the flow. The location where k_{s2} occurs was estimated by applying linear best fit functions to the appropriate plot region and observing where the data diverges from the line. Identifying k_{s2} proved difficult for 30° and 45° discharges due to the lack of data beyond the perceived change in spread rate and the overall consistency of the data. In contrast, a clearer depiction of this behavioural change is apparent for the 60° case. Locations for $k_{s2}(30^o)$ and $k_{s2}(45^o)$ are similar while $k_{s2}(60^o)$ is situated further upstream. The position of k_{s2} is not explicitly stated in Crowe et al. (2015) however visual estimates have been taken. These results are within the vicinity of values from the present study and also demonstrate the same relationship with the discharge angle where the position of k_{s2} for 30° and 45° discharges is similar while for 60° discharges, k_{s2} occurs earlier along the flow path. The spread data in Crowe et al. (2015) is more comprehensive and provides a convincing case for the observed relationship between k_{s2} and the discharge angle. The reduction of the inner spreading rate implies that the effects of buoyant instabilities are no longer as significant. This suggests that the flow is oriented vertically downwards so fluid is no longer being detrained. With respect to the location of k_{s2}, these observations are consistent with the fact that for steeper source angles, the buoyancy (vertical motion) is more dominant and hence the reduction of the inner spreading rate would occur earlier along the flow path. A summary of this analysis is given in Table 5.3.

Table 5.3: Summary of inner spread characteristics from the present study and Crowe et al. (2015).

	Present Study			Crowe et al. (2015)	
	k_{s1}	k_{s2}	Spread Rate $k_{s1} < s/F_0 d < k_{s2}$	k_{s1}	k_{s2}
30°	*0.80*	*3.51*	*0.45*	*1.00*	*3.26*
45°	*0.80*	*3.50*	*0.54*	*1.00*	*3.24*
60°	*0.80*	*3.02*	*0.67*	*1.00*	*2.99*

5.5 Dilution

5.5.1 Centreline Dilution

The following section investigates time-averaged concentration fields of INBJ's and quantifies the centreline or minimum dilution achieved along the centreline flow path. Figure 5.17 shows a time-averaged concentration field of a 30° INBJ. Upon discharge, the high velocity turbulent flow entrains and mixes with clean ambient fluid thereby reducing its concentration. Detrained fluid is clearly visible in Figure 5.17 and is represented by the elongated concentration contours on the inner side of the discharge.

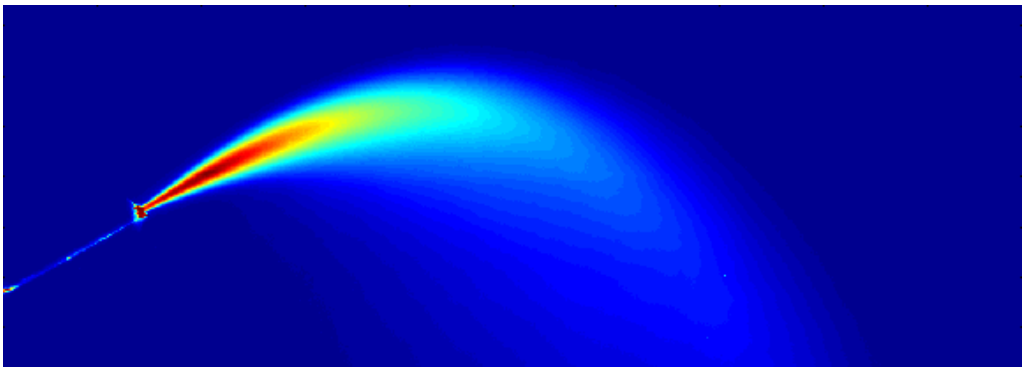

Figure 5.17: Time-averaged concentration field, 30° discharge, F_0 = 21.00, Re = 3499.

The concentration or dilution along the centreline is of particular interest. Dilution also displays a dependence on the Froude number (Kikkert et al., 2007; Oliver et al., 2013), which is used to collapse each data set when presented in the following manner; $C_0/C_m F_0$. This is illustrated in Figure 5.18a - c where the centreline dilution is plotted against the flow path ($s/F_0 d$) for the three discharge angles. The average path lengths to the maximum height and return point are also included. Data prior to the maximum height is very consistent, which is expected because this consistency is an inherent part of the data quality assurance process (as per Section 3.5.2). Beyond the maximum height the data sets remain consistent, but there is a slight increase in scatter. For 30° experiments the variability between data sets is more

considerable. However on closer inspection, only one experiment (F_0 = 59.76) appears slightly out of place.

The noticeable increase in the rate of dilution (at approximately s/F_0d = 2.20 for each angle) represents the transition from jet to plume like flow and occurs after the flow reversal. While our understanding of the jet region is relatively well established, the same cannot be said with regards to the plume like characteristics of the descending arm of the flow. As noted previously, many integral models cannot account for the detrainment of fluid driven by buoyant instabilities and therefore under-estimate the dilution rate in this region. In these models, the dilution rate is a function of the relative contribution of the initial momentum flux imparted to the discharge (M_0) and the buoyancy generated momentum flux (M_B). As the buoyancy generated momentum grows, the dilution rate asymptotically approaches the pure plume solution given in Equation 5.5 where k_{pc} = 11.1 (Wang and Law, 2002).

$$\frac{C_0}{C_m F_0} = \left(\frac{z}{F_0 d}\right)^{5/3} \frac{1}{k_{pc}\left(\frac{\pi}{4}\right)^{2/3}} \qquad 5.5$$

Equation 5.5 assumes the plume is discharged vertically or alternatively the fluid has moved sufficiently far from the source that the dilution is a function of 'z'. The model presented in Kikkert et al. (2007) adopted the plume dilution rate when the buoyancy generated momentum flux matched the initial momentum flux. Oliver (2012) compared Equation 5.5 with the plume region of 45^o discharge experiments (replacing 'z' with 's') and found that the dilution rate could only be captured by changing k_{pc} to 9.9. Figure 5.19 displays the dilution recorded beyond the jet region for each angle tested. While each plot lies close to each other, distinctions between the data sets are somewhat evident and appear to be related to the corresponding discharge angle. Within the plume region, steeper discharge angles generally display higher centreline dilutions for a given path distance. This observation can be attributed to the relative intensity of buoyant instabilities and by extension, the accelerated spread rate between k_{s1} and k_{s2} along the inner side of the flow. The associated dilution rate in the plume region can be used to characterise differences between the data sets. Although plume flows do not have a linear dilution rate, the data in Figure 5.18 suggests that the dilution rate within the plume region can be approximated as linear. The relationship between

the dilution rate and the accelerated inner spreading rate between k_{s1} and k_{s2} is demonstrated in Table 5.4 where these values have been tabulated for each discharge angle.

Table 5.4: Dilution rate within the plume region and inner spread rate between k_{s1} and k_{s2}.

	Dilution Rate, Plume Region	Inner Spread Rate $k_{s1} < s/F_0 d < k_{s2}$
30°	*0.54*	*0.45*
45°	*0.58*	*0.54*
60°	*0.60*	*0.67*

Within the flow region considered, it is clear that some correlation exists between the dilution rate and the flow angle. However, if the flow far from the source is considered, where the discharge is predominantly oriented vertically, buoyant instabilities no longer exist as a flow feature (i.e. $s/F_0 d >> k_{s2}$). In this region it is expected that the dilution rate will be independent of the inclination at the source and resemble the plume solution from Equation 5.5. It should be noted that these observations are limited to the discharge inclinations tested (30°, 45° and 60°) and cannot be generalised beyond this angle range. For example source angles steeper than 80° are susceptible to re-entrainment (Ferrari and Querzoli, 2010) where fluid from the falling arm of the flow is entrained back into the ascending arm. The effects of this feature are likely to be reflected in dilution measurements.

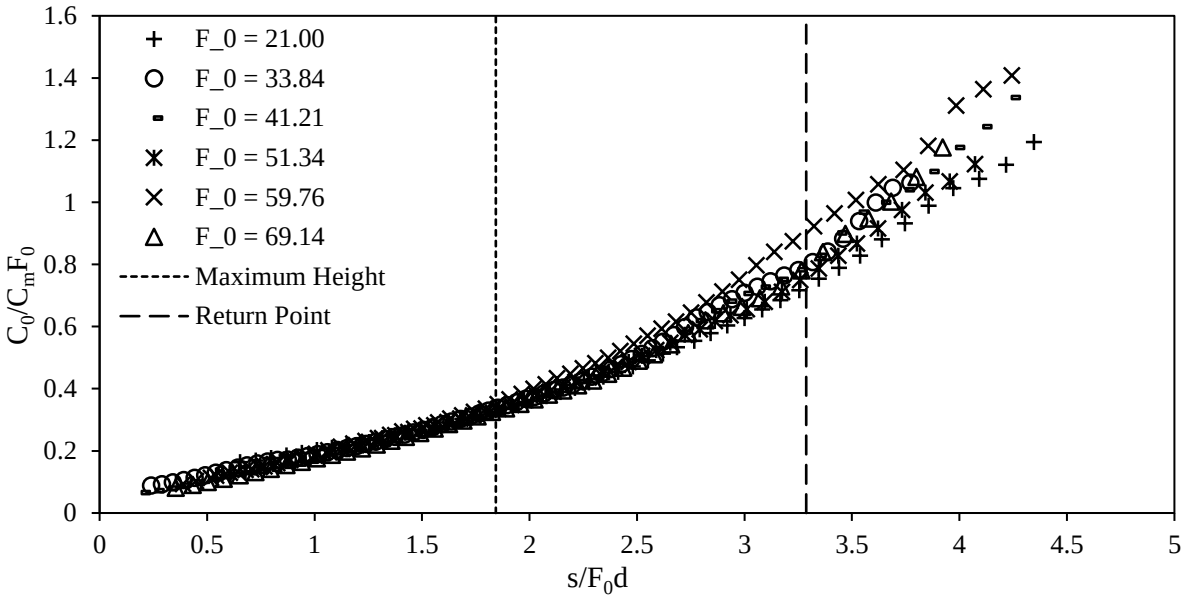

a) 30° discharges.

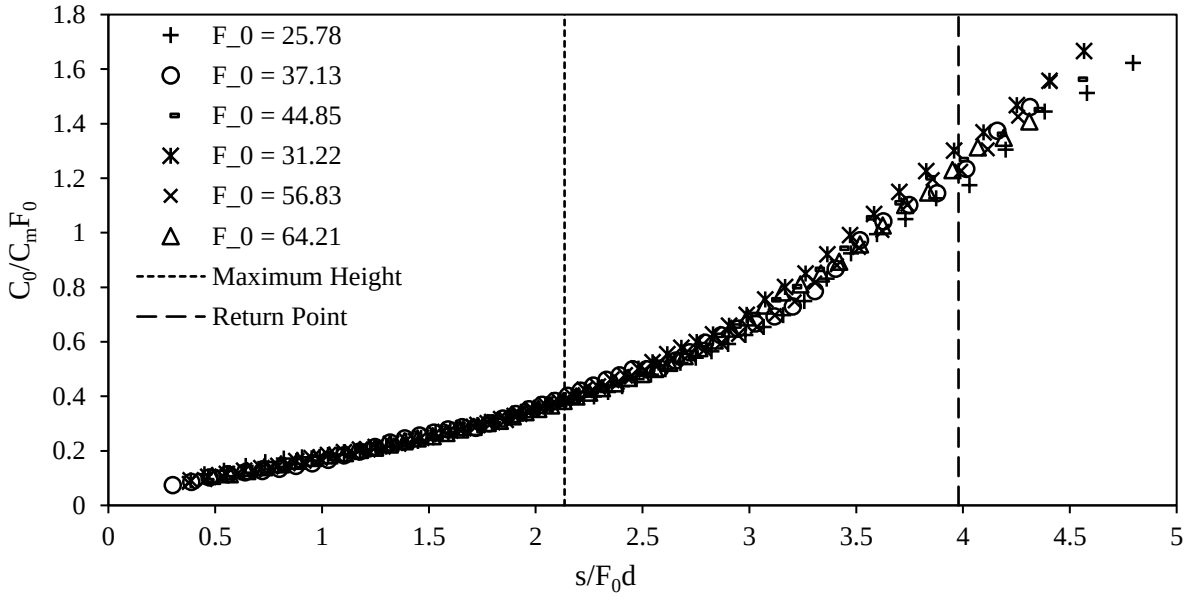

b) 45° discharges.

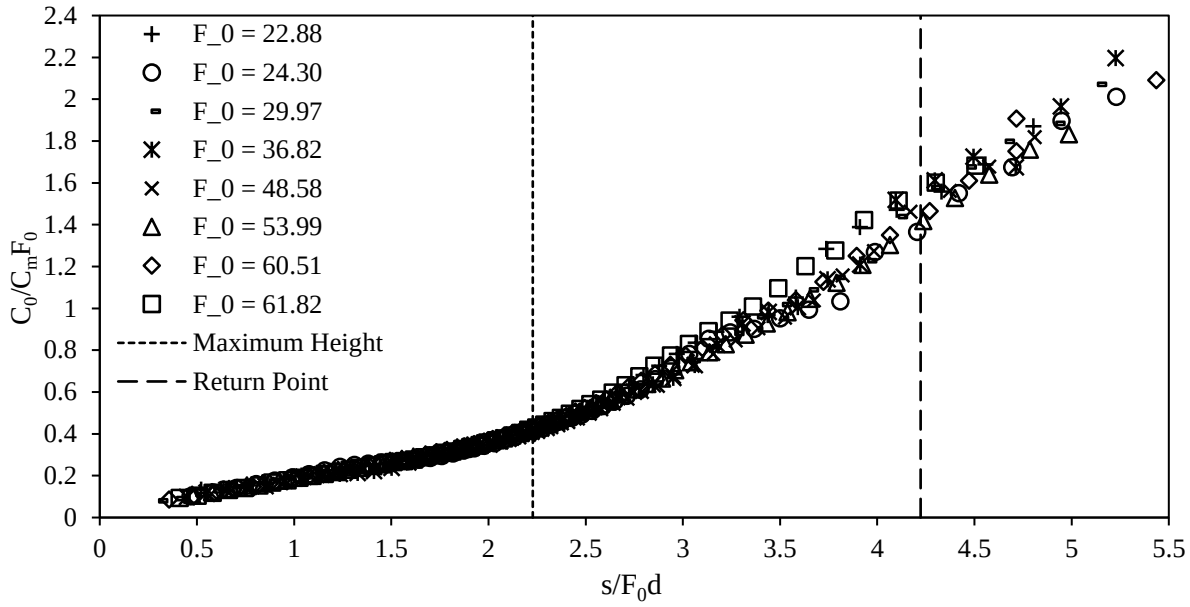

a) 60° discharges.

Figure 5.18: Centreline dilution along the path length for each angle tested.

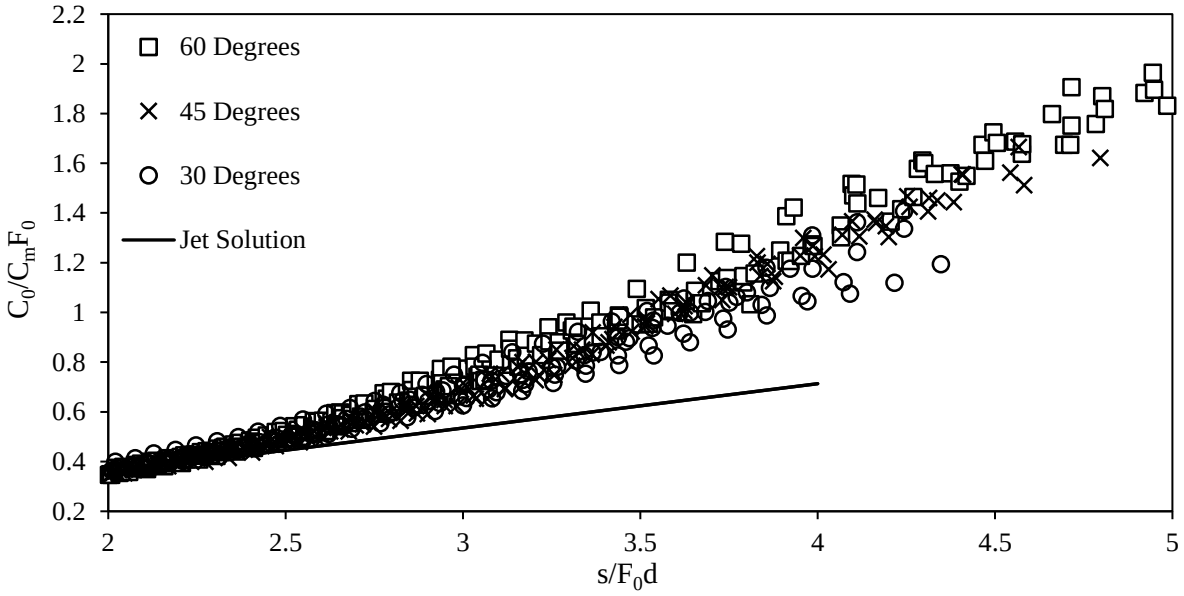

Figure 5.19: Centreline dilution within the plume region for each angle tested.

5.5.2 Comparisons with Other Studies

Similar to the geometric results, dilution values at the maximum height (C_0/C_{ma}) and at the return point (C_0/C_r) have been obtained. As illustrated in Figure 5.18a – c the dilution can be collapsed by scaling measurements with the Froude number. The linear dependence on the Froude number is displayed in Figure 5.20 and Figure 5.21 where the centreline dilution at the maximum height and return point for 30º, 45º and 60º discharge inclinations have been plotted. Comparisons with other studies have been made using the collapsed version of these measurements that is;

Dilution at maximum centreline height (S_m):

$$\frac{C_0}{C_{ma}F_0} = S_m(\theta_0) \qquad 5.6$$

Dilution at return point (S_r):

$$\frac{C_0}{C_rF_0} = S_r(\theta_0) \qquad 5.7$$

The discrepancies between dilution values in the literature have been well documented by Oliver et al. (2013) who in part attributed this to differing lower boundary conditions. Many studies have justified the placement of the boundary due to its practical significance citing cases where discharges are released close to the seabed. Unfortunately these studies have not discussed the extent to which the boundary has affected the mixing potential of the flow or considered how to incorporate the boundary into a modelling framework. Comparisons presented in Oliver et al. (2013) clearly suggest that the mixing potential of the flow is reduced when the lower boundary is present. This issue is important, but in order to effectively model these flows, it is necessary to first understand the case where lower boundary effects can be ignored. For this reason return point dilutions have only been compared with Oliver et al. (2013) and the MRBF model. Results from other studies are discussed more closely in Chapter 6, where boundary effects are imposed on the flow. At the maximum height it is less likely that mixing is affected by the boundary, therefore all studies are included in the discussion of this parameter.

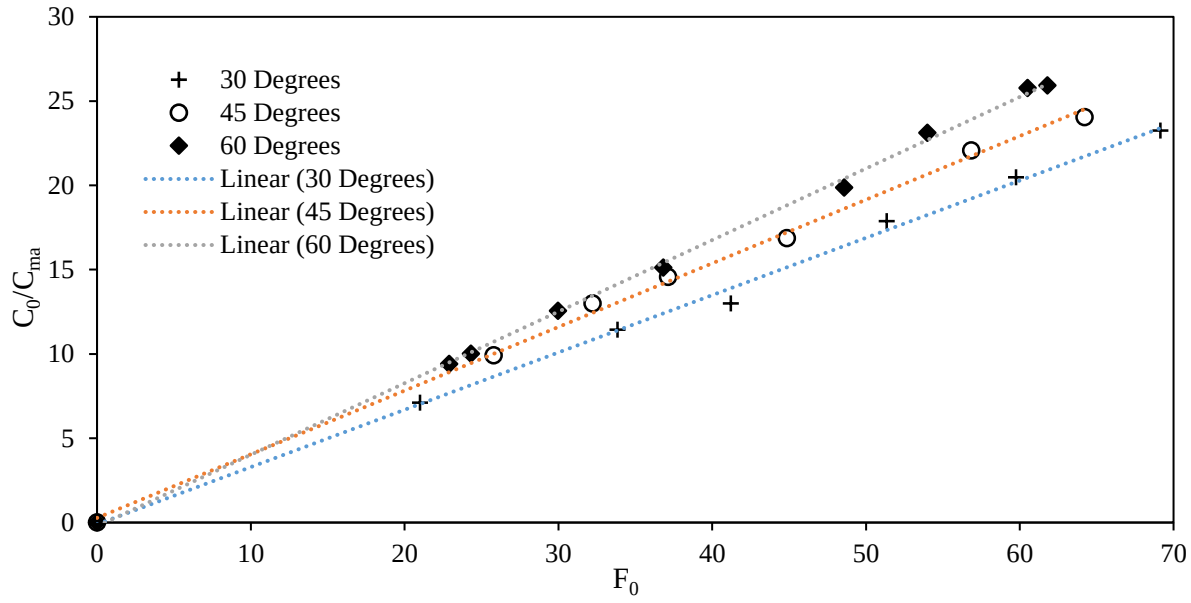

Figure 5.20: Centreline dilution at maximum height against Froude number.

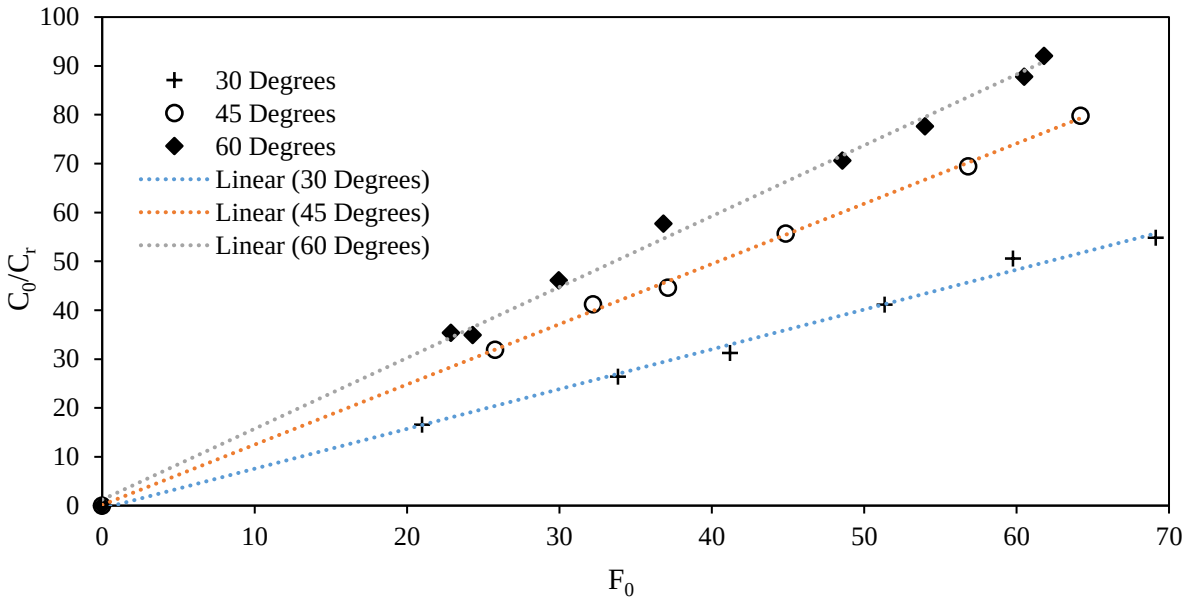

Figure 5.21: Centreline dilution at return point against Froude number.

5.5.2.1 Dilution at Maximum Height

Table 5.5 features the dilution at the maximum height from previous studies and the present study. Due to the limited number of studies that have measured concentrations, outliers have not been excluded. With the exception of 30^o tests, past results are relatively close to one another with error percentages of below 20% (calculated from standard deviations). 30^o results from Shao and Law (2010) are significantly higher than the remaining data points and heavily influence the average literature value and standard deviation. Removing these results dramatically reduces this value to 0.37 ± 0.03. Oliver (2012) cited issues with determining the centreline as the reason for the high dilution values in this study. If the concentration was in fact taken from either side of the actual centreline point (along the radial axis) then dilutions would be amplified. However, the corresponding centreline maximum height (k_{zm}) is well within estimates from other researchers so it is unlikely that this would be the sole cause. Results from the present study are slightly lower than the average literature values however are consistent with Oliver et al. (2013). It is improbable that differences between the present study and the remaining literature can be attributed to boundary influences as flow confinement would reduce the level of mixing that takes place. Excluding Shao and Law (2010), the literature displays a positive trend between nozzle angle and maximum height dilution. This result is intuitive given that the dilution is a function of path length, which is also shown to increase with the discharge angle (Figure 5.10 and Figure 5.11). Predictions from the MRBF model are close to the present study for 30^o and 45^o, however for 60^o discharges the predicted dilution decreases to the same value as 30^o inclinations. This result is not consistent with the model's trajectory predictions where 60^o flows have the longest path length to the maximum height. Crowe et al. (2016) attributes the decrease in S_m for steep angles to the rapid loss in momentum near the maximum height (while spread rate remains constant), resulting in a reduced dilution rate over a short distance of the flow path. It was noted that this issue was not limited to the MRBF model but all integral formulations that use a constant spread assumption, especially when steeper angles are being modelled ($> 60^o$).

Table 5.5: Centreline dilution at the maximum height from the literature and the present study.

	Dilution at Max Height (S_m)		
	30°	45°	60°
Zeitoun et al. (1970)	*0.36*		*0.56*
Roberts and Toms (1987)			*0.38*
Lane-Serff et al. (1993)		*0.42*	
Papakonstantis et al. (2011b)		*0.52 ± 0.05*	*0.56 ± 0.05*
Shao and Law (2010) $0.10 \leq H_0/l_m \leq 0.15$		*0.46*	
Shao and Law (2010) $H_0/l_m > 0.15$	*0.62*		
Shao and Law (2010) $H_0/l_m > 0.05$	*0.66*		
Lai and Lee (2012)	*0.40 ± 0.01*	*0.45 ± 0.05*	*0.44 ± 0.05*
Oliver et al. (2013)	*0.34*	*0.39*	*0.42*
Average	*0.48 ± 0.15*	*0.45 ± 0.05*	*0.47 ± 0.08*
Present Study	***0.34 ± 0.01***	***0.39 ± 0.01***	***0.42 ± 0.01***
MRBF model, Crowe et al. (2016)	*0.35*	*0.38*	*0.35*

5.5.2.2 Dilution at the Return Point

As noted previously, due to the issues surrounding the setup of previous experimental programs, return point dilution comparisons have been limited to results from Oliver et al. (2013) and predictions from the MRBF model. Table 5.6 presents the results from each study. The largest discrepancy between the data relates to 30° inclinations where the MRBF model predictions are 10% higher than present study. The remaining dilution values all exhibit good consistency and are within 5% of each other. This result is important as it illustrates that the mixing rate near the return point is faster as a result of the boundaries exclusion. Oliver et al. (2013) demonstrated this using the dilution ratio (S_r/S_m).

Table 5.6: Centreline dilution at the return point from the literature and the present study

	Dilution at Return Point (S_r)		
	30°	45°	60°
Oliver et al. (2013)	*0.84*	*1.22*	*1.55*
Present Study	***0.80 ± 0.03***	***1.24 ± 0.03***	***1.49 ± 0.05***
MRBF model, Crowe et al. (2016)	*0.88*	*1.22*	*1.50*

The dilution ratio removes potential issues with regards to calibration and provides an indicative measure of the dilution rate between the maximum height and return point. Oliver et al. (2013) shows that in comparison to other studies the dilution ratio was consistently higher for all angles tested. This parameter is discussed further in Chapter 6 where dilution ratios have been explicitly calculated from past studies and compared with the present study. With reference to the studies included in Table 5.7, the only noticeable inconsistency applies to the MRBF model prediction for 60^o inclinations where the dilution rate has been over-estimated in comparison with experimental estimates. This reflects the conservative nature of the models dilution prediction at the maximum height for this discharge angle. Dilution ratios between the two experimental studies are generally consistent.

Table 5.7: Dilution Ratio from the literature and the present study

	Dilution Ratio (S_r/S_m)		
	30^o	45^o	60^o
Oliver et al. (2013)	*2.47*	*3.13*	*3.69*
Present Study	***2.36***	***3.20***	***3.58***
MRBF model, Crowe et al. (2016)	*2.53*	*3.22*	*4.28*

5.6 Summary

Previous analysis from Oliver et al. (2013) suggested that the behaviour of INBJ's was different if the lower boundary was completely removed. To date this study represents the only experimental program to have measured concentration fields where boundary influences are removed from the measured flow field. To verify the assertions made in this study, an independent series of experiments has been carried out using the same experimental conditions. Experiments were conducted for three discharge angles (30^o, 45^o and 60^o) and the flow behaviour was quantified using mean geometric and dilution parameters extracted from time-averaged concentration fields. Measurements at key reference points were presented (maximum rise height and return point) and the quality of the data was scrutinised through comparisons with past studies in the literature. Geometric coefficients were largely consistent with the literature at the maximum height while greater variability was observed for return

point measurements. Boundary influences are more likely to affect the flow structure near the return point, however comparisons with studies where the boundary was included did not indicate any systematic changes to the flow geometry. Buoyant instabilities were explored using perpendicular concentration profiles and more notably using the lateral spread along the inner and outer sides of the flow. The behaviour of inner spread measurements in comparison to the outer spread provides new insight into the flow structure and clearly illustrates the asymmetry of this flow configuration. The increasing intensity of buoyant instabilities for steeper discharge angles was reflected in the spread rate measured along the inner side of the flow. These observations were also related to dilution measurements along the flow centreline where the inner spreading rate correlated well with the dilution rate within the plume region of the discharge. For a given path length, steeper discharge angles provide higher dilution values. Dilution comparisons were predominantly limited to the maximum height as return point dilutions from past studies were shown to exhibit significant variability. Experimental data from Oliver et al. (2013) provided the most relevant comparison due to similarities in experimental setups (i.e. no lower boundary) and were relatively consistent with the present study. Overall the results obtained from this series of experiments validates the reliability and repeatability of the experimental processes and provides new insight into the implications of buoyant instabilities and the dilution potential of the flow without boundary influences. The discussion on boundary influences is presented in the subsequent chapter where the boundary is investigated in detail.

Chapter 6 Boundary Interaction of Inclined Negatively Buoyant Jets

Evidence from numerous studies suggests that the inclusion of a lower horizontal boundary within the measured region of the negatively buoyant jet alters the flow behaviour significantly in the vicinity of the solid surface. While this aspect has not been explicitly dealt with in the literature, the lack of consensus between dilution results from different studies implies that an improved understanding of the influence of this boundary condition would assist in the interpretation of these discrepancies. Experimental studies where lower boundary effects are present, have focused their efforts on obtaining geometric and dilution coefficients rather than assessing potential changes in flow behaviour as a result of the boundaries presence. Results in Chapter 4 indicate that mixing is inhibited as the flow approaches the boundary due to the lack of clean ambient fluid available for entrainment into the main flow. Centreline dilutions were shown to reflect this observation where measured values became constant at a specific location above the lower boundary. Similar behaviour near the boundary is expected for the current flow scenario. Return point conditions are naturally more susceptible to lower boundary influences and dilutions measured at this location exhibit the greatest amount of variation in the literature. This chapter explores the issue of boundary influence for INBJs through a series of experiments where a raised horizontal platform or lower boundary, is placed within the vicinity of the initial discharge location (initial conditions included in Table B.3 – B.5 of Appendix B). Three source angles (30^o 45^o and 60^o) are considered and the boundary distance below the source or 'source height parameter' (represented in non-dimensional form as $H/F_0 d$) is varied. There has been a conscious shift in focus away from analysing the boundary flow due to the complexity of this region in comparison to the radial pure jet case. This region of the flow is only discussed briefly in a qualitative manner. Emphasis has been placed on investigating boundary influences up to the

impact point and resolving discrepancies between various experimental studies in the literature. Detailed comparisons are made with experiments presented in Chapter 5 (no lower boundary within the measuring area) using geometric and dilution results. This series of experiments is referred to as 'boundary free experiments' throughout this chapter. Dilution results at the return point and impact point from the literature have been included in these comparisons. New dilution and geometric coefficients are introduced to quantify boundary effects in the flow region prior to impact. These parameters are potentially significant in the context of outfall design.

6.1 Flow Configuration

The general characterisation of an INBJ impacting a solid horizontal boundary is depicted in Figure 6.1. In addition to the nozzle diameter (d), discharge Froude number (F_0) and discharge angle (θ_0), this flow configuration requires the source height (H) to be incorporated into the analysis. Different combinations of initial conditions were tested such that the governing boundary parameter ($H/F_0 d$) was varied between 0.058 and 1.84. It should be noted that the term 'source height', 'source height parameter' or 'boundary parameter' in the remainder of the text refers to this non-dimensional variable, unless otherwise specified.

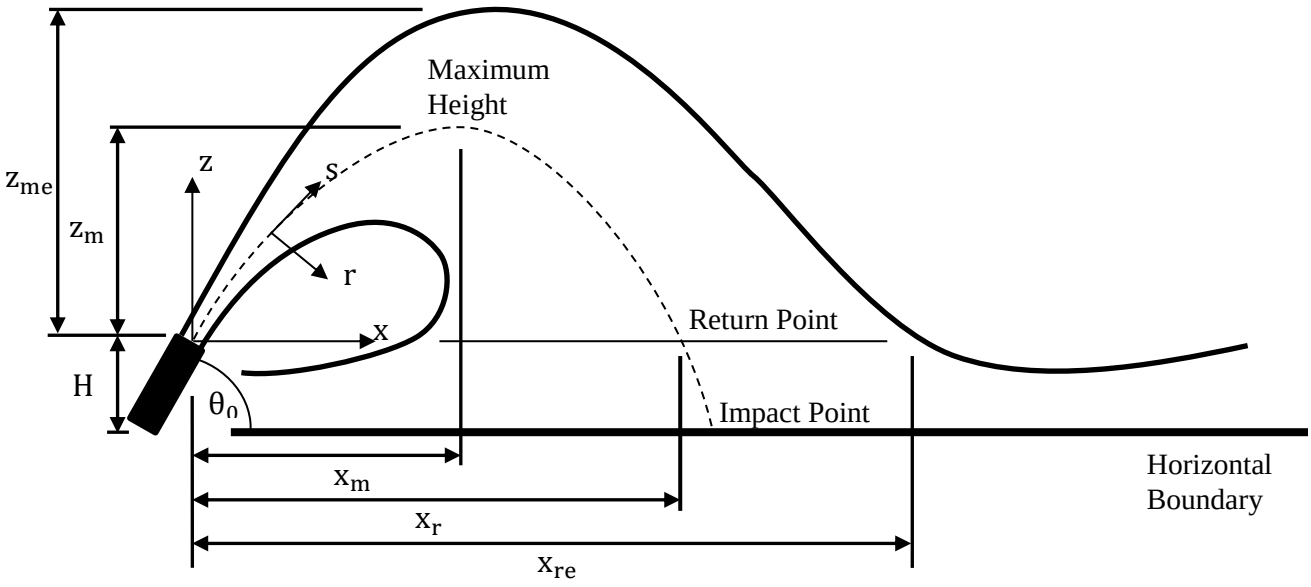

Figure 6.1: Flow configuration of an INBJ released onto a horizontal boundary located within the vicinity of the discharge location.

The experimental configuration employed a combination of the previous setups used for vertical discharges and boundary free INBJ's. The nozzle was inclined at an angle of 30 ^{o}, 45^{o} or 60^{o} and placed at a known height above the raised circular platform (10 – 131 mm). In comparison to the experiments discussed in Chapter 4 and 5, resolving the behaviour of these flows proved challenging, particularly near the boundary. In order to achieve consistent time averaged results, experiments were run for longer durations. This was necessary to account for the larger scale and rapid deceleration of the flow within the impact region which extended the time required to achieve steady state conditions. The initial conditions (F_0, d) were selected to limit the scale of the flow at the impact point and thereby limit the recording time required. Often, this strategy was constrained by the need to ensure that the flow was turbulent upon release and thus Reynolds number independent (i.e. Re > 3000). This problem was resolved by increasing the initial density difference between the source fluid and ambient (i.e. modified gravity term). For a given Froude number and source diameter combination, the initial velocity at the discharge outlet could be increased if the density difference was also raised. Consequently the Reynolds number for each experiment could be set above the specified threshold value.

6.2 Flow Observations

Prior to impact, observations relating to this flow type are similar to the boundary free case. INBJ's discharged into unbounded environments have already been qualitatively discussed in Section 5.2 therefore flow descriptions primarily relate to the impact region and the ensuing boundary flow. Figure 6.2 shows three instantaneous, calibrated concentration fields of this region for 30^{o}, 45^{o} and 60^{o} discharge angles. The relevant initial conditions are included in each figure. As shown, the flow is re-directed in the radial direction with a majority of the flow moving downstream. The amount of fluid directed back towards the discharge nozzle is dependent on the source inclination. Shallower discharge angles resulted in the least amount of backflow due to the relatively large horizontal momentum flux in the direction of the discharge. For some 60^{o} and 45^{o} experiments, discharged fluid near the source appeared to re-entrain the backflow. This observation was particularly noticeable for experiments where the source was positioned close to the boundary. It is unlikely that the dilution of the remaining flow would be significantly affected as the concentration of the backflow relative to the

source fluid, is low. Furthermore results from these experiments were not noticeably different from other boundary experiments where this form of entrainment was not observed. Detrainment from the underside of the jet is clearly evident. As opposed to simply falling out of the viewing area, the boundary interrupts the path of the detrained fluid and it is entrained into the backflow. As expected the ensuing spreading layer, post impingement (moving away from the source) behaves differently to the corresponding pure jet case. The flow along the boundary continued to entrain fluid and spread vertically before collapsing due to buoyancy effects (marking the transition to the far field) and eventually falling off the sides of the platform. The collapse point for inclined negatively buoyant flows was only visible for smaller scale flows and steeper discharge inclinations where the horizontal distance between the flow impact point and the edge of the raised platform was relatively large.

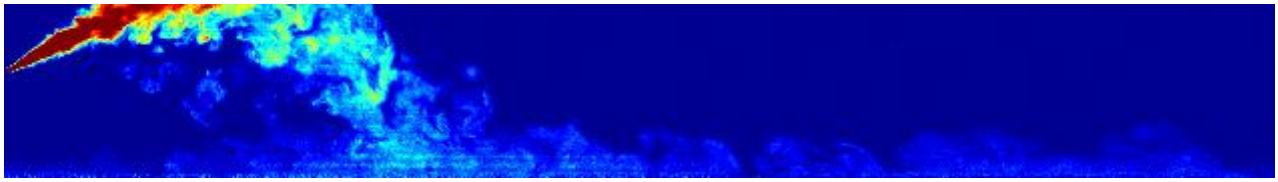

a) 30º discharge, $H/F_0 d = 0.822$, Re = 3598.

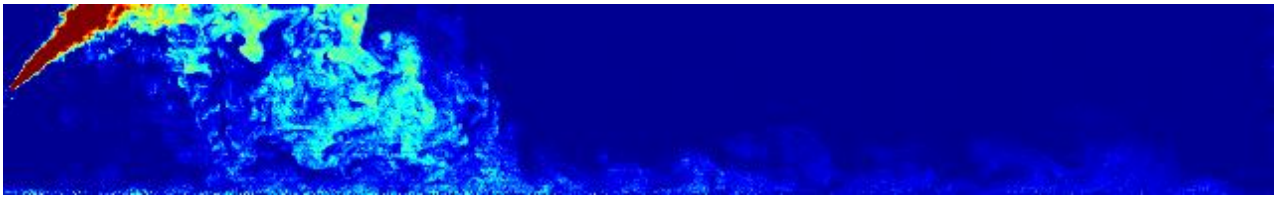

b) 45º discharge, $H/F_0 d = 0.822$, Re = 3611.

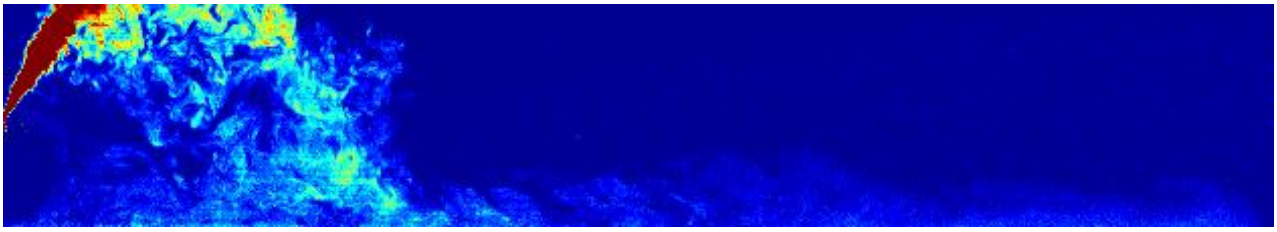

c) 60º discharge, $H/F_0 d = 0.876$, Re = 3387.

Figure 6.2: Instantaneous concentration fields of the impact and boundary regions of an INBJ discharged onto a horizontal boundary.

6.3 Experimental Results

6.3.1 Conditions at Maximum Height

It is generally assumed that the behaviour at maximum height is unaffected as there is no direct interaction between this region of the flow and the lower boundary. To verify this assumption, comparisons between boundary affected and boundary free tests are made using dilution and geometric coefficients obtained at this reference location (Table 6.1). Standard deviations are included alongside each coefficients as well.

Table 6.1: Geometric parameters at maximum height for boundary and boundary free tests.

	Boundary	Horizontal Dist. Centreline Max. Height (k_{xm})	Vertical Dist. Centreline Max. Height (k_{zm})	Vertical Dist. Flow Edge Max. Height (k_{zme})	Path length to Max Height (k_{sm})	Dilution at Max Height (S_m)
30°	*No*	*1.70 ± 0.05*	*0.62 ± 0.01*	*1.14 ± 0.04*	*1.84 ± 0.03*	*0.34 ± 0.01*
	Yes	*1.73 ± 0.05*	*0.63 ± 0.02*	*1.12 ± 0.02*	*1.86 ± 0.04*	*0.33 ± 0.01*
45°	*No*	*1.83 ± 0.07*	*1.11 ± 0.02*	*1.69 ± 0.03*	*2.14 ± 0.02*	*0.39 ± 0.01*
	Yes	*1.78 ± 0.06*	*1.10 ± 0.02*	*1.67 ± 0.03*	*2.13 ± 0.04*	*0.39 ± 0.01*
60°	*No*	*1.51 ± 0.03*	*1.54 ± 0.03*	*2.22 ± 0.04*	*2.23 ± 0.02*	*0.42 ± 0.01*
	Yes	*1.50 ± 0.03*	*1.56 ± 0.02*	*2.22 ± 0.06*	*2.24 ± 0.03*	*0.41 ± 0.01*

There is very little difference between boundary and boundary free tests at the maximum height and any discrepancies between coefficients are within the variability of the data. A similar comparison was performed in Crowe (2013) in which the same conclusion was drawn. For shallow angled discharges with small source heights, Shao and Law (2010) hypothesised that the flow ascent to the maximum height may be affected due to the possibility of Coanda attachment. When these initial conditions are imposed on the flow, there is a significant difference in the volume of ambient fluid on either side of the discharge due to confinement from the boundary. Consequently a pressure differential arises between the outer and inner edge of the flow that may cause the jet to be drawn towards the boundary, thereby inhibiting its vertical trajectory. Shao and Law (2010) found that for 30° inclinations and $H/F_0 d < 0.20$, the slope of the ascending arm of the centreline profile is slightly milder. The vertical distance to the maximum height was however, similar to other 30° tests.

Therefore as a result of the milder trajectory, the corresponding horizontal location was further downstream. In the present study, only a few 30^o experiments were performed at source heights (H/F_0d) below 0.20 and in each instance, no evidence of Coanda effects could be determined from trajectory profiles or geometric coefficients. The centreline trajectory up to the maximum height for 30^o experiments where $H/F_0d < 0.20$, is shown in Figure 6.3. Two additional tests carried out at $H/F_0d = 0.606$ and 1.31 have been included to demonstrate the similar behaviour between these flows. Based on this evidence, Coanda effects or other boundary influences do not affect the flow at the maximum height.

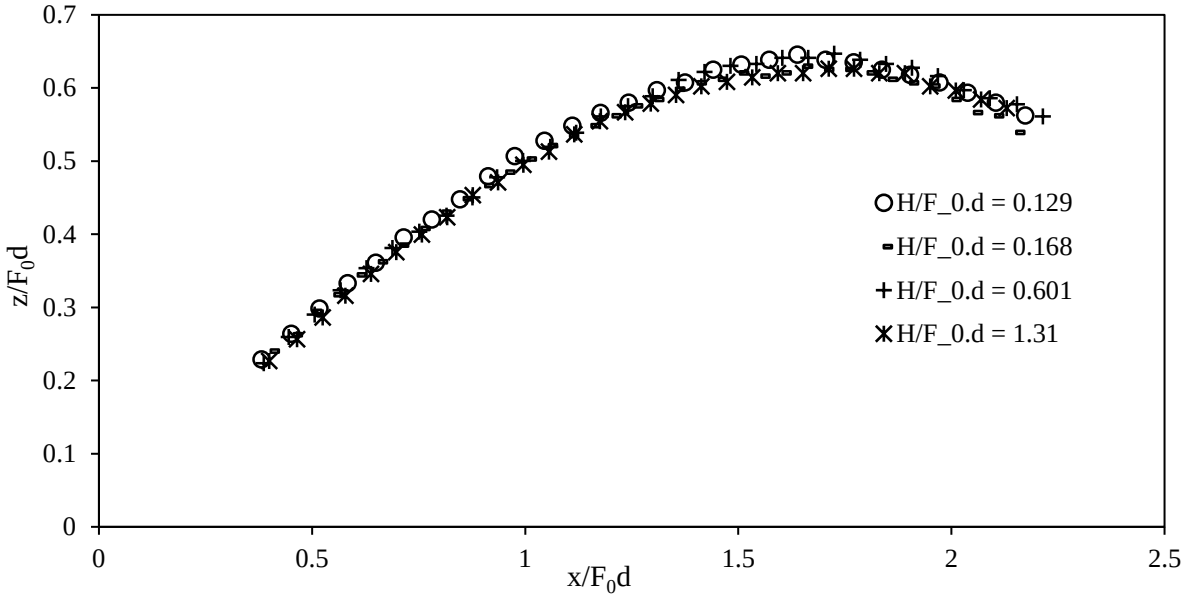

Figure 6.3: Centreline Trajectory of 30^o discharges just beyond maximum height. Source height parameters have been selected to demonstrate the potential of Coanda effects (or lack thereof) in altering the trajectory of flows discharged at smaller source heights

6.3.2 Return point and Impact Region

6.3.2.1 Flow Profiles

Near the boundary the flow undergoes a complex transition from a predominantly vertical flow orientation, to a horizontal spreading layer. This process is qualitatively exemplified using flow profiles (perpendicular to the centreline trajectory) acquired near the boundary.

Figure 6.4 and Figure 6.5 depicts intensity fields and perpendicular flow profiles from mean concentration, intermittency and concentration RMS data for a single experiment with initial conditions of θ_0 = 60°, H/F_0d = 0.876, Re_0 = 3388. Corresponding profiles for 30° and 45° experiments are given in Figure C.1 and C.2 in Appendix C. Each profile is labelled based on the vertical distance of the centreline location (i.e. at r/b_c = 0) from the return point. This labelling system has been adopted so that it is possible to identify where each profile is located on the relevant intensity field provided in Figure 6.4. The outer and inner sides of the flow are represented by the positive and negative radial axis respectively. Due to the physical presence of the boundary, the extent of each profile decreases as cross-sections further along the flow path are considered. Details of a similar region have been discussed in Section 4.3.3 for vertical jets.

Mean concentration profiles in Figure 6.5a only exhibit self-similarity on the outer side of the cross-section. Near the centreline and the inner side of the flow, some profiles include a region where the peak concentration (C/C_m ~ 1) is relatively constant over an extended distance along the cross-section. For example the profile corresponding to z/F_0d = -0.398 remains constant between the radial limits -1.00 < r/b_c< 0.05. This behaviour is an indication that the mixing processes that take place in this region are not as effective in reducing the tracer concentration. This observation is reflected in the intermittency profiles where Figure 6.5b illustrates the decline of this flow property. Intermittency data is based on the same threshold criteria as Figure 4.5c (2.4% of the initial concentration, C_0) where the probability of finding fluid with a concentration less than the threshold is high if highlighted in red and low if blue. Changes to the flow intermittency are particularly evident near the centreline and towards the inner side of each profile where self-similarity is lost. RMS concentration profiles depict additional detail regarding the diminishing mixing ability of the flow near the boundary. The data sets in Figure 6.5c show a progressive reduction in turbulent fluctuations as the flow approaches the boundary. Self-similarity is also lost towards the centreline and inner side of the flow where the profiles diverge.

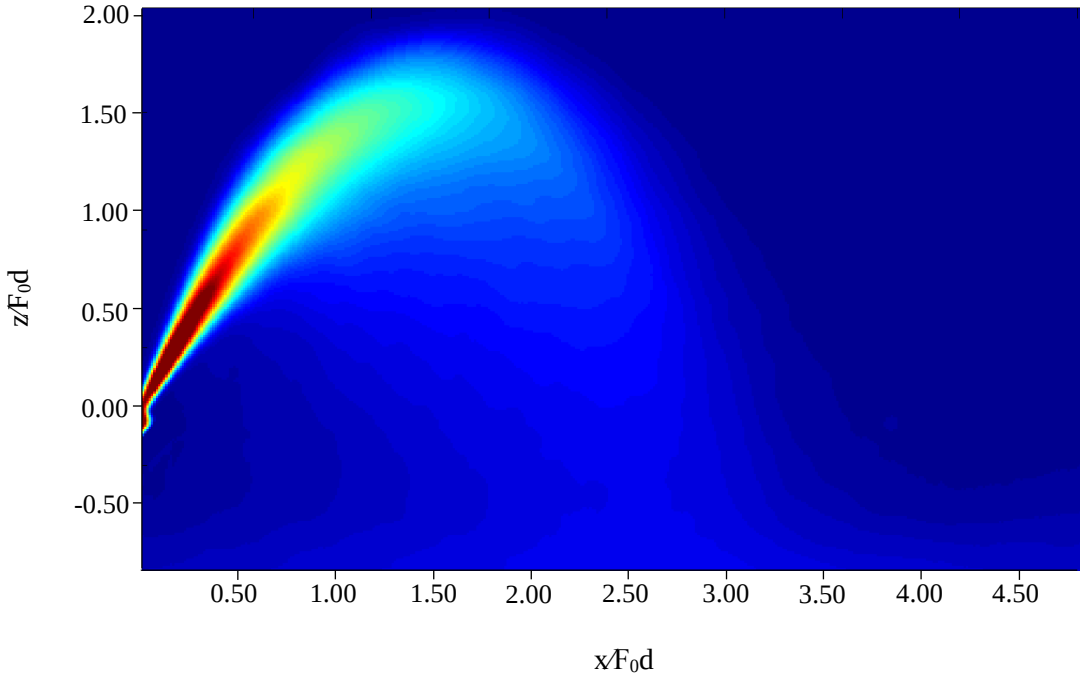

a) Time-averaged concentration field.

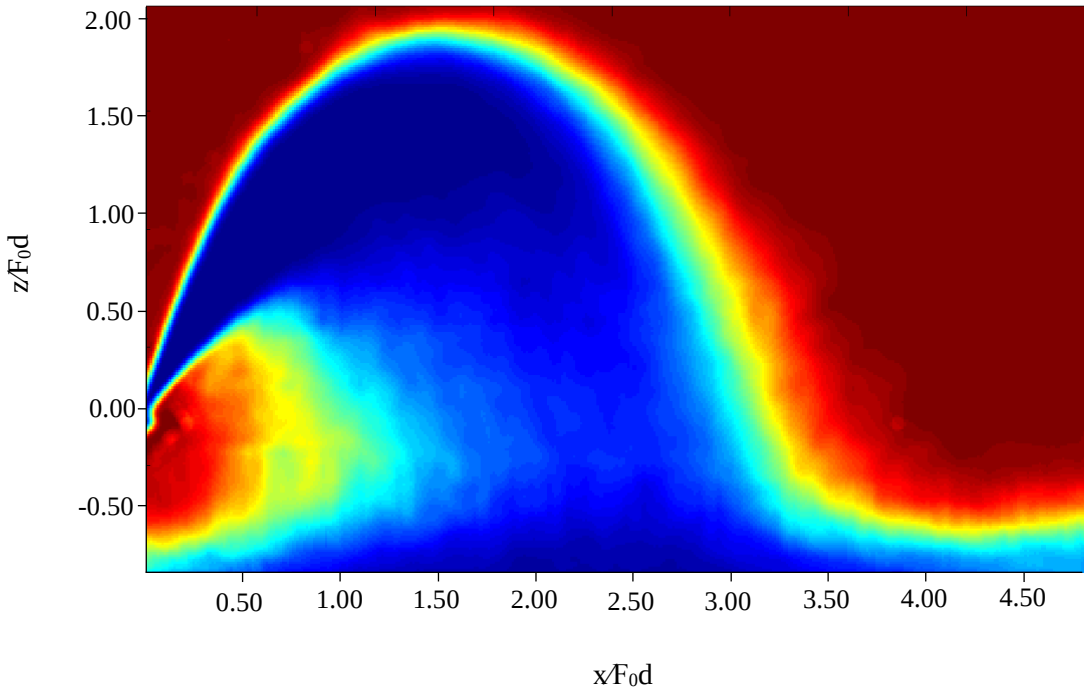

b) Intermittency field.

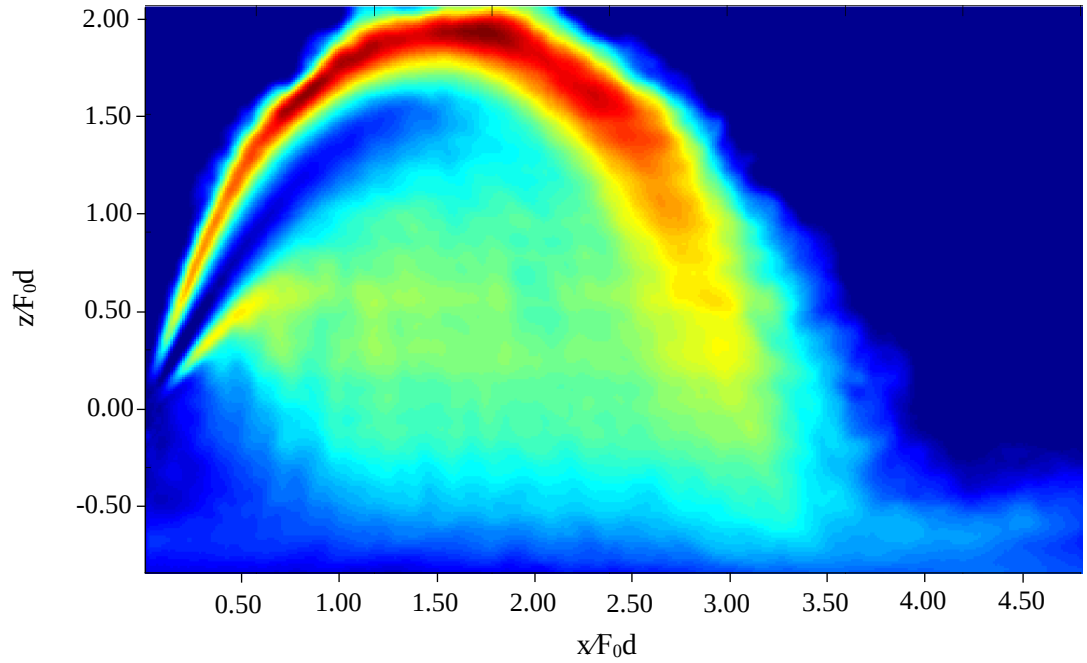

c) RMS concentration field.

Figure 6.4: Flow intensity fields, 60° discharge, $H/F_0d = 0.822$, Re = 3388.

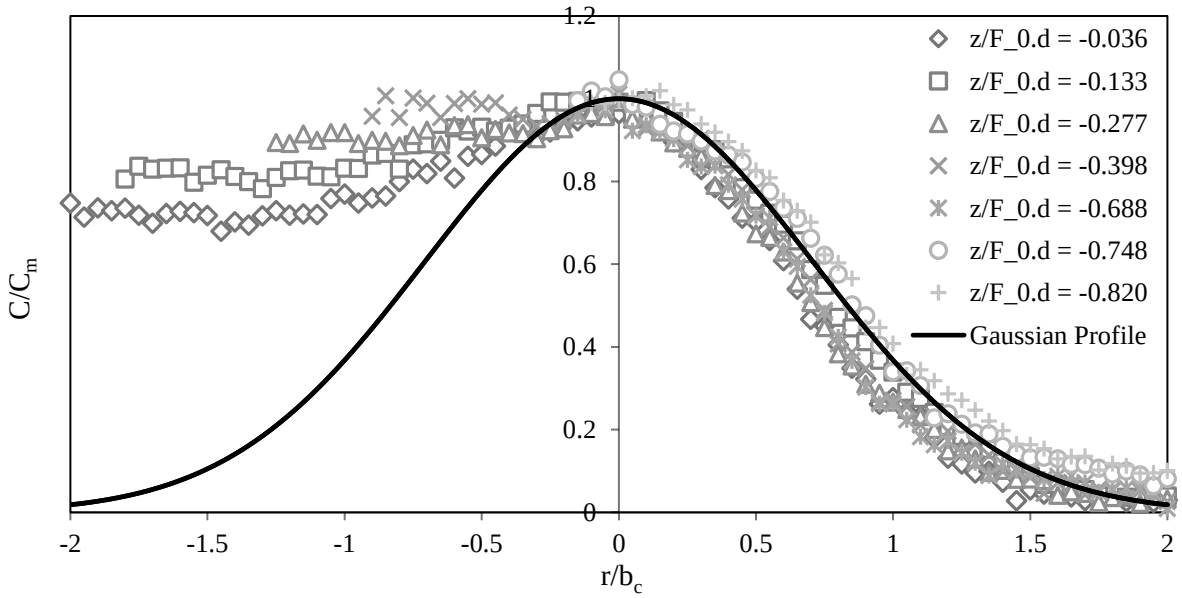

a) Time-averaged concentration profiles.

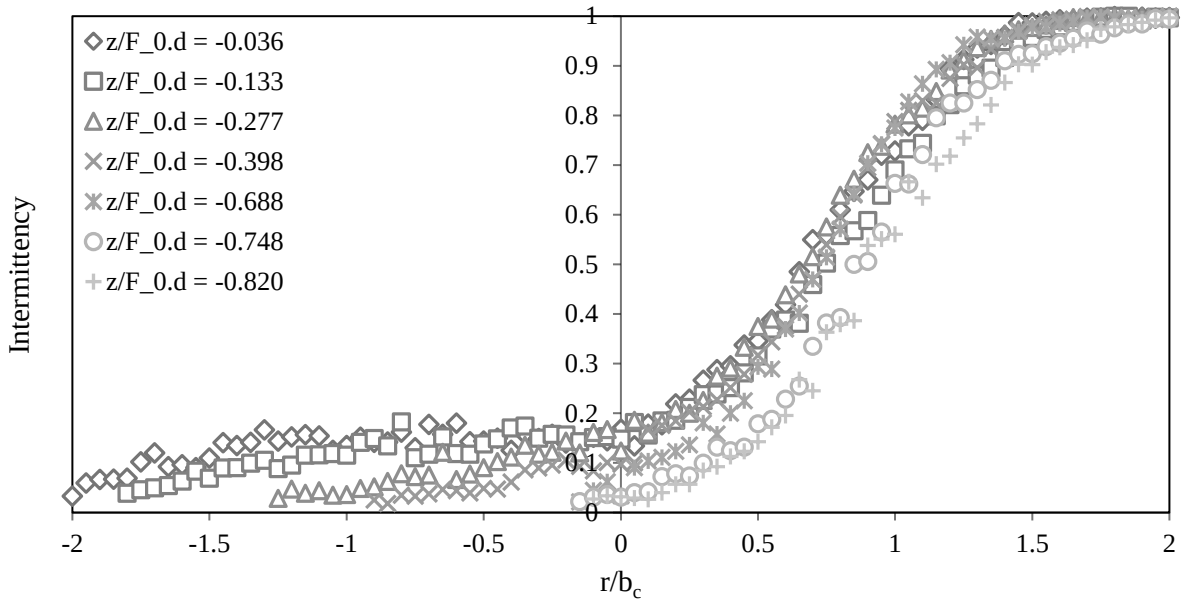

b) Intermittency profiles.

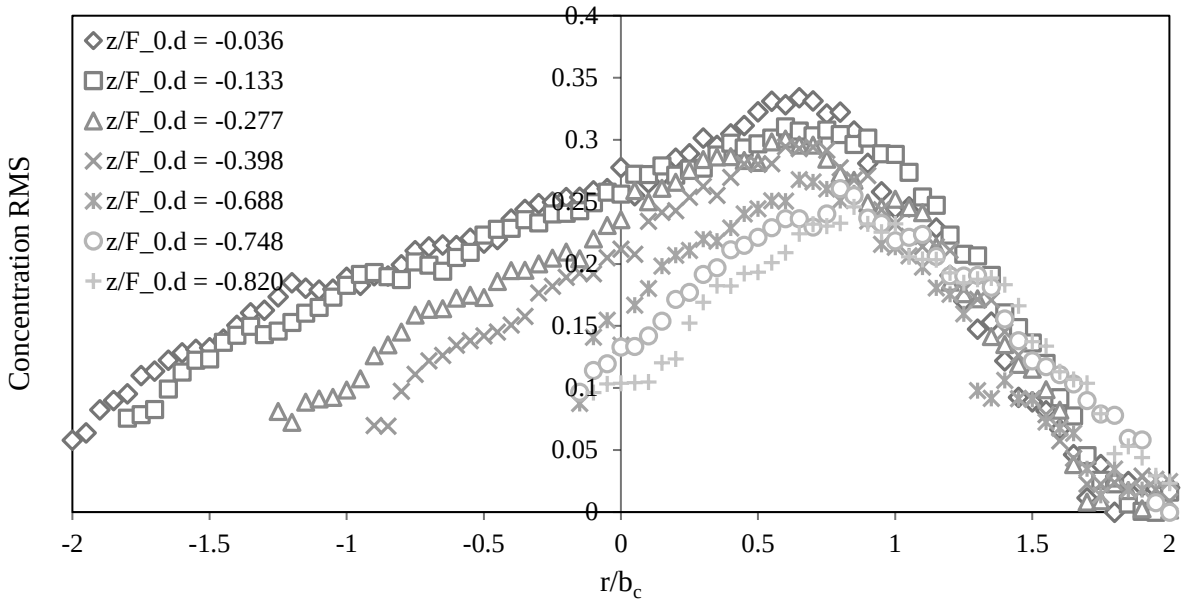

c) RMS concentration profiles.

Figure 6.5: Flow profiles, 60° discharge, $H/F_0d = 0.876$, Re = 3388.

The data presented in Figure 6.4 and Figure 6.5 suggests that the lower boundary inhibits mixing near this region. This behaviour is consistent for shallow angle discharges as well. To illustrate this fact, Intermittency and RMS concentration data have been extracted for 45^o and 30^o discharges along the flow centreline (i.e. values corresponding to $r/b_c = 0$ along perpendicular flow profiles). Values are plotted against the vertical distance above the boundary ($(H + z)/F_0 d$) in Figure 6.6 and include data points between the maximum centreline height (RHS) and the boundary (LHS). Some scatter is present, however centreline RMS and Intermittency values are shown to significantly decline upon approach to the boundary for each discharge angle. The diminishing mixing ability of the discharge near the boundary is likely to have implications for mean concentrations within this region of the flow.

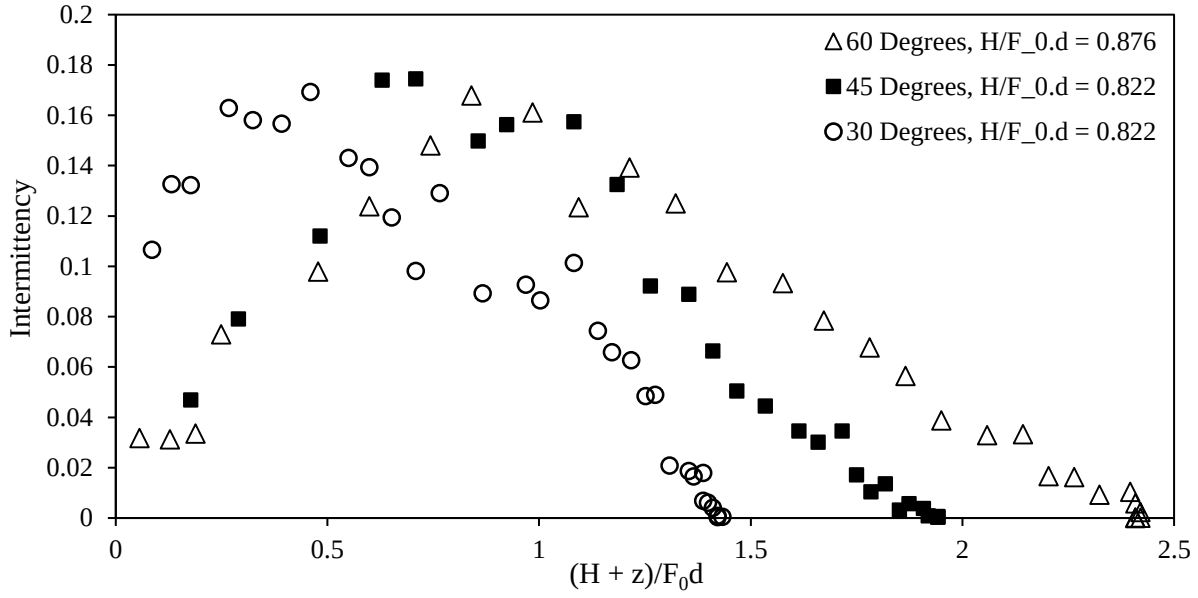

a) Centreline Intermittency values.

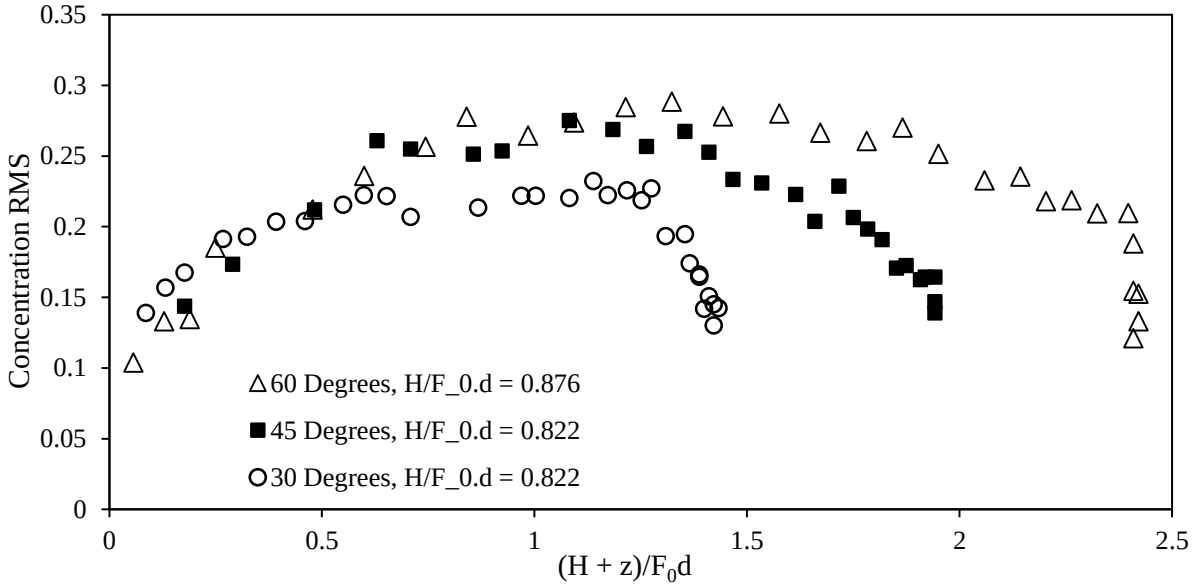

b) Centreline RMS values.

Figure 6.6: Centreline temporal statistics against the vertical distance above the boundary for each discharge angle tested.

6.3.2.2 Flow Spread

The lateral dispersion of the flow (flow spread, b_c) is discussed in this section. An example is provided in Figure 6.7 for 45° experiments (corresponding figures for 30° and 60° experiments included in Appendix C). The same criteria was used to calculate the spread as for previous flow configurations (perpendicular distance from the centreline to the point corresponding to $e^{-1}\,C_m$). Unfortunately this criteria was not met when determining the inner spread because of the proximity of the boundary. This aspect is shown in Figure 6.5 where some profiles do not reach $e^{-1}\,C_m$. For this reason only the outer spread is included in Figure 6.7. The behaviour is very similar to the boundary free case (Figure 5.16) however boundary effects are evident further along the path where the spread begins to increase in a non-linear manner. The linear spread coefficient (k_{bc}), prior to where boundary effects are evident, was determined as 0.132 and is almost identical to the rate determined for boundary free experiments. While it was difficult to identify where non-linearity begins for each test, the data demonstrates dependence on the source height. The location where the spread rate

begins to increase is pushed further downstream as the source height increases. Flow edge measurements are closely linked to the variation in spread therefore it is expected that experiments corresponding to smaller source heights would result in larger values of k_{xre}.

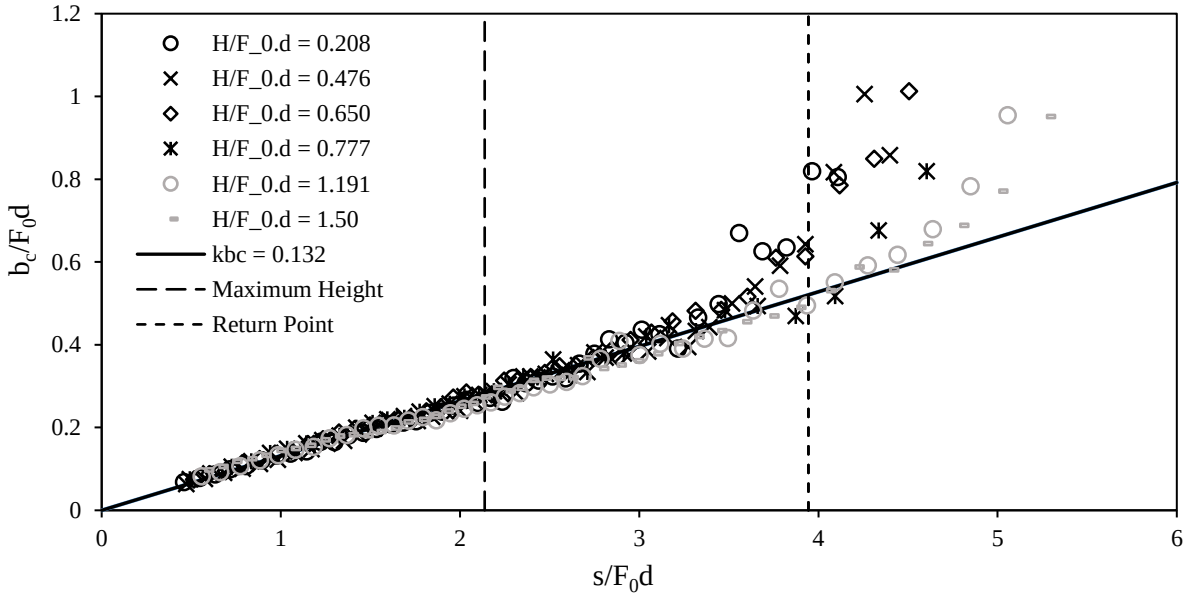

Figure 6.7: Outer spread measurements along the path length for 45° experiments.

For certain experiments, spread measurements were able to be captured as the flow moved through the impact region and evolved into the boundary region. Two 30° tests have been identified to illustrate this behaviour and are displayed in Figure 6.8 along with the corresponding centreline trajectory. In this figure the spread is plotted against the horizontal trajectory (x/F_0d). The spread is initially linear before undergoing a small period of non-linear growth as a result of the lower boundary. Beyond this, spread values are shown to decrease. For both tests, the decrease in outer spread corresponds to a flow re-direction, evident in the trajectory plot. While it is difficult to draw definitive conclusions from only two experiments, the observations from Figure 6.8 are supported by spread results reported in Crowe (2013) and Shao and Law (2010).

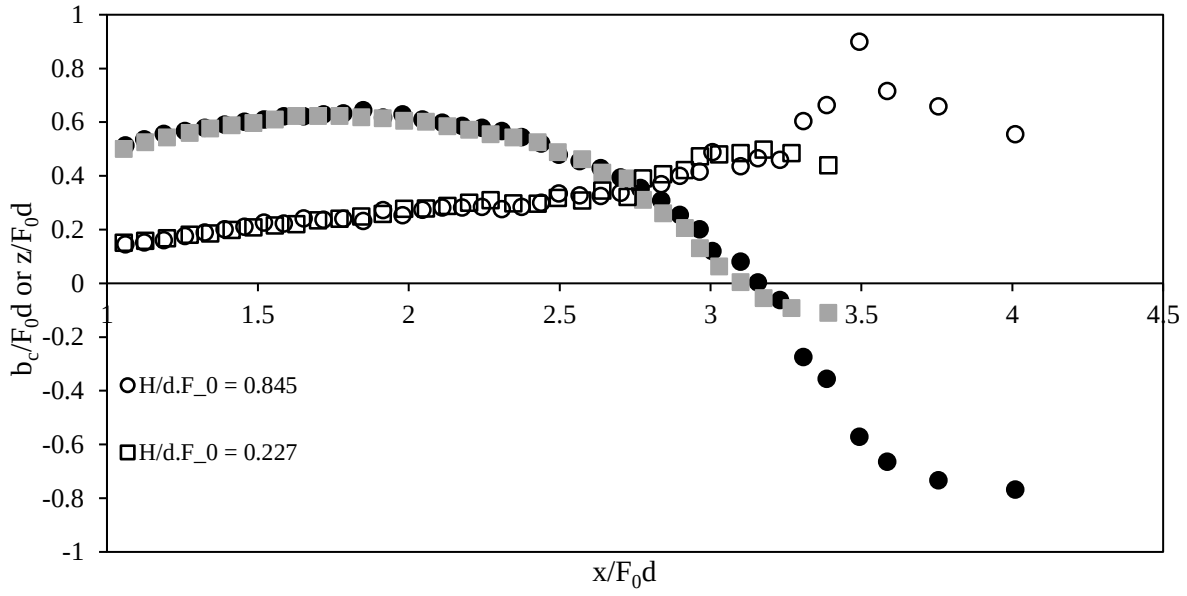

Figure 6.8: Flow trajectory (filled symbols) and spread (unfilled symbols) comparison for selected 30° tests.

6.3.2.3 Return Point Flow Geometry

Geometric coefficients at the centreline and flow edge of the return point are compared to the boundary free case for all angles tested (Table 6.2). It should be noted that for some experiments conducted with small source heights, the return point measured at the flow edge (k_{xre}) could not be determined. The thickness of the spreading layer was found to be larger than the source height from the boundary in these cases. For all three angles, the spreading layer interfered with this measurement when the boundary parameter tested (H/F_0d) was below approximately 0.40 – 0.50.

Table 6.2: Geometric parameters at the return point for boundary and boundary free tests

	Boundary	Horizontal Dist. Centreline Return Point (k_{xr})	Horizontal Dist. Flow Edge Return Point (k_{xre})	Path length to Return Point (k_{sr})
30°	*No*	*2.96 ± 0.11*	*4.06 ± 0.13*	*3.28 ± 0.11*
	Yes	*3.04 ± 0.09*	*4.37 ± 0.28*	*3.36 ± 0.08*
45°	*No*	*3.09 ± 0.07*	*4.39 ± 0.12*	*3.93 ± 0.04*
	Yes	*3.08 ± 0.08*	*4.51 ± 0.22*	*3.98 ± 0.06*
60°	*No*	*2.52 ± 0.07*	*3.76 ± 0.12*	*4.22 ± 0.07*
	Yes	*2.58 ± 0.03*	*3.95 ± 0.15*	*4.27 ± 0.10*

At the return point, boundary experiments generally produced larger coefficients. This includes the horizontal distance and path length to the return point centreline (k_{xr}, k_{sr}), however these coefficients are within one standard deviation of the corresponding boundary free results. More compelling evidence is given at the flow edge (k_{xre}) where the boundary has clearly extended the distance to this reference location for all three source angles. Coefficients measured from these tests also have larger standard deviations, suggesting that averaging across all boundary parameters tested may not be appropriate. Further insight is obtained when k_{xre} is plotted against the boundary parameter ($H/F_0 d$). Results from 30° tests are plotted in Figure 6.9 where a negative trend is observed. Flow edge coefficients at the return point corresponding to lower source heights are likely to be affected by the rapid increase in lateral spread due to the proximity of this location to the boundary. It is also expected that for larger source heights, this geometric parameter would be independent of boundary effects. Due to the relatively subtle changes in these measurements it was difficult to identify a threshold source height beyond which horizontal flow edge distances at the return point are independent of the source height.

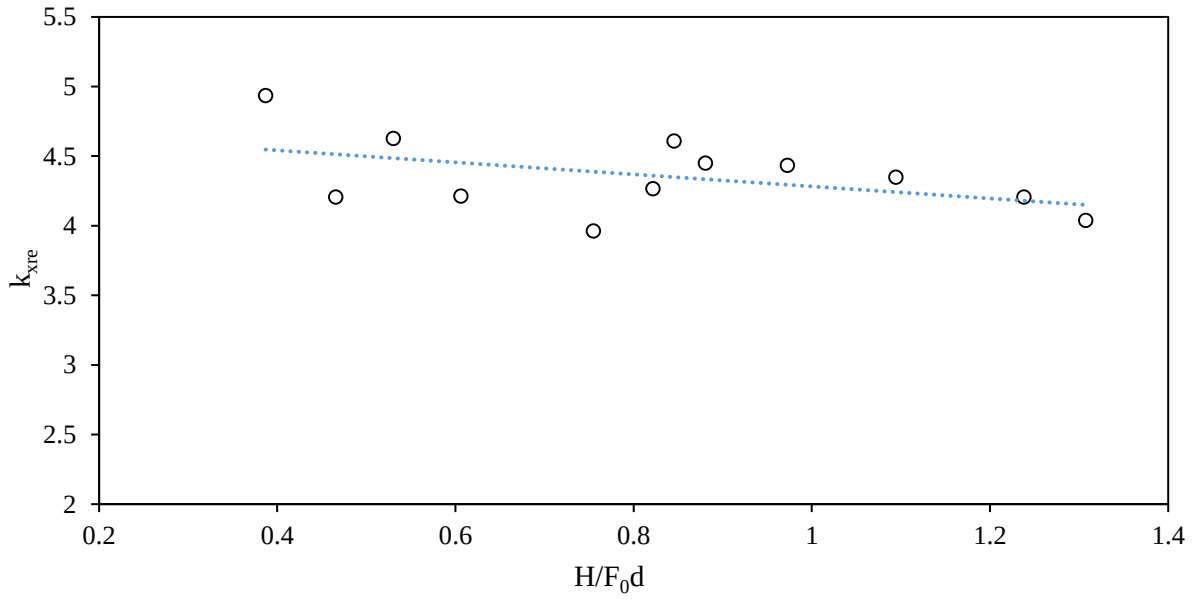

Figure 6.9: Variation of horizontal distance to the return point at the flow edge with source height for 30° experiments.

Geometric coefficients in Crowe (2013) demonstrated similar behaviour where experiments conducted with a lower boundary resulted in longer distances to the return point. These

measurements were derived from velocity fields and are consistently larger than the present study. Observations from Shao and Law (2010) shed some light on this discrepancy where the trajectory from both velocity and concentration flow fields were investigated. They reported that near the boundary, the concentration centreline was observed to descend more rapidly towards the boundary than its velocity counterpart. Although measurements at the return point were not explicitly compared, this result implies that geometric coefficients determined from velocity data would be greater than corresponding concentration values.

6.3.2.4 Centreline Dilution

Time-averaged centreline dilutions are presented in Figure 6.10 for each angle. The centreline dilution profile of the corresponding boundary free case is shown for comparative purposes. In each plot, the centreline dilution follows the boundary free form consistently through the maximum height. Data sets collapse when normalised by the Froude number, further verifying the lack of boundary influence in this region. Near the return point, the centreline dilution ceases to increase and levels off at a particular value. In the present study this value is referred to as the impact dilution ($S_i = C_0/C_iF_0$). The vertical distance from the return point where dilutions level off is referred to as the boundary influence height (z_b/F_0d) and is discussed further in Section 6.3.2.7.

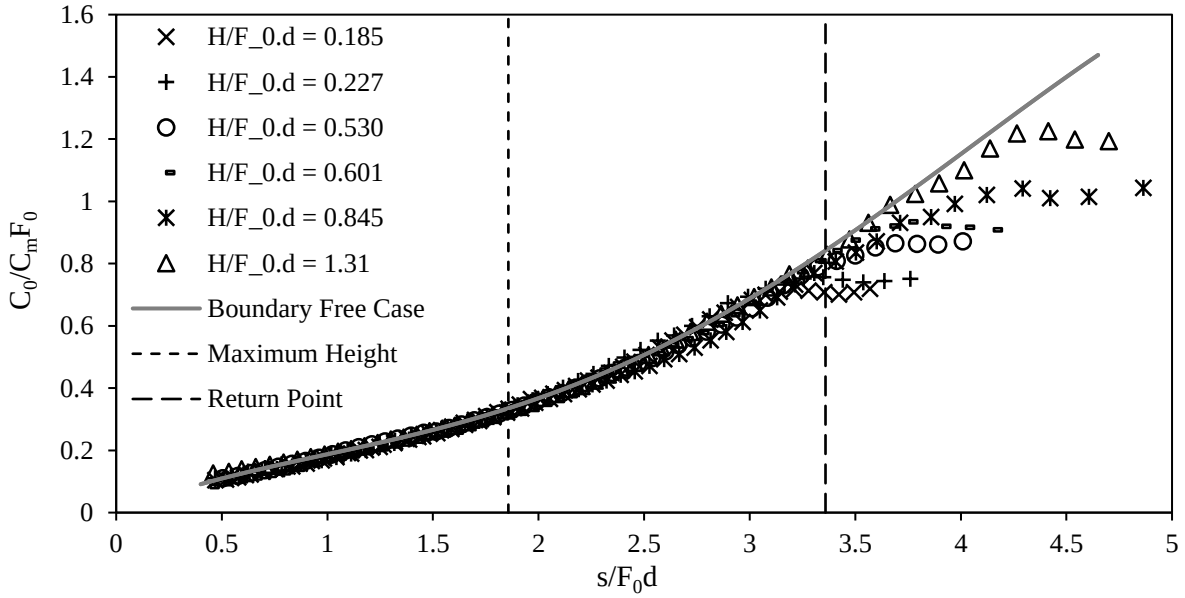

a) 30° discharges.

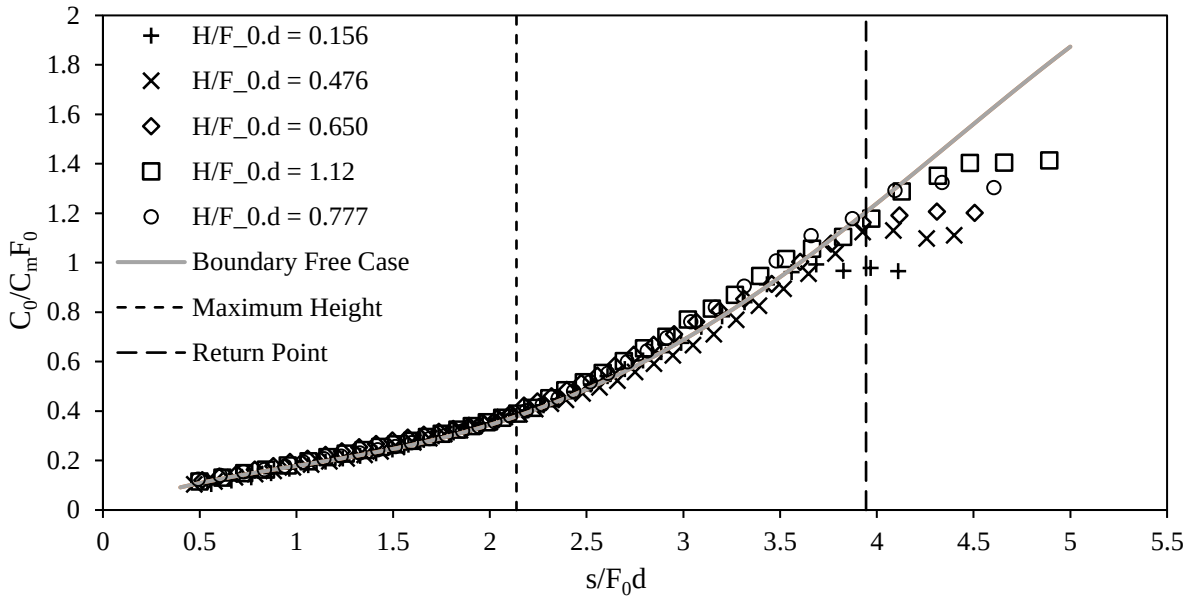

b) 45° discharges.

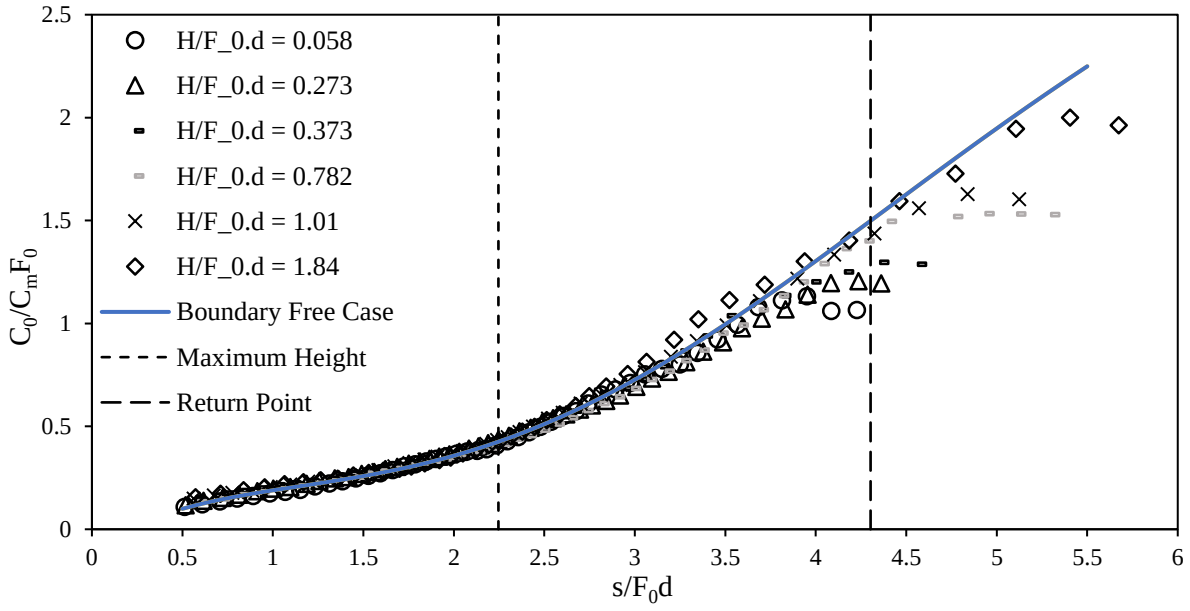

c) 60° discharges.

Figure 6.10: Centreline dilution along the path length prior to boundary impingement. Representative plot from the corresponding boundary free case is included.

Conceptually, a reduction in mixing is expected near the boundary because the entrainment processes are inhibited by the presence of the boundary and there is a decrease in ambient fluid available to be entrained into the primary flow. The impact dilution (S_i) and the location at which the centreline dilution levels off exhibit some dependence on the source height parameter (H/F_0d). Figure 6.10 also shows that for certain source heights, the location at which the dilution stabilises is upstream of the return point. In such cases, the return point and impact dilution are the same. It should be noted that experiments are referred to as 'unaffected', when boundary influence occurs downstream of the return point. Where the opposite is true, the experiments are referred to as 'boundary influenced'. These figures suggest that H/F_0d must be considered as a governing variable for both the return point dilution and the impact dilution.

6.3.2.5 Dilution at the Return Point

Figure 6.11 plots the return point dilution for each source height. Flows discharged nearer to the boundary (boundary influenced experiments) display a linear variance with the source height parameter and were found to collapse when the corresponding centreline maximum height was incorporated into the scaling method. For each data point the source height is referenced with respect to the maximum centreline position of the flow as opposed to the return point ($(H + z_m)/F_0d$). The maximum centreline position provides a standardised location above the boundary from which measurements can be referenced and is equivalent to the scaling procedure used to collapse vertical flows discharged on to the boundary. The collapsed plot is given in Figure 6.12. The best fit equation (Equation 6.1) defines the relationship between the return point dilution from boundary influenced experiments and $(H + z_m)/F_0d$.

$$S_r = 0.477\frac{H + z_m}{F_0d} + 0.355 \qquad 6.1$$

Above a certain source height, it is evident that the return point dilutions are constant (i.e. unaffected experiments). For experiments conducted above this source height, the flow region affected by the boundary does not encompass the return point. This point is referred to as the threshold boundary parameter or source height (H_T/F_0d). The average return point

dilution, calculated over each unaffected experiment, is relatively consistent with return point dilutions from the boundary free experiments. For 45° and 60° experiments the return point dilutions are slightly lower but within the experimental error of 4% and for 30° discharges the results are almost the same as their boundary free counterpart. While similar behaviour is observed for all three source angles, the threshold boundary parameter differs. From Equation 6.1, the threshold boundary parameter was determined using the average dilution from unaffected experiments and maximum rise height values (z_m/F_0d) taken from Table 6.1. The resultant threshold heights are H_T/F_0d (30°) = 0.35, H_T/F_0d (45°) = 0.66 and H_T/F_0d (60°) = 0.74. These thresholds provide limits to the applicability of Equation 6.1 for each discharge angle (i.e. for 45° inclinations, Equation 6.1 can only be used for boundary parameters below 0.66). The uncertainty associated with the calculation of H_T/F_0d was based on the consistency of return point dilutions from the relevant unaffected experiments. For each angle, the upper and lower bounds of H_T/F_0d were resolved by calculating the source heights corresponding to the upper and lower bounds of the unaffected return point dilution (average ± standard deviation). A summary of results is included in Table 6.3.

Table 6.3: Return point dilution and threshold source height for each angle tested

	Return Point Dilution (S_r), Boundary Free Experiments	Return Point Dilution (S_r), Unaffected Experiments	Threshold Source height (H_T/F_0d)
30°	*0.80 ± 0.03*	*0.81 ± 0.02*	*0.35 ± 0.05*
45°	*1.24 ± 0.03*	*1.19 ± 0.05*	*0.66 ± 0.11*
60°	*1.49 ± 0.05*	*1.44 ± 0.04*	*0.74 ± 0.08*

The variation of H_T/F_0d with the source angle illustrates that steeper source angles are more sensitive to boundary influence. This observation may be linked to the suppression of mixing processes being less significant for shallow angled discharges. The greater horizontal momentum flux near the impact point continues to drive the mixing processes and hence the boundary influence is less severe. In contrast, momentum fluxes from steeper discharges involve more significant changes in direction within the impact region, hence mixing is more adversely affected for these experiments. Accordingly, changes to the dilution rate along the centreline are observed earlier along the flow path.

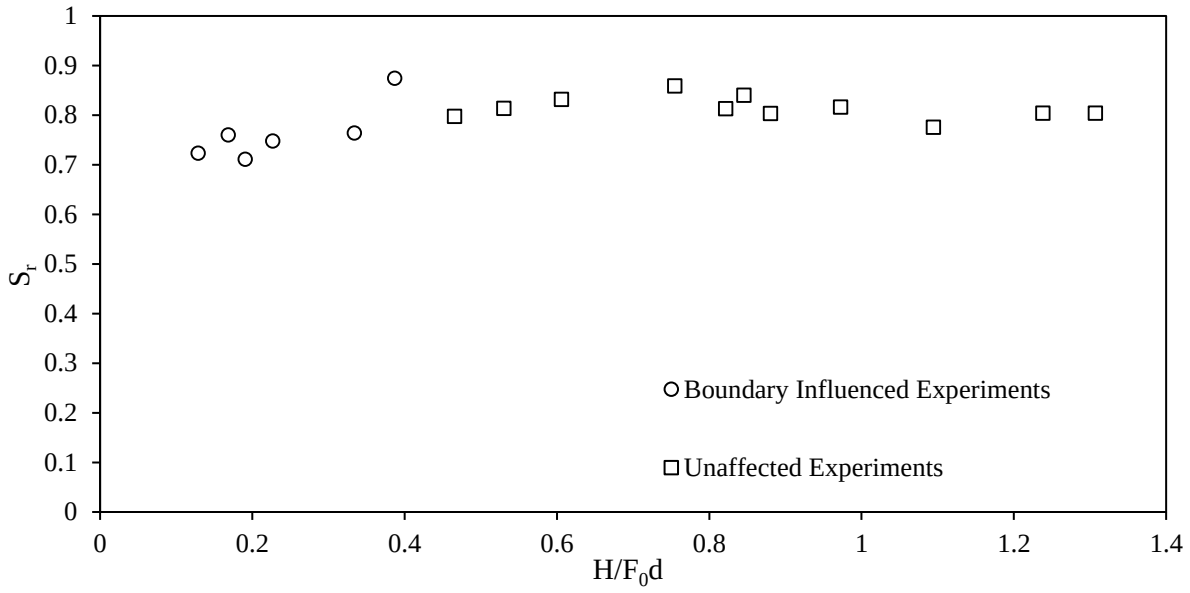

a) 30º discharges.

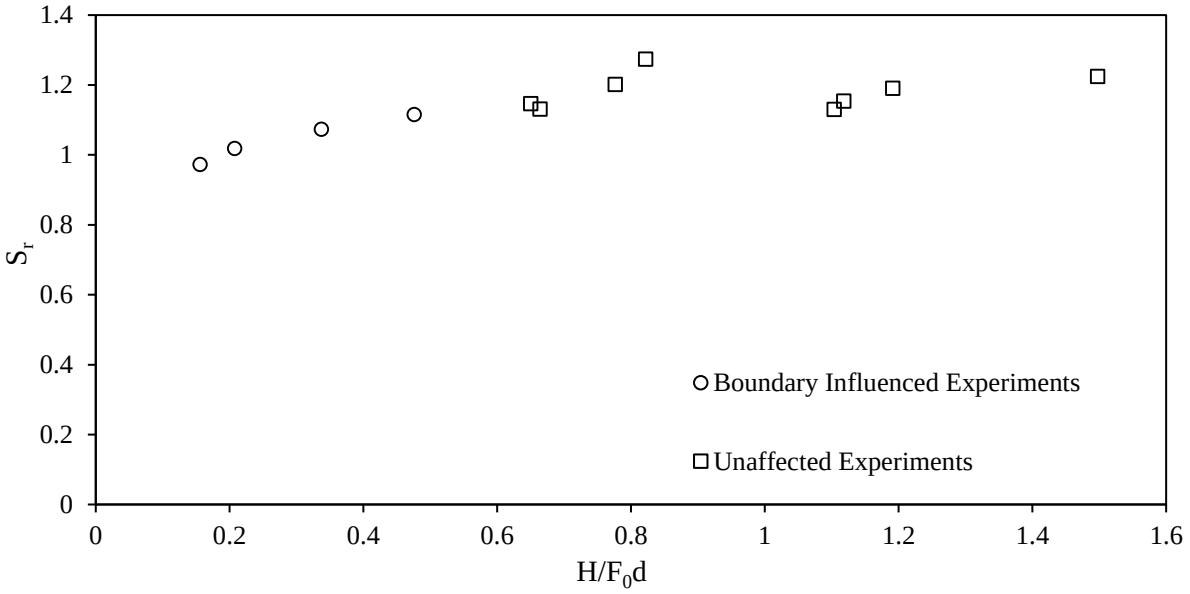

b) 45º discharges.

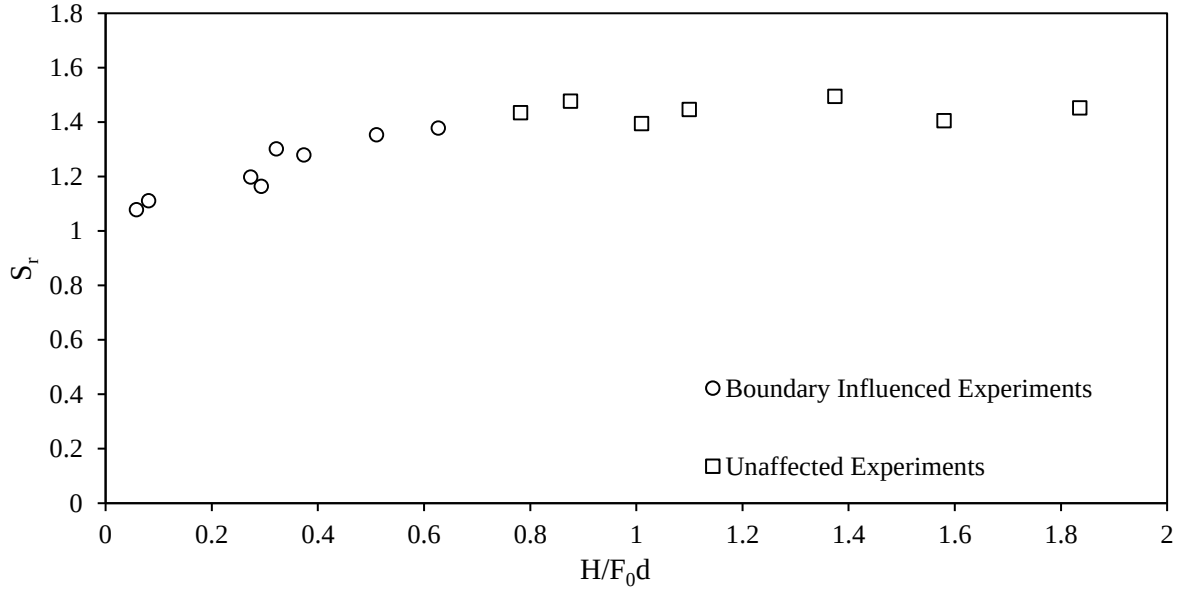

c) 60° discharges.

Figure 6.11: Return point dilution against source height for each angle.

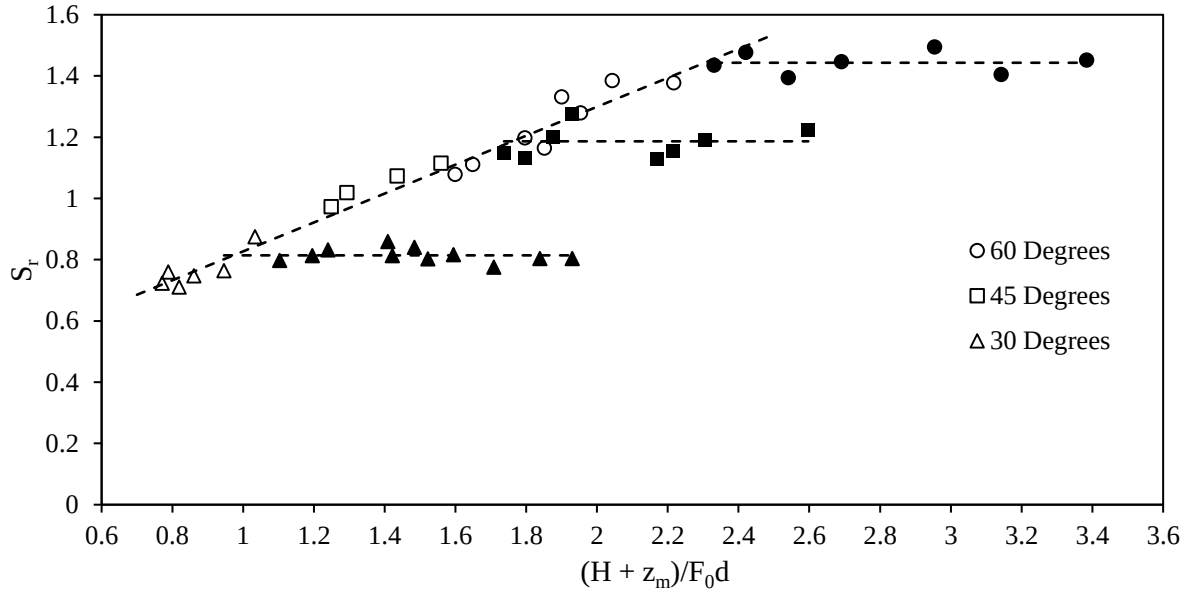

Figure 6.12: Return point dilution against the source height parameter referenced with respect to the maximum centreline height. Boundary influenced experiments are denoted using unfilled symbols and unaffected experiments are denoted using filled symbols.

6.3.2.6 Dilution at Impact Point

The impact dilution ($S_i = C_0/C_iF_0$) is plotted in Figure 6.13 for each test. A linear relationship is evident with H/F_0d and each measurement was once again found to collapse when the corresponding centreline maximum height was considered ($(H + z_m)/F_0d$). The relationship between these two parameters is provided in Equation 6.2 and is applicable for all discharge angles between 30° and 60°. If the location of the boundary coincides with the return point (i.e. $H/F_0d = 0$) the return point dilutions as per Equation 6.2 are $S_r(30^o)$ = 0.638, $S_r(45^o)$ = 0.874 and $S_r(60^o)$ = 1.11. In comparison to the corresponding boundary free return point dilution, these values represent substantial reductions by approximately 22 – 29%.

$$S_i = 0.504\frac{H + z_m}{F_0 d} + 0.320 \qquad 6.2$$

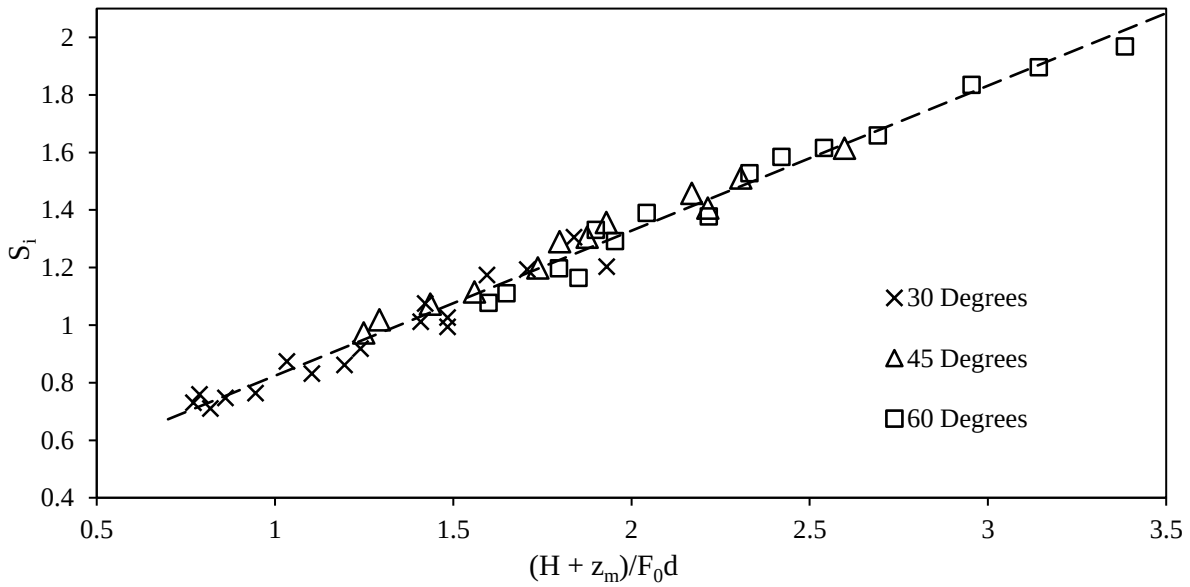

Figure 6.13: Impact dilution against the source height parameter referenced with respect to the maximum centreline height.

Recalling the discussion in Chapter 4 regarding the relationship between the impact dilution and the boundary parameter (Figure 4.18). If the boundary parameter is large enough where the flow has transitioned to a plume at the point of impact, it is expected that z_m will be irrelevant and the impact dilution will be dependent on $(H/F_0d)^{5/3}$ (as shown in Figure 4.18

for plume type flows). At this stage it is unclear whether inclined flow configurations follow the same inequalities set out in Equation 4.1. To further investigate this aspect, the boundary parameter would need to be presented in an equivalent form to vertical flow experiments where the entire path length from discharge to boundary impact is incorporated. Due to the complexities associated with defining the entire flow path this analysis could not be conducted.

6.3.2.7 Location of Boundary Influence

The boundary influence height (z_b/F_0d) is defined as the vertical location along the flow path where the dilution is observed to level off. This location has been extracted from each boundary experiment and is measured relative to the discharge location (or return point). To estimate this parameter, the relationship between the centreline dilution (C_0/C_mF_0) and the vertical distance from the source (z/F_0d) was considered. Figure 6.14 plots these variables for the 45^o experiments. The boundary influence height was determined by representing data points prior to the dilution stabilising, as a linear function. Substituting the corresponding impact dilution (S_i) into this linear approximation provided an estimate of the boundary influence height. The relationship between the boundary influence height and the source height parameter is provided for each angle in Figure 6.15. A linear relationship is evident and each data set collapses when the centreline maximum height is incorporated into the scaling. In Figure 6.15, data points were scaled by referencing both the influence height and the source height to the maximum centreline position. Accordingly, $(z_m - z_b)/F_0d$ was plotted against $(H + z_m)/F_0d$. The threshold source height could also be determined from the plot using the best fit relationship (Equation 6.3) and setting $z_b/F_0d = 0$. The relevant maximum centreline height is taken from Table 6.1.

$$\frac{z_m - z_b}{F_0 d} = 0.819 \frac{H + z_m}{F_0 d} + 0.215 \qquad 6.3$$

Threshold heights from Equation 6.1 and Equation 6.3 are given in

Table 6.4. Values are similar for 30^o experiments however Equation 6.3 generally provides lower threshold heights for steeper angle discharges. The specific reasons for the discrepancies between data sets are unclear other than the different criteria used to formulate

the best fit equations. One important distinction is the number of data points used to determine each equation. More information was available to produce Equation 6.3 hence the threshold source heights determined using this formulation are more reliable and would be less susceptible to variation if more data was added. Despite this, threshold heights determined from this analysis also correlate positively with the source angle showing that boundary influence is intensified for steeper source angles.

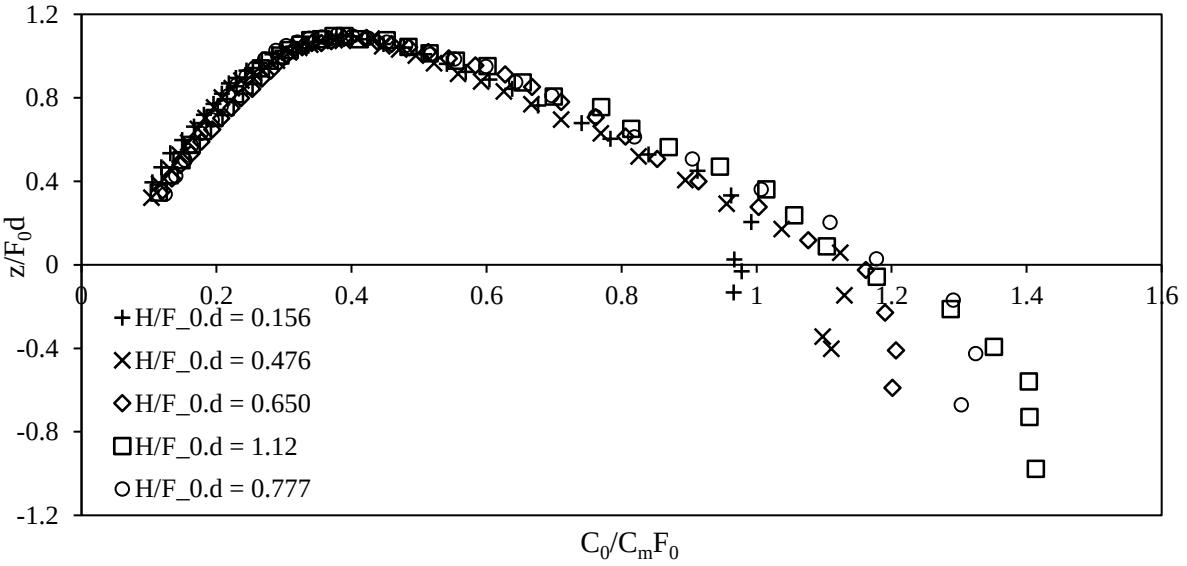

Figure 6.14: Centreline dilution against the vertical height (measured with respect to the discharge nozzle location).

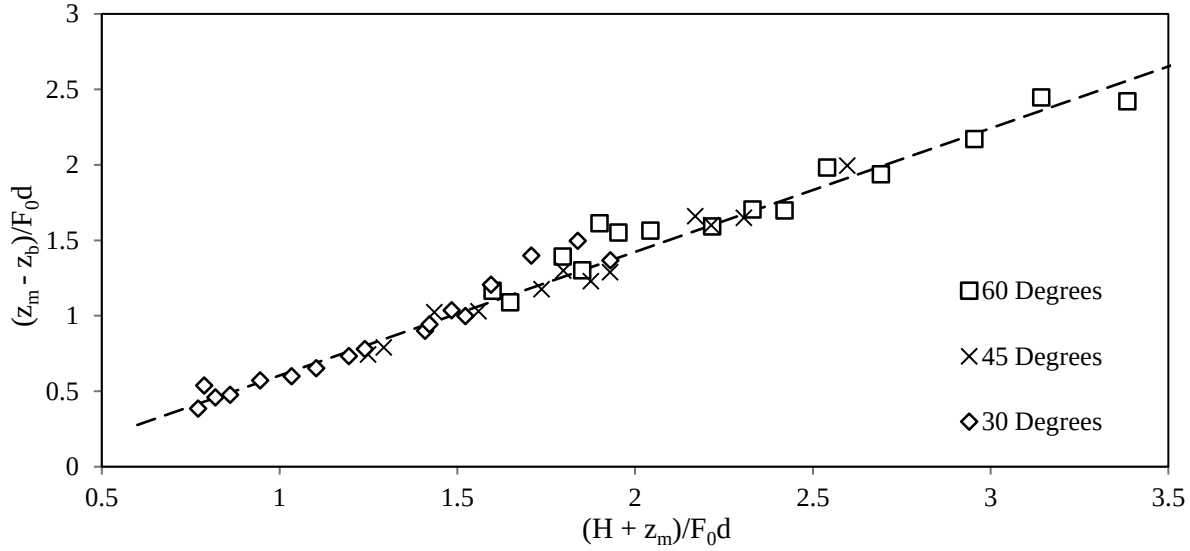

Figure 6.15: Boundary influence height against the source height parameter referenced with respect to the maximum centreline height for each angle.

Table 6.4: Comparison of threshold source heights.

	H_T/F_0d (Equation 6.3)	H_T/F_0d (Equation 6.1)
30°	*0.40*	*0.35 ± 0.05*
45°	*0.50*	*0.66 ± 0.11*
60°	*0.60*	*0.74 ± 0.08*

In Chapter 4, this parameter was presented slightly differently and it was determined that the centreline dilution discontinued at approximately $z/H = 0.93 – 0.94$ (or a height of 0.06H – 0.07H above the boundary). It is unclear whether this value still holds for the inclined case, however the linear relationship shown in Figure 6.15 indicates that the boundary influence height would be consistent for all experiments if analysed in the same way. As stated in section 6.3.2.6 there were issues regarding defining the entire path length for inclined experiments, therefore it was not possible to conduct this alternative analysis.

6.3.3 Comparisons with Previous Research

6.3.3.1 Dilution

Boundary experiments provide the most applicable comparison with previous studies for dilution measurements at the return point and impact point. A direct comparison with the literature was performed in Oliver et al. (2013) and discrepancies were found to be significant and somewhat counterintuitive. Dilution coefficients from studies where the boundary was in close proximity to the source were relatively greater, thereby suggesting additional mixing. Clearly factors other than the boundary were contributing to these inconsistencies. More intuitive comparisons were obtained when the dilution ratio (S_r/S_m or S_i/S_m) was considered. Results from Oliver et al. (2013) were generally higher than other studies, which is expected given that boundary influence was removed during these experiments. The advantage of using the dilution ratio as a comparative measure is that it provides a standardised indication of the mixing that takes place post flow reversal and leading up to the return point and boundary. Any errors associated with calibration issues are largely eliminated. In this section, comparisons with the literature are solely performed using the

dilution ratio. Six previous studies have been used to compare results with the present study. The boundary conditions used in each experimental program are outlined in Table 6.5. Experiments have only been included where the dilution at the maximum height and return point/impact point are given. Some studies have not included specific details of the boundary conditions hence values for the boundary parameter could not be determined. For these cases the boundary parameter is listed as a range of possible values. For example Shao and Law (2010) reported a single dilution value over the range of source heights. Papakonstantis et al. (2011b) also provided ambiguous boundary conditions. Two nozzle diameters (6 mm and 8 mm) were used while carrying out experiments, however specific diameters were not assigned to each test. Each experiment in Table 6.5 has been highlighted depending on whether boundary influence is expected to affect the return point dilution. Threshold values determined from Equation 6.1 provide the most relevant parameter for comparison. Source heights lower than these thresholds are marked ** and source heights within the error margins of these thresholds are marked *.

Return point and impact dilution ratios from previous studies are plotted alongside results from the present study in Figure 6.16 for each angle. Many of these results have been obtained from experiments where small source heights are imposed on the discharge. Therefore, for the purpose of clarity the boundary parameter has been presented in its inverse form ($F_0 d/H$). For lower values of $F_0 d/H$, boundary influence is clearly less significant, hence dilutions recorded at the impact point (S_i) are higher than those at the return point. For larger values of this parameter the return point and impact point dilutions are essentially the same. Oliver et al. (2013) reports the only set of results that are considered 'boundary free' hence they are plotted at $F_0 d/H = 0$. Return point dilution ratios are initially shown to be constant before they converge and are the same as dilution ratios at the impact point. This denotes conditions where the boundary begins to influence the flow behaviour at the return point. The threshold source height ($H_T/F_0 d$), determined from Equation 6.1, is shown in each figure and is relatively consistent with the point of convergence between these two dilution quantities. The relationship between the impact dilution ratio (S_i/S_m) and $F_0 d/H$ resembles an inverse relationship. This relationship is more apparent for 30^o experiments than 45^o and 60^o discharges, where dilution ratios for larger values of $F_0 d/H$ (or smaller values of $H/F_0 d$)

tend to 'level off'. The inverse relationship is expected given that a linear variance was evident between the impact dilution and H/F_0d in Figure 6.13.

Importantly, the data included in Figure 6.16 displays a reasonably consistent trend with the non-dimensional source height, but it also highlights some discrepancies. Dilutions from Lai and Lee (2012) and some tests from Papakonstantis et al. (2011b) are lower than the present study and do not follow any perceivable relationship. The 60^o results from Papakonstantis et al. (2011b) are particularly difficult to interpret. Return point dilution ratios from two tests have been included in Figure 6.16 and these two measurements vary by almost 44%, despite using similar boundary parameters. The reasons for these differences are not clear, however probe measurements were used to acquire concentrations. The intrusive nature of this measurement system may have compromised the consistency of their results. Conversely, 45^o tests from this study are more in line with the present study. With the exception of 60^o experiments, data from Abessi and Roberts (2015) compares well to the present study. This comparison is interesting as Abessi and Roberts (2015) accounted for a thin layer of high concentrated fluid along the boundary when reporting the dilution. The expectation is that the impact dilution would therefore be lower than the present study. It was difficult to accurately gauge how dilutions from Shao and Law (2010) compare due to the range of source heights over which each dilution was reported. Despite this, their results are consistent with the general trend exhibited by the remainder of the data. Roberts and Toms (1987) reported exclusively on 60^o discharges. These results are reasonably consistent with those from the present study, but some of the data displays a counter intuitive relationship with the boundary parameter where dilutions appear to slightly increase with F_0d/H. These results were obtained using relatively primitive probe measurements hence it is possible that the observed trend falls within the variations associated with the measuring system. Finally, the return point dilution ratio from Oliver et al. (2013) is included and is largely comparable with results from the present study. From a holistic perspective, comparisons with previous studies are encouraging. In contrast to the severe inconsistencies illustrated in Figure 2.3 this new analysis suggests that discrepancies between studies are associated with varying boundary influences as well as difficulties in calibrating concentration measurements accurately.

Table 6.5: Source height parameter and corresponding dilution ratios from previous studies. Tests where boundary conditions are expected to influence return point dilutions are highlighted using * and **.

	30°			45°			60°		
	H/F_0d	S_r/S_m	S_i/S_m	H/F_0d	S_r/S_m	S_i/S_m	H/F_0d	S_r/S_m	S_i/S_m
Roberts and Toms (1987)							*0.039***		*2.97*
							*0.039***		*2.61*
							*0.038***		*2.53*
							*0.039***		*2.49*
							*0.041***		*2.58*
							*0.048***		*2.12*
							*0.079***		*2.08*
							*0.049***		*2.25*
							*0.051***		*2.11*
Lai and Lee (2012)				*0.840*	*2.08*		*0.893*	*2.37*	
				*0.629**	*2.48*		*0.535***	*2.55*	
				*0.503**	*2.39*		*0.446***	*2.47*	
				*0.418**	*2.34*				
Shao and Law (2010)	*0.094 – 0.140***	*1.90*		*0.047***	*2.74*				
	*0.164 – 0.414***	*2.20*							
Papakonstantis et al. (2011b)				*0.663 - 0.884**	*2.32*		*0.665 - 0.887**	*4.09*	
				*0.527 - 0.703**	*3.22*		*0.510 - 0.680**	*2.85*	
				*0.502 - 0.670**	*2.66*				
Oliver et al. (2013)	-	*2.48*		-	*3.13*		-		*3.69*
Abessi and Roberts (2015)	*0.218***		*2.36*	*0.351***		*2.81*	*0.171***		*2.73*
	*0.161***		*1.93*	*0.234***		*2.59*	*0.251***		*2.18*
	*0.181***		*2.20*	*0.319***		*2.49*	*0.210***		*2.55*
	*0.238***		*2.55*	*0.439***		*2.46*	*0.147***		*2.87*
							*0.206***		*2.69*

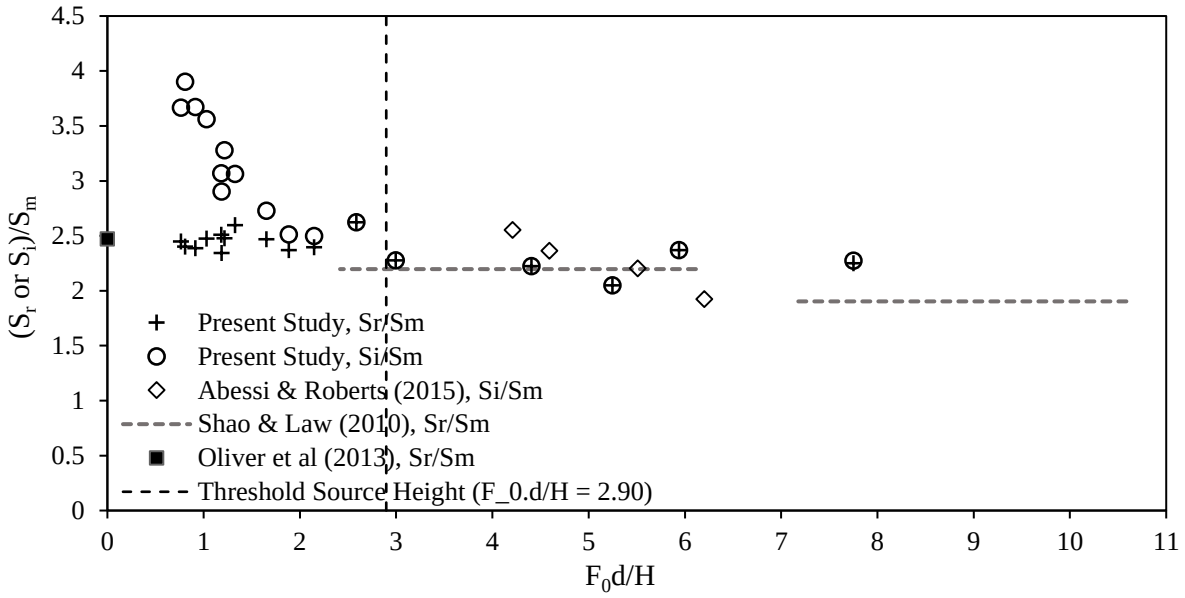

a) 30º discharges.

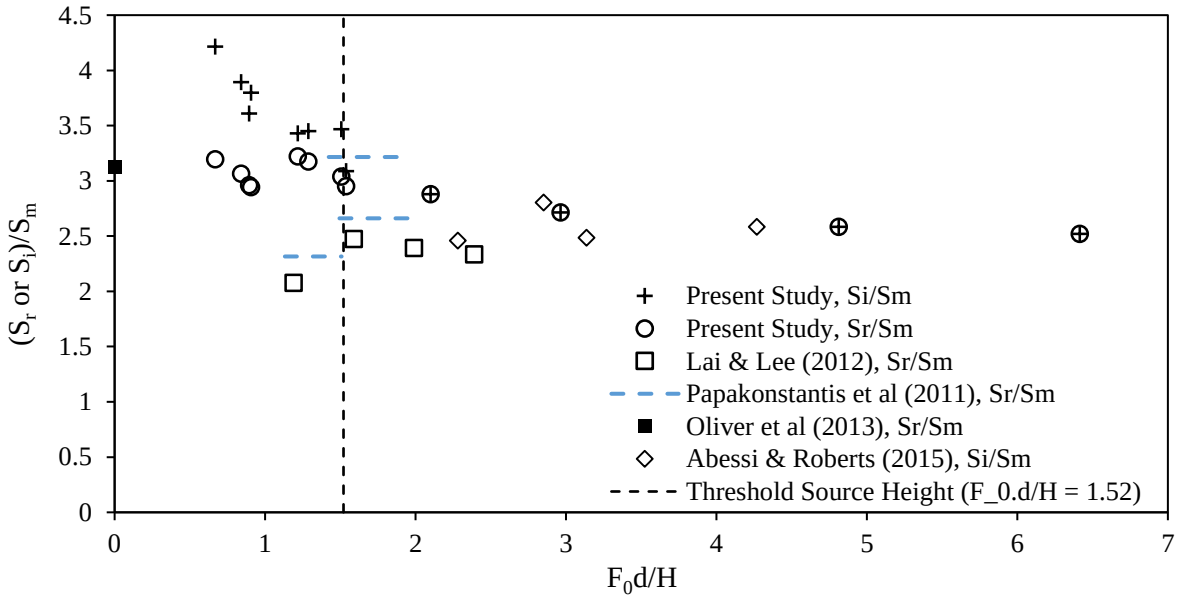

b) 45º discharges.

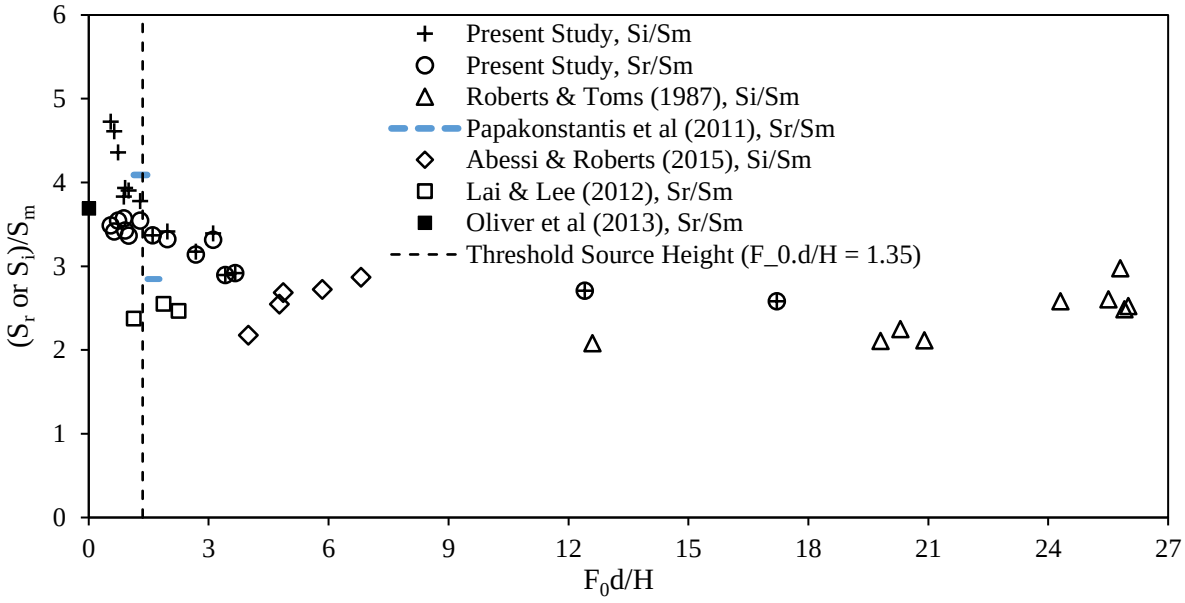

c) 60° discharges.

Figure 6.16: Variation of dilution ratios from the literature and present study with the source height parameter for each angle.

6.3.3.2 Location of Boundary Influence

There is a dearth of information in the literature with regards to locating where boundary influences become evident in INBJs. On numerous occasions simple vertical jets discharged onto a boundary have been subjected to this type of analysis, however this cannot be directly translated to INBJ's. Crowe (2013) is one of the few previous study where this issue has been investigated in detail. Two methods were used to identify changes in the flow's behaviour near the boundary. The first method involved the centreline trajectory. A representative curve was fitted through each centreline profile and the inflection point along the trajectory was identified for each experiment. An inflection point arises when the rate of change of the gradient (second derivative) is equal to zero. This feature was used to signify where the boundary had altered the trajectory of the centreline. The vertical distance of the inflection point above the source was subsequently deemed the beginning of the impact region. The inflection point was found to vary linearly with the boundary parameter. The second method considered vertical and horizontal velocities of the flow. The impact region coincides with

the flow rapidly decelerating. Consequently the velocity components in the horizontal and vertical direction reach a minimum value, before the flow transitions to a horizontal spreading layer. The vertical heights corresponding to this minimum velocity were examined in relation to the source height and a linear relationship was also apparent for each component. Although the threshold boundary parameter was not explicitly determined in Crowe (2013), these values have been inferred and included in Table 6.6. The vertical velocity criteria results in the largest threshold values and is clearly the most sensitive parameter to the boundary. Inflection point data exhibited the most consistency between experiments while figures illustrating the minimum horizontal and vertical velocities were quite scattered. In comparison to the present study, these results are different to the threshold heights tabulated in

Table 6.4, however they follow the same trend with regards to the discharge angle.

Table 6.6: Threshold source heights from Crowe (2013).

	H_T/F_0d (Inflection point)	H_T/F_0d (Horizontal Velocity)	H_T/F_0d (Vertical Velocity)
30°	*0.223*	*0.177*	*0.608*
45°	*0.393*	*0.371*	*0.791*
60°	*0.547*	*0.546*	*0.957*

6.4 Potential Design Implications

The findings presented in this chapter can potentially benefit the design of desalination diffuser systems. Design coefficients describing the dilution and geometric behaviour of INBJ's discharged into a stagnant and unbounded environment have already been established in the existing literature. From a practical perspective, such an idealised environment is not a realistic approximation of boundary conditions. Topographic constraints as well as other design limitations may require diffuser systems to be installed near the sea bed or other solid boundaries. Depending on the proximity of the boundary to the discharge nozzle, the possibility of reduced mixing near the impact region should be accounted for. Results show

that centreline dilutions at the return point can reduce by up to 29%. These findings also shed light on the applicability of integral model predictions to such discharge configurations. Integral model predictions facilitate the design of outfalls and can typically account for a range of ambient conditions such as external ambient currents and density stratified ambient environments. Unfortunately, they are presently unable to account for boundary effects to an acceptable degree of accuracy. While no solution has been provided to improve model predictions, the data presented here can identify the extent to which these predictions are valid. The lack of accuracy of integral models emphasises the importance of the empirical relationships developed. The variation of the impact dilution with source height is a valuable result in guiding the resolution of issues associated with high salinity discharges. This data can contribute to more robust design guides and aid in ensuring that effluent concentrations at the boundary meet environmental regulations.

6.5 Summary

Large discrepancies between experimental studies on INBJ's have previously been attributed to the presence of a lower boundary. In particular, direct comparisons of dilution results near the return point have proved to be inconclusive and somewhat counter-intuitive. This issue has been investigated in detail by analysing potential changes in the behaviour of INBJ's as a result of a horizontal boundary positioned within the vicinity of the discharge nozzle. A series of experiments were conducted for three discharge angles (30^o 45^o and 60^o) with non-dimensional source heights (H/F_0d) ranging between 0.058 and 1.84. Flow behaviour was quantified using dilution and geometric measurements and were compared with results from Chapter 5 where no boundary influence existed in the measurement region. Experimental coefficients at the maximum height indicated no perceivable boundary influence. The potential of Coanda effects was also analysed using trajectories from 30^o experiments conducted at low source heights, however no evidence of this was apparent.

In contrast, the behaviour at the return point was substantially affected by the lower boundary. Comparisons with the boundary free case revealed that horizontal distances to the return point were extended as a result of the boundaries presence. Flow edge measurements increased significantly and appeared to exhibit a negative trend when plotted against the

source height. Increases in flow edge measurements could be attributed to non-linear variations in the spread near the impact region. Outer spread measurements for 45^o experiments demonstrated that beyond a certain location along the flow path, the flow spread would increase in a non-linear manner. This location was pushed further downstream as the source height increased. Preceding this, the outer spread increased at a linear rate resulting in a spread coefficient similar to the boundary free case (k_{bc} = 0.132). Within the impact region, the lower boundary influence was qualitatively investigated. Mean, Intermittency and RMS information were presented and highlighted the flow's diminishing ability to mix with ambient fluid as it approached the boundary.

Dilution measurements near the return point and boundary confirmed qualitative observations. The dilution along the flow centreline was presented for a range of source heights and compared to the boundary free case. Centreline dilutions were consistent with the boundary free case until the influence of the lower boundary resulted in negligible variation along the flow path and the dilution became constant (i.e. impact point dilution). Dilution variations corresponding to smaller source heights were impacted earlier along the flow path indicating greater boundary influence. The return point and impact point dilution were investigated in relation to the source height. Both measurements displayed dependence on the source height parameter to varying degrees. Return point dilutions were shown to vary up to a threshold source height (H_T/F_0d). For source heights above this threshold, dilutions were constant and reasonably consistent with results from boundary free tests. Dilutions recorded at the impact point increased linearly over the entire range of source heights tested. In each instance, dilutions were shown to collapse for a given angle when the corresponding maximum centreline height was incorporated into the scaling. Empirical relationships were determined for return point dilutions where variation was apparent (Equation 6.1) and for impact dilutions (Equation 6.2). Linear dependency was also observed for the boundary influence height (z_b/F_0d) when plotted against the source height. This parameter represents the vertical distance from the return point (or source) to where the centreline dilution becomes constant along the flow path. Results from each angle also collapsed onto a single line when referenced to the maximum centreline height (Equation 6.3). Using this equation, an additional threshold source height (H_T/F_0d) could be determined for each discharge angle. Each threshold parameter correlated positively with the source angle, showing that boundary

influence is more significant for steeper discharge inclinations. Threshold source heights were directly compared to Crowe (2013) who quantified boundary influence based on velocity field measurements. The inferred source heights were different to the present study but exhibited the same trend with respect to the discharge angle.

The threshold source height was useful in assessing whether results from previous studies were potentially affected by the presence of a lower boundary and therefore a contributing factor to the well-documented discrepancies in the literature. This issue was further investigated by analysing dilution ratios at the return point and impact point (S_r/S_m or S_i/S_m) in the context of the source height. Results from the literature were plotted alongside the present study and revealed an intuitive variation with the source height.

In summary the analysis conducted in this chapter enables design protocols for desalination outfalls to incorporate potential boundary effects. Most modelling packages cannot account for lower boundary influences, and this underlines the importance of the empirical relationships determined from this experimental study.

Chapter 7 Conclusions

Over the past several decades, desalination technologies have become a popular method of extracting and distributing potable water. A primary environmental drawback of this process is the resulting hyper-saline brine effluent. For modern large scale facilities this brine is discharged back into the ocean as an inclined negatively buoyant jet (INBJ) via an offshore pipeline and diffuser system. Due to global increase in the use of desalination technologies, numerous experimental studies have been conducted to examine this flow scenario and obtain empirical relationships for various parameters that characterise the flow behaviour. Concentration (or dilution) measurements have typically been used to describe the flow behaviour and results between different studies exhibit substantial discrepancies. Within the experimental literature, most studies have included a lower horizontal boundary to replicate the flow impinging the seabed, however its effect on the mixing processes within the measured flow region have not been specifically considered. The wide variation of lower boundary conditions used in different experimental programs has been proposed as a possible reason for the observed inconsistencies. This issue has been addressed in the present study where a series of experiments were conducted to investigate the influence of the boundary on various discharge configurations. The flow behaviour was portrayed using concentration measurements obtained using the laser induced fluorescence (LIF) method. A summary of the main findings from this study are presented below.

Boundary Interaction of Vertical Buoyant Jets

Boundary interaction was initially investigated using vertical buoyant jets. Each experiment included a buoyancy component and flows were classified as jet, transitional and plume type, depending on the extent to which buoyancy affected the measured flow region.

Jet discharges were assessed using concentration and velocity experimental data where non-dimensional source heights of between H/d = 36.30 – 173.30 were tested. A top-hat integral model was also developed to provide a simplistic framework for quantifying and interpreting jet behaviour. The influence of the boundary was illustrated using a number of flow parameters. Perpendicular flow profiles of mean concentration, intermittency and RMS measurements showed the reduced mixing ability of the flow within the impact region. Dilution and RMS concentrations measured along the centreline reflected these observations and displayed considerable changes in behaviour due to the presence of the boundary. The delineation of the impact region was determined based on the failure of the integral model to predict the flow behaviour. The critical parameter was found to be the flow spread which marked the start and end of the impact region based on the applicability of the linear spread assumption. This criteria defined an impact region that commenced at z/H = 0.86 (height of z/H = 0.14 from the lower boundary) and concluded at a radial distance of r/H = 0.30 from the impact point. Model predictions of the flow along boundary were reasonably consistent with experimental results however some discrepancies were observed when the minimum dilution was considered. Issues surrounding the validity of top-hat conversion factors and the possibility of boundary friction effects from changes in the experimental setup may have contributed to the observed inconsistencies.

Results from transitional and plume type flows showed that the influence of the boundary and the characteristics of the impact region were similar to jet experiments. Experiments were conducted for source heights ($H/F_0 d$) ranging from 3.24 – 6.16. Changes to the flow behaviour as a result of boundary interaction were evident through spread and centreline dilution measurements. The size of the impact region was again determined based on the applicability of the linear spread assumption. This defined the limits to be z/H = 0.88 and r/H = 0.28, which are similar to those for jet type discharges. These results demonstrated that the flow behaviour in the impact region is independent of conditions at the discharge source and is governed by the boundary. Along the boundary, the flow behaved differently to the jet case and was observed to physically collapse due to buoyancy effects. This marked the transition from the near field to the far field region where mixing with the ambient is limited. The flow was qualitatively analysed using concentration profiles and the transition to the far field region was reflected by the gradual distortion of concentration profiles away from the

familiar Gaussian form. The experimental results from these flow types indicated that a similar modelling framework to the jet case can be established. Adjustments would be required to model the flow along the boundary in order to account for changes to the flow profile and the transition to the far field mixing regime.

Inclined Negatively Buoyant Jets

Experiments on inclined negatively buoyant jets were conducted in unbounded ambient environments to provide an additional data set to Oliver et al. (2013), where boundary influences are removed from the measured flow region. This was ensured by placing the discharge location at least 720 mm above the bottom of the tank. Three discharge angles were considered (30^o 45^o and 60^o) and time-averaged geometric and dilution parameters were acquired from concentration fields.

Geometric and dilution results were extracted from the centreline and flow edge and displayed good consistency when scaled appropriately. In comparison to the literature, these results were generally within the scatter of data from past studies. Many of these studies utilised a lower boundary in their experimental setups however boundary influences could not be discerned from these comparisons. Dilution coefficients from the present study supported the findings from Oliver et al. (2013). It was evident that the dilution potential of the discharge increased when the lower boundary is removed from the vicinity of the measured flow field. Important insight into buoyancy induced instabilities was also ascertained from these experiments. Concentration profiles taken at various locations along the flow path illustrated the increasing asymmetry as a result of this flow feature. The asymmetric nature of the flow was also observed using spread measurements along the inner and outer sides of the discharge. Under the influence of these instabilities, inner spread measurements were shown to increase substantially faster than the outer spread. These observations correlated well with centreline dilution measurements. This was particularly evident within the plume region of the discharge where steeper discharge angles resulted in higher inner spreading rates as well as higher dilutions for a given path length.

Boundary Interaction of Inclined Negatively Buoyant Jets

To quantify the influence of the lower boundary, a separate series of experiments was conducted for the three discharge angles (30^o 45^o and 60^o) with the source height ($H/F_0 d$) varied between 0.058 and 1.84. Boundary influence was assessed by comparing dilution and geometric parameters to boundary free results from Chapter 5 and results reported in the literature.

At the maximum height, boundary influence was not evident as experimental coefficients displayed almost no difference when compared to the boundary free case. In contrast, numerous flow parameters recorded near the return point and impact region revealed substantial changes to the flow behaviour as a result of boundary interaction. Geometric coefficients recorded at this location were extended and outer spread measurements were shown to diverge from typical linear variations. Changes in the flow behaviour were also characterised by a sharp decrease in the flow's mixing ability and was demonstrated using perpendicular flow profiles and mean centreline dilution data. Centreline dilutions from each discharge angle were shown to closely match the corresponding boundary free case. However, near the return point further concentration decay was prevented and resulted in constant dilution up to the impact point. A detailed analysis of flow parameters near this region showed that the source height was a governing initial condition. For experiments conducted with small source heights, return point dilutions were lower than the boundary free case and would increase linearly up to a threshold source height. Above this threshold condition return point dilutions became constant and were relatively consistent with the corresponding boundary free result. Steeper discharge angles corresponded to larger threshold source heights, suggesting that this discharge configuration is more sensitive to boundary interaction. Comparisons with results from previous studies were performed using dilution ratios at the return point and impact point (S_r/S_m or S_i/S_m). When considered in the context of the source height, these measurements revealed a discernible relationship with this parameter. This result indicated that discrepancies between studies can be attributed in part to the presence of a lower boundary.

7.1 Scope for Future Research

There is considerable scope for further research on inclined negatively buoyant jets. The existing literature includes a plethora of 2-D concentration data. From an experimental perspective there is an opportunity to improve existing methods in order to obtain more detailed and reliable data. For example, 3-D LIF evaluations of INBJs require further examination. Existing 3-D systems are yet to provide consistent results and studies that have utilised this technique have not provided quantitatively significant results outside of the capabilities of 2-D systems. In particular, cross-sections perpendicular to the flow direction have not been analysed and may offer valuable insight into buoyancy induced instabilities. In addition, there is also potential to investigate INBJs using combined LIF and PTV systems. At present only a few studies have used this system and there is significant potential to obtain new information regarding the turbulent characteristics of the flow using turbulent flux measurements ($\overline{c'u'}$). Most experimental results have been generated for discharges released into idealised ambient environments. Practical ambient environments such as; flowing ambients, inclined lower boundaries, density stratified environments and free surface interaction could be further investigated.

Finally, more focus should be placed on developing versatile and reliable models. Integral models have largely been unsuccessful in representing INBJ behaviour as detrainment effects from the underside of the flow have proved difficult to replicate. Recent models have looked to address this issue however they are limited in their predictive capacities. Sophisticated CFD modelling techniques such as large eddy simulation (LES) provide more scope with which to develop this area of research. In addition, different ambient environments can potentially be incorporated into the modelling framework which is important from a design perspective.

Appendix A: MATLAB Processing Algorithm

```
% CALIBRATION ALGORITHM

% The relationship between the raw light intensity recorded from the camera
% and the concentration (recorded as laser wattage) is linear (i.e. in the
% form y = mx + c). For each pixel the gradient (m) and y-intercept (c) was
% determined. A default value of 0 was set as the y-intercept for all
% cases.

B1 = xlsread(''); % Blank image taken with calibration cell removed from
                  % the tank

A1 = xlsread(''); % Calibration image (Laser set at 1W)
A2 = xlsread(''); % Calibration image (Laser set at 2W)
A3 = xlsread(''); % Calibration image (Laser set at 3W)
A4 = xlsread(''); % Calibration image (Laser set at 4W)

[m,n] = size(B1);

% Removing background intensity from each calibration image
A1 = A1-B1;
A2 = A2-B1;
A3 = A3-B1;
A4 = A4-B1;

A1_new = zeros(m,n); %

% Concentration values tested (row vector, reocrded as laser wattage)
C = [0 1 2 3 4];

% Setting up 3-D matrix which will store each raw intensity value.
T = zeros(m, n, length(C));

% Filling the matrix (T) with each calibration image
T(:, :, 1) = A1_new;
T(:, :, 2) = A1;
T(:, :, 3) = A2;
T(:, :, 4) = A3;
T(:, :, 5) = A4;

% The concentration - intensity relationship for each pixel is stored in
% the array 'R' which includes the gradient and y-intercept (set at zero).

R = zeros(m,n,2);  % Contains the gradient and y-intercept values.
R1 = zeros(m,n);   % Contains correlation coefficients describing the
                   % goodness of fit of each linear relationship

for Q = 1:m
    for P = 1:n
        B =  [T(Q,P,1) T(Q,P,2) T(Q,P,3) T(Q,P,4) T(Q,P,5)];
        x = transpose(C);
        y = transpose(B);
        N=1;
        Nv = repmat(N:-1:1, length(x), 1);
        Xm = repmat(x, 1, N);
        DataMatrix = Xm.^Nv;
        Temp(1) = DataMatrix\y;
```

```
        Temp(2) = 0;
        R(Q,P,1) = Temp(1);
        R(Q,P,2) = Temp(2);
        yfit = zeros(1,length(B));
        ytot = zeros(1,length(B));
        yerror = zeros(1,length(B));
        for S = 1:length(B)
            yfit(1,S) = polyval(Temp,C(S));
            ytot(1,S) = (T(Q,P,S)-mean(B))^2;
            yerror(1,S) = (T(Q,P,S) -  yfit(1,S))^2;
        end
        SStot = sum(ytot);
        SSerror = sum(yerror);
        R1(Q,P) = 1-SSerror/SStot;
    end
end


% Raw intensity fields are converted into a calibrated concentration field
% using the array 'R'

Image_new = xlsread(''); % The time-averaged raw intensity image
Image_blank = B1;        % Blank image (no flow)

Image_new = Image_new-Image_blank;

[m,n] = size(Image_blank);

for Z = 1:m
    for X = 1:n
        Image_new(Z,X) = ((Image_new(Z,X)) - R(Z,X,2))/R(Z,X,1);
    end
end
```

```
% POST PROCESSING ALGORITHM - INCLINED FLOWS

% The following series of code provides a snapshot of the post processing
% method used to obtain time averaged flow information.
clear
clc

% The calibrated time averaged image is loaded into the algorithm. During
% the calibration process, the image was saved as 'Image_new'
load('')
Image = Image_new;

% The empty regions of the image were removed
Y_pos = '';
X_pos = '';
Image(1:Y_pos,:) = [];
Image(:,1:X_pos) = [];

% The initial conditions of the experiment are stated below
Fr_0 = '';                      % Froude Number
C_0 = '';                       % Initial Concentration
d = '';                         % Diameter (measured in pixels)

% The limits of analysis are stated below. These varied depending on the
% scale and relative positioning of the flow field within the image
So_Co_x = ''-X_pos;             % Starting x-coordinate
So_Co_y = ''-Y_pos;             % Starting y-coordinate
End_Co_x = ''-X_pos;            % Ending x-coordinate
End_Co_y = ''-Y_pos;            % Ending y-coordinate
Search_Origin_x = ''-X_pos;     % Search origin x-coordinate
Search_Origin_y = ''-Y_pos;     % Search origin y-coordinate

Source_Actual_x = ''-X_pos;     % Source x-coordinate
Source_Actual_y = ''-Y_pos;     % Source y-coordinate

% Number of slices/centreline points taken within the limits of analysis
No_Centreline_points = '';
No_Cross_Sections = No_Centreline_points;
No_Cross_Sections_Spread = No_Centreline_points;

[Max_y Max_x] = size(Image);

% The gradient of the start and end 'slice' taken from the search origin
% is calculated below
m_start =(Search_Origin_y-So_Co_y)/(Search_Origin_x-So_Co_x);
m_end = (Search_Origin_y-End_Co_y)/(Search_Origin_x-End_Co_x);

% The gradients of the slices calculated above are converted to angles

if So_Co_y > Search_Origin_y && So_Co_x > Search_Origin_x
    m_start = atan(m_start);
end
if So_Co_y > Search_Origin_y && So_Co_x < Search_Origin_x
    m_start = atan(m_start)+pi();
end
if So_Co_y < Search_Origin_y && So_Co_x < Search_Origin_x
```

```
    m_start = atan(m_start)+pi();
end
if So_Co_y < Search_Origin_y && So_Co_x > Search_Origin_x
    m_start = 2*pi()+atan(m_start);
end

if End_Co_y > Search_Origin_y && End_Co_x > Search_Origin_x
    m_end = atan(m_end);
end
if End_Co_y > Search_Origin_y && End_Co_x < Search_Origin_x
    m_end = atan(m_end)+pi();
end
if End_Co_y < Search_Origin_y && End_Co_x < Search_Origin_x
    m_end = atan(m_end)+pi();
end
if End_Co_y < Search_Origin_y && End_Co_x > Search_Origin_x
    m_end = 2*pi()+atan(m_end);
end

% Based on the number of centreline points chosen, the increment between
% slices is calculated below
Ang_increment = ((m_end) - (m_start))/No_Centreline_points;

% An initial estimation of the centreline profile is determined by taking
% slices through the flow field, starting from the search origin
Gradient_matrix = zeros(No_Centreline_points+1,1);
Intercept_y = zeros(No_Centreline_points+1,1);
Centreline_Coordinates = zeros((No_Centreline_points+1),3);

for I = 1:length(Gradient_matrix)
    % The equation of the slice taken from the search origin and through
    % the flow field is calculated. Concentration values and x and
    % y-coordinates along this slice are stored in the 'Centre_Line' array
    Gradient_matrix(I) = tan((m_start+Ang_increment*(I-1)));
    Intercept_y(I) = Search_Origin_y-Gradient_matrix(I)*Search_Origin_x;
    if abs(atan(Gradient_matrix(I)))<(pi()/4)
        Centre_Line = zeros(3,(Max_x-1+1));
        for G = Search_Origin_x:Max_x
            y = round(Gradient_matrix(I)*G+Intercept_y(I));
            if y > 0 && y < Max_y
                Centre_Line(1,G) = G;          % x-coordinate
                Centre_Line(2,G) = y;          % y-coordinate
                Centre_Line(3,G) = Image(y,G); % Concentration
            else
                Centre_Line(1,G) = 1;
                Centre_Line(2,G) = G;
                Centre_Line(3,G) = 0;
            end
        end
    else
        if abs(atan(Gradient_matrix(I)))>(pi()/4)
            Centre_Line = zeros(3,(Max_y-1+1));
            for J = Search_Origin_y:Max_y
                x = round((J-Intercept_y(I))/Gradient_matrix(I));
                if x > 0 && x < Max_x
                    Centre_Line(1,J) = x;
                    Centre_Line(2,J) = J;
```

```
                    Centre_Line(3,J) = Image(J,x);
                else
                    Centre_Line(1,J) = 1;
                    Centre_Line(2,J) = J;
                    Centre_Line(3,J) = 0;
                end
            end
        end
    end

    [m Col] = max(Centre_Line(3,:));

    Centreline_Coordinates(I,1) = Centre_Line(1,Col); % x-coordinate
    Centreline_Coordinates(I,2) = Centre_Line(2,Col); % y-coordinate
    Centreline_Coordinates(I,3) = Centre_Line(3,Col); % Centreline
                                                        Concentration
end

% The centreline profile is modelled as a 4th order polynomial
[fitobject,gof,output] =
fit(Centreline_Coordinates(:,1),Centreline_Coordinates(:,2),'poly4');

% Using the estimate taken above, the centreline position is refined.
% Perpendicular lines are taken from the centreline profile to determine a
% new centreline position.
No_iterations_1 = '';                % Number of iterations
R_Square = zeros(No_iterations_1,1); % R^2 values (Correlation
                                     % coefficients)

x_increment = round((abs(So_Co_x - End_Co_x))/No_Cross_Sections);

for M = 1:length(R_Square)
    Centreline_Coordinates_New = zeros((No_Cross_Sections+1),6);
    for C = 1:No_Cross_Sections+1
        F = So_Co_x+x_increment*(C-1);
        % The equation of the perpendicular lines passing through each
        % centreline point is calculated. Concentration values and x and
        % y-coordinates along this line are stored in the
         'Centre_Line_Temp' array
        Deriv_Y = round(feval(fitobject,F));
        DerivGrad = differentiate(fitobject,F);
        Deriv_Grad = -1/DerivGrad;
        Deriv_Y_Int = Deriv_Y-Deriv_Grad*F;
        if abs(atan(Deriv_Grad))<(pi()/4)
            Centre_Line_Temp = zeros(4,Max_x);
            for W = 1:Max_x
                y = round(Deriv_Grad*W+Deriv_Y_Int);
                if y > 0 && y < Max_y
                    Centre_Line_Temp(1,W) = W;          % x-coordinate
                    Centre_Line_Temp(2,W) = y;          % y-coordinate
                    Centre_Line_Temp(3,W) = Image(y,W); % Concentration
                else
                    Centre_Line_Temp(1,W) = W;
                    Centre_Line_Temp(2,W) = 0;
                    Centre_Line_Temp(3,W) = 0;
                end
            end
```

```
else
    if abs(atan(Deriv_Grad))>(pi()/4)
        Centre_Line_Temp = zeros(4,Max_y);
        for E = 1:Max_y
            x = round((E-Deriv_Y_Int)/Deriv_Grad);
            if x > 0 && x < Max_x
                Centre_Line_Temp(1,E) = x;
                Centre_Line_Temp(2,E) = E;
                Centre_Line_Temp(3,E) = Image(E,x);
            else
                Centre_Line_Temp(1,E) = 0;
                Centre_Line_Temp(2,E) = E;
                Centre_Line_Temp(3,E) = 0;
            end
        end
    end
end

[m Col] = max(Centre_Line_Temp(3,:));

% Centreline properties are extracted from the
  'Centreline_Line_Temp' array

% Centreline x-coordinate
Centreline_Coordinates_New(C,1) = Centre_Line_Temp(1,Col);

% Centreline y-coordinate
Centreline_Coordinates_New(C,2) = Centre_Line_Temp(2,Col);

% Centreline Concentration
Centreline_Coordinates_New(C,3) = Centre_Line_Temp(3,Col);

% Calculating Spread
Spread = m*exp(-1);
for X = 1:length(Centre_Line_Temp)
    Centre_Line_Temp(4,X) = Centre_Line_Temp(3,X)-Spread;
    if Centre_Line_Temp(4,X) < 0 && X > Col
        break
    end
end

row = X;
row1 = X-1;

C_Actual = Spread;

Conc_1 = Centre_Line_Temp(3,row);
Conc_2 = Centre_Line_Temp(3,row1);

Spread_1 = sqrt((Centre_Line_Temp(2,Col)-
           Centre_Line_Temp(2,row))^2+(Centre_Line_Temp(1,Col)-
           Centre_Line_Temp(1,row))^2);
Spread_2 = sqrt((Centre_Line_Temp(2,Col)-
           Centre_Line_Temp(2,row1))^2+(Centre_Line_Temp(1,Col)-
           Centre_Line_Temp(1,row1))^2);

Centreline_Coordinates_New(C,4) = Spread_2+(Spread_1-
```

```
                                        Spread_2)*(C_Actual-
                                        Conc_2)/(Conc_1-Conc_2);
    end

    % The centreline profile is modelled as a 4th order polynomial and the
    % R^2 value is calculated.
    [fitobject,gof,output] =
    fit(Centreline_Coordinates_New(:,1),Centreline_Coordinates_New(:,2),
    'poly4');

    for H = 1:length(Centreline_Coordinates_New(:,1))

        Centreline_Coordinates_New(H,5) =
        round(feval(fitobject,Centreline_Coordinates_New(H,1)));

        Centreline_Coordinates_New(H,6) = (Centreline_Coordinates_New(H,5)-
        Centreline_Coordinates_New(H,2))^2;

        Centreline_Coordinates_New(H,7) = (Centreline_Coordinates_New(H,2)-
        mean(Centreline_Coordinates_New(:,2)))^2;
    end

    SS_Tot = sum(Centreline_Coordinates_New(:,7));
    SS_Err = sum(Centreline_Coordinates_New(:,6));
    R_Square(M,1) = 1-(SS_Err/SS_Tot);

end

% The centreline position is further refined by modelling perpendicular
% concentration profiles as gaussian curves for each centreline point.
No_Iterations_2 = '';
R_Square_New = zeros(No_Iterations_2,1);
x_increment_spread = round((abs(So_Co_x -
End_Co_x))/No_Cross_Sections_Spread);
New_Centreline_Position = zeros(No_Cross_Sections_Spread+1,7);

for L = 1:length(R_Square_New)
    for C = 1:No_Cross_Sections_Spread+1
        F = So_Co_x+x_increment_spread*(C-1);

        % The equation of the perpendicular lines passing through each
        % centreline point is calculated. Concentration values and x and
        % y-coordinates along this line are stored in the
        % 'Centre_Line_Temp' array
        Deriv_Y = round(feval(fitobject,F));
        DerivGrad = differentiate(fitobject,F);
        Deriv_Grad = -1/DerivGrad;
        Deriv_Y_Int = Deriv_Y-Deriv_Grad*F;
        if abs(atan(Deriv_Grad))<(pi()/4) && Deriv_Grad < 0
            Centre_Line_Temp = zeros(3,round(F*1.4));
            for W = 1:round(F*1.4)
                y = round(Deriv_Grad*W+Deriv_Y_Int);
                if y > 0 && y < Max_y
                    Centre_Line_Temp(1,W) = W;
                    Centre_Line_Temp(2,W) = y;
                    Centre_Line_Temp(3,W) = Image(y,W);
                else
```

```
            Centre_Line_Temp(1,W) = 0;
            Centre_Line_Temp(2,W) = 0;
            Centre_Line_Temp(3,W) = 0;
        end
    end
end

if abs(atan(Deriv_Grad))>(pi()/4)
    Centre_Line_Temp = zeros(3,Max_y);
    for E = round(0.7*Deriv_Y):Max_y
        x = round((E-Deriv_Y_Int)/Deriv_Grad);
        if x > 0 && x < Max_x
            Centre_Line_Temp(1,E) = x;
            Centre_Line_Temp(2,E) = E;
            Centre_Line_Temp(3,E) = Image(E,x);
        else
            Centre_Line_Temp(1,E) = 0;
            Centre_Line_Temp(2,E) = 0;
            Centre_Line_Temp(3,E) = 0;
        end
    end
end

if abs(atan(Deriv_Grad))<(pi()/4) && Deriv_Grad > 0
    Centre_Line_Temp = zeros(3,Max_x);
    for W = round(0.7*F):Max_x
        y = round(Deriv_Grad*W+Deriv_Y_Int);
        if y > 0 && y < Max_y
            Centre_Line_Temp(1,W) = W;
            Centre_Line_Temp(2,W) = y;
            Centre_Line_Temp(3,W) = Image(y,W);
        else
            Centre_Line_Temp(1,W) = 0;
            Centre_Line_Temp(2,W) = 0;
            Centre_Line_Temp(3,W) = 0;
        end
    end
end

% Concentration values between -0.25 < r/bc < 2 are extracted from
% 'Centre_Line_Temp' and stored in 'Centre_Line_Temp_new'
[max_val pos] = max(Centre_Line_Temp(3,:));
Centre_Line_Temp_new = zeros(6,length(Centre_Line_Temp(1,:)));
for Q = 1:length(Centre_Line_Temp(1,:))
    if abs(atan(Deriv_Grad))<(pi()/4) && Deriv_Grad < 0
        if Centre_Line_Temp(1,Q) < Centre_Line_Temp(1,pos)
            if sqrt((Centre_Line_Temp(2,Q)-
               Centre_Line_Temp(2,pos))^2+(Centre_Line_Temp(1,Q)-
               Centre_Line_Temp(1,pos))^2) < 1.0*Spread_bc(C,1)

                Centre_Line_Temp_new(3,Q) =
                sqrt((Centre_Line_Temp(2,Q) -
                Centre_Line_Temp(2,pos))^2 +
                (Centre_Line_Temp(1,Q) -
                Centre_Line_Temp(1,pos))^2);
                Centre_Line_Temp_new(1,Q) = Centre_Line_Temp(1,Q);
                Centre_Line_Temp_new(2,Q) = Centre_Line_Temp(2,Q);
                Centre_Line_Temp_new(4,Q) = Centre_Line_Temp(3,Q);
```

```
            end
        else
            if sqrt((Centre_Line_Temp(2,Q)-
                Centre_Line_Temp(2,pos))^2+(Centre_Line_Temp(1,Q)-
                Centre_Line_Temp(1,pos))^2) < 0.25*Spread_bc(C,1);

                 Centre_Line_Temp_new(3,Q) = -
                 sqrt((Centre_Line_Temp(2,Q)-
                 Centre_Line_Temp(2,pos))^2 +
                 (Centre_Line_Temp(1,Q)-
                 Centre_Line_Temp(1,pos))^2);
                 Centre_Line_Temp_new(1,Q) = Centre_Line_Temp(1,Q);
                 Centre_Line_Temp_new(2,Q) = Centre_Line_Temp(2,Q);
                 Centre_Line_Temp_new(4,Q) = Centre_Line_Temp(3,Q);
            end
        end
    end

    if abs(atan(Deriv_Grad))>(pi()/4)
        if Centre_Line_Temp(2,Q) > Centre_Line_Temp(2,pos)
            if sqrt((Centre_Line_Temp(2,Q)-
               Centre_Line_Temp(2,pos))^2+(Centre_Line_Temp(1,Q)-
               Centre_Line_Temp(1,pos))^2) < 1.0*Spread_bc(C,1)

                Centre_Line_Temp_new(3,Q) =
                sqrt((Centre_Line_Temp(2,Q)-
                Centre_Line_Temp(2,pos))^2
                +(Centre_Line_Temp(1,Q)-
                Centre_Line_Temp(1,pos))^2);
                Centre_Line_Temp_new(1,Q) = Centre_Line_Temp(1,Q);
                Centre_Line_Temp_new(2,Q) = Centre_Line_Temp(2,Q);
                Centre_Line_Temp_new(4,Q) = Centre_Line_Temp(3,Q);
            end
        else
            if sqrt((Centre_Line_Temp(2,Q) -
               Centre_Line_Temp(2,pos))^2 +
               (Centre_Line_Temp(1,Q) -
               Centre_Line_Temp(1,pos))^2) < 0.25*Spread_bc(C,1);

                Centre_Line_Temp_new(3,Q) = -
                sqrt((Centre_Line_Temp(2,Q)-
                Centre_Line_Temp(2,pos))^2 +
                (Centre_Line_Temp(1,Q)-
                Centre_Line_Temp(1,pos))^2);
                Centre_Line_Temp_new(1,Q) = Centre_Line_Temp(1,Q);
                Centre_Line_Temp_new(2,Q) = Centre_Line_Temp(2,Q);
                Centre_Line_Temp_new(4,Q) = Centre_Line_Temp(3,Q);
            end
        end
    end

    if abs(atan(Deriv_Grad))<(pi()/4) && Deriv_Grad > 0
        if Centre_Line_Temp(1,Q) > Centre_Line_Temp(1,pos)
            if sqrt((Centre_Line_Temp(2,Q) -
            Centre_Line_Temp(2,pos))^2 +
            (Centre_Line_Temp(1,Q) -
            Centre_Line_Temp(1,pos))^2) < 1.0*Spread_bc(C,1)
```

```
                    Centre_Line_Temp_new(3,Q) =
                    sqrt((Centre_Line_Temp(2,Q) -
                    Centre_Line_Temp(2,pos))^2 +
                    (Centre_Line_Temp(1,Q)-
                    Centre_Line_Temp(1,pos))^2);
                    Centre_Line_Temp_new(1,Q) = Centre_Line_Temp(1,Q);
                    Centre_Line_Temp_new(2,Q) = Centre_Line_Temp(2,Q);
                    Centre_Line_Temp_new(4,Q) = Centre_Line_Temp(3,Q);
                end
            else
                if sqrt((Centre_Line_Temp(2,Q) -
                Centre_Line_Temp(2,pos))^2 +
                (Centre_Line_Temp(1,Q) -
                Centre_Line_Temp(1,pos))^2) < 0.25*Spread_bc(C,1);

                    Centre_Line_Temp_new(3,Q) =
                    -sqrt((Centre_Line_Temp(2,Q)-
                    Centre_Line_Temp(2,pos))^2 +
                    (Centre_Line_Temp(1,Q) -
                    Centre_Line_Temp(1,pos))^2);
                    Centre_Line_Temp_new(1,Q) = Centre_Line_Temp(1,Q);
                    Centre_Line_Temp_new(2,Q) = Centre_Line_Temp(2,Q);
                    Centre_Line_Temp_new(4,Q) = Centre_Line_Temp(3,Q);
                end
            end
        end
    end

    % 'Centre_Line_Temp_new' includes zeros at either ends of the
    % array. The location of the non-zero values need to be identified
    if Centre_Line_Temp_new(1,1) > 0
        Start_Col = 1;
    end

    for S = 2:length(Centre_Line_Temp_new(1,:))
        if Centre_Line_Temp_new(1,S-1) == 0 &&
           Centre_Line_Temp_new(1,S) > 0
            Start_Col = S;
        end
        if Centre_Line_Temp_new(1,S-1) > 0 && Centre_Line_Temp_new(1,S)
           == 0
            End_Col = S-1;
        end
        if S == length(Centre_Line_Temp_new(1,:)) &&
           Centre_Line_Temp_new(1,S) > 0
            End_Col = S;
        end
    end

    % Fitting Gaussian profile to cross-sections and extracting
    % centreline concentration and spread
    r_profile = Centre_Line_Temp_new(3,Start_Col:End_Col)
    c_profile = Centre_Line_Temp_new(4,Start_Col:End_Col)
    gauss_fit = fit(r_profile,c_profile,'gauss1');
    Coeff_Val = coeffvalues(gauss_fit);
    C_m = Coeff_Val(1); % Centreline concentration
```

```
        r_o = Coeff_Val(2); % Offset from centreline
        b_c = Coeff_Val(3); % Spread


        for T = Start_Col:End_Col
            Centre_Line_Temp_new(6,T) = Centre_Line_Temp_new(3,T) - r_o;
        end

        for O = Start_Col+1:End_Col
            if Centre_Line_Temp_new(6,O)/Centre_Line_Temp_new(6,O-1)<0
                row2 = O;
                row3 = O-1;
            end
        end

        % Centreline properties are extracted from the above analysis and
        % stored in the 'New_Centreline_Position' array

        New_Centreline_Position(C,1) =
        round(Centre_Line_Temp_new(1,row3)+(Centre_Line_Temp_new(1,row2)-
        Centre_Line_Temp_new(1,row3))*(r_o-
        Centre_Line_Temp_new(3,row3))/(Centre_Line_Temp_new(3,row2)-
        Centre_Line_Temp_new(3,row3))); % x-coordinate

        New_Centreline_Position(C,2) =
        round(Centre_Line_Temp_new(2,row3)+(Centre_Line_Temp_new(2,row2)-
        Centre_Line_Temp_new(2,row3))*(r_o-
        Centre_Line_Temp_new(3,row3))/(Centre_Line_Temp_new(3,row2)-
        Centre_Line_Temp_new(3,row3))); % y-coordinate

        New_Centreline_Position(C,3) = C_m; % Centreline Concetration

        New_Centreline_Position(C,4) = b_c; % Spread

    end

    % The centreline profile is modelled as a 4th order polynomial and the
    % R^2 value is calculated.
    [fitobject,gof,output] =
    fit(New_Centreline_Position(:,1),New_Centreline_Position(:,2),'poly4');

    for H = 1:length(New_Centreline_Position(:,1))
        New_Centreline_Position(H,5) =
        round(feval(fitobject,New_Centreline_Position(H,1)));

        New_Centreline_Position(H,6) = (New_Centreline_Position(H,5)-
                                        New_Centreline_Position(H,2))^2;
        New_Centreline_Position(H,7) = (New_Centreline_Position(H,2)-
                                       mean(New_Centreline_Position(:,2)))^2;
    end

    SS_Tot = sum(New_Centreline_Position(:,7));
    SS_Err = sum(New_Centreline_Position(:,6));

    R_Square_New(L,1) = 1-(SS_Err/SS_Tot);

end
```

```
% Non-dimensionalising centreline statistics

Final_Centreline = zeros(No_Cross_Sections_Spread+1,4);

% x-coordinate
Final_Centreline(:,1) = New_Centreline_Position(:,1)./(d*Fr_0)-
                        Source_Actual_x./(d*Fr_0);

% y-coordinate
Final_Centreline(:,2) = New_Centreline_Position(:,2)./(d*Fr_0)-
                        Source_Actual_y./(d*Fr_0);

% Centreline Concentration
Final_Centreline(:,3) = C_0./(New_Centreline_Position(:,3).*Fr_0);

% Spread
Final_Centreline(:,4) = New_Centreline_Position(:,4)./(d*Fr_0);
```

Appendix B: Experimental Conditions and Coefficients

Table B.1: Experimental Conditions, Vertical Buoyant Jets, Chapter 4.

Jet Experiments, Present Study (LIF)						Jet Experiments, Crowe (2013) (PTV)					Transitional and Plume Experiments, Present Study (LIF)					
H/d	$\frac{H}{F_0 d}$	H (mm)	d (mm)	U_0 (m/s)	Re_0	H/d	H (mm)	d (mm)	U_0 (m/s)	Re_0	$\frac{H}{F_0 d}$	H (mm)	d (mm)	F_0	U_0 (m/s)	Re_0
36.74	*0.307*	*164*	*4.52*	*0.835*	*3775*	*79.09*	*348*	*4.40*	*0.805*	*3230*	*3.25*	*274*	*4.52*	*18.63*	*0.672*	*3035*
46.77	*0.125*	*152*	*3.25*	*1.88*	*6116*	*90.91*	*400*	*4.40*	*0.804*	*3205*	*4.08*	*352*	*4.52*	*19.10*	*0.689*	*3113*
54.00	*0.386*	*244*	*4.52*	*0.854*	*3859*	*113.64*	*500*	*4.40*	*0.803*	*3184*	*4.76*	*423*	*4.52*	*19.67*	*0.777*	*3512*
67.69	*0.185*	*220*	*3.25*	*1.85*	*6008*						*5.12*	*431*	*4.52*	*18.63*	*0.672*	*3035*
70.80	*0.423*	*320*	*4.52*	*0.859*	*3884*						*5.87*	*501*	*4.52*	*18.89*	*0.746*	*3373*
87.00	*0.237*	*283*	*3.25*	*1.72*	*5579*						*6.16*	*553*	*4.52*	*19.87*	*0.715*	*3230*
98.45	*0.522*	*442*	*4.52*	*0.968*	*4373*											
104.7	*0.174*	*244*	*2.33*	*2.57*	*5979*											
108.4	*0.298*	*352*	*3.25*	*1.70*	*5529*											
135.7	*0.234*	*316*	*2.33*	*2.48*	*5768*											
173.3	*0.473*	*563*	*3.25*	*1.72*	*5579*											

Table B.2: Experimental Conditions and Coefficients, Boundary Free Experiments, Chapter 5.

Initial Conditions					Maximum Height					Return Point			
θ_0	d (mm)	F_0	U_0 (m/s)	Re_0	x_m/d	z_m/d	z_{me}/d	s_m/d	C_0/C_m	x_r/d	x_{re}/d	s_r/d	C_0/C_r
30	*4.32*	*21.00*	*0.81*	*3500*	*37.05*	*13.33*	*24.65*	*39.55*	*7.11*	*65.22*	*88.94*	*72.24*	*16.57*
30	*3.25*	*33.84*	*1.13*	*3684*	*57.39*	*21.30*	*38.68*	*63.41*	*11.44*	*99.38*	*136.46*	*110.01*	*26.44*
30	*3.25*	*41.21*	*1.38*	*4486*	*68.85*	*25.96*	*46.86*	*75.13*	*13.00*	*117.11*	*172.35*	*130.05*	*31.26*
30	*2.33*	*51.34*	*1.45*	*3389*	*89.85*	*31.82*	*59.19*	*95.29*	*17.87*	*157.00*	*206.57*	*173.54*	*41.17*
30	*2.33*	*59.76*	*1.70*	*3962*	*98.46*	*36.23*	*64.00*	*107.41*	*20.48*	*169.94*	*230.71*	*190.11*	*50.61*
30	*2.33*	*69.14*	*1.51*	*3527*	*116.76*	*42.29*	*80.36*	*126.19*	*23.25*	*204.12*	*278.98*	*227.24*	*54.85*
45	*4.52*	*25.78*	*0.80*	*3598*	*49.81*	*28.77*	*44.77*	*55.18*	*9.91*	*82.23*	*118.37*	*105.66*	*31.96*
45	*4.52*	*31.22*	*0.96*	*4357*	*57.14*	*35.82*	*53.89*	*69.88*	*12.99*	*98.72*	*142.52*	*126.58*	*41.21*
45	*4.52*	*37.13*	*1.15*	*5182*	*66.57*	*41.35*	*63.07*	*78.75*	*14.56*	*114.00*	*157.35*	*147.13*	*44.65*
45	*4.52*	*44.85*	*1.38*	*6259*	*82.67*	*50.41*	*75.72*	*95.90*	*16.86*	*133.75*	*196.33*	*176.66*	*55.74*
45	*3.25*	*56.83*	*1.49*	*4836*	*106.16*	*63.02*	*96.10*	*121.65*	*22.07*	*175.56*	*247.59*	*225.87*	*69.51*
45	*2.33*	*64.21*	*1.82*	*4243*	*111.86*	*68.59*	*106.17*	*134.97*	*24.05*	*202.74*	*278.47*	*254.96*	*79.81*
60	*4.52*	*22.88*	*0.71*	*3202*	*34.11*	*35.65*	*50.04*	*50.66*	*9.42*	*57.55*	*84.78*	*97.11*	*35.38*
60	*4.52*	*24.30*	*0.74*	*3366*	*36.77*	*38.22*	*54.78*	*54.26*	*10.02*	*60.71*	*96.46*	*103.96*	*34.96*
60	*4.52*	*29.97*	*0.92*	*4152*	*45.20*	*46.86*	*65.98*	*67.49*	*12.55*	*76.04*	*111.55*	*127.50*	*46.15*
60	*4.52*	*36.82*	*0.89*	*4044*	*57.02*	*57.45*	*84.10*	*81.75*	*15.13*	*92.35*	*136.48*	*156.87*	*57.77*
60	*3.25*	*48.58*	*1.13*	*3677*	*71.58*	*74.79*	*109.33*	*109.59*	*19.88*	*120.25*	*201.86*	*202.93*	*70.65*
60	*2.33*	*53.99*	*1.54*	*3579*	*84.88*	*81.87*	*117.27*	*120.40*	*23.12*	*143.00*	*209.87*	*230.45*	*77.70*
60	*2.33*	*60.51*	*1.72*	*4012*	*91.74*	*91.79*	*131.57*	*133.98*	*25.78*	*154.78*	*219.52*	*256.41*	*87.82*
60	*2.33*	*61.80*	*1.76*	*4098*	*91.41*	*92.94*	*137.19*	*136.19*	*25.92*	*147.40*	*229.69*	*251.27*	*92.10*

Table B.3: Experimental Conditions and Coefficients, 30° Boundary Experiments, Chapter 6.

Initial Conditions							Maximum Height					Return Point/Impact Point					
θ_0	$\frac{H}{F_0 d}$	d (mm)	F_0	H (mm)	U_0 (m/s)	Re_0	x_m/d	z_m/d	z_{me}/d	s_m/d	C_0/C_m	x_r/d	x_{re}/d	s_r/d	z_b/d	C_0/C_r	C_0/C_i
30	*0.129*	*3.25*	*52.47*	*22*	*1.75*	*5702*	*87.38*	*33.68*	*57.27*	*93.36*	*16.87*	*162.18*		*177.89*	*0.26*	*37.93*	*38.32*
30	*0.168*	*3.25*	*40.20*	*22*	*1.34*	*4368*	*66.59*	*24.91*	*43.90*	*71.96*	*12.89*	*120.45*		*132.26*	*0.08*	*30.54*	*30.54*
30	*0.191*	*3.25*	*51.67*	*32*	*1.34*	*4357*	*87.51*	*32.47*	*57.67*	*98.74*	*17.92*	*158.49*		*172.52*	*0.17*	*36.72*	*36.72*
30	*0.227*	*4.52*	*31.20*	*32*	*0.95*	*4310*	*54.71*	*19.78*	*35.53*	*57.06*	*10.49*	*99.13*		*107.60*	*0.16*	*23.32*	*23.32*
30	*0.334*	*4.52*	*21.20*	*32*	*0.65*	*2932*	*37.24*	*12.97*	*23.73*	*40.24*	*7.11*	*62.41*		*68.89*	*0.04*	*16.20*	*16.20*
30	*0.387*	*3.25*	*63.62*	*80*	*1.65*	*5372*	*109.70*	*41.13*	*69.74*	*118.80*	*21.22*	*192.89*	*314.02*	*214.49*	*0.05*	*54.60*	*55.62*
30	*0.465*	*3.25*	*52.88*	*80*	*1.37*	*4465*	*89.53*	*33.72*	*58.46*	*96.65*	*17.61*	*149.83*	*222.42*	*170.03*	*-0.02*	*42.18*	*43.97*
30	*0.530*	*4.52*	*33.38*	*80*	*1.02*	*4622*	*59.62*	*22.19*	*37.91*	*62.52*	*11.46*	*104.02*	*154.46*	*114.70*	*-0.07*	*27.15*	*28.79*
30	*0.601*	*3.25*	*66.01*	*129*	*1.71*	*5573*	*112.46*	*41.85*	*74.33*	*122.87*	*22.22*	*203.46*	*278.09*	*223.64*	*-0.15*	*54.88*	*60.62*
30	*0.749*	*3.25*	*53.00*	*129*	*1.38*	*4475*	*91.29*	*34.68*	*59.66*	*97.31*	*17.53*	*161.42*	*210.01*	*179.59*	*-0.25*	*45.52*	*53.66*
30	*0.822*	*3.25*	*32.20*	*86*	*1.11*	*3598*	*53.21*	*19.31*	*35.31*	*58.41*	*10.56*	*95.55*	*137.39*	*106.14*	*-0.34*	*26.17*	*34.63*
30	*0.842*	*4.52*	*21.01*	*80*	*0.64*	*2910*	*37.13*	*13.49*	*24.08*	*41.12*	*7.03*	*65.24*	*93.48*	*72.43*	*-0.4*	*17.65*	*21.58*
30	*0.846*	*4.52*	*34.01*	*130*	*1.04*	*4710*	*62.88*	*21.73*	*39.25*	*62.97*	*11.65*	*107.38*	*156.72*	*119.36*	*-0.36*	*27.31*	*33.83*
30	*0.973*	*4.32*	*23.80*	*100*	*0.92*	*3964*	*41.35*	*14.80*	*25.71*	*44.00*	*7.85*	*72.21*	*105.52*	*79.44*	*-0.59*	*19.43*	*27.94*
30	*1.09*	*4.32*	*20.10*	*95*	*0.77*	*3347*	*35.43*	*12.33*		*37.93*	*6.53*	*59.59*	*87.41*	*65.70*	*-0.79*	*15.58*	*23.98*
30	*1.24*	*4.32*	*18.70*	*100*	*0.72*	*3114*	*33.16*	*11.23*	*21.25*	*34.62*	*6.26*	*56.31*	*78.64*	*63.11*	*-0.9*	*15.03*	*24.42*
30	*1.31*	*4.52*	*22.00*	*130*	*0.67*	*3047*	*37.67*	*13.71*	*24.50*	*40.56*	*7.22*	*65.41*	*88.84*	*72.27*	*-0.74*	*17.68*	*26.48*

Table B.4: Experimental Conditions and Coefficients, 45º Boundary Experiments, Chapter 6.

Initial Conditions							Maximum Height					Return Point/Impact Point					
θ_0	$\frac{H}{F_0 d}$	d (mm)	F_0	H (mm)	U_0 (m/s)	Re_0	x_m/d	z_m/d	z_{me}/d	s_m/d	C_0/C_m	x_r/d	x_{re}/d	s_r/d	z_b/d	C_0/C_r	C_0/C_i
45	*0.156*	*3.25*	*63.15*	*32*	*1.64*	*5334*	*109.70*	*69.02*	*105.94*	*133.87*	*24.38*	*196.28*		*245.73*	*21.98*	*61.45*	*61.45*
45	*0.208*	*4.52*	*33.00*	*31*	*1.01*	*4572*	*63.35*	*35.82*	*54.85*	*73.75*	*13.00*	*104.76*		*132.23*	*9.71*	*33.61*	*33.61*
45	*0.338*	*4.52*	*20.32*	*31*	*0.62*	*2815*	*37.01*	*22.31*	*34.24*	*44.90*	*8.03*	*65.96*		*81.81*	*1.52*	*21.82*	*21.82*
45	*0.476*	*2.33*	*69.41*	*77*	*1.85*	*4315*	*129.88*	*75.20*	*113.57*	*152.29*	*26.87*	*215.64*	*348.60*	*275.71*	*3.72*	*77.43*	*77.43*
45	*0.650*	*2.33*	*52.13*	*79*	*1.48*	*3453*	*93.12*	*56.66*	*87.36*	*111.59*	*20.24*	*156.48*	*229.94*	*203.23*	*-4.71*	*62.53*	*59.80*
45	*0.664*	*3.25*	*36.15*	*78*	*1.14*	*3692*	*63.60*	*41.01*	*61.00*	*76.09*	*13.45*	*111.48*	*160.38*	*141.96*	*-6.01*	*46.66*	*40.89*
45	*0.777*	*4.52*	*22.50*	*79*	*0.69*	*3106*	*40.05*	*24.72*	*38.17*	*47.41*	*8.52*	*67.46*	*97.25*	*87.88*	*-2.97*	*29.39*	*27.04*
45	*0.822*	*3.25*	*32.20*	*86*	*1.11*	*3611*	*54.22*	*35.67*	*52.56*	*65.82*	*12.74*	*99.72*	*151.21*	*127.25*	*-5.85*	*43.70*	*41.04*
45	*1.10*	*3.25*	*35.68*	*128*	*1.19*	*3873*	*64.45*	*38.00*	*57.84*	*76.24*	*13.70*	*107.43*	*155.46*	*138.62*	*-21.22*	*52.05*	*40.33*
45	*1.12*	*2.33*	*49.13*	*128*	*1.40*	*3254*	*85.62*	*53.86*	*84.05*	*103.30*	*19.14*	*146.88*	*217.24*	*192.33*	*-24.78*	*69.12*	*56.70*
45	*1.19*	*3.25*	*33.06*	*128*	*1.10*	*3589*	*59.85*	*36.86*	*55.11*	*71.85*	*12.83*	*102.72*	*144.88*	*132.24*	*-17.67*	*49.97*	*39.36*
45	*1.50*	*4.32*	*19.94*	*129*	*0.77*	*3317*	*33.71*	*21.93*	*33.34*	*42.33*	*7.64*	*61.01*	*91.27*	*78.84*	*-17.84*	*32.20*	*24.41*

Table B.5: Experimental Conditions and Coefficients, 60º Boundary Experiments, Chapter 6.

Initial Conditions							Maximum Height					Return Point/Impact Point					
θ_0	$\frac{H}{F_0 d}$	d (mm)	F_0	H (mm)	U_0 (m/s)	Re_0	x_m/d	z_m/d	z_{me}/d	s_m/d	C_0/C_m	x_r/d	x_{re}/d	s_r/d	z_b/d	C_0/C_r	C_0/C_i
60	*0.058*	*4.52*	*38.07*	*10*	*1.18*	*5313*	*58.01*	*58.66*	*82.86*	*85.14*	*15.90*	*96.72*		*161.17*	*14.30*	*41.05*	*41.05*
60	*0.081*	*4.52*	*27.45*	*10*	*0.85*	*3831*	*41.35*	*43.05*	*61.63*	*61.61*	*11.26*	*69.74*		*116.89*	*13.11*	*30.50*	*30.50*
60	*0.273*	*2.33*	*48.70*	*31*	*1.30*	*3024*	*71.82*	*74.18*	*106.82*	*109.42*	*19.98*	*126.27*		*203.04*	*6.38*	*58.34*	*58.34*
60	*0.293*	*3.25*	*32.55*	*31*	*1.02*	*3311*	*49.26*	*50.72*	*73.27*	*73.49*	*13.08*	*84.08*		*140.21*	*8.36*	*37.89*	*37.89*
60	*0.321*	*4.52*	*22.72*	*33*	*0.84*	*3791*	*32.73*	*35.86*	*51.59*	*50.19*	*8.92*	*59.77*		*96.28*	*0.26*	*30.26*	*30.26*
60	*0.373*	*4.52*	*19.55*	*33*	*0.73*	*3285*	*29.14*	*30.89*	*44.39*	*43.32*	*7.96*	*50.42*		*82.81*	*0.53*	*25.00*	*25.27*
60	*0.510*	*4.32*	*18.60*	*41*	*0.72*	*3110*	*27.82*	*28.51*	*40.58*	*41.24*	*7.57*	*48.86*	*73.19*	*78.98*	*0.69*	*25.76*	*25.85*
60	*0.626*	*2.33*	*54.14*	*79*	*1.44*	*3362*	*82.72*	*86.12*	*116.02*	*125.67*	*22.14*	*142.23*	*217.24*	*234.51*	*0.95*	*74.59*	*74.59*
60	*0.781*	*3.25*	*31.11*	*79*	*1.04*	*3395*	*46.40*	*48.62*	*71.91*	*69.80*	*12.58*	*88.39*	*130.33*	*139.53*	*-4.85*	*44.63*	*47.54*
60	*0.876*	*3.25*	*30.21*	*86*	*1.04*	*3388*	*44.47*	*46.65*	*68.70*	*67.27*	*12.49*	*76.95*	*121.55*	*130.04*	*-4.64*	*44.61*	*47.88*
60	*1.01*	*4.32*	*18.79*	*82*	*0.74*	*3217*	*28.90*	*28.76*	*41.07*	*40.95*	*7.78*	*48.10*	*72.59*	*79.49*	*-8.50*	*26.19*	*30.36*
60	*1.10*	*4.52*	*20.12*	*100*	*0.80*	*3601*	*29.99*	*32.03*	*44.78*	*45.90*	*8.49*	*58.58*	*83.61*	*91.33*	*-6.96*	*29.10*	*33.40*
60	*1.37*	*3.25*	*31.13*	*139*	*1.05*	*3397*	*47.19*	*49.19*	*71.16*	*70.96*	*13.12*	*79.00*	*119.16*	*133.23*	*-18.40*	*46.52*	*57.16*
60	*1.58*	*4.32*	*19.19*	*131*	*0.76*	*3286*	*28.71*	*29.72*	*40.32*	*42.84*	*7.89*	*49.54*	*78.25*	*82.33*	*-16.95*	*26.95*	*36.40*
60	*1.84*	*4.32*	*16.90*	*134*	*0.62*	*2691*	*25.77*	*26.18*	*37.19*	*38.02*	*7.04*	*43.89*	*66.06*	*71.94*	*-14.76*	*24.54*	*33.28*

Appendix C: Additional Figures

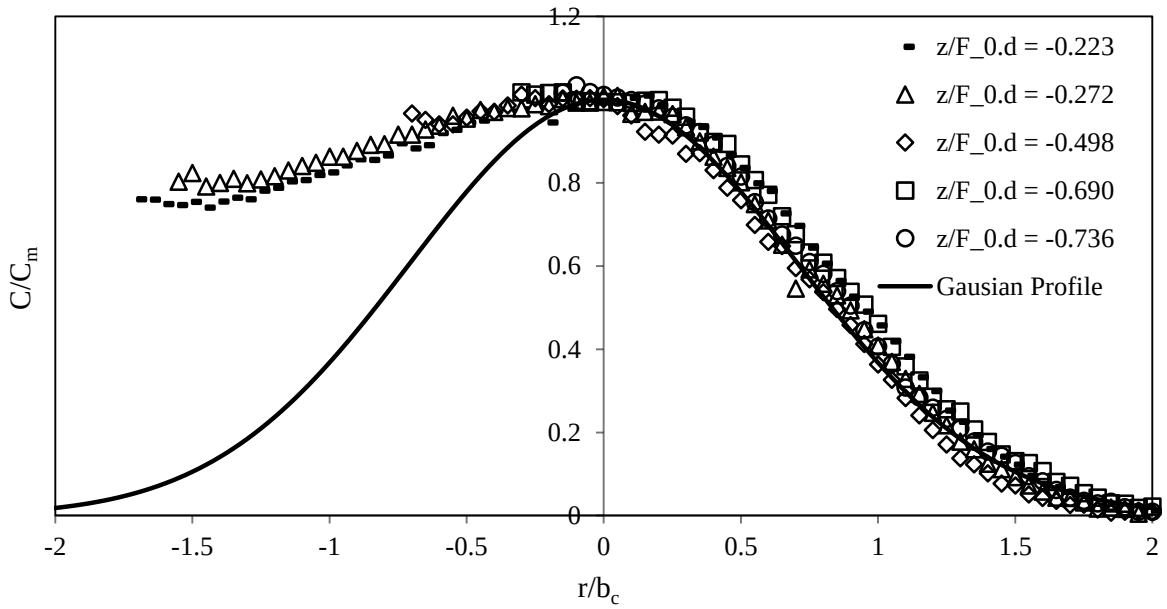

a) Time-averaged concentration profiles.

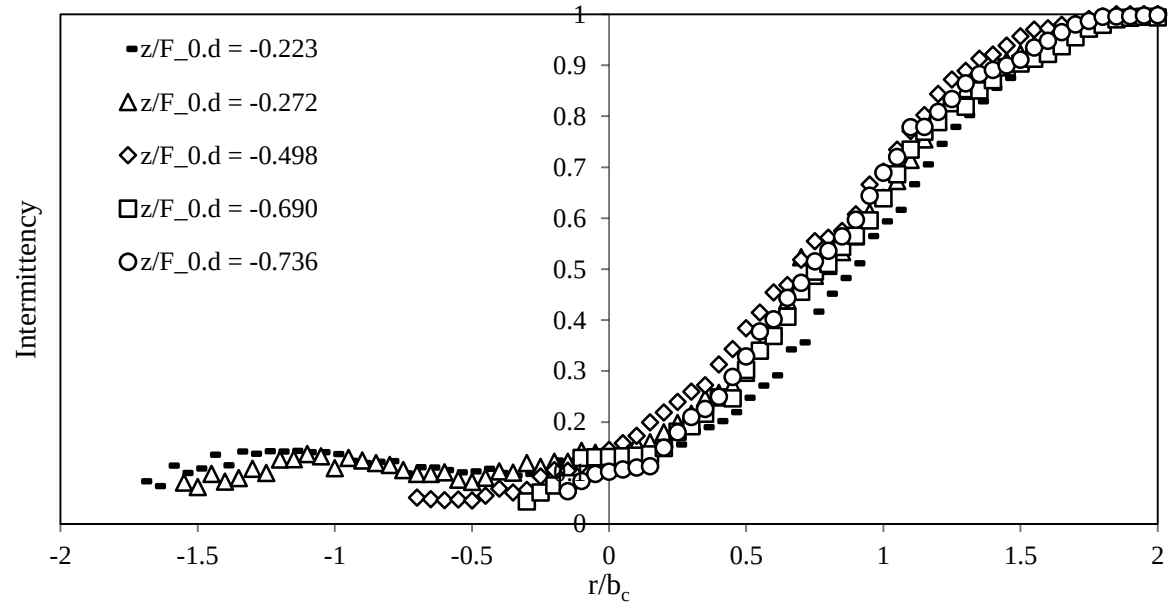

b) Intermittency profiles.

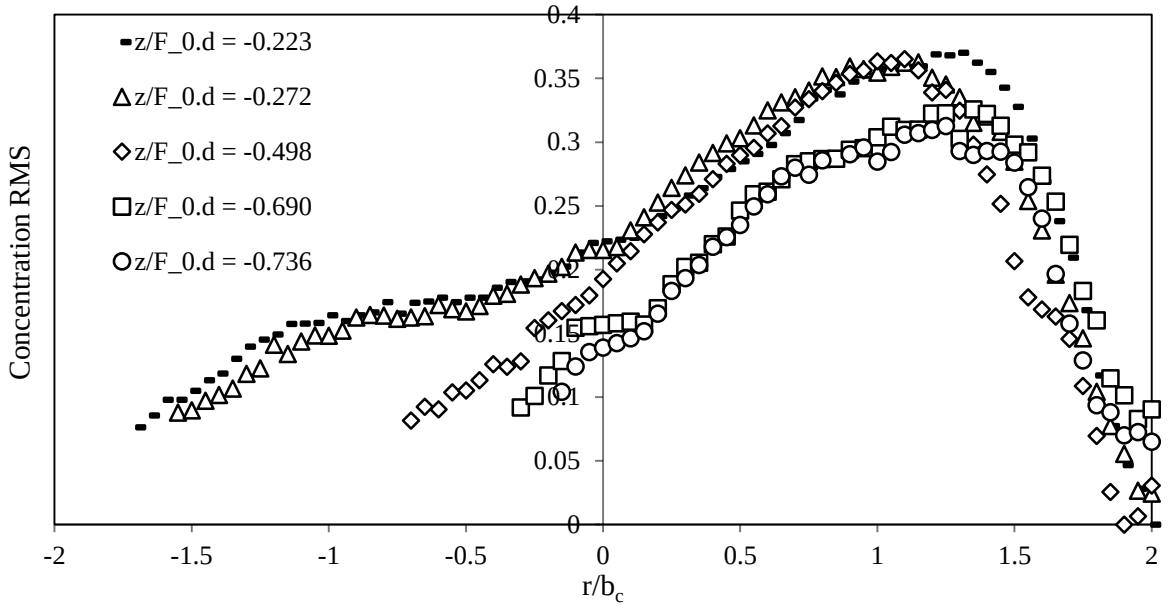

c) RMS concentration profiles.

Figure C.1: Flow profiles, 30º discharge, $H/F_0d = 0.822$, Re = 3598.

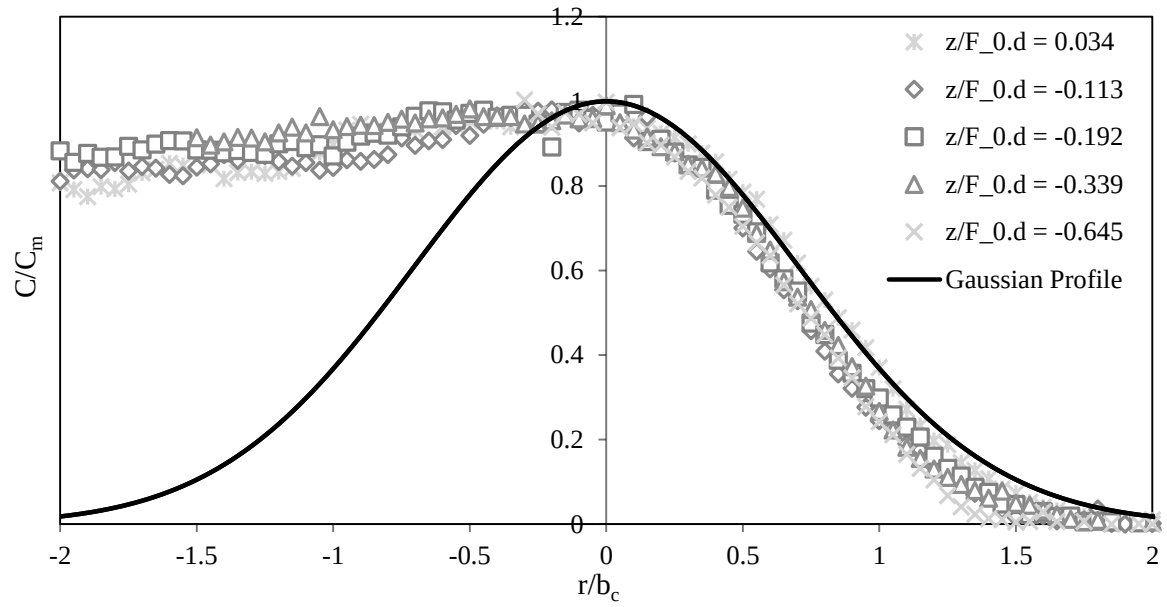

a) Time-averaged concentration profiles.

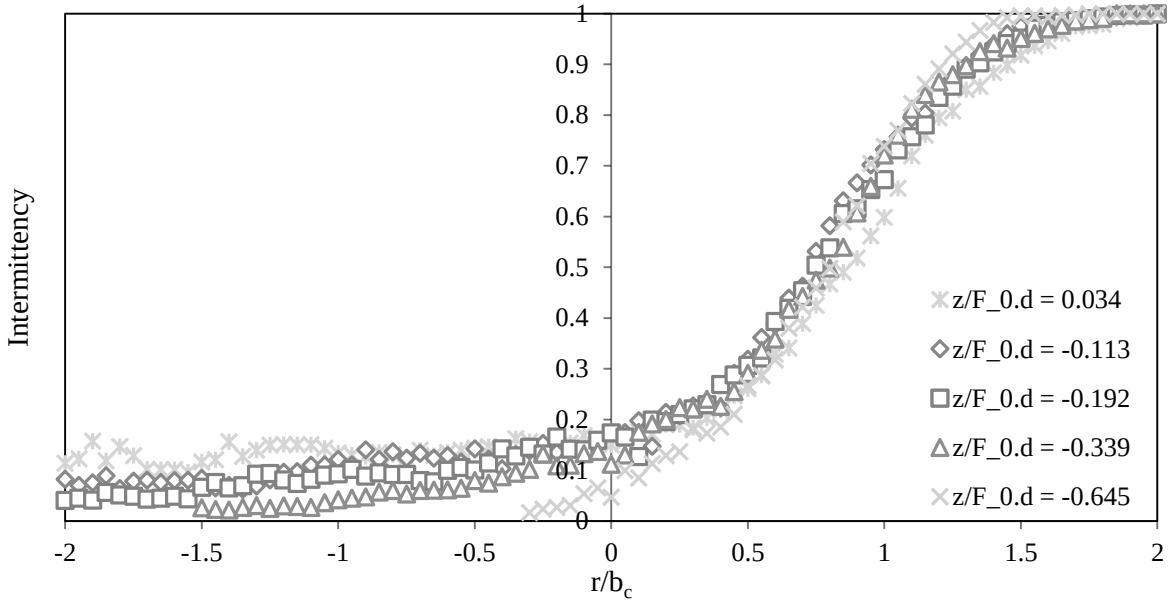

b) Intermittency profiles.

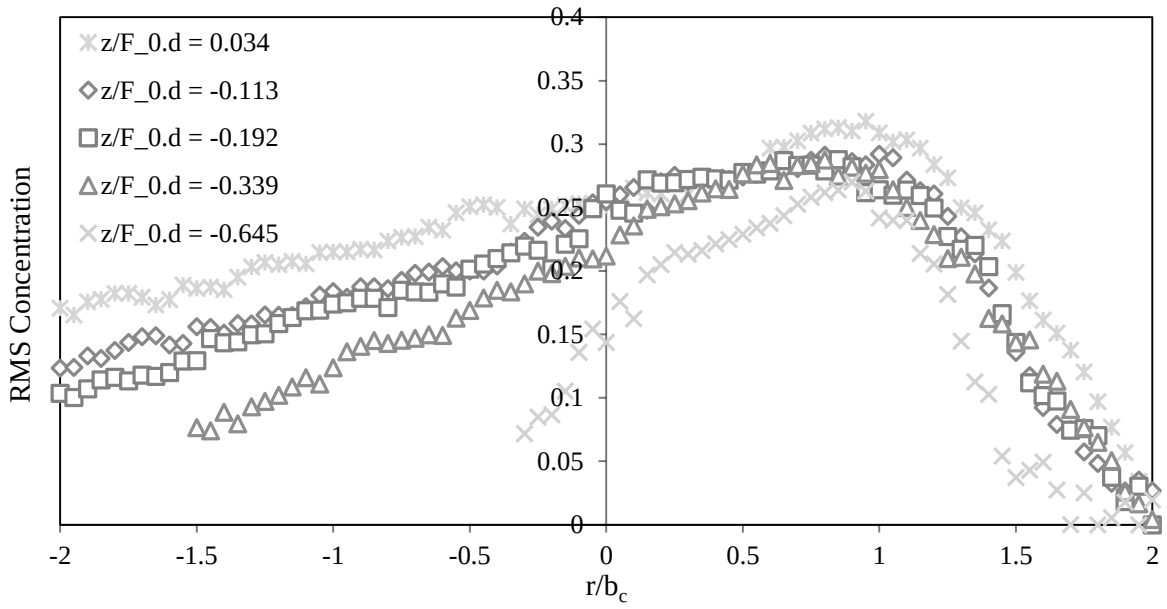

c) RMS concentration profiles.

Figure C.2: Flow profiles, 45º discharge, $H/F_0d = 0.822$, Re = 3611.

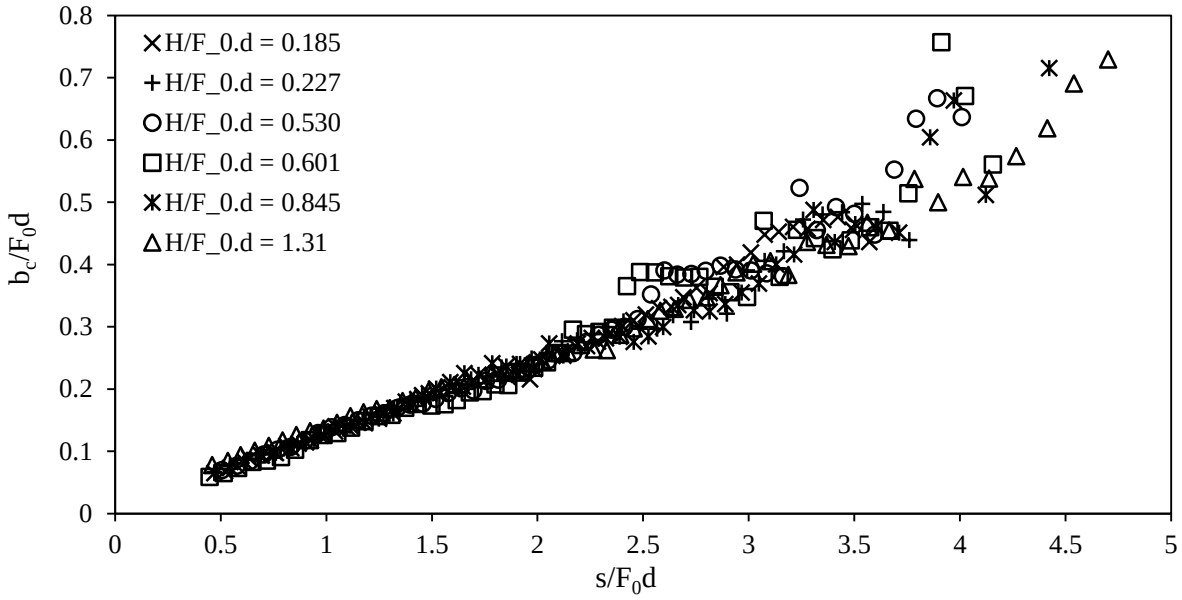

a) 30º Discharges.

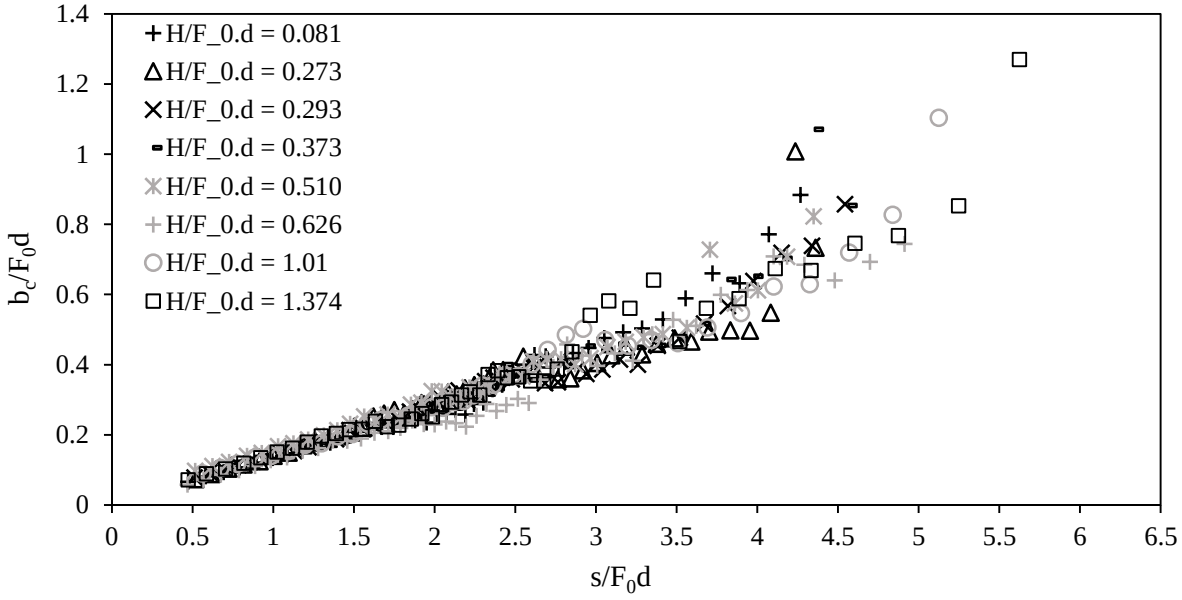

b) 60º Discharges.

Figure B.3: Outer spread measurements, Boundary Experiments.

References

Abessi, O., & Roberts, P. J. W. (2015). Effect of Nozzle Orientation on Dense Jets in Stagnant Environments. *Journal of Hydraulic Engineering,* 141(8).

Ahmad, N., & Baddour, R. E. (2014). A review of sources, effects, disposal methods, and regulations of brine into marine environments. *Ocean & Coastal Management, 87*, 1-7.

Al-Mutaz, I. S. (1996). A comparative study of RO and MSF desalination plants. *Desalination, 106*(1–3), 99-106.

Bashitialshaaer, R., Larson, M., & Persson, K. M. (2012). An Experimental Investigation on Inclined Negatively Buoyant Jets. *Water, 4*(3), 750-768.

Beltaos, S., & Rajaratnam, N. (1974). Impinging Circular Turbulent Jets. *Journal of the Hydraulics Division, 100*, 1313-1328.

Beltaos, S., & Rajaratnam, N. (1977). Impingement of Axisymmetric Developing Jets *Journal of Hydraulic Research, 15*(4), 311-326.

Birch, A. D., Cleaver, R. P., Fairweather, M., & Hargrave, G. K. (2005). Velocity and concentration field measurements in a turbulent, impinging flammable jet. *Chemical Engineering Science, 60*(1), 219-230.

Bleninger, T., & Jirka, G. (2010). Environmental planning, prediction and management of brine discharges from desalination plants: Middle East Desalination Research Center (MEDRC): Muscat, Sultanate of Oman.

Bloomfield, L. J., & Kerr, R. C. (2002). Inclined turbulent fountains. *Journal of Fluid Mechanics, 451*, 283-294.

Bosanquet, C. H., Horn, G., & Thring, M. W. (1961). The Effect of Density Differences on the Path of Jets. *Proceedings of the Royal Society of London. Series A, Mathematical and Physical Sciences, 263*(1314), 340-352.

Cavalletti, A., & Davies, P. A. (2003). Impact of Vertical, Turbulent, Planar, Negatively Buoyant Jet With Rigid Horizontal Bottom Boundary. *Journal of Hydraulic Engineering, 129*(1), 54-62.

Chen, J.-C. (1980). *Studies on gravitational spreading currents.* (Ph.D Thesis). California Institute of Technology, Pasadena, California.

Cheung, V., & Lee, J. H. W. (1990). Generalized Lagrangian Model for Buoyant Jets in Current. *Journal of Environmental Engineering, 116*(6), 1085-1106.

Christodoulou, G. C., Nikiforakis, I. K., Diamantis, T. D., & Stamou, A. I. (2015). Near-field dilution of a vertical dense jet impinging on a solid boundary. *Desalination and Water Treatment*, 1-8.

Cipollina, A., Brucato, A., Grisafi, F., & Nicosia, S. (2005). Bench-Scale Investigation of Inclined Dense Jets. *Journal of Hydraulic Engineering, 131*(11), 1017-1022.

Coherent Inc. (2016). *Verdi Family of OPSL and DPSS Pump Lasers.* Available at: http://www.coherent.com/products/?873/Verdi-Family-of-Lasers [Accessed 18 Jan. 2016].

Cooley, H. (2010). *Seawater Desalination: Panacea or Hype?* Available at: http://www.actionbioscience.org/environment/cooley.html#primer [Accessed 18 Jan. 2016].

Cooley, H., Ajami, N., & Heberger, M. (2013). Key Issues in Seawater Desalination in California: Marine Impacts. Oakland California: Pacific Institute.

Cooper, D., Jackson, D. C., Launder, B. E., & Liao, G. X. (1993). Impinging jet studies for turbulence model assessment—I. Flow-field experiments. *International Journal of Heat and Mass Transfer, 36*(10), 2675-2684.

Crimaldi, J. P. (2008). Planar laser induced fluorescence in aqueous flows. *Experiments in Fluids, 44*(6), 851-863.

Crowe, A. T. (2013). *Inclined negatively buoyant jets and boundary interaction.* (Ph.D Thesis), University of Canterbury, Christchurch.

Crowe, A. T., Davidson, M. J., & Nokes, R. I. (2015). Velocity measurements in inclined negatively buoyant jets. *Environmental Fluid Mechanics*. *16*, 503.

Crowe, A. T., Davidson, M. J., & Nokes, R. I. (2016). Modified reduced buoyancy flux model for desalination discharges. *Desalination, 378*, 53-59.

Danoun, R. (2007). *Desalination Plants: Potential impacts of brine discharge on marine life.* The Ocean Technology Group, University of Sydney.

Davidson, M. J., & Oliver, C. J. (2012). Desalination and the environment. In H. J. Fernando (Ed.), *Handbook of Environmental Fluid Mechanics, Vol 2: Systems, Pollution, Modeling, and Measurements* (pp. 41-54). Boca Raton: CRC Press, Taylor & Francis Group.

Didden, N., & Ho, C.-M. (1985). Unsteady separation in a boundary layer produced by an impinging jet. *Journal of Fluid Mechanics, 160*, 235-256.

Doneker, R. L., & Jirka, G. H. (1999). Discussion of Mixing in Inclined Dense Jets. *Journal of Hydraulic Engineering, 125*(3), 317-318.

Einav, R., Harussi, K., & Perry, D. (2003). The footprint of the desalination processes on the environment. *Desalination, 152*(1–3), 141-154.

El Saliby, I., Okour, Y., Shon, H. K., Kandasamy, J., & Kim, I. S. (2009). Desalination plants in Australia, review and facts. *Desalination, 247*(1), 1-14.

Fairweather, M., & Hargrave, G. (2002a). Experimental investigation of an axisymmetric, impinging turbulent jet. 1. Velocity field. *Experiments in Fluids, 33*(3), 464-471.

Fairweather, M., & Hargrave, G. (2002b). Experimental investigation of an axisymmetric, impinging turbulent jet. 2. Scalar field. *Experiments in Fluids, 33*(4), 539-544.

Ferrari, S., & Querzoli, G. (2004). *Sea discharge of brine from desalination plants: a laboratory model of negatively buoyant jets.* Paper presented at the MWWD 2004 – 3rd International Conference on Marine Waste Water Disposal and Marine Environment.

Ferrari, S., & Querzoli, G. (2010). Mixing and re-entrainment in a negatively buoyant jet. *Journal of Hydraulic Research, 48*(5), 632-640.

Ferrier, A. J., Funk, D. R., & Roberts, P. J. W. (1993). Application of optical techniques to the study of plumes in stratified fluids. *Dynamics of Atmospheres and Oceans, 20*(1), 155-183.

Fischer, H. B., List, E. J., Koh, C., Imberger, J., & Brooks, N. (1979). *Mixing in inland and coastal waters*. New York: Academic Press.

Ghaneeizad, S., Atkinson, J., & Bennett, S. (2015). Effect of flow confinement on the hydrodynamics of circular impinging jets: implications for erosion assessment. *Environmental Fluid Mechanics, 15*(1), 1-25.

Gibbons, J., Papapetrou, M., & Epp, C. (2008). Assessment of EU policy: Implications for the implementation of autonomous desalination units powered by renewable resources in the Mediterranean region. *Desalination, 220*(1–3), 422-430.

Gildeh, H., Mohammadian, A., Nistor, I., & Qiblawey, H. (2015). Numerical modeling of 30 and 45 degree inclined dense turbulent jets in stationary ambient. *Environmental Fluid Mechanics, 15*(3), 537-562.

Guillard, F., Fritzon, R., Revstedt, J., Trägårdh, C., Aldén, M., & Fuchs, L. (1998). Mixing in a confined turbulent impinging jet using planar laser-induced fluorescence. *Experiments in Fluids, 25*(2), 143-150.

International Desalination Association. (2014). Desalination by the Numbers. from http://idadesal.org/desalination-101/desalination-by-the-numbers/

Jirka, G. H. (2004). Integral Model for Turbulent Buoyant Jets in Unbounded Stratified Flows. Part I: Single Round Jet. *Environmental Fluid Mechanics, 4*(1), 1-56.

Karasso, P. S., & Mungal, M. G. (1997). PLIF measurements in aqueous flows using the Nd:YAG laser. *Experiments in Fluids, 23*(5), 382-387.

Khawaji, A. D., Kutubkhanah, I. K., & Wie, J.-M. (2008). Advances in seawater desalination technologies. *Desalination, 221*(1–3), 47-69.

Kikkert, G. (2006). *Buoyant jets with two and three-dimensional trajectories.* (Ph.D Thesis), University of Canterbury, Christchurch.

Kikkert, G., Davidson, M. J., & Nokes, R. I. (2007). Inclined Negatively Buoyant Discharges. *Journal of Hydraulic Engineering, 133*(5), 545-554.

Knowles, K., & Myszko, M. (1998). Turbulence measurements in radial wall-jets. *Experimental Thermal and Fluid Science, 17*(1–2), 71-78.

Koched, A., Pavageau, M., & Aloui, F. (2011). Experimental Investigations of Transfer Phenomena in a Confined Plane Turbulent Impinging Water Jet. *Journal of Fluids Engineering, 133*(6), 061204-061204.

Koop, C. G., & Browand, F. K. (1979). Instability and turbulence in a stratified fluid with shear. *Journal of Fluid Mechanics, 93*(1), 135-159.

Kubin, R. F., & Fletcher, A. N. (1982). Fluorescence quantum yields of some rhodamine dyes. *Journal of Luminescence, 27*(4), 455-462.

Lai, C. C. K., & Lee, J. H. W. (2012). Mixing of inclined dense jets in stationary ambient. *Journal of Hydro-environment Research, 6*(1), 9-28.

Lane-Serff, G. F., Linden, P. F., & Hillel, M. (1993). Forced, angled plumes. *Journal of Hazardous Materials, 33*(1), 75-99.

Lattemann, S., & Höpner, T. (2008). Environmental impact and impact assessment of seawater desalination. *Desalination, 220*(1–3), 1-15.

Law, A., & Herlina. (2002). An Experimental Study on Turbulent Circular Wall Jets. *Journal of Hydraulic Engineering, 128*(2), 161-174.

Lawrence, G. A., & Maclatchy, M. R. (2001). Radially spreading buoyant flows. *Journal of Hydraulic Research, 39*(6), 583-590.

Lean, G. H., & Willock, A. R. (1965). *The Behaviour of a Warm Water Layer Flowing over Sill Water*. Paper presented at the International Congress of Hydraulic Research, 11th Congress, Leningrad.

Lindberg, W. R. (1994). Experiments on Negatively Buoyant Jets, with and without Cross-Flow. In P. A. Davies & M. J. V. Neves (Eds.), *Recent Research Advances in the Fluid Mechanics of Turbulent Jets and Plumes* (Vol. 255, pp. 131-145): Springer Netherlands.

List, E. J. (1982). Turbulent Jets and Plumes. *Annual Review of Fluid Mechanics*, 14(1), 189-212.

MacLatchy, M. R. (1993). *Radial Spreading of Vertical Buoyant Jets in Shallow Water.* (MASc Thesis), University of British Columbia, Vancouver, Canada.

Marti, C. L., Antenucci, J. P., Luketina, D., Okely, P., & Imberger, J. (2011). Near-Field Dilution Characteristics of a Negatively Buoyant Hypersaline Jet Generated by a Desalination Plant. *Journal of Hydraulic Engineering, 137*(1), 57-65.

Maurel, S., & Solliec, C. (2001). A turbulent plane jet impinging nearby and far from a flat plate. *Experiments in Fluids, 31*(6), 687-696.

Morton, B. R., Taylor, G., & Turner, J. S. (1956). Turbulent Gravitational Convection from Maintained and Instantaneous Sources. *Proceedings of the Royal Society of London. Series A, Mathematical and Physical Sciences, 234*(1196), 1-23.

Nellen, A. (2011). Desalination: A Viable Answer to Deal with Water Crises? : Future Directions International.

Nemlioglu, S., & Roberts, P. J. W. (2006). *Experiments on dense jets using 3D laser-induced fluorescence.* Paper presented at the 4th Int. Conf., Marine Waste Water Disposal and Marine Environment & 2nd Int. Exhibition Materials Equipment and Services for Coastal WWTP, Outfalls and Sealines, Antalya, Turkey.

Oliver, C. J., Davidson, M. J., & Nokes, R. I. (2008). k-ε Predictions of the initial mixing of desalination discharges. *Environmental Fluid Mechanics, 8*(5-6), 617-625.

Oliver, C. J. (2012). *Near field mixing of negatively buoyant jets.* (Ph.D Thesis), University of Canterbury, Christchurch.

Oliver, C. J., Davidson, M. J., & Nokes, R. I. (2013). Removing the boundary influence on negatively buoyant jets. *Environmental Fluid Mechanics, 13*(6), 625-648.

Palomar, P., Lara, J. L., & Losada, I. J. (2012). Near field brine discharge modeling part 2: Validation of commercial tools. *Desalination, 290*, 28-42.

Papakonstantis, I. G., Christodoulou, G. C., & Papanicolaou, P. N. (2011a). Inclined negatively buoyant jets 1: geometrical characteristics. *Journal of Hydraulic Research, 49*(1), 3-12.

Papakonstantis, I. G., Christodoulou, G. C., & Papanicolaou, P. N. (2011b). Inclined negatively buoyant jets 2: concentration measurements. *Journal of Hydraulic Research, 49*(1), 13-22.

Papanicolaou, P. N., & List, E. J. (1988). Investigations of round vertical turbulent buoyant jets. *Journal of Fluid Mechanics, 195*, 341-391.

Poreh, M., Tsuei, Y. G., & Cermak, J. E. (1967). Investigation of a Turbulent Radial Wall Jet. *Journal of Applied Mechanics, 34*(2), 457-463.

Rajaratnam, N. (1976). *Turbulent jets* (Vol. 5). Amsterdam: Elsevier.

Rajaratnam, N., & Mazurek, K. A. (2005). Impingement of circular turbulent jets on rough boundaries. *Journal of Hydraulic Research, 43*(6), 689-695.

Rajaratnam, N., Zhu, D. Z., & Rai, S. P. (2010). Turbulence measurements in the impinging region of a circular jet. *Canadian Journal of Civil Engineering, 37*(5), 782-786.

Roberts, P. J. W., Daviero, G., & Ferrier, A. (1997). Mixing in Inclined Dense Jets. *Journal of Hydraulic Engineering, 123*(8), 693-699.

Roberts, P. J. W., Daviero, G., & Maile, K. (2001). Mixing in Stratified Jets. *Journal of Hydraulic Engineering, 127*(3), 194-200.

Roberts, P. J. W., & Toms, G. (1987). Inclined Dense Jets in Flowing Current. *Journal of Hydraulic Engineering, 113*(3), 323-340.

Shao, D., & Law, A. W.-K. (2010). Mixing and boundary interactions of 30° and 45° inclined dense jets. *Environmental Fluid Mechanics, 10*(5), 521-553.

Tani, I., & Komatsu, Y. (1966). Impingement of a round jet on a flat surface. In H. Görtler (Ed.), *Applied Mechanics* (pp. 672-676): Springer Berlin Heidelberg.

Tian, X., & Roberts, P. J. W. (2003). A 3D LIF system for turbulent buoyant jet flows. *Experiments in Fluids, 35*(6), 636-647.

Ulasir, M. (2001). *Experimental and numerical study of round, submerged buoyant jets impinging on a horizontal surface.* (Ph.D Thesis), University of Michigan.

Ulasir, M., & Wright, S. J. (2003). Influence of Downstream Control and Limited Depth on Flow Hydrodynamics of Impinging Buoyant Jets. *Environmental Fluid Mechanics, 3*(2), 85-107.

United Nations. (2003). Water for People, Water for Life *World Water Development Report*.

United Nations Environment Programme. (2007). Global Environment Outlook: environment for development.

Voutchkov, N. (2011). Overview of seawater concentrate disposal alternatives. *Desalination, 273*(1), 205-219.

Wang, H., & Law, A. (2002). Second-order integral model for a round turbulent buoyant jet. *Journal of Fluid Mechanics, 459*, 397-428.

Wangnick, K. (2004). IDA Worldwide Desalting Plants Report No. 18: Wangnick Consulting GmbH, 27442 Gnarrenburg, Germany.

Webster, D. R., Rahman, S., & Dasi, L. P. (2003). Laser-Induced Fluorescence Measurements of a Turbulent Plume. *Journal of Engineering Mechanics, 129*(10), 1130-1137.

Welker Environmental Consultancy, Western Australia Environmental Protection Authority, & Water Corporation Western Australia. (2002). Perth metropolitan desalination proposal environmental protection statement: Welker Environmental Consultancy.

Wilkinson, D. L., & Wood, I. R. (1971). A rapidly varied flow phenomenon in a two-layer flow. *Journal of Fluid Mechanics, 47*(02), 241-256.

Wright, S. J., Roberts, P. J. W., Zhongmin, Y., & Bradley, N. E. (1991). Surface dilution of round submerged buoyant jets. *Journal of Hydraulic Research, 29*(1), 67-89.

Wright, S. J., & Ulasir, M. (2000). *Mixing controlled by buoyancy in submerged turbulent jets impinging on a free surface*. Paper presented at the Fifth International Symposium on Stratified Flows, Vancouver, Canada.

Yannopoulos, P. C., & Bloutsos, A. A. (2012). Escaping mass approach for inclined plane and round buoyant jets. *Journal of Fluid Mechanics, 695*, 81-111.

Zeitoun, M. A., Mcllhenny, W. F., & Reid, R. O. (1970). Conceptual designs of outfall systems for desalting plants. Washington, D.C., 1139.: U.S. Dept of the Interior.

Zhang, S., Jiang, B., Law, A., & Zhao, B. (2015). Large eddy simulations of 45° inclined dense jets. *Environmental Fluid Mechanics*, 1-21.